144
Structure and Bonding

Series Editor: D. M. P. Mingos

Editorial Board:
F. A. Armstrong · P. Day · X. Duan · L. H. Gade
K. R. Poeppelmeier · G. Parkin · J.-P. Sauvage ·
M. Takano

For further volumes:
http://www.springer.com/series/430

Structure and Bonding

Series Editor: D. M. P. Mingos

Recently Published and Forthcoming Volumes

Structure-Property Relationships in Non-Linear Optical Crystals I
Volume Editors: Xin-Tao Wu, Ling Chen
Vol. 144, 2012

Molecular Electronic Structures of Transition Metal Complexes II
Volume Editors: D. M. P. Mingos, Peter Day, Jens Peder Dahl
Vol. 143, 2012

Molecular Electronic Structures of Transition Metal Complexes I
Volume Editors: D. M. P. Mingos, Peter Day, Jens Peder Dahl
Vol. 142, 2012

Fuel Cells and Hydrogen Storage
Volume Editors: Andrew Bocarsly, D. M. P. Mingos
Vol. 141, 2011

Zintl Ions
Principles and Recent Developments
Volume Editor: Thomas F. Fässler
Vol. 140, 2011

Zintl Phases
Principles and Recent Developments
Volume Editor: Thomas F. Fässler
Vol. 139, 2011

Inorganic 3D Structures
Volume Editor: Angel Vegas
Vol. 138, 2011

Molecular Catalysis of Rare-Earth Elements
Volume Editor: Peter W. Roesky
Vol. 137, 2010

Metal-Metal Bonding
Volume Editor: Gerard Parkin
Vol. 136, 2010

Functional Phthalocyanine Molecular Materials
Volume Editor: Jianzhuang Jiang
Vol. 135, 2010

Data Mining in Crystallography
Volume Editors: Hofmann, D. W. M., Kuleshova, L. N.
Vol. 134, 2010

Controlled Assembly and Modification of Inorganic Systems
Volume Editor: Wu, X.- T.
Vol. 133, 2009

Molecular Networks
Volume Editor: Hosseini, M. W.
Vol. 132, 2009

Molecular Thermodynamics of Complex Systems
Volume Editors: Lu, X., Hu, Y.
Vol. 131, 2009

Contemporary Metal Boron Chemistry I
Volume Editors: Marder, T. B., Lin, Z.
Vol. 130, 2008

Recognition of Anions
Volume Editor: Vilar, R.
Vol. 129, 2008

Liquid Crystalline Functional Assemblies and Their Supramolecular Structures
Volume Editor: Kato, T.
Vol. 128, 2008

Organometallic and Coordination Chemistry of the Actinides
Volume Editor: Albrecht-Schmitt, T. E.
Vol. 127, 2008

Halogen Bonding
Fundamentals and Applications
Volume Editors: Metrangolo, P., Resnati, G.
Vol. 126, 2008

High Energy Density Materials
Volume Editor: Klapötke, T. H.
Vol. 125, 2007

Structure-Property Relationships in Non-Linear Optical Crystals I

The UV-Vis Region

Volume Editors:
Xin-Tao Wu · Ling Chen

With contributions by

A. Brenier · W.-D. Cheng · M.-C. Hong · Y.-Z. Huang · F. Kong · J.-F. Li · C.-S. Lin · J.-G. Mao · C.-F. Sun · C.-Y. Tu · Y. Wang · G.-F. Wang · L.-M. Wu · B.-P. Yang · N. Ye · Z. You · W.-L. Zhang · H. Zhang · Z.-J. Zhu

Springer

Editors
Xin-Tao Wu
Ling Chen

Fujian Institute of Research on the
Structure of Matter (FJIRSM)
Chinese Academy of Sciences
Fuzhou, Fujian
China

ISSN 0081-5993 ISSN 1616-8550 (electronic)
ISBN 978-3-642-29617-8 ISBN 978-3-642-29618-5 (eBook)
DOI 10.1007/978-3-642-29618-5
Springer Heidelberg New York Dordrecht London

Library of Congress Control Number: 2012938650

© Springer-Verlag Berlin Heidelberg 2012
This work is subject to copyright. All rights are reserved by the Publisher, whether the whole or part of the material is concerned, specifically the rights of translation, reprinting, reuse of illustrations, recitation, broadcasting, reproduction on microfilms or in any other physical way, and transmission or information storage and retrieval, electronic adaptation, computer software, or by similar or dissimilar methodology now known or hereafter developed. Exempted from this legal reservation are brief excerpts in connection with reviews or scholarly analysis or material supplied specifically for the purpose of being entered and executed on a computer system, for exclusive use by the purchaser of the work. Duplication of this publication or parts thereof is permitted only under the provisions of the Copyright Law of the Publisher's location, in its current version, and permission for use must always be obtained from Springer. Permissions for use may be obtained through RightsLink at the Copyright Clearance Center. Violations are liable to prosecution under the respective Copyright Law.
The use of general descriptive names, registered names, trademarks, service marks, etc. in this publication does not imply, even in the absence of a specific statement, that such names are exempt from the relevant protective laws and regulations and therefore free for general use.
While the advice and information in this book are believed to be true and accurate at the date of publication, neither the authors nor the editors nor the publisher can accept any legal responsibility for any errors or omissions that may be made. The publisher makes no warranty, express or implied, with respect to the material contained herein.

Printed on acid-free paper

Springer is part of Springer Science+Business Media (www.springer.com)

Series Editor

Prof. D. Michael P. Mingos

Inorganic Chemistry Laboratory
Oxford University
South Parks Road
Oxford OX1 3QR, UK
michael.mingos@st-edmund-hall.oxford.ac.uk

Volume Editors

Xin-Tao Wu
Ling Chen

Fujian Institute of Research on the
Structure of Matter (FJIRSM)
Chinese Academy of Sciences
Fuzhou, Fujian
China

Editorial Board

Prof. Fraser Andrew Armstrong

Department of Chemistry
Oxford University
Oxford OX1 3QR
UK

Prof. Peter Day

Director and Fullerian Professor
of Chemistry
The Royal Institution of Great Britain
21 Albermarle Street
London W1X 4BS, UK
pday@ri.ac.uk

Prof. Xue Duan

Director
State Key Laboratory
of Chemical Resource Engineering
Beijing University of Chemical Technology
15 Bei San Huan Dong Lu
Beijing 100029, P.R. China
duanx@mail.buct.edu.cn

Prof. Lutz H. Gade

Anorganisch-Chemisches Institut
Universität Heidelberg
Im Neuenheimer Feld 270
69120 Heidelberg, Germany
lutz.gade@uni-hd.de

Prof. Dr. Kenneth R. Poeppelmeier

Department of Chemistry
Northwestern University
2145 Sheridan Road
Evanston, IL 60208-3133
USA
krp@northwestern.edu

Prof. Gerard Parkin

Department of Chemistry (Box 3115)
Columbia University
3000 Broadway
New York, New York 10027, USA
parkin@columbia.edu

Prof. Jean-Pierre Sauvage

Faculté de Chimie
Laboratoires de Chimie
Organo-Minérale
Université Louis Pasteur
4, rue Blaise Pascal
67070 Strasbourg Cedex, France
sauvage@chimie.u-strasbg.fr

Prof. Mikio Takano

Institute for Integrated Cell-Material
Sciences (iCeMS)
Kyoto University
Yoshida Ushinomiya-cho
Sakyo-ku
Kyoto 606-8501
Japan

Structure and Bonding
Also Available Electronically

Structure and Bonding is included in Springer's eBook package *Chemistry and Materials Science*. If a library does not opt for the whole package the book series may be bought on a subscription basis. Also, all back volumes are available electronically.

For all customers who have a standing order to the print version of *Structure and Bonding*, we offer the electronic version via SpringerLink free of charge.

If you do not have access, you can still view the table of contents of each volume and the abstract of each article by going to the SpringerLink homepage, clicking on "Chemistry and Materials Science," under Subject Collection, then "Book Series," under Content Type and finally by selecting *Structure and Bonding*.

You will find information about the

– Editorial Board
– Aims and Scope
– Instructions for Authors
– Sample Contribution

at springer.com using the search function by typing in *Structure and Bonding*.

Color figures are published in full color in the electronic version on SpringerLink.

Aims and Scope

The series *Structure and Bonding* publishes critical reviews on topics of research concerned with chemical structure and bonding. The scope of the series spans the entire Periodic Table and addresses structure and bonding issues associated with all of the elements. It also focuses attention on new and developing areas of modern structural and theoretical chemistry such as nanostructures, molecular electronics, designed molecular solids, surfaces, metal clusters and supramolecular structures. Physical and spectroscopic techniques used to determine, examine and model structures fall within the purview of *Structure and Bonding* to the extent that the focus

is on the scientific results obtained and not on specialist information concerning the techniques themselves. Issues associated with the development of bonding models and generalizations that illuminate the reactivity pathways and rates of chemical processes are also relevant.

The individual volumes in the series are thematic. The goal of each volume is to give the reader, whether at a university or in industry, a comprehensive overview of an area where new insights are emerging that are of interest to a larger scientific audience. Thus each review within the volume critically surveys one aspect of that topic and places it within the context of the volume as a whole. The most significant developments of the last 5 to 10 years should be presented using selected examples to illustrate the principles discussed. A description of the physical basis of the experimental techniques that have been used to provide the primary data may also be appropriate, if it has not been covered in detail elsewhere. The coverage need not be exhaustive in data, but should rather be conceptual, concentrating on the new principles being developed that will allow the reader, who is not a specialist in the area covered, to understand the data presented. Discussion of possible future research directions in the area is welcomed.

Review articles for the individual volumes are invited by the volume editors.

In references *Structure and Bonding* is abbreviated *Struct Bond* and is cited as a journal.

Impact Factor in 2010: 4.659; Section “Chemistry, Inorganic & Nuclear”:
Rank 4 of 43; Section “Chemistry, Physical”: Rank 25 of 127

In memory of the 100th birthday of Prof. Jia-Xi Lu (1915–2015)
Dedicated to Fujian Institute of Research on the Structure of Matter, Chinese Academy of Sciences, on the occasion of its 55th anniversary (1960–2015)

Preface

Nonlinear optics (NLO) is a branch of optics which describes the behavior of light in *nonlinear media*, that is, media in which the dielectric polarization P responds nonlinearly to the electric field E of the light. This nonlinearity is generally only observed at very high light intensities such as those provided by pulsed lasers. The discovery of lasers in the 1960s revolutionized the study of nonlinear optical materials. Nonlinear optics gives rise to a host of optical phenomena based on the frequency mixing processes such as second, third, and higher harmonic generation, sum and difference frequency generation, optical parametric amplification, oscillation and generation, and optical rectification. Nonlinear optics is now a multidisciplinary field of study, which incorporates not only fundamental studies on the theoretical basis of the phenomenon, but also the fabrication of nonlinear optical devices and the discovery of new nonlinear optical crystalline materials. New crystalline materials are of great importance to the development of the field of nonlinear optics, especially since the continuous discovery of novel, effective, high quality of nonlinear optical crystals provides great opportunities for the development of nonlinear devices, which promote the wide application of laser frequency conversion techniques in many fields, such as laser communication, laser medical treatment, laser nuclear fusion, laser distance measurement, and fundamental spectroscopic research.

In 1960, the founder of Fujian Institute of Research on the Structure of Matter, Chinese Academy of Sciences (FJIRSM), Prof. Jia-Xi Lu, initiated and motivated a comprehensive research base in China specializing in structural chemistry and new crystalline materials. After more than 50 years of untiring efforts, the Institute remains devoted to this area of fundamental research and the development manufacturing and marketing of a wide range of nonlinear optical crystals. CASTECH, the company founded by FJIRSM in 1988, has become the leading supplier for LBO, BBO, and numerous other nonlinear optical crystals in the world.

We have organized two volumes to summarize some of the recent progress in the field focusing particularly on structure–property relationships in nonlinear optical crystals. Volume 144 is devoted to the UV-vis region and contains six review-type chapters written by seven of our faculty members who are the leading scientists in

their fields. These chapters discuss the structural design and characterization of second-harmonic generation materials by Prof. W.-D. Cheng; the nonlinear optical properties of iodates, selenites, and tellurites by Prof. J.-G. Mao; the structure, growth, nonlinear optics, and laser properties of $RX_3(BO_3)_4$ by Prof. G.-F. Wang; the self-frequency conversion of borate laser crystals by Prof. C.-Y. Tu; the structure design and crystal growth of UV borates by Prof. N. Ye, and cation effects in doped BBO and halogen anion effects in $Pb_2B_5O_9X$ by Profs. L.-M. Wu and M.-C. Hong.

We wish to acknowledge our deep appreciations for all of the authors who unselfishly spent their most precious time writing contributions for this volume. We also gratefully acknowledge the continuous support from CAS, NNSF, MOST, and Fujian Province.

Fuzhou Xin-Tao Wu and Ling Chen
April 2012

Contents

Structural Designs and Property Characterizations for Second-Harmonic Generation Materials 1
Wen-Dan Cheng, Chen-Sheng Lin, Wei-Long Zhang, and Hao Zhang

Second-Order Nonlinear Optical Materials Based on Metal Iodates, Selenites, and Tellurites 43
Fang Kong, Chuan-Fu Sun, Bing-Ping Yang, and Jiang-Gao Mao

Structure, Growth, Nonlinear Optics, and Laser Properties of $RX_3(BO_3)_4$ (R = Y, Gd, La; X = Al, Sc) 105
Guo-Fu Wang

The Recent Development of Borate SF-Conversion Laser Crystal 121
Chaoyang Tu, Zhaojie Zhu, Zhenyu You, Jianfu Li, Yan Wang, and Alain Brenier

Structure Design and Crystal Growth of UV Nonlinear Borate Materials 181
Ning Ye

Cation Effect in Doped BBO and Halogen Anion Effect in $Pb_2B_5O_9X$ ($X^- = I^-$, Br^-, Cl^-) 223
Yi-Zhi Huang, Li-Ming Wu, and Mao-Chun Hong

Index 235

Struct Bond (2012) 144: 1–42
DOI: 10.1007/430_2011_64
© Springer-Verlag Berlin Heidelberg 2012
Published online: 31 January 2012

Structural Designs and Property Characterizations for Second-Harmonic Generation Materials

Wen-Dan Cheng, Chen-Sheng Lin, Wei-Long Zhang, and Hao Zhang

Abstract Second-harmonic generation (SHG) materials only exist in solids that have no inversion center space groups, and they are constructed by the building blocks or chromophores of noncentrosymmetricity (NCS). In this chapter, we employed one or multiple chromophores that result from the coordination structure distortions of a d^0 cation, polar displacement of d^{10} cation center, a stereochemically active lone pair (SCALP) of cations, and asymmetrical delocalization π-charge systems, as building blocks to obtain some new compounds with NCS space group. The single-crystal structures were characterized, and physical properties, in particular SHG responses, were measured for these compounds. The electronic structures and density of states were calculated by DFT method, and the SHG properties are simulated to gain an insight into the relations between structure and NLO properties for the materials. The electronic origination of large SHG responses was assigned in terms of the calculated results.

Keywords Density functional theory calculations · Photophysical characterization · Second-order harmonic generation · Structural design

Contents

1 Introduction 2
2 POA Crystal by Packing of Chromophores with π-Charge Asymmetrical Distributions . 3
2.1 Syntheses of POA and Descriptions of the Crystal Structure 3
2.2 Electronic Spectra and Second-Harmonic Generations of POA 8
3 Effect of Lone Pair on SHG Responses in Eulytite-Type Compounds of $Pb_3Bi(PO_4)_3$ and $Ba_3Bi(PO_4)_3$ 14
3.1 Preparation Processes and Structural Descriptions 14
3.2 Electronic Structures and SHG Properties 17

W.-D. Cheng (✉), C.-S. Lin, W.-L. Zhang, and H. Zhang
State Key Laboratory of Structural Chemistry Fujian Institute of Research on the Structure of Matter, Chinese Academy of Sciences, Fuzhou 350002, People's Republic of China
e-mail: cwd@fjirsm.ac.cn

4 ZnO-Based SHG Materials of KZn_4SbO_7 and $KZn_4Sb_3O_{12}$ 20
4.1 Simple Descriptions of Synthesis and Structures of KZn_4SbO_7 and $KZn_4(SbO_4)_3$. 20
4.2 Second-Harmonic Generation Investigations 23
5 A Strong SHG Material $Cd_4BiO(BO_3)_3$ with 3-Chromophore Asymmetric Building Units 28
5.1 Preparation and Structure of Single Crystal of CBOB 29
5.2 Electronic Structural Calculations of CBOB 32
5.3 Investigations of Nonlinear Optical Response of CBOB 34
6 Conclusions 38
References 39

1 Introduction

The development of NLO can be essentially traced to the improvement of the performances of the NLO materials [1–8]. At the first demonstration of SHG, a weak output signal was recorded on photographic paper when a quartz crystal was used as NLO media and a ruby laser was used as incident light resource [9]. It has became the most popular for visible and UV applications since beta-barium borate (β-BBO) crystal was discovered [10, 11]; the applications of lithium triborate (LBO) [12] mainly concentrated around SHG of near IR radiation and OPO (optical parametric oscillator) in visible and near IR ranges. Lithium niobate (LN) has very high value of effective second-order nonlinear coefficient along optical axis, and the periodically poled LN has become one of the most popular nonlinear materials since the 1990s [13, 16]. Potassium titanyl phosphate (KTP) is a basic NLO crystal for the construction of compact visible solid-state laser systems applied to diode-pumped Nd:laser [15]. We believe that it will be higher demands for the nature and performance of NLO materials with the developments of laser technology and scientific experiments. In short, large frequency-doubling coefficients and figure of merit (FOM) are essentials for NLO material applications. They depend on the inherent nature of the material, in which the FOM value is proportional to the square of the SHG effective coefficient and inversely proportional to about cube of the refractive index ($\mathrm{FOM} = d_{\mathrm{eff}}^2/n_\omega^2 n_{2\omega}$) [16]. Now, the understanding of the material structure characteristics relating with the NLO mechanisms has been considerably improved. The new development of the fabrication techniques and growth of artificial materials has dramatically contributed to this evolution.

It is known that SHG response requires noncentrosymmetricity (NCS), and so it only exists in solids that have no inversion center space groups. Crystallographically, the 230 space groups can be classified into 32 classes or point groups, in which 20 are not a center of symmetry except of point group 432 (or O). Accordingly, NLO behavior is achieved by off-centering of ions in polyhedra or NCS chromophores cooperatively effect in solid-state materials. Here, the chromophore can result from the coordination structure distortion of a d^0 cation with a second-order Jahn–Tellere effect [17–19], polar displacement of d^{10} cation centers [20], distortion from a stereochemically active lone pair (SCALP) of cations [21, 22], or borate π-orbital systems [23–25]. Sometimes, two NCS chromophores occur naturally in the same material [17, 26–28]. For example, $PbTiO_3$ has a SCALP on the Pb

ion, as well as SOJT off-centering of the Ti [27]. However, only one example of three-chromophore asymmetrical building units existing in the same SHG material has been reported until now [29].

In this chapter, we will describe some new NLO materials with a large SHG response by the controlling cooperativity of NCS chromophore and the choices of the chromophore that will lead to asymmetrical distortion, and we will calculate the electronic structures and simulate NLO properties to gain an insight into the relations between structure and NLO properties for the materials. We will introduce that the NLO crystal material of 2-carboxylic acid-4-nitropyridine-1-oxide (POA) was synthesized to use POA chromophore with π-charge asymmetrical distortion, and charge transfers among the chromophores make great contribution to SHG response of POA crystal [30]. We will discuss lone-pair enhancement of SHG responses in inorganic solid-state compound of $Pb_3Bi(PO_4)_3$, and three off-centering chromophores cooperative effect led to a strong SHG material of $Cd_4BiO(BO_3)_3$ [29, 31].

2 POA Crystal by Packing of Chromophores with π-Charge Asymmetrical Distributions

In this respect, we develop two new crystals as candidates of second-order nonlinear optical (NLO) materials with the choice of chromophore and crystal engineering method [32–34]. First, we design a new chromophore of 2-carboxylic acid-4-nitropyridine-1-oxide (POA) with large hyperpolarizability, then we control growing conditions to obtain two POA crystals with two different crystallizing forms but with the same space group [30].

2.1 Syntheses of POA and Descriptions of the Crystal Structure

A mixture of glacial acetic acid and pyridine-2-carboxylic acid contained in a round-bottomed flask was shaken, with cold (0–5°C) 30% hydrogen peroxide added, and the mixture was heated in an oil bath for 24 h. After the excess acetic acid and water were removed under reduced pressure, the residue was cooled to 0–5°C in an ice–salt bath, and cold (0–5°C) 40% aqueous sodium hydroxide solution was added slowly with shaking and neutralized with shaking. The solution was extracted with chloroform, and the extracts were filtered and concentrated by distillation under reduced pressure. The residue was cooled, and the white crystalline powder of POA was obtained. This white powder is of mp. 172 ± 0.5°C. The white powder of this middle product was added to cold (0–5°C) sulfuric acid (sp. gr. 1.84) contained in a round-bottomed flask immersed in an ice–salt bath. The resulting mixture was cooled to about 10°C, and fuming yellow nitric acid was

added with shaking. An efficient spiral condenser was attached to the flask, and latter was placed in an oil bath. The temperature was slowly raised to 95–100°C, and the heating was continued at 100–105°C for 4 h. The reaction mixture was cooled to 10°C and poured onto crushed ice contained in a beaker. Addition of sodium carbonate monohydrate in small portions with stirring caused the separation of the yellow crystalline product along with sodium sulfate. The mixture was then allowed to stand for 3 h to expel nitrogen oxides. The yellow solid was collected by suction filtration, thoroughly washed with water, and rendered as dry as possible on the filter. The filtrates were transferred to separator funnel. The collected solid was extracted with portions of boiling chloroform, the combined extracts were used to extract the aqueous filtrates contained in the separator funnel, and the extraction was repeated with several fresh portions of chloroform. The combined chloroform extracts were given preliminary drying over anhydrous sodium sulfate and evaporated to dryness by distillation under reduced pressure. The pale-yellow-colored product of POA was filtered by suction, the filtrates were removed and saved, and the collected solid was washed with ether and dried. The pale yellow powder of POA is of mp. 146 ± 1°C. The synthetic route of POA is outlined in Scheme 1.

The pale yellow powder of POA was dissolved in boiling mixture of methanol and dichloromethane to obtain POA crystals. The solution was cooled to about 30°C and carefully filtered. The filtered solution was maintained at few degrees above the saturation temperature for homogenization, and the microcrystals were formed in the mother liquid. It was placed in the constant temperature bath whose temperature was controlled to the accuracy of 35 ± 0.05°C to ensure microcrystal to be dissolved sufficiently. Growth commenced at this temperature. Solvent evaporation was controlled by tight covering at the top of the beakers using polyethene sheets. Transparent pale-yellow-colored crystal (POA-I crystal) was harvested after a period of 20 days, mp. 148 ± 0.5°C. The grown crystal was prism in shape and had the dimensions of 4.0 × 3.0 × 3.0 mm^3. A mixture of dichloromethane and pale yellow powder of POA was added to a mixture of methanol and potassium hydroxide. After 48 h, a mixture of water and glacial acetic acid that serves as a pH control was added to the abovementioned mixture

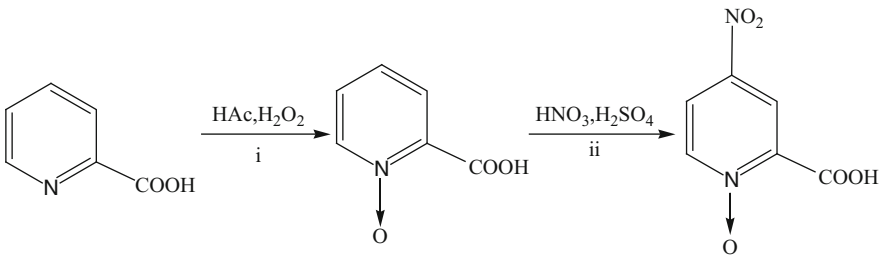

Scheme 1 Preparation of POA. (*i*) Pyridine-2-carboxylic acid, glacial acetic acid, 30% hydrogen peroxide, 80°C oil bath for 24 h; (*ii*) sulfuric acid (sp. gr. 1.84), fuming yellow nitric acid, 100–105°C oil bath for 4 h

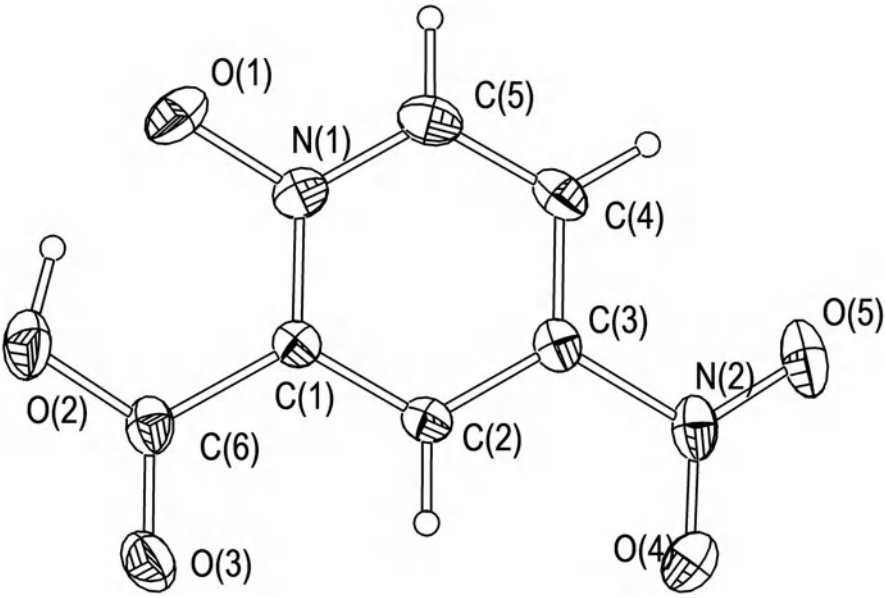

Fig. 1 ORTEP diagram of POA

and carefully filtered. Transparent pale-yellow-colored crystal (POA-II crystal) was harvested after a period of 7 days, mp. 156 ± 0.5°C. The grown crystal was needle in shape and had the dimensions of 0.80 × 0.18 × 0.14 mm^3.

POA-I and POA-II crystal structures were determined by single-crystal X-ray diffraction at room temperature and solved by direct methods [30]. The molecular configuration parenthesis atomic symbol of POA is presented in Fig. 1, and selected interatomic distances and angles are presented in Table 1.

Single-crystal X-ray analysis showed that the atoms of crystal POA-I are all in a plane. Its least-square equation is 6.389(5) X + 2.944 (1) Y − 6.565(3) Z − 2.064 (4) Å = 0 with 0.0704 Å of r.m.s. deviation. The length of O(1)–N(1) bond (1.323 (2) Å) is longer than the corresponding bond (1.285(3) Å) in 2-POM and the bond (1.288(2) Å) in POM [35, 36]. The length of C(3)–N(2) bond (1.469(3) Å) is longer than the corresponding bond (1.450(3) Å) in 2-POM and is in an agreement with the corresponding bond (1.460(3) Å) in POM. The lengths of O(4)–N(2) and O(5)–N(2) bonds (1.218(3) Å and 1.221(3) Å) are in agreement with the corresponding bonds (1.223(3) Å and 1.238(3) Å) in 2-POM and bonds (1.224(3) Å and 1.226(3) Å) in POM. The environments of oxygen atoms in carbonic acid are not the same. One oxygen (O(2)) is linked by a hydrogen (the length of O(2)–H(02) is 1.0701 Å), and another (O(3)) is not. The length of O(3)–C(6) bond (1.203(3) Å) is shorter than that of O(2)–C(6) (1.305(3) Å). There are intramolecular hydrogen bonds in the crystal POA-I. The hydrogen bond length of O(2)–H···O(1) is 2.460(2) Å. The angle of O(2)–H···O(1) hydrogen bond is 159.6°. There are four molecules in one unit cell.

Table 1 Selected bond lengths (Å) and angles (°) of POA crystals

Bond (Å)	Crystal I	Crystal II
C(1)–N(1)	1.368(2)	1.363(4)
C(1)–C(2)	1.377(3)	1.360(4)
C(1)–C(6)	1.511(3)	1.505(4)
C(2)–C(3)	1.369(3)	1.371(4)
C(2)–H(2A)	0.9300	0.9300
C(3)–C(4)	1.376(3)	1.371(5)
C(3)–N(2)	1.469(3)	1.472(4)
C(4)–C(5)	1.367(3)	1.361(5)
C(4)–H(4A)	0.9300	0.9300
C(5)–N(1)	1.353(2)	1.352(4)
C(5)–H(5A)	0.9300	0.9300
C(6)–O(3)	1.203(3)	1.206(4)
C(6)–O(2)	1.305(3)	1.306(4)
N(1)–O(1)	1.323(2)	1.318(4)
N(2)–O(4)	1.218(3)	1.216(4)
N(2)–O(5)	1.221(3)	1.220(4)
O(2)–H(02)	1.0701	0.8925
Angle (°)	Crystal I	Crystal II
N(1)–C(1)–C(2)	118.9(2)	118.9(3)
N(1)–C(1)–C(6)	120.7(2)	120.4(3)
C(2)–C(1)–C(6)	120.3(2)	120.6(3)
C(3)–C(2)–C(1)	119.2(2)	120.3(3)
C(2)–C(3)–C(4)	121.6(2)	120.5(3)
C(2)–C(3)–N(2)	119.2(2)	119.6(3)
C(4)–C(3)–N(2)	119.1(2)	119.9(3)
C(5)–C(4)–C(3)	118.2(2)	118.4(3)
N(1)–C(5)–C(4)	120.7(2)	121.1(3)
O(3)–C(6)–O(2)	123.9(2)	123.0(3)
O(3)–C(6)–C(1)	119.5(2)	119.7(3)
O(2)–C(6)–C(1)	116.6(2)	117.3(3)
O(1)–N(1)–C(5)	118.0(2)	118.3(3)
O(1)–N(1)–C(1)	120.7(2)	120.9(3)
C(5)–N(1)–C(1)	121.4(2)	120.8(3)
O(4)–N(2)–O(5)	124.2(2)	124.4(4)
O(4)–N(2)–C(3)	118.0(2)	117.8(3)
O(5)–N(2)–C(3)	117.8(2)	117.7(4)

The molecules are not parallel with each other in unit cell. The dihedral angles between neighbored molecules are 88.46(3)°, 59.13(3)°, and 59.08(3)°, respectively (shown in Fig. 2a). It can be seen from the one-dimensional chain structure that there exist C(5)–H···O(3a) (symmetry code: a, $-1/2 + x$, $1/2 - y$, $1 - z$) intermolecular hydrogen bonds in the crystal POA-I (shown in Fig. 3a). The C(5)–H groups act as proton donor in the hydrogen-bonded system [37]. The bond lengths of C(5)–H and H···O(3a) are 0.930 and 2.576 Å, respectively, and the bond angle of C(5)–H···O(3a) is 140.1°. The calculation using B3LYP [38] in

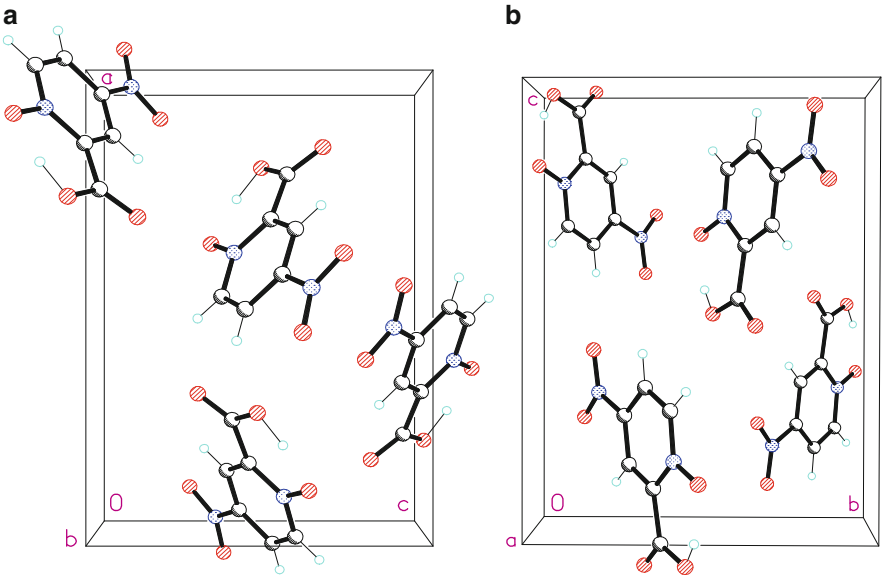

Fig. 2 Packing arrangement in a unit cell for (**a**) POA-I and (**b**) POA-II

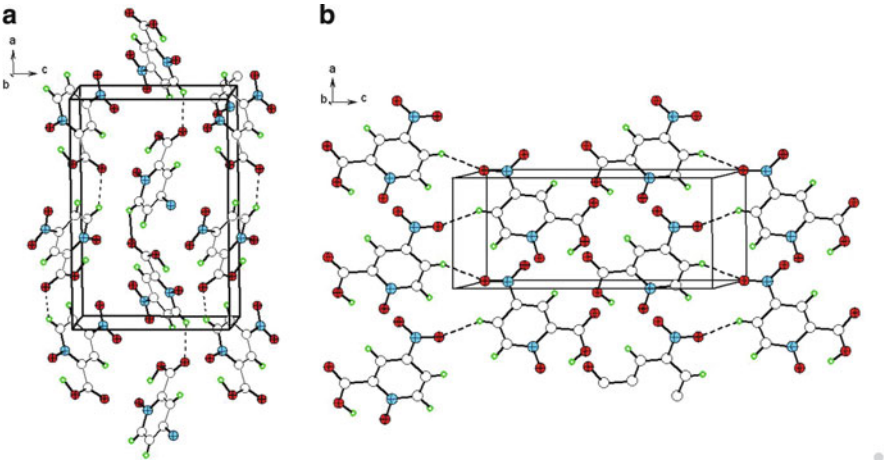

Fig. 3 Packing arrangement with hydrogen bonds for (**a**) POA-I and (**b**) POA-II

conjunction with the 6–311 + G(3df,2p) basis set indicates that the binding energy of C(5)–H···O(3a) hydrogen bond is about 0.64 kJ mol^{-1}, which is a weak hydrogen bond.

The atoms of crystal POA-II are all in a plane too. Its least-square equation is 3.015(3) X − 8.226 (4) Y + 0.633(8) Z − 4.285 (5) Å = 0 with 0.0332 Å of r.m.s. deviation, excelled deviation of crystal POA-I. The lengths of O(1)–N(1) bond (1.318(4) Å), C(3)–N(2) bond (1.472(4) Å), O(4)–N(2) bond (1.216(4) Å), O (5)–N(2) bond (1.220(4) Å), O(3)–C(6) bond (1.206(4) Å), and O(2)–C(6) bond (1.306(4) Å) are in agreement with those of crystal POA-I, respectively. The environments of oxygen atoms in carbonic acid are not the same as POA-I. The length of O(2)–H(02) bond (0.8925 Å) is shorter than that (1.0701 Å) of crystal POA-I. There are intramolecular hydrogen bonds in the crystal POA-II too. The hydrogen bond length of O(2)–H···O(1) is 2.461(2) Å. The angle of O(2)–H···O(1) hydrogen bond is 151.5°. The stacking of crystal POA-II is not the same as that of crystal POA-I. The dihedral angles between neighbor molecules in crystal POA-II are 66.09(4)°, 65.81(4)°, and 5.47(8)°, respectively (shown in Fig. 2b). It can be seen from the one-dimensional chain structure that there exist C(4)–H···O(5a) (symmetry code: *a*, −1/2 + *x*, 1/2 − *y*, 1 − *z*) intermolecular hydrogen bonds in the crystal POA-II (shown in Fig. 3b). The bond lengths of C(4)–H and H···O(5a) are 0.930 and 2.381 Å, respectively, and the bond angle of C(4)–H···O(5a) is 154.0°. The two molecules in the POA crystals are held together by weak hydrogen bond of C–H···O, and one of molecules donates one hydrogen bond to the other. The one-dimensional chains are formed, and the POA crystals are stabilized by these weak hydrogen bonds. In effect, weak hydrogen bonds are employed collectively to work as effectively as their stronger counterparts [39].

Here, we describe the distinguishing of syntheses and crystal structures between the POA-I and POA-II crystals. The preparing measure and conditions are different between the POA-I and POA-II crystals. The POA-I crystal is formed through the filtrating and recrystal processes; however, the POA-II crystal is only through the filtrating process. The molecular arrangements are different between the POA-I and POA-II crystals. The dihedral angles between neighbor molecules in a unit cell are 88.46°, 59.08°, 59.13°, 59.13°, 59.08°, and 88.46°, respectively, for POA-I crystals and are 66.09°, 5.47°, 65.81°, 65.81°, 5.47°, and 66.09°, respectively for POA-II crystals.

2.2 Electronic Spectra and Second-Harmonic Generations of POA

The absorption spectra were recorded by UV-3101PC spectrometer at 300 K from 200 to 800 nm. Figure 4 shows the absorption spectra of POA-I and POA-II powder determined from reflection measurements. The strongest absorption peaks locate at 274 and 278 nm, and the second ones are localized at 373 and 353 nm for the POA-I and POA–II powder, respectively. In order to assign the electronic absorption peaks, we made the quantum chemical calculations. Density functional theory (DFT) calculations were performed with Gaussian 03 package. The properties of

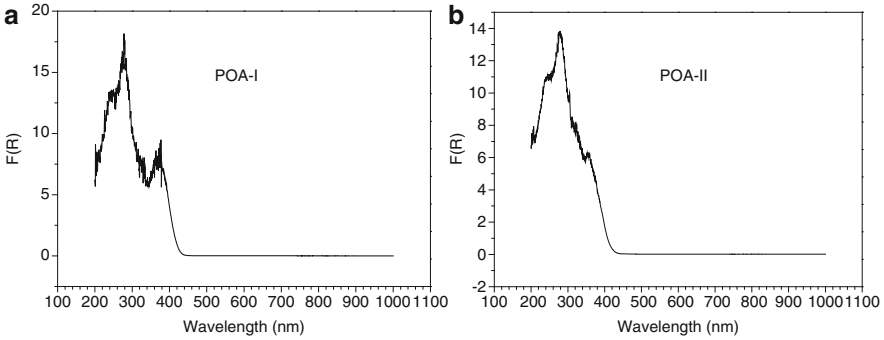

Fig. 4 Electronic absorption spectra of POA powder: (**a**) POA-I and (**b**) POA-II

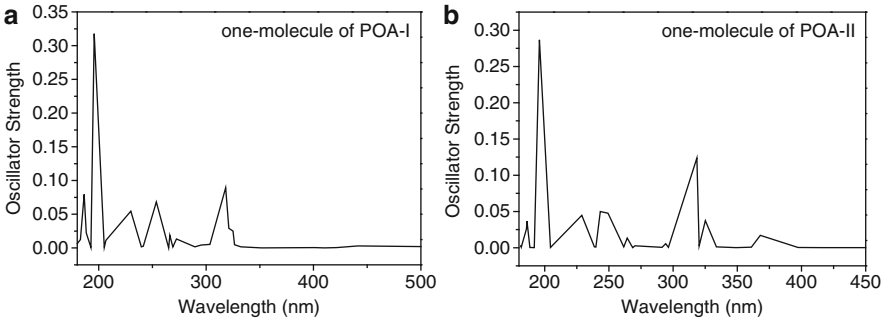

Fig. 5 The calculated absorption spectra of one molecule: (**a**) POA-I and (**b**) POA-II

excited states were calculated by using time-dependent density functional theory (TD-DFT) with BP86 functional [40, 41] and 3-21G* basis set. The calculated absorption spectra of one molecule of POA at TD-BP86/3-21G* level are plotted in Fig. 5. The measurement absorption bands from 180 to 340 nm and from 340 to 440 nm correspond to calculated ones from 180 to 310 nm and from 310 to 350 nm for POA-I and correspond to calculated ones from 180 to 300 nm and 300 to 380 nm for POA-II, individually. Here, we noted that absorption spectrum of crystal is different from that of single molecule and intermolecular excitonic interactions result in the red shift of absorption spectra from molecule to crystal. These results were discussed in detail in the published paper by M. Pierre et al. [42]. We make systemic comparisons between the single molecule and corresponding crystal in order to give an assignment of crystal absorption spectrum. Our calculations indicate that the maximum absorption band observed in the experiment corresponds to the S_{11} state that has larger oscillator strength. The analysis of TDDFT wave function indicates that the S_{11} state has the π–π^* transition characteristics. This shows that the largest absorption band of POA crystals mainly originates from π–π charge transfer transitions.

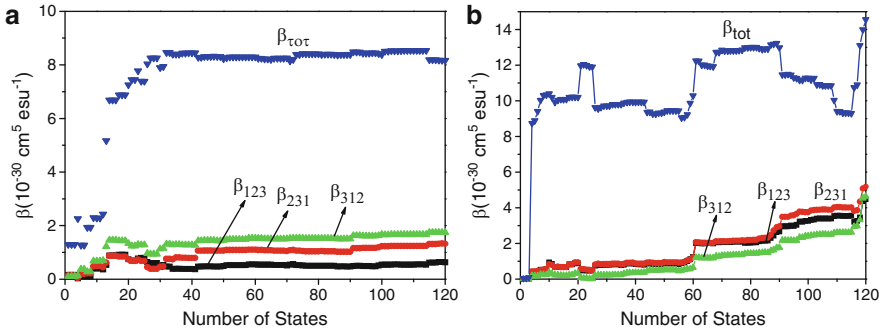

Fig. 6 Convergent behavior of β values with number of states for 4-molecule cluster: (**a**) POA-I and (**b**) POA-II

We choose the 4-molecular cluster from one unit cell as basic model to calculate the second-order polarizabilities $\beta(-2\omega; \omega, \omega)$ of SHG process to include the supramolecular interactions in the POA-I and POA-II crystal materials. The x, y, z directions in the Cartesian coordination correspond to the unit cell a, b, c axes of orthorhombic system, respectively. With the calculated dipole moments and transition moments of excited states of 4-molecule cluster in a POA crystal, the sum over states (SOS) formalism [43, 44] was employed to evaluate the NLO responses of 4-molecular cluster and the optical physical property superposition of 4-molecular cluster is applied to obtain optical susceptibility of POA crystal. For the calculations of β, we first consider how to truncate the infinite SOS expansion to a finite one. Figure 6 shows the plots of the calculated second-order polarizabilities β_{xyz}, β_{yzx}, β_{zxy} and $\beta_{tot}(-2\omega; \omega, \omega)$ at the TDBP86/3-21G* level vs the number of states for POA-I and POA-II at input photon energy of $\hbar\omega = 1.165$ eV.

The curve of $\beta_{tot}(-2\omega; \omega, \omega)$ of POA-I shows good convergence after state 32 and convince that the truncation with 120 states is reasonable. The 13th state makes a large contribution to the β_{tot} value, and the calculated β_{tot} value including the first 13 states is about 63% of the β_{tot} value including 120 states. While the $\beta_{tot}(-2\omega;\omega,\omega)$ of POA-II is considered, the curve has oscillation and the convergence is not as good as that of POA-I. But it can be found that all the values after six states fall in the range of 9–15 $\times$ 10^{-30} cm^5 esu^{-1}, which is acceptable for the deviations. The fourth state of 4-molecule cluster in POA-II crystal makes the largest contribution to the β_{tot} value. Both the 13th state of POA-I and 4th state of POA-II have the significant configurations of HOMO-3→LUMO, where HOMO-3 is the π-bonding orbital mainly located at one monomer but with a small mixing from neighboring monomer, and LUMO is π*-antibonding orbital located on another monomer in the 4-molecule cluster (shown in Fig. 7). From the analysis of the molecular orbitals and configuration contributions, it can be found that charge transfers between the monomers make mainly contributions to the hyperpolarizability of POA-I and POA-II 4-molecule clusters. Furthermore, structure–property relations at molecular level are discussed in details for POA molecules.

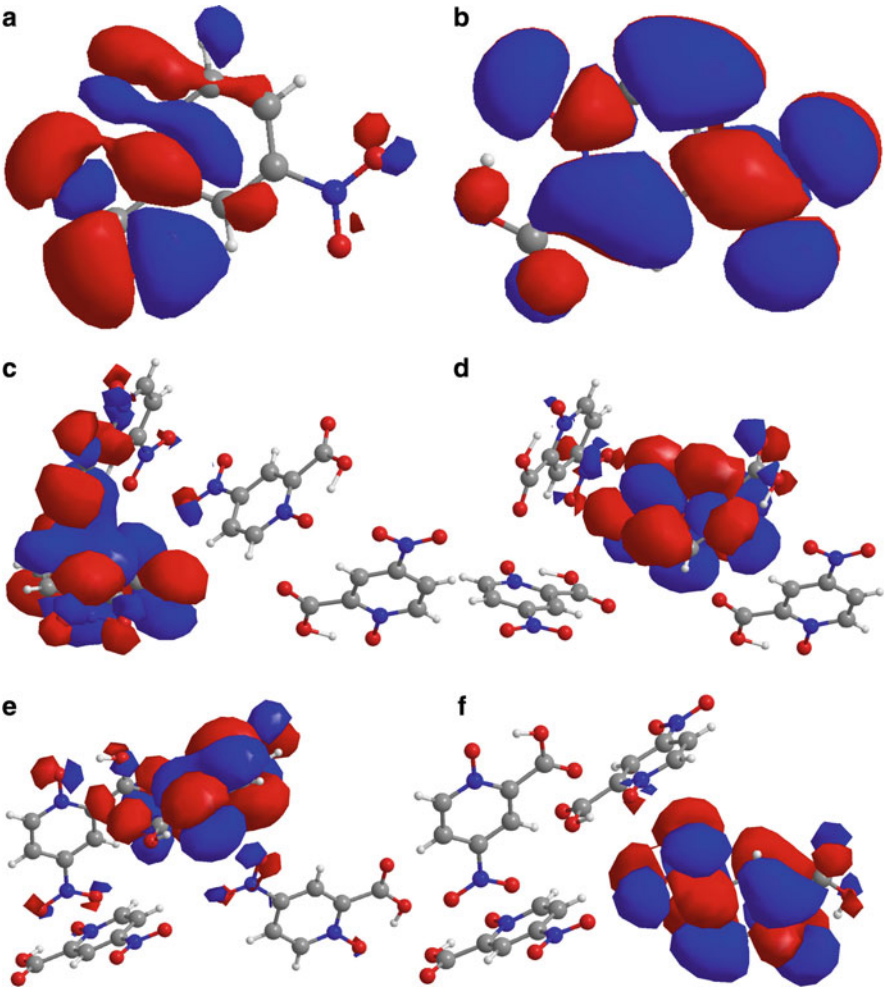

Fig. 7 Frontier molecular orbitals: (**a**) HOMO of POA one molecule, (**b**) LUMO of POA one molecule, (**c**) HOMO-3 of POA-I molecular cluster, (**d**) LUMO of POA-I molecular cluster, (**e**) HOMO-3 of POA-II molecular cluster, (**f**) LUMO of POA-II molecular cluster

The molecules both in the POA-I and POA-II crystals are planar with 0.0704 and 0.0332 Å of r.m.s. deviation of atoms, and intramolecular hydrogen bonds form between the hydroxyl group of COOH and oxygen of N-oxide for the molecules as mentioned above. The COOH is a planar structure and is composed of hydroxyl and carbonyl groups. The changes in chemical and physical properties result from the competition interaction between the hydroxyl and carbonyl functions within the COOH. A hydrogen bond formed with neighbor oxygen of N-oxide donates a proton and results in reduced ability of charge transfer of N-oxide; however, the excess charges of carbonyl group withdrawing from oxygen atom of hydroxyl group in the

COOH group transfer into 4-nitropyridine-1-oxide while hydrogen bond forms. The accepting charge effect of nitro group has no substantial changes due to the compensatory effect between the hydroxyl and carbonyl group in the POA molecules. Hence, the POA chromophore would not interfere destructively with the basic charge transfer mechanism from the N-oxide group to the nitro group, which results in the expected optical nonlinearity. Figure 7a, b gives the plots of HOMO and LUMO of POA single molecule, and they show the evidence of the charge transfers from the N-oxide and COOH groups to the nitro group while an electron is promoted from HOMO to LUMO. On the contrary, the atoms in POM (3-methyl-4-nitropyridine-1-oxide) is not coplanar since the methyl group in 3-position of POM is not planar structure itself. Accordingly, the methyl induces a rotation of the nitro group and results in a reduced conjugation between the donor oxygen of the oxide and the nitro acceptor. This means that a reduced charge transfers from the N-oxide to the nitro groups will result in weak optical response of POM chromophore. Additionally, the intermolecular hydrogen bonds formed from the C–H of pyridine ring and O of C=O in COOH group also lead to a quasi-optimal molecular orientation and enhancement of NLO response in the POA crystals. These conclusions have been also found in N-(4-nitrophenyl)-(L)-prollnol (NPP) and 2-methyl-4-nitroaniline (MNA) crystals [45].

In fact, molecule or molecular cluster is a building component of bulk materials, the physical properties of the bulk materials are dependent on their molecular components and the manners of arrangement and linking of the components in the crystalline state. The molecular clusters are taken as calculating models in this study, which are exactly four molecules in a unit cell of POA-I and POA-II, respectively. The inherent noncovalent force interaction and optimal arrangement among 4-molecular cluster are included into the extended solid-state architectures. For the solid state constructed through the noncovalent force interaction among the molecules, the optical properties of the solid state simply arise from the 4-molecular structure and the packing manner among the molecules. For this reason, the studies of optical properties of materials predigest the investigations of molecular cluster optical properties. Accordingly, the NLO susceptibility $\chi^{(2)}_{abc}$ of bulk material can be estimated from the first-order hyperpolarizability of the 4-molecular cluster β_{abc} corrected by the local field factor along the three crystal axes.

$$\chi^{(2)}_{abc}(-2\omega;\omega,\omega) = NLb_{abc}(-2\omega;\omega,\omega). \tag{1}$$

Here, N can be evaluated with $N = 1/V_{\text{cell}}$ (V_{cell} is the volume of the unit cell of POA crystal). The local field correction factor is calculated from $L = f_a(2\omega)f_b(\omega)f_c(\omega)$, and the $f(\omega) = [n(\omega)^2 + 2]/3 = 1/[1-(4\pi/3)N\alpha(\omega)]$ with the assumption of Lorentz-Lorenz local field, in which $n(\omega)$ is the refractive index and $\alpha(\omega)$ is the first-order microscopic polarizability. With SOS formalism, we can evaluate $\alpha(\omega)$ and thus calculate the macroscopic susceptibility. The calculated main values of $\chi^{(2)}$ are listed in Table 2 for the SHG optical process at an input wavelength of 1064 nm. The Kurtz powder SHG measurement shows that POA-I and POA-II

Table 2 Parameters for calculating the NLO susceptibilities of POA at 1064 nm for SHG optical process

	N^a	$\chi_{123}^{(2)\,b}$	$\chi_{231}^{(2)\,b}$	$\chi_{312}^{(2)\,b}$	$\chi_{tot}^{(2)b}$	$\chi^{(2)}(expt)^b$
POA-I	1.390	0.78	1.02	2.46	11.56	14.72
POA-II	1.385	6.69	7.76	6.95	21.80	31.80

[a] 10^{21} cm^{-3}
[b] 10^{-9} esu

exhibit powder SHG efficiency about 4.6 times and 9.8 times as that of KDP. The selected value of the KDP d_{36} coefficient originating from an averaging data is 1.6×10^{-9} esu [46], and thus, our measured d coefficient ($2d = \chi^{(2)}$) are about 7.36×10^{-9} (14.72×10^{-9}) esu and 15.68×10^{-9} (31.36×10^{-9}) esu, respectively. Accordingly, the estimated values of $\chi_{tot}^{(2)}$ listed in Table 2 are smaller than those in experiment but are quite satisfactory estimation.

In our cluster model, molecular orientations and interactions in crystalline state have been considered in 4-molecular cluster calculations. The influence of individual molecular orientation in crystalline state on optical property has not been analyzed in details. At the moment, we make some discussions about structure–property relations in terms of the definition of "b" tensor, which is dimensionless parameter developed by Zyss and Oudar [47]. The crystal NLO parameter of d varies directly with angular factors of molecular orientation within crystalline state while the b tensor is taken as a unit. For the 222 point group, the optimal value of angular factor ($\sin\phi \times \cos\phi \times \cos\theta \times \sin^2\theta$, $\phi = 45°$, $\theta = 54.7°$) is 0.1924 for maximizing crystal nonlinearity in regular tetrahedral configuration constructed by the four dipole axes of four molecular plans [47]. Both the POA-I and POA-II crystals belong to the 222 point group, and the four dipole axes of four molecular plans form a pseudotetrahedral structure, the angular factor is 0.1622 (about $\phi = 29.5°$, $\theta = 59°$) and 0.1550 (about $\phi = 33°$, $\theta = 66°$), separately for POA-I and POA-II crystals. It is shown that the angular factor of the POA-II crystal has a larger difference from the ideal optimum value. However, the POA-II crystals have larger NLO parameters by compared with ones of the POA-I crystals both in our calculations and measurements. These results indicate that one-dimensional dipole model is not good treatment on the POA crystals. It is a good scheme that the POA crystals are treated to employ multipolar (octupolar) molecular engineering method [48, 49] due to the COOH substituent in 2-position of 4-nitropyridine-1-oxide.

There are different optical properties between the POA-I and POA-II crystals. The SHG effect is larger for POA-II than POA-I crystals. A large SHG response of POA-II crystal comes from a large hyperpolarizability of 4-molecule cluster of POA-II crystal. The large charge transfers between the molecules will make a large contribution to hyperpolarizability of 4-molecular cluster of POA-II crystal. The calculated important state contributing mostly to hyperpolarizabilities has small transition moment and large electronic transition energy of POA-I molecular cluster and has large transition moment and small transition energy of POA-II molecular cluster.

3 Effect of Lone Pair on SHG Responses in Eulytite-Type Compounds of $Pb_3Bi\ (PO_4)_3$ and $Ba_3Bi\ (PO_4)_3$

In this respect, we describe the fabrication, SHG response, and electronic origin of optical property of eulytite-like orthophosphates $Pb_3Bi\ (PO_4)_3$ and $Ba_3Bi\ (PO_4)_3$ [31]. With the design idea that metal ion including lone pairs will result in coordinated structural distortion, we introduce Bi^{3+} into lead phosphates of ternary systems to obtain SHG materials.

3.1 Preparation Processes and Structural Descriptions

The syntheses of single crystals $Pb_3Bi(PO_4)_3$ were carried out using Bi_2O_3, $PbCl_2$, and $NH_4H_2PO_4$ in a molar ratio corresponding to Bi/Pb/P = 1:3:5 of a mass of 2 g, the excess amount of $NH_4H_2PO_4$ to be used in order to promote crystal growth. During the preparing processes, first, the mixture was ground in an agate mortar, the resulting mixture was introduced into a platinum crucible and was heated at 673 K for 10 h in order to decompose $NH_4H_2PO_4$; then heated for 1 day at 1,323 K and cooled down to 1,023 K at a rate of 3 K/h; and finally cooled to 573 K at 5 K/h before switching off the furnace. Some colorless crystals of $Pb_3Bi(PO4)_3$ were selected carefully from a sintered product. After boiled in water, some prism-shaped colorless crystals of $Pb_3Bi(PO4)_3$ were selected carefully for X-ray single-crystal diffraction. Monophase power of $Pb_3Bi(PO_4)_3$ was prepared from the stoichiometric mixture of PbO, Bi_2O_3, and $NH_4H_2PO_4$ in a molar ratio of 6:1:6. This mixture was ground in an agate mortar and then calcined at 1,153 K in air for 24 h with several intermediate grindings in an opening Pt crucible. The monophase products of homologous compounds $Ba_3Bi(PO_4)_3$ were prepared using $NH_4H_2PO_4$, $BaCO_3$, and Bi_2O_3 by high-temperature solid reaction method at 1,273 K for 1 day. The final product was analyzed by X-ray powder diffractions [31].

Single crystal of $Pb_3Bi(PO_4)_3$ was selected and mounted on glass fibers, and data collection was performed on a Rigaku SCXmini at the temperature of 293 K. Absorption correction by the multiscan method, Lorentz and polarization corrections, was applied to data. The structure was solved by direct method and then refined on F^2 by full-matrix least-squares method and performed in the Shelxl/PC programs [50]. Atomic positions of Bi/Pb, P, and O were determined using direct method. The final refinement of the structure was achieved using a fixed site occupancy ratio 3:1 for Pb and Bi equal to the ideal values in accordance with the chemical formula $Pb_3Bi(PO_4)_3$. The atomic and thermal parameters of bismuth were fixed to be same as that of lead. All atoms in $Pb_3Bi(PO_4)_3$ were refined with anisotropic thermal parameters [31]. The atomic coordinates, selected important bond lengths, are listed in Tables 3 and 4 , respectively. The final refined solutions obtained were checked with the ADDSYM algorithm in the program PLATON [51], and no higher symmetry was found. Energy-dispersive X-ray spectrometry (EDS) using a JSM6700F scanning electron

Table 3 Atomic coordinates ($\times 10^4$) and displacement parameters ($A^2 \times 10^3$) for $Pb_3Bi(PO_4)_3$

Atom	*x*	*y*	*z*	*U*(eq)[a]	Occupancy factor
Bi1	752(1)	752(1)	752(1)	14(1)	0.25
Pb1	752(1)	752(1)	752(1)	14(1)	0.75
P1	2,500	3,750	0	9(1)	
O1	1,390(8)	2,912(8)	513(9)	29(2)	

[a]$U_{(eq)}$ is defined as one-third of the trace of the orthogonalized U_{ij} tensor

Table 4 Important bond lengths (Å) and angles (°) for $Pb_3Bi(PO_4)_3$

Bond distances			
Pb1/Bi1-O1	2.347(8)	Pb1/Bi1-O11	2.347(8)
Pb1/Bi1-O13	2.629(8)	Pb1/Bi1-O14	2.629(8)
Pb1/Bi1-O12	2.347(8)	Pb1/Bi1-O15	2.629(8)
P1-O1	1.537(9)	P1-O16	1.537(9)
P1-O17	1.537(9)	P1-O18	1.537(9)
Important angles			
O1-Pb1/Bi1-O11	82.1(3)	O1-Pb1/Bi1-O12	82.1(3)
O11-Pb1/Bi1-O12	82.1(3)	O11-Pb1/Bi1-O13	74.1(3
O12-Pb1/Bi1-O13	81.51(13)	O1-Pb1/Bi1-O14	81.51(13)
O12-Pb1/Bi1-O14	74.1(3)	O13-Pb1/Bi1-O14	114.53(15)
O1-Pb1/Bi1-O15	74.1(3)	O11-Pb1/Bi1-O15	81.51(13)
O13-Pb1/Bi1-O15	114.53(15)	O14-Pb1/Bi1-O15	114.53(15)
O16-P1-O1	108.6(3)	O16-P1-O17	108.6(3)
O1-P1-O17	111.2(6)	O16-P1-O18	111.2(6)
O1-P1-O18	108.6(3)	O17-P1-O18	108.6(3)

Symmetry code: [1](z, x, y); [2](y, z, x); [3]$(z + 0, -x + 0, -y + 1/2)$; [4]$(-y + 1/2, z + 0, -x + 0)$; [5]$(-x + 0, -y + 1/2, z + 0)$; [6]$(z + 1/4, -y + 3/4, -x + 1/4)$; [7]$(-x + 1/2, y + 0, -z + 0)$; [8]$(-z + 1/4, -y + 3/4, x - 1/4)$

microscope of the single crystals indicated the presence of Pb, Bi, P, and O elements. Inductively coupled plasma (ICP) measurement result indicated that the mixture of Pb and Bi is in a molar ratio of 2.92:1, which was in good agreement with that one obtained by the refinement of the crystal structure (Pb:Bi = 3:1) [31].

The structure of compound $Pb_3BiP_3O_{12}$ exhibits a complicated three dimension network structure, as shown in Fig. 8. This structure composes of asymmetric Pb/BiO_6 octahedra and PO_4 tetrahedra that are interconnected via corner or edge sharing. There are three types atomic positions in the asymmetric unit of $Pb_3Bi(PO_4)_3$, which is different from the compound $Ba_3Bi(PO_4)_3$ [52]. In compound $Pb_3Bi(PO_4)_3$, P1 and O1 atoms are occupying two single positions, atoms Pb1 and Bi1 are occupying the same position and not able to distinguish, and Pb and Bi are at fixed site occupancy ratio 3:1 equal to the ideal values in accordance with the chemical formula $Pb_3BiP_3O_{12}$. It has been described in [52] that the unit cell of $Ba_3Bi(PO_4)_3$ contains two distinguished sites for large cations (Ba1 and Bi1) and two other positions for oxygen anions (O1 and O2). The unique P^{5+} cations are coordinated by four oxygen atoms to form a regular tetrahedron with the P–O distance at 1.537 Å. The mixed Pb1/Bi1 atoms were bonded to six oxygen atoms

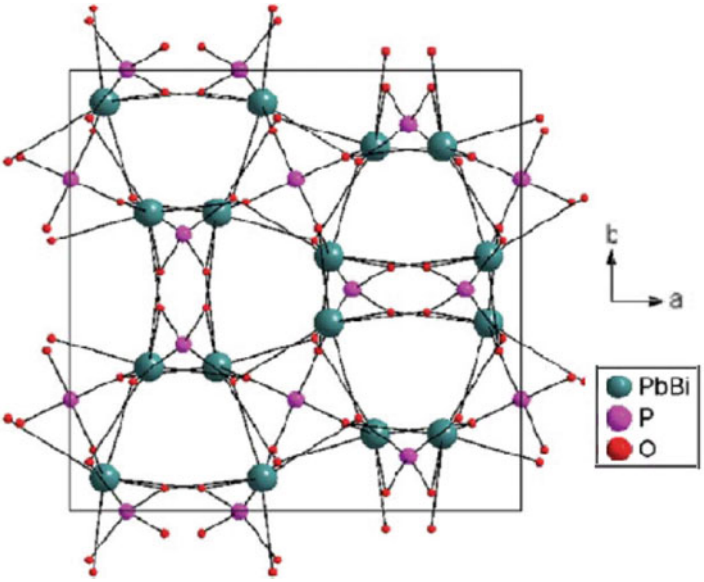

Fig. 8 View of the structure of $Pb_3Bi(PO_4)_3$ along the [001] direction. (Pb^{II}/Bi^{III}), P, and O atoms are represented by *teal*, *purple*, and *red circles*, respectively

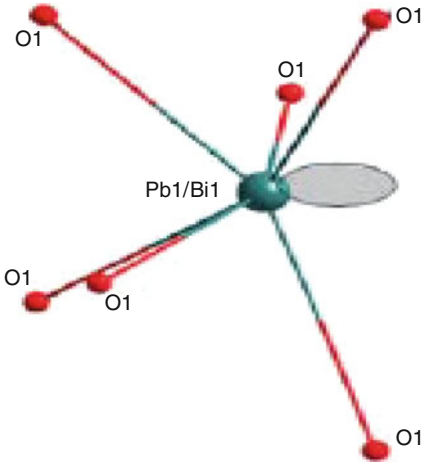

Fig. 9 The coordination of oxygen atoms around Pb1/Bi1 showing the stereoactivity of the lone pair

from six $[PO_4]^{3-}$ tetrahedral to form a strongly distorted octahedral with the Pb/Bi–O bond distances ranging from 2.348 to 2.629 Å, which is schemed in Fig. 9. It is well established that Pb^{2+} and Bi^{3+} ions generate distorted structures due to the electrostatic effect of the lone pair of electrons [53, 54]. The structure of $Pb_3Bi(PO_4)_3$ can also be viewed as a three-dimensional network formed by edge-sharing-mixed (Pb^{II}/Bi^{III}) metal–oxygen octahedra, forming corrugated

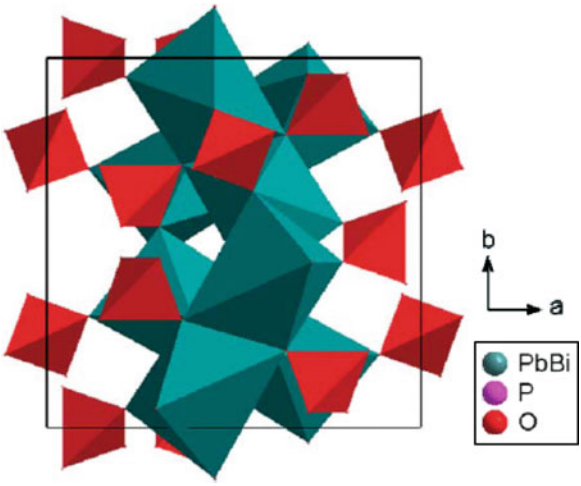

Fig. 10 The corrugated chains formed by edge sharing of (Pb^{II}/Bi^{III}) octahedral and further linked by tetrahedral phosphate groups via corner sharing

chains linked by tetrahedral phosphate groups via corner sharing, as shown in Fig. 10. By the comparison of structures between $Pb_3Bi(PO_4)_3$ and $Ba_3Bi(PO_4)_3$ [52], there is a distinct order in the ionic radius of cations: $Ba^{2+} > Pb^{2+} > Bi^{3+}$. The main structural feature of almost all eulytite-like compounds is a presence of different types of disorder in the cation or anion (or both) frameworks. Atomic positions and the site occupancy appear to be directly related to the nature and size of the metallic cations involved in the eulytite structure. In the compound $Ba_3Bi(PO_4)_3$, two oxygen positions (O1 and O2) as well as peculiar sites for Ba and Bi are clearly distinguished within the lattice [52]. The Ba^{2+} is bonded to twelve oxygen atoms with the Ba–O bond distances ranging from 2.662 to 2.766 Å, and the Bi^{3+} is asymmetrically coordinated by six oxygen atoms to form a distorted octahedron with the Bi–O bond distances ranging from 2.378 to 2.599 Å [31]. In the compound $Pb_3Bi(PO_4)_3$, the Pb^{2+} and Bi^{3+} are not able to distinguish due to the closed ionic radii of them and surrounded by six oxygen atoms with "normal" bond distances (2.348–2.629 Å) to form the large distorted octahedral. So we deem that the relative smaller ligand and same coordinational environment give rise to the accordant direction of the $6s^2$ lone pairs, which enhance the efficiency of the SHG.

3.2 Electronic Structures and SHG Properties

To gain further insights into the electronic origination of optical properties, band structure and density of states (DOS) calculations of $Pb_3Bi(PO_4)_3$ based on DFT were performed using the total-energy code CASTEP [55, 56]. The crystallographic data of $Pb_3Bi(PO_4)_3$ determined by X-ray single-crystal diffraction was used for the band structure calculation, no further geometry optimizations was performed in theoretical study. The calculation of band structure was made by the DFT with the

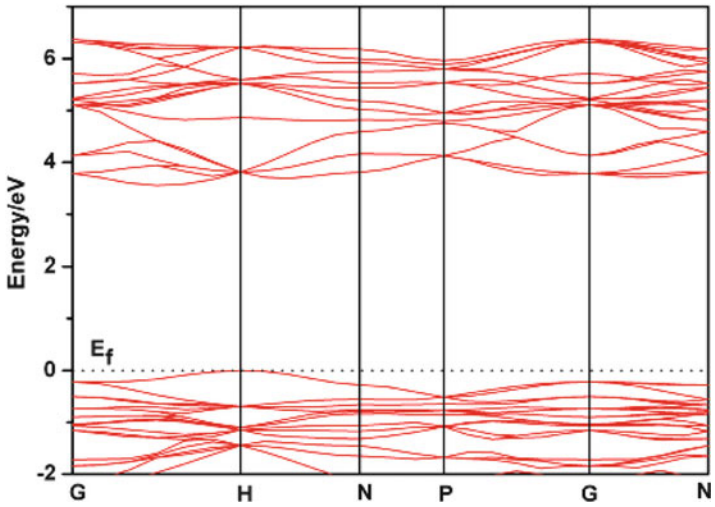

Fig. 11 The calculated band structures of $Pb_3Bi(PO_4)_3$, crystal in the range of −2.0 and 7.0 eV. The Fermi level is set at 0.0 eV

Perdew–Burke–Ernzerh of generalized gradient approximation, which uses a plane wave basis set for the valence electrons and norm-conserving pseudopotential for the core states. The number of plane wave included in the basis was determined by a cutoff energy of 500 eV. Pseudoatomic calculations were performed for Bi-$5d^{10}6s^26p^3$, P-$3s^23p^3$, O-$2s^22p^4$, and Pb-$5d^{10}6s^26p^2$. The calculating parameters and convergent criterions were set by the default values of CASTEP code. Figure 11 gives the plot of band structure at the first Brillouin zone. It is observed that the valence bands are very flat, and the conduction bands have some oscillating. The lowest energy of the conduction bands is located at the point between the G and H k-points and is 3.56 eV, whereas the highest energy (0.0 eV) of the valence bands is at k-point of H points, as shown in Fig. 12. 8; hence, $Pb_3Bi(PO_4)_3$ has an indirect band gap of 3.56 eV. On the other hand, the optical diffuse reflectance absorption spectrum of $Pb_3Bi\ (PO_4)_3$ was measured ranging from 200 to 1200 nm, and it indicates that the band gap of $Pb_3Bi(PO_4)_3$ is approximately 3.97 eV [31]. Accordingly, the calculated band gap of 3.56 eV is a little smaller than the experimental values of 3.97 eV.

The bands can be assigned according to the total and partial densities of states (DOS) as plotted in Fig. 12. The regions below the Fermi level can be divided into three regions. The VBs ranging from −21.2 eV to −15.0 eV are mainly formed by the states of Pb-5d, Bi-5d, and O-2s states. The VBs ranging from −10.5 eV to −4.0 eV are mainly composed of Pb-6s and Bi-6p states mixing with a small amount of the P-3p and O-2p states. The VBs just below the Fermi level ranging from −4.0 eV to the Fermi level (0.0 eV) are mainly from O-2p and Bi-6p states. The bands just above the Fermi level are derived from Pb-6p and Bi-6p states ranging from 3.4 eV to 7.0 eV. The states of Bi-6s, Pb-6s, and P-3p dominate the

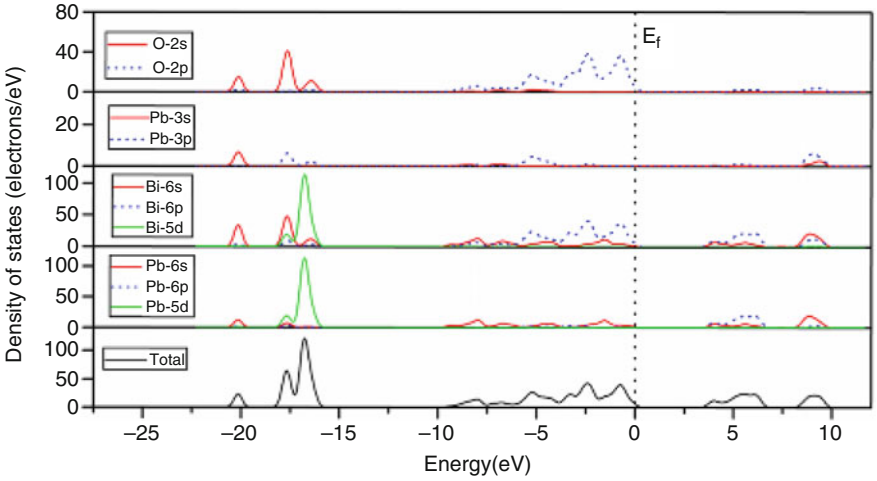

Fig. 12 Total and partial DOS of $Pb_3Bi(PO_4)_3$. The Fermi level is set at 0.0 eV

VB ranging from 7.0 eV to 10.2 eV mixing with a small amount of the Bi-6p. Analyzing the PDOSs, we note that the Pb–O and Bi–O interactions are dominant at the bottom part of the conduction band and also contribute considerably below the Fermi level. It is shown that the highest occupied states should contain the majority of O-2p states and less mixed Bi/Pb-6s and Bi/Pb-6p states; the lowest unoccupied states should involve strong unoccupied Bi/Pb-6p states, much less unoccupied O-2p states, and least unoccupied Bi/Pb-6s states. Such character is intimately related to the lone-pair distortion resulting from the mixings among the cation 6s, 6p orbitals, and ligand O-2p orbitals [56–58]. Therefore, the charge transfers within irregular octahedral of Pb/BiO_6 make a significant contribution to NLO response.

Eulytite-like $A_3^{II}M^{III}(PO_4)_3$ compounds crystallize in the acentric space group $I4^-3d$. Hence, it prompts us to study their SHG properties. The Kurtz–Perry method is a simple and quick experimental technique that requires only the material in powder form to estimate its NLO effect before the effort is made to grow large single crystals [59]. SHG measurements on a Q-switched Nd:YAG laser with the sieved powder sample (80–100 mesh) revealed that the SHG signal of $Pb_3Bi(PO_4)_3$ is about 3.0 times of that of KDP. The SHG efficiency can be attributed to the synergistic effect of the polarizations of the multiple Pb/BiO_6 irregular octahedra due to stereochemical activity of the Pb^{2+} and Bi^{3+} multiple lone-pair electrons (Fig. 9). At the same time, in order to search the relationship of SHG response and lone-pair stereochemical activity, the SHG measurement of $Ba_3Bi(PO_4)_3$ was also performed. As it is expected, SHG measurement on powder sample reveals that $Ba_3Bi(PO_4)_3$ exhibits a weak SHG signal of about 0.5 times that of KDP. Here, the former is only one lone-pair electron of Bi^{3+} ion by the comparison with those of $Pb_3Bi(PO_4)_3$. It is shown that the SHG efficiency is an increasing as the strengthening of stereochemically active lone-pair electrons in eulytite-like $A_3^{II}M^{III}(PO_4)_3$ compounds. It speculated on that the compounds of $Pb_3Bi(PO_4)_3$ and $Ba_3Bi(PO_4)_3$

were phase matchable from size dependence of SHG signal measurements (see Fig. 5 in [31]). These results are maybe false appearance of saturation obtained from measurements of few points and mislead to phase matching. As we have known, the most common procedure to obtain phase matching is to make use of the birefringence displayed by the crystals. The crystals belonging to the cubic crystal system are optically isotropic and no birefringence. The compounds of $Pb_3Bi(PO_4)_3$ and $Ba_3Bi(PO_4)_3$ both crystallize in the space group $I4^{-}3d$, and they belong to cubic crystal system. Accordingly, it is impossible for these two compounds to be phase matchable in normal conditions.

4 ZnO-Based SHG Materials of KZn_4SbO_7 and $KZn_4Sb_3O_{12}$

ZnO crystal lacking a center of inversion is of piezoelectric property (NLO property) [60]. In most cases, ZnO-based compounds are technologically more important than its pure phase. The discovery of a polar $ZnSnO_3$ reveals a new strategy in searching noncenter symmetrical (NCS) materials containing only cations with an electronic configuration of $(n-1)d^{10}ns^0$ [20]. The features of ZnO and its doped species suggest using ZnO as reaction precursor to synthesize SHG materials of KZn_4SbO_7 and $KZn_4(SbO_4)_3$ [61].

4.1 Simple Descriptions of Synthesis and Structures of KZn_4SbO_7 and $KZn_4(SbO_4)_3$

Single crystals of KZn_4SbO_7 (**1**) and $KZn_4(SbO_4)_3$ (**2**) were grown by a high-temperature solid-state reaction. The reagents were weighted in the molar ratio of 2 (K_2CO_3):4 ($ZnCO_3$):2 (Sb_2O_3) for **1** and 2 (K_2CO_3):8 (ZnO):1 (Sb_2O_3) for **2**. These starting materials were finely ground in an agate mortar to ensure the best homogeneity and reactivity. For the synthesis processes of **1**, the mixture was firstly preheated in a platinum crucible; secondly, the products were held at high temperature for 10 h, then slowly cooled down and finally quenched to room temperature. A few of colorless crystals were obtained from the melt of the mixture. For **2**, the mixture was, firstly, heated to 1,173 K and kept on the temperature for 5 h in a platinum crucible in air; secondly, the mixture was slowly heated to 1,773 K, and the products were held at this temperature for 24 h, then slowly cooled down to 1,573 K at a rate of 2 K/h and finally quenched to room temperature. A few of colorless crystals were obtained from the melt of the mixture. The powders of compounds **1** and 2 were prepared from the stoichiometric mixture of K_2CO_3, $ZnCO_3$, and Sb_2O_3 in the molar ratio of 1:8:1 for **1** and K_2CO_3, ZnO, and Sb_2O_3 in the molar ratio of 1:8:3 for **2**. These mixtures were ground in an agate mortars and then calcined at 1,473 K in air for 15 h for **1** and at 1,373 K in air for 40 h for

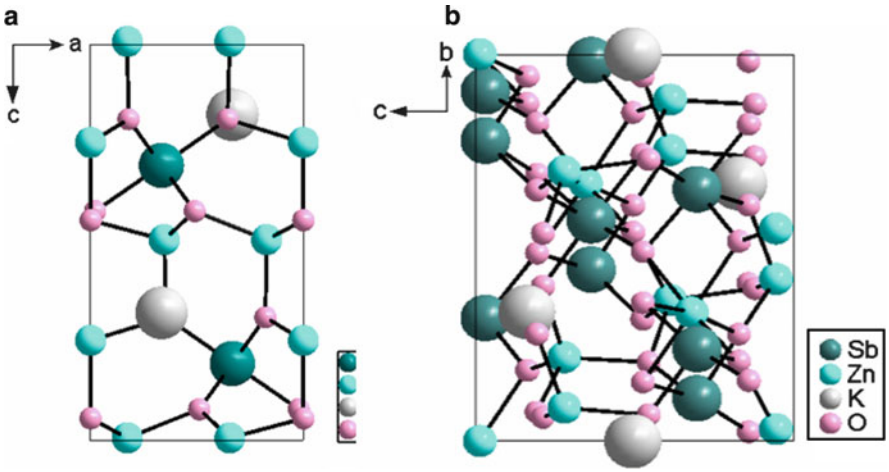

Fig. 13 Ball-and-stick representation of (**a**) KZn_4SbO_7 (*left*) and (**b**) $KZn_4(SbO_4)_3$ (*right*)

2 with several intermediate grindings in an opening Pt crucibles. The final products were analyzed, and the monophases were confirmed by X-ray powder diffraction studies [61].

The unit cells of single-crystal structures of compounds **1** and **2** are plotted in Fig. 13. Crystallographic analysis reveals that crystal **1** possesses the same space group of $P6_3mc$ as wurtzite-type ZnO crystal, and the cell parameters of *a*, *b*, *c* are equal to the two times of *a*, *b*, and *c*-axis of wurtzite-type ZnO crystal [62], individually. There are two crystallographically different Zn atoms, and both of them are tetrahedrally coordinated by four oxygen atoms in crystal **1**. $Zn3O_4$ tetrahedra are linked to each other by a sharing corner to form infinite chains along the *a*-axis and *b*-axis, which are similar to the ZnO4 tetrahedra in wurtzite-type ZnO crystal. Zn3–O distances are 1.903, 1.942 (×2), and 1.948 Å (see Table 5). $Zn2O_4$ tetrahedra are interconnected to SbO_6 octahedra by sharing corners and also form infinite chains along the *a*-axis and *b*-axis. The Zn2–O bond distances are 1.954 Å and 1.982 Å (×3), and all of the Sb–O bond distances are about 2.02 Å in the regular SbO_6 octahedron of crystal **1** (see Table 5). These two types of chains result in a layered structure down the *c*-axis, and then, K+ cations are located inside the vacancy between two types of chains (Fig. 13a). The crystal structure of compound **1** can be regarded as that of the ZnO submatrix of interconnected ZnO tetrahedra that is diluted by Sb^{5+} ions (i.e., replaced by SbO_6 octahedra) relative to the wurtzite-type ZnO itself as crystal structure, as shown in Fig. 14. Crystal **2** belongs to the space group R_3, and it is a novel structural type. There are two crystallographically different Zn atoms, the $Zn2O_4$ is tetrahedrally coordinated by four oxygen atoms, and the average distance of Zn2–O is 1.960 Å (see Table 5). The $Zn3O_6$ is octahedrally coordinated by six oxygen atoms, and Zn3–O lengths are 2.074 (×3) and 2.158 (×3) Å in crystal **2** (see Table 5). These two coordination fashions only separately appear at hexagonal type ZnO crystal ($P6_3mc$ symmetry)

Table 5 The selected bond distances (Å) for crystals **1** and **2**

1 (**KZn_4SbO_7**)			
Sb1–O3	2.017(5)	Zn3–O1	1.903(2)
Sb1–$O3^1$	2.017(5)	Zn3–$O3^{11}$	1.942(3)
Sb1–$O3^2$	2.017(5)	Zn3–$O3^2$	1.942(3)
Sb1–$O2^2$	2.018(4)	Zn3–$O2^{12}$	1.948(5)
Sb1–O2	2.018(4)	K4–$O3^1$	3.046(5)
Sb1–$O2^1$	2.018(4)	K4–O3	3.046(5)
Zn2–O1	1.954(8)	K4–$O3^2$	3.046(5)
Zn2–$O2^6$	1.982(4)	K4–$O3^{16}$	3.068(5)
Zn2–O2	1.982(4)	K4–$O3^{17}$	3.068(5)
Zn2–$O2^7$	1.982(4)	K4–$O3^{18}$	3.068(5)
K4–$O2^{19}$	3.0751(14)	K4–$O2^{12}$	3.0751(14)
K4–$O2^{20}$	3.0751(14)	K4–$O2^{22}$	3.0751(14)
K4–$O2^{21}$	3.0751(14)	K4–$O2^{23}$	3.0751(14)
2 (**$KZn_4Sb_3O_{12}$**)			
Sb1–O4	1.922(6)	Zn2–$O3^6$	1.953(5)
Sb1–O3	1.949(6)	Zn2–O4	1.953(6)
Sb1–$O2^1$	1.980(5)	Zn2–O1	1.970(5)
Sb1–O2	2.009(5)	Zn2–$O3^7$	1.965(6)
Sb1–$O1^2$	2.010(5)	Zn3–O4	2.074(5)
Sb1–$O1^3$	2.043(5)	Zn3–$O4^{10}$	2.074(5)
Zn3–$O4^3$	2.074(5)	Zn3–O2	2.158(5)
Zn3–$O2^3$	2.158(5)	Zn3–$O2^{10}$	2.158(5)
K1–$O3^{12}$	2.690(6)	K1–$O1^{14}$	3.173(6)
K1–$O3^{13}$	2.690(6)	K1–$O1^6$	3.173(6)
K1–$O3^7$	2.690(6)	K1–$O1^{15}$	3.173(6)
K1–$O4^{10}$	2.999(6)	K1–$O2^{16}$	3.243(6)
K1–$O4^3$	2.999(6)	K1–$O2^{17}$	3.243(6)
K1–$O3^{12}$	2.690(6)	K1–$O2^{18}$	3.243(6)

Symmetry code

For compound KZn_4SbO_7: $(-y+1, x-y+1, z)^1$; $(-x+y, -x+1, z)^2$; $(-x, -y+1, z-1/2)^3$; $(-x+1, -y+2, z-1/2)^4$ $(-x+1, -y+1, z-1/2)^5$; $(-y, x-y, z)^6$; $(-x+y, -x, z)^7$; $(-x, -y, z-1/2)^8$; $(y, -x+y, z-1/2)^9$; $(x-y, x, z-1/2)^{10}$; $(x, y-1, z)^{11}$; $(y, -x+y, z+1/2)^{12}$; $(-x+y+1, -x+1, z)^{13}$; $(-y+1, x-y, z)^{14}$; $(-x, -y, z+1/2)^{15;}$ $(-x+1, -y+2, z+1/2)^{16}$; $(y-1, -x+y, z+1/2)^{17}$; $(x-y+1, x, z+1/2)^{18}$; $(y, -x+y+1, z+1/2)^{19}$; $(-x, -y+1, z+1/2)^{20;}$ $(x-y, x, z+1/2)^{21}$; $(x-y+1, x+1, z+1/2)^{22}$; $(-x+1, -y+1, z+1/2)^{23}$; $(x, y+1, z)^{24}$

For compound $KZn_4(SbO_4)_3$: $(-y+4/3, x-y+2/3, z-1/3)^1$; $(x-1/3, y-2/3, z+1/3)^2$; $(-y+2, x-y+1, z)^3$; $(-x+y+2/3, -x+4/3, z+1/3)^4$; $(x-2/3, y-1/3, z+2/3)^5$; $(-x+y+1/3, -x+5/3, z-1/3)^6$; $(-y+5/3, x-y+4/3, z-2/3)^7$; $(-y+5/3, x-y+4/3, z+1/3)^8$; $(x-1/3, y+1/3, z+1/3)^9$; $(-x+y+1, -x+2, z)^{10}$; $(x, y, z+1)^{11}$; $(-x+y+2/3, -x+4/3, z-2/3)^{12}$; $(x+2/3, y+1/3, z-2/3)^{13}$; $(-y+7/3, x-y+5/3, z-1/3)^{14}$; $(x+1/3, y-1/3, z-1/3)^{15}$; $(x, y, z-1)^{16}$; $(-y+2, x-y+1, z-1)^{17}$; $(-x+y+1, -x+2, z-1)^{18}$; $(x+1/3, y+2/3, z-1/3)^{19}$; $(-x+y+1/3, -x+5/3, z+2/3)^{20}$

at room temperature [62] and cubic type ZnO crystal (*Fm-3 m* symmetry) at high-pressure phases [63, 64]. For **2**, four Zn atoms are interconnected to the Sb atoms via O atoms, and they form a cage-like structure with an open end, and K

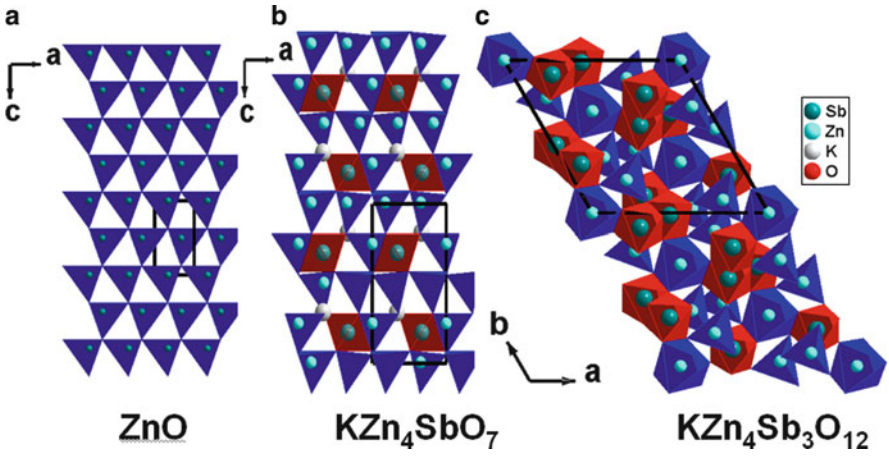

Fig. 14 Coordinate polyhedron representations of (**a**) ZnO, (**b**) KZn_4SbO_7, and (**c**) $KZn_4(SbO_4)_3$

atom is located in the vacancy that nears to the open end of a cage. The Sb–O bond distances range from 1.922 to 2.043 Å in crystal **2**. One of the reasons for the crystal structure transition from high-symmetry *P6₃mc* to low-symmetry *R3* arises from the large contents of Sb^{5+} diluter, with $Zn^{2+}/Sb^{5+} = 4/1$ and 4/3 for crystals **1** and **2**, respectively.

4.2 Second-Harmonic Generation Investigations

The crystal structures of both compounds **1** and **2** belong to NCS space groups, and it is interesting to study their NLO properties.

4.2.1 SHG Measurements and Results

The measurement of the powder SHG effect was carried out by means of the method of Kurtz and Perry [59]. The fundamental wavelength is 1064 nm generated by a Q-switched Nd: YAG laser. The SHG wavelength is 532 nm. All of the samples were placed in separate capillary tubes. No index-matching fluid was used in any of the experiments. Under the same particle size and fundamental wave intensity, the SHG intensity ratio can be calculated by [59]. Figure 15 gives the plots of relative SHG intensity for four powder samples of KZn_4SbO_7, $KZn_4Sb_3O_{12}$, ZnO, and KDP. Here, the particle sizes of the samples are smaller than 30 μm, and the SHG measurements of ZnO and KDP only give comparisons. We can find three features of SHG intensity from Fig. 15: (1) the SHG intensity of compound **1** is closed to the intensity of KDP, (2) the SHG intensity of compound **1** is larger than that of compound **2**, and (3) the SHG intensities of both **1** and **2** compounds are smaller than that of ZnO. The reasons of the last two features

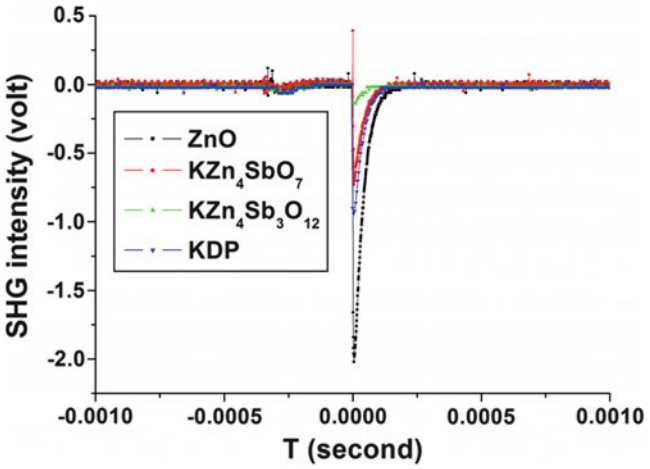

Fig. 15 Oscilloscope traces of the second-harmonic generation signals of KZn_4SbO_7, $KZn_4Sb_3O_{12}$, ZnO, and KDP

are explained in view of the crystal structures (seen in Fig. 14). Some NLO chromophores of ZnO_4 tetrahedra in ZnO crystal are replaced by the non-NLO active groups of regular SbO_6 octahedra, and it leads to a small macropolarization and SHG intensity in **1** and **2** crystals. Furthermore, the more replacements of NLO chromophores by non-NLO active groups are in ZnO crystal, the smaller SHG intensity of ZnO-based compounds. As mentioned above, the compound **2** has larger Sb^{5+} contents relative to the compound **1**; accordingly, the compound **2** exists at a smaller SHG intensity.

4.2.2 Calculations of SHG Coefficients

The second-order susceptibilities $\chi^{(2)}_{ijk}(-\omega_3;\omega_1,\omega_2)$ can be calculated according to the formula [65]

$$2d_{ijk}(-\omega_3;\omega_1,\omega_2) = \chi^{(2)}_{ijk}(-\omega_3;\omega_1,\omega_2) \;=\; F^{(2)}\chi^{(1)}_{ii}(\omega_3)\chi^{(1)}_{jj}(\omega_1)\chi^{(1)}_{kk}(\omega_2). \quad (2)$$

Here, the $\chi^{(1)}_{mm}(\omega_n)$ is the first-order nonresonant susceptibility at low-frequency region, and it is given by $\chi^{(1)}(\omega)_{mm} = [\varepsilon(\omega)_{mm} - 1]/4\pi$, and the dielectric function $\varepsilon(\omega)$ can be directly obtained from the output of CASTEP code from Materials Studio at low-frequency region [56, 66]. In (2), the $F^{(2)} = ma/(N^2e^3)$, and it is derived from a classical anharmonic oscillator (AHO) model [65]. The m and e are respectively the electron mass and charge, and the parameters a, characterizing the nonlinearity of the response, can be obtained from experimental or theoretical estimations. It is noted that N is a density number of unit cells in

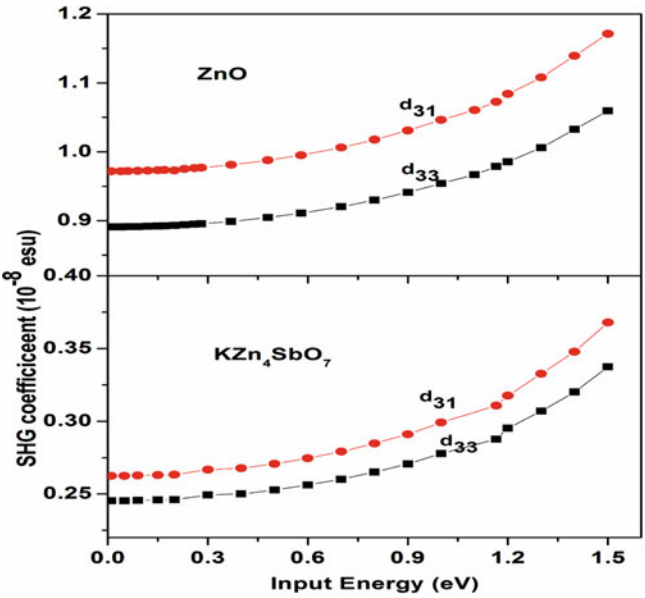

Fig. 16 The frequency-dependent second-order susceptibility components

a crystal instead of density number of atoms in a classical AHO model. The calculated susceptibility components of KZn_4SbO_7 and wurtzite-type ZnO crystals are given, with the same space group of $P6_3mc$. KZn_4SbO_7 and ZnO belong to the crystal class 6 mm. According to Kleinman's symmetry conditions, only two independent components *zzz* and *zxx* exist. The frequency-dependent (dynamic) second-order susceptibilities of d_{33}, d_{31} calculated by (2) are shown in Fig. 16 (here in (2), $F^{(2)} = 13.9975 \times 10^{-6}$ and 6.6511×10^{-6} esu for KZn_4SbO_7 and ZnO, respectively). It finds from Fig. 16 that the KZn_4SbO_7 bulk susceptibilities are about one third of ZnO ones. For example, the calculated values of $d_{33}, d_{31} (d_{33} = 1/2\chi^{(2)}_{zzz}, d_{31} = 1/2\chi^{(2)}_{zxx})$ are about 2.88×10^{-9}, 3.11×10^{-9} esu for KZn_4SbO_7 bulk and 9.79×10^{-9}, 10.73×10^{-9} esu for ZnO bulk at a wavelength of 1064 nm (1.165 eV), respectively. The variation trends match with our measured ones, as shown in Fig. 16. It was reported that the ZnO powder SHG intensity with particle size of 75–150 μ is about 15 time of quartz one [59]. If the quartz susceptibility is 0.96×10^{-9} esu [65], the ZnO powder susceptibility is estimated about 14.4×10^{-9} esu. This value is closed to our calculated value of 10.73×10^{-9} esu for ZnO. Accordingly, our calculated susceptibilities are reliable. Our experimental and theoretical results show that the SHG intensity will be reduced upon diminishing NCS chromophores in inorganic materials.

4.2.3 Band Structures and Electronic Originations of SHG

To gain an insight into the relation between electronic structure and optical properties, the band structure and state density were calculated by using hybrid B3LYP functional and running code CASTEP version 4.4 [55, 56, 66]. The crystallographic data of **1** and **2** [61], and that of ZnO and Sb_2O_5 provided [62, 67], were used for theoretical calculations. The total energy was calculated using exchange–-correlation parameters of the hybrid B3LYP functional. The interactions between the ionic cores and the electrons were described by the custom pseudopotential. The following orbital electrons were treated as valence electrons: K–$3s^2 3p^6 4s^1$, Zn–$3d^{10}4s^2$, Sb–$5s^2 5p^3$, and O–$2s^2 2p^4$. The basis set accuracy is medium. The other calculation parameters and convergent criteria were the default values of the CASTEP code [66].

The calculated band structures of Fig. 17 show that **1** is a direct gap material with a band gap of 2.083 eV and **2** is an indirect gap material with a band gap of 3.113 eV. The calculated band structures of ZnO and Sb_2O_5 are also plotted in Fig. 17 to make comparisons. The measured UV–VIS absorption cutoff is about 380 nm (3.263 eV) and 302 nm (4.106 eV) that deduces from optical diffuse reflectance spectrum for compounds **1** and **2**, respectively, as shown in Fig. 18. By comparisons of experimental gaps between **1** or **2** and ZnO, it is evident that the gap of **1** is close to the band gap of ZnO (3.37, 3.26 eV) [68, 69] and that of **2** is larger than that of ZnO. Here, we noted that the calculated gaps are smaller than the experiment values due to a general underestimation of band gap by using the DFT calculations [70–72]. Fortunately, the underestimated gap can be compensated by scissors operator, and the obtained results will not change band structures and DOS distributions. The calculated densities of states plotted in Fig. 19 indicate that the highest valence bands (H-VB) most contribute from O-2p states and the lowest conduction bands have some contributions from the unoccupied states of Sb^{5+} ions, respectively, for **1** and **2**. It finds from Fig. 19 and Fig. 17 that the **1** and **2** are large band gaps while Sb^{5+} is diluted into ZnO submatrix (the calculated gaps of ZnO and Sb_2O_3 are 1.463 and 2.287 eV, respectively), and that increases of Sb^{5+} contents extend conduction band width and result in a larger band gap of **2**, comparing with the **1** compound. It also finds from Fig. 19 that the Sb^{5+} density of states at conduction band is about 2.8 and 2.0 states/eV for **2** and **1**, respectively, and O^{2-} density of states are almost the same (about 20.0 states/eV) between **2** and **1** at valence band edge. These cases show that the charge transfers from O^{2-} to Sb^{5+} states are stronger for compound **2** than compound **1**, leading to the blue shifts of absorption edge for **2**. Further, the charge transfers within centrosymmetric chromophores SbO_6 will reduce charge polarization and descend SHG responses in the KZn_4SbO_7 comparing with that of parent ZnO, and the stronger charge transfers from O^{2-} to Sb^{5+} states, the weaker SHG responses are in $KZn_4(SbO_4)_3$. Accordingly, we can assign that the SHG originates from the charge transfers from O 2p to Sb and Zn unoccupied atomic states, and the decrease of Sb^{5+} ions lead to increase of SHG intensity in ZnO-based compounds of KZn_4SbO_7 and $KZn_4(SbO_4)_3$.

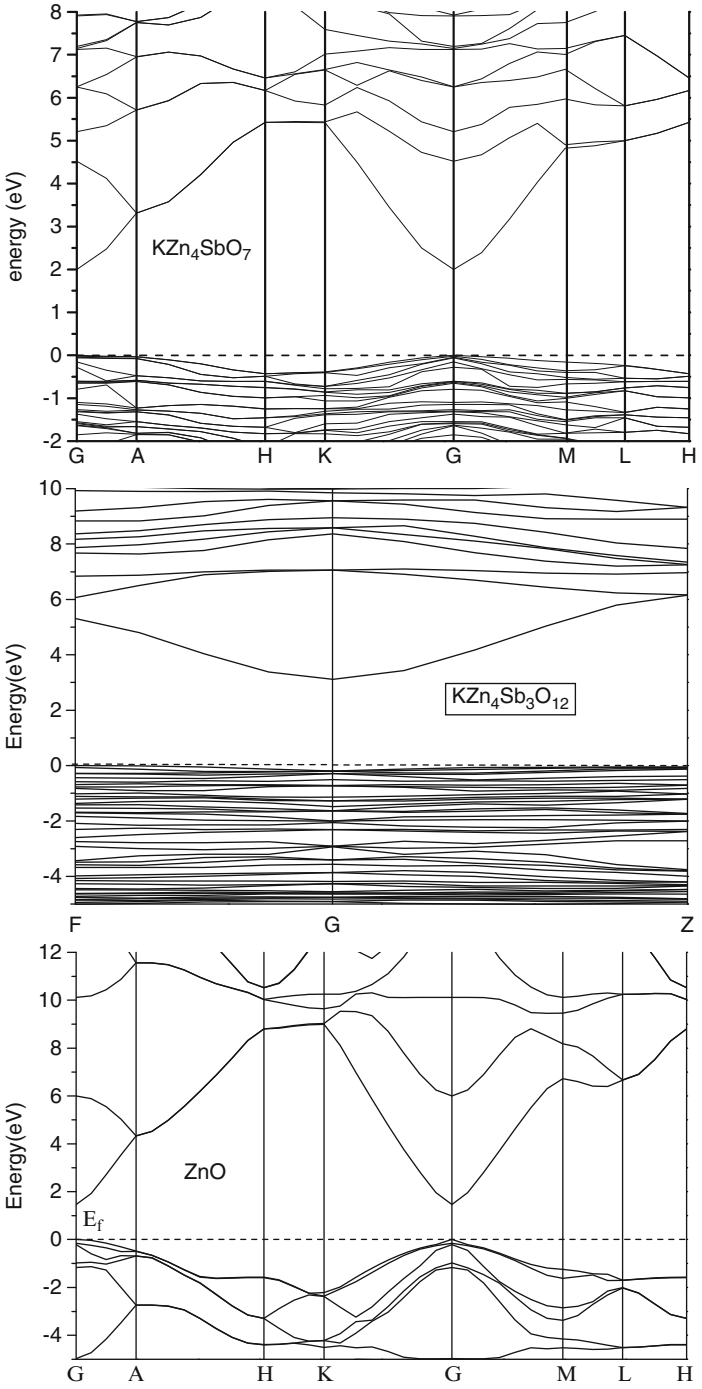

Fig. 17 (Continued)

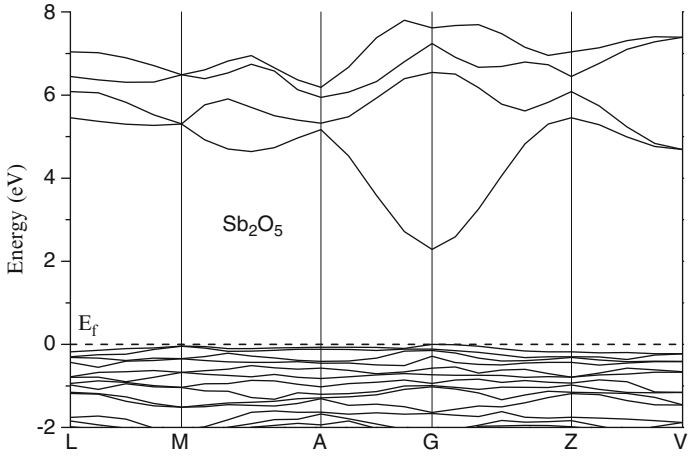

Fig. 17 The band structures of plots. The lowest conduction band is at G-point and the highest valence band at F-point for $KZn_4Sb_3O_{12}$ crystal; both the lowest conduction band and highest valence band are at G-point for KZn_4SbO_7, ZnO, and Sb_2O_5 crystals

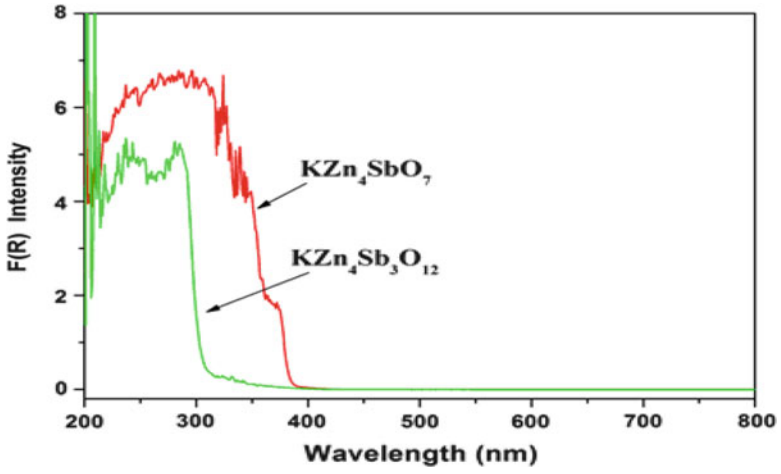

Fig. 18 Optical diffuse reflectance spectra of KZn_4SbO_7 and $KZn_4Sb_3O_{12}$

5 A Strong SHG Material $Cd_4BiO(BO_3)_3$ with 3-Chromophore Asymmetric Building Units

In $Cd_4BiO(BO_3)_3$ (hereafter we call CBOB), the strong SHG effect originates from the cooperation of the 3-chromophore asymmetric structures composed of the polar displacement of the d^{10} Cd^{2+} ion, SCALP effect of Bi^{3+}, and π-delocalization of BO_3 [29]. It is the first example of SHG with 3-chromophore asymmetrical building

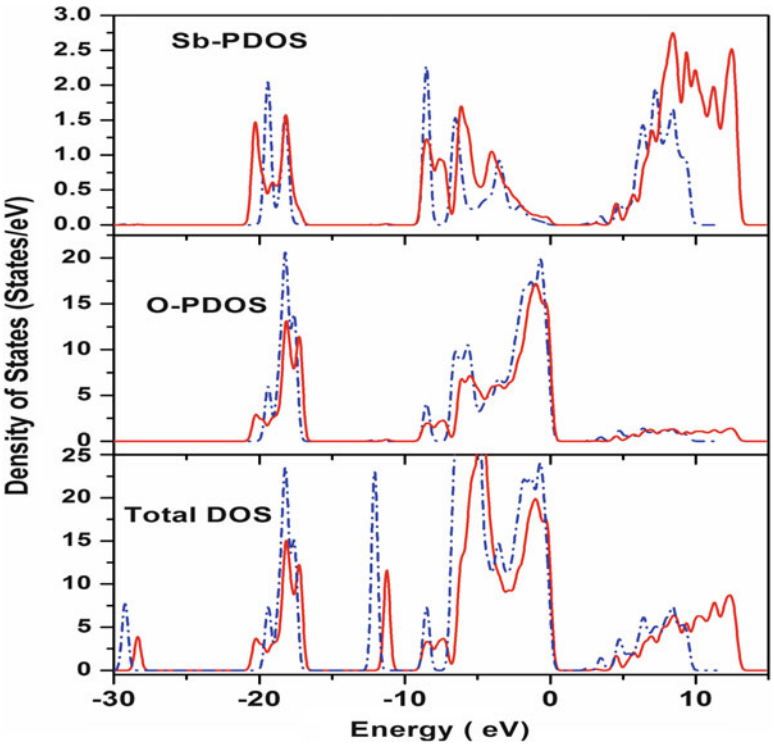

Fig. 19 Total density of states and O- and Sb- atomic partial density of states. The *blue dash dot* and *red solid lines* symbolize DOS or PDOS of KZn_4SbO_7 and $KZb_4Sb_3O_{12}$ bulks, respectively

units. Recently, it has been reported in another Cd^{2+}-rich compound of Cd_2InVO_6, in which the major part of the SHG coefficient may originate from the Cd^{2+}- and In^{3+}-centered polyhedra with strong distortions [73].

5.1 Preparation and Structure of Single Crystal of CBOB

Single crystals of CBOB were prepared by the high-temperature solid-state reaction in $CdO–Bi_2O_3–B_2O_3$ ternary system, and the obtained crystals by this reaction method have better chemical and thermal stability to ensure the feasibility of the industrial applications [29]. Crystallographic analysis revealed that the CBOB crystal belongs to the space group Cm. Its structure exhibits a complicated three-dimensional (3D) network composed of BiO_6, CdO_n ($n = 6,7$) distorted polyhedra, and π-delocalization BO_3 groups that are interconnected via corner or edge sharing as shown in Fig. 20a, b. In a $Cd1O_6$ octahedron, the Cd1-O2, Cd1-O3 (2) distances of 2.278, 2.313, and 2.327 Å are all shorter than the corresponding distances Cd1-O6, Cd1-O4 (2) of 2.286, 2.329, and 2.337 Å, and the $(Cd1)^{2+}$ cation

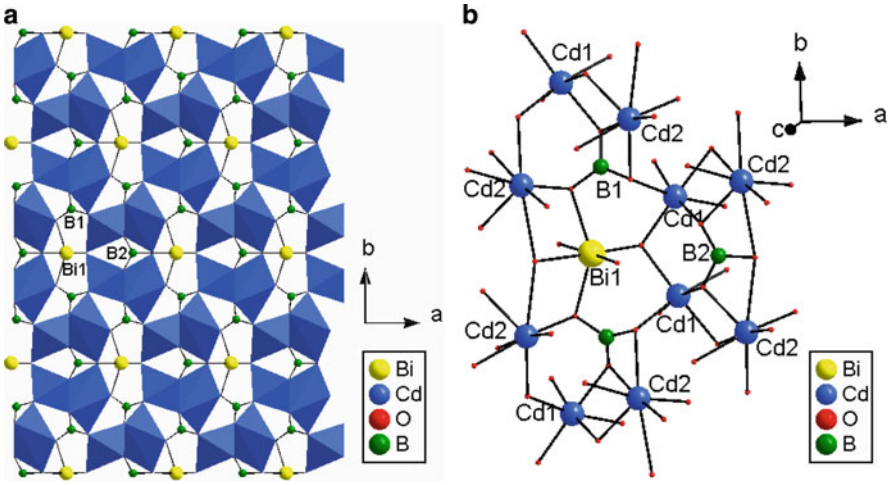

Fig. 20 View of the structure of $Cd_4BiO(BO_3)_3$ down the (**a**) *c* axis and (**b**) cation coordinate environments

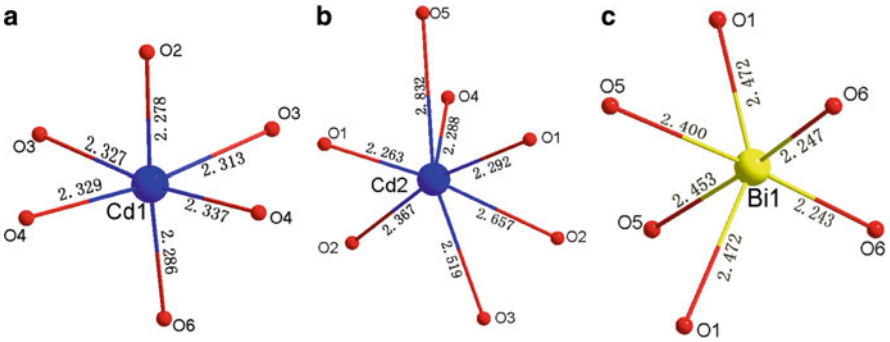

Fig. 21 The coordination of oxygen atoms around (**a**) Cd1, (**b**) Cd2, and (**c**) Bi cations

displacement is along the threefold rotational axis of the octahedron that pass through the triangle faces O3O2O3′ and O4O6O4′, as shown in Fig. 21a. This displacement of the cation leads to loss of symmetrical center of $Cd1O_6$ polyhedra. The $Cd2O_7$ is a distorted pentagonal bipyramid with Cd2–O bond distances ranging from 2.263(14) to 2.832(2) Å, as plotted in Fig. 21b. The 6-coordination Bi^{2+} is localized within the distorted octahedron BiO_6 resulting from the repulsive interactions between lone-pair electron of Bi^{2+} and electron pairs of Bi–O bonding. There are a larger Bi–O1 distance 2.472 Å and a smaller O1-Bi-O1′ angle 144.1° (perfect value 180°) due to the repulse interaction in the BiO_6 octahedron, as shown in Fig. 21c. $Cd1O_6$ and $Cd2O_7$ polyhedra are interconnected via sharing edges into a 1D double chain along the *c* axis (Fig. 22). The double chains are further interconnected via sharing corner into a 3D framework with the eight-member

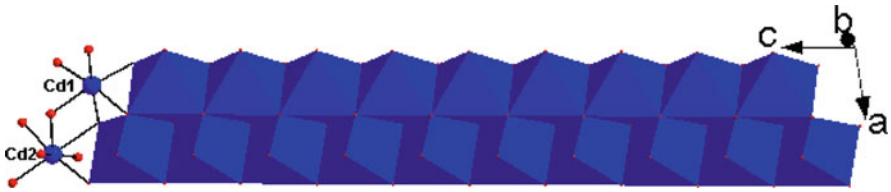

Fig. 22 1D chain formed by $Cd1O_6$ and $Cd2O_7$ polyhedra within $Cd_4BiO(BO_3)_3$

Table 6 The selected bond lengths (Å) and angles (°) for $Cd_4BiO(BO_3)_3$

Select important bond lengths			
Bi(1)–O(6)	2.242(16)	Bi(1)–O(6)#1	2.247(15)
Bi(1)–O(5)#2	2.45(2)	Bi(1)–O(1)#3	2.473(14)
Bi(1)–O(5)	2.40(2)	Bi(1)–O(1)	2.473(14)
Cd(1)–O(2)	2.278(14)	Cd(1)–O(6)#4	2.286(9)
Cd(1)–O(3)	2.327(15)	Cd(1)–O(4)#1	2.329(13)
Cd(1)–O(3)#2	2.313(12)	Cd(1)–O(4)	2.338(14)
Cd(2)–O(1)#1	2.263(14)	Cd(2)–O(4)	2.288(13)
Cd(2)–O(2)	2.365(15)	Cd(2)–O(3)#5	2.518(16)
Cd(2)–O(1)	2.293(13)	Cd(2)–O(2)#9	2.657(13)
Cd(2)–O(5)	2.831(4)	B(1)–O(1)#10	1.38(2)
B(1)–O(3)#5	1.33(2)	B(1)–O(2)#2	1.40(2)
B(2)–O(5)	1.45(3)	B(2)–O(4)#3	1.339(19)
B(2)–O(4)	1.330(19)		
Select important angles			
O(6)–Bi(1)–O(6)#1	102.0(6)	O(6)#1–Bi(1)–O(5)	83.5(7)
O(5)–Bi(1)–O(5)#2	92.1(7)	O(6)–Bi(1)–O(1)#3	97.8(3)
O(5)–Bi(1)–O(1)#3	80.7(3)	O(1)#3–Bi(1)–O(1)	144.1(6)
O(2)–Cd(1)–O(4)#1	83.3(5)	O(2)–Cd(1)–O(3)#2	88.0(6)
O(2)–Cd(1)–O(4)	79.6(5)	O(3)#2–Cd(1)–O(4)	82.2(4)
O(6)#4–Cd(1)–O(4)	96.0(5)	O(6)#4–Cd(1)–O(3)	92.7(5)
O(1)#1–Cd(2)–O(2)	89.4(5)	O(1)#1–Cd(2)–O(4)	109.6(5)
O(1)#1–Cd(2)–O(1)	100.0(5)	O(1)#1–Cd(2)–O(3)#5	119.2(4)
O(4)–Cd(2)–O(2)	78.8(5)	O(2)–Cd(2)–O(3)#5	79.1(5)
O(3)#5–B(1)–O(1)#10	122.4(16)	O(3)#5–B(1)–O(2)#2	119.2(15)
O(1)#10–B(1)–O(2)#2	118.3(15)	O(4)–B(2)–O(5)	117.8(11)
O(4)#3–B(2)–O(4)	123(2)	O(4)#3–B(2)–O(5)	117.8(11)

Symmetry transformations used to generate equivalent atoms
#1 $x, y, z + 1$; #2 $x, y, z - 1$ #3 $x, -y + 1, z$; #4 $x - 1, y, z + 1$; #5 $x + 1/2, -y + 3/2, z - 1$;#6 $x + 1/2, -y + 3/2, z$ #7 $x - 1/2, -y + 3/2, z + 1$ #8 $x + 1, y, z - 1$; #9 $x + 1, -y + 1, z - 1$; #10 $x - 1/2, -y + 3/2, z$

and four-member tunnels. Then, the B1 and Bi atoms are located in eight-member tunnels, while the B2 atoms are located in four-member tunnels. The important bond lengths and angles are listed in Table 6 for CBOB.

5.2 Electronic Structural Calculations of CBOB

5.2.1 Band Structure and Density of State

The compound CBOB crystallizes in the acentric monoclinic space group Cm with unit cell parameters of $a = 8.044(2)$ Å, $b = 15.913(5)$ Å, $c = 3.4891(10)$ Å, $\beta = 100.08(2)^{\circ\sim}$, and $Z = 2$ [29]. The crystallographic data determined by X-ray single-crystal diffraction [29] is used for the calculations of band structure and density of state. The total-energy code CASTEP [55, 56, 66] which employs pseudopotentials to describe electron–ion interactions and represents electronic wave functions using a plane wave basis set is employed for the calculations. The total energy is calculated within the framework of nonlocal gradient-corrected approximations Perdew–Burke–Ernzerhof (PBE) functional. The interactions between the ionic cores and the electrons are described by the norm-conserving pseudopotential. The following orbital electrons are treated as valence electrons: Bi-$5d^{10}6s^26p^3$, Cd-$4d^{10}5s^2$, B-$2s^22p^1$, and O-$2s^22p^4$. The number of plane waves included in the basis is determined by a cutoff energy of 450 eV, and the numerical integration of the Brillouin zone is performed using a $3 \times 3 \times 6$ Monkhorst–Pack k-point sampling for CBOB. The total energy convergence threshold is 2×10^{-6} eV per atom, and the other calculating parameters and convergent criteria are set by the default values of CASTEP code [66]. The calculated state energies (eV) of the lowest conduction band (L-CB) and the H-VB at some k-points are listed in Table 7. The lowest energy of the conduction bands (L-CB) located at the k-point of G is 2.23 eV, and the highest energy (−0.01 eV) of the valence bands (H-VB) is located at the k-point of M. Accordingly, the CBOB compound is wide-band material with the indirect band gap of 2.23 eV, which is significantly smaller than the measurement value (3.16 eV) [29] as a result of the limitations of DFT method [70–72]. The band structures of the CBOB along high-symmetry points within the first Brillouin zone are plotted in Fig. 23a by using the scissor operator with shift energy of 0.92 eV. The bands can be assigned according to the total and partial densities of states (DOS) as plotted in Fig. 23b. The bands just above the Fermi level are predominately derived from Bi-6p, B-2p, and some unoccupied O-2p and Cd-5s5p states, whereas the band just below the Fermi level is composed of O-2p, mixing with small amounts of Bi-6s states. The bands ranging from −20.0 to −15.0 eV mostly originates from mixed

Table 7 State energies (eV) of the lowest conduction band and the highest valence band at some k-points

Compound	K-point	L-CB	H-VB
CBOB	L (−0.500, 0.000, 0.500)	3.7758	−0.0145
	M (−0.500, −0.500, 0.500)	3.8405	−0.0092
	A (−0.500, 0.000, 0.000)−0.08016	2.3521	−0.3384
	G (0.000, 0.000, 0.000)	2.2291	−0.4100
	Z (0.000, −0.500, 0.500)	3.7758	−0.0145
	V (0.000, 0.000, 0.500)	3.8947	−0.1246

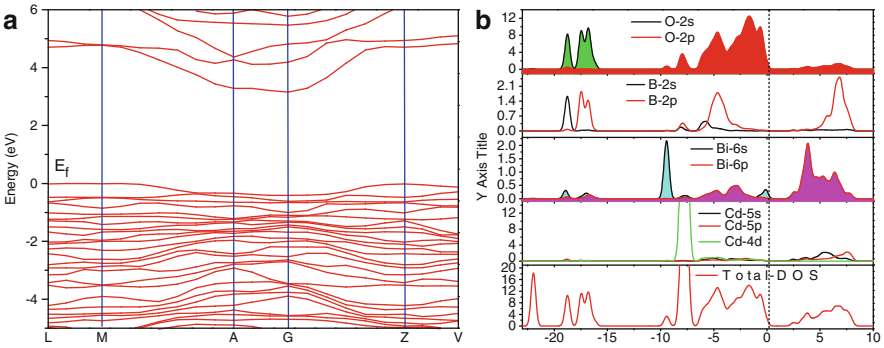

Fig. 23 (**a**) The band structure ranging from −5.0 to 6.0 eV; (**b**) the density of state and Fermi level localized at 0.0 eV for CBOB

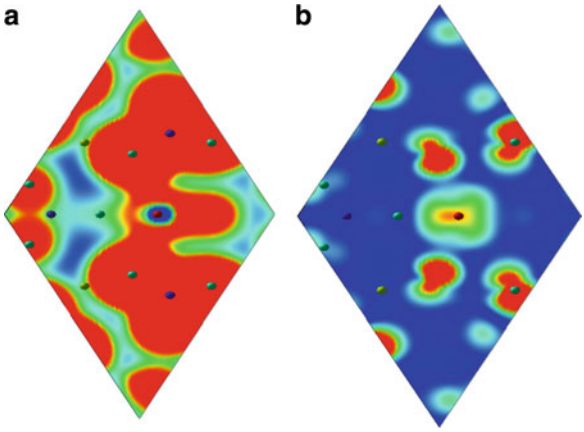

Fig. 24 (**a**) Partial charge density (0 to 0.01 e/Å^3) from −19 to −17 eV; (**b**) partial charge density (0 to 0.05 e/Å^3) from −1.0 eV to Fermi level

states of O-2s2p and B-2s2p. The bands from −12.5 to −2.5 eV are composed of O-2p, B-2p, and Cd-4d states mixing with small Bi-6s state.

5.2.2 Stereochemically Active Evidences of Bi^{3+}-$6s^2$ Lone Pair

Here, it notes an interesting fact from the Bi atomic PDOS of Fig. 23b. The broad distributions Bi-6s states from −19.0 to −17.0 eV result from bonding interactions between the Bi-6s and O-2p states, and the less contributions are found at near the top valence band (from −1.0 eV to Fermi level) resulting from the antibonding interactions between the Bi-6s and O-2p states according to the partial charge density distributions of Fig. 24a, b, respectively. The indirect mixings between Bi-6s and -6p states are mediated by hybridizations O-2p states at the top of valence bands. The formation of the Bi^{3+} $6s^2$ lone pair is shown to have O^{2-} anion dependence, and this dependence on the electronic states of the anion can be

Fig. 25 The plot of electron-density difference map containing Bi–O1 plane in $Cd_4BiO(BO_3)_3$, charges increasing from *blue* to *red color*

stereochemically active evidence of the lone pair. The other one evidence of the SCALP effect of Bi^{3+} cation is also provided by the electron-density difference map contained Bi–O1 plane in Fig. 25. This plot gives visualization of the lone pair, and it clearly reveals highly asymmetric lobes on the Bi^{3+}cations. This asymmetric lobe is thought of as SCALP.

5.3 *Investigations of Nonlinear Optical Response of CBOB*

5.3.1 SHG, Transmission, and Thermal Stability

The monophase powder of CBOB was prepared from the stoichiometric mixture of Bi_2O_3, CdO, and H_3BO_3, and the powder sample of CBOB was confirmed by XRD powder diffraction studies [29]. The obtained monophase powder samples were used for SHG measurements by means of the method of Kurtz and Perry [59]. The fundamental wavelength is 1064 nm generated by a Q-switched Nd: YAG laser. The SHG wavelength is 532 nm. KDP was used as reference to assume the effect. The SHG efficiency of powder sample has been shown to depend strongly on particle size; thus, samples of KDP and CBOB were ground and sieved into several distinct particle size ranges (25–44, 44–53, 53–74, 74–105, 105–149, 149–210 μm). All of the samples were placed in separate capillary tubes. No index-matching fluid

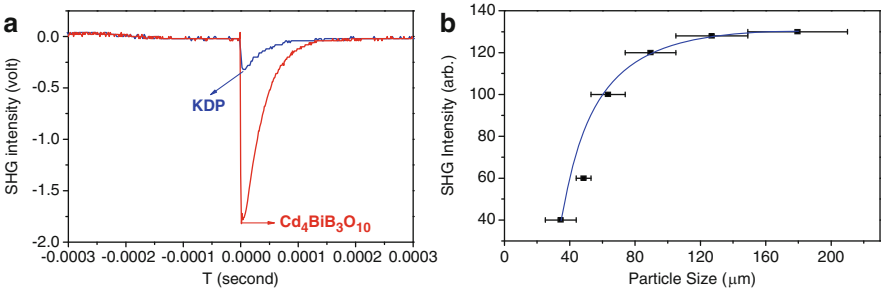

Fig. 26 (**a**) Oscilloscope traces of the second-harmonic generation signals KDP and $Cd_4BiO(BO_3)_3$ and (**b**) particle size vs SHG intensity of $Cd_4BiO(BO_3)_3$

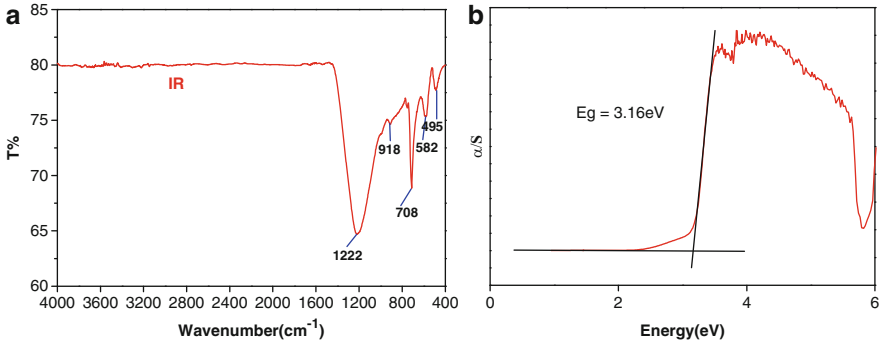

Fig. 27 (**a**) Infrared absorption spectra and (**b**) optical diffuse reflectance spectra for $Cd_4BiO(BO_3)_3$

was used in any of the experiments. Under the same particle size and fundamental wave intensity for the measured samples, the measured SHG intensity ratio is plotted in Fig. 26a, and the ratio can be calculated by [59]. It is shown from Fig. 26a that the SHG signal of CBOB is about 6.0 times of that of KDP standard of similar grain size. Figure 26b shows a plot of second-harmonic intensity vs particle size of CBCO powders. It finds that for the particle size less than 100 μm, second-harmonic intensity is linearly increase with the increasing particle size, and for the particle size larger than 120 μm, second-harmonic intensity is essentially independent of particle size. This feature suggests that the compound is phase-matchable material based on the SHG measurements of powder [59].

To investigate the light transmission, infrared absorption spectroscopy of CBOB powder sample was measured, and it is shown in Fig. 27a. It indicates that the CBOB is transparent in the range of 4,000–1,500 cm^{-1}. An optical diffuse reflectance spectrum was also measured at room temperature, and it is shown in Fig. 27b. The UV–vis absorption spectrum was calculated from reflectance spectra by using the Kubelka–Munk function [74]: $F(R) = (1–R)^2/2R$, where R is the reflectance and $F(R)$ is the Kubelka–Munk remission function. The optical diffuse reflectance

spectrum indicated an optical band gap of 3.16 eV, and UV absorption cutoff edge at 392 nm, as shown in Fig. 27b.

For insight into the thermal stability of CBOB, thermogravimetric analyses (TGA) and differential thermal analyses (DTA) were carried out under an air atmosphere, and it is shown in Fig. 28a, b, respectively. The samples were placed in Al_2O_3 crucibles and heated from 35°C to 1,200°C at the rate of 10.0°C/min. The compound CBOB exhibits only one main step of weight loss, and the total weight loss is 27.3% at 1,200°C. The sharp weight loss corresponds to the decomposition of the compound. The DTA trace for the CBOB also exhibits an endothermic peak at 885°C on the heating curve, which tentatively suggests that CBOB melts congruently at 885°C, and the thermal analysis indicates that the CBCO is thermally stable up to about 900°C.

5.3.2 Calculations of Susceptibilities

The first-order susceptibility and linear refractive index can be derived from the dielectric function. The first-order nonresonant susceptibility at low-frequency region is given by $\chi^{(1)}(\omega)_{ii} = [\varepsilon(\omega)_{ii} - 1]/4\pi$, and the linear refractive index $[n(\omega \to 0)]^2_{ii} = \varepsilon_1(\omega \to 0)_{ii}$. The second-order susceptibility $\chi^{(2)}$ and doubling frequency coefficient d_{ij} can be expressed in terms of the first-order susceptibilities according to formula (2). The calculated dispersion of linear refractive index appears at the anisotropy as plotted in Fig. 29a, which arises from the anisotropy of the dielectric function, $\varepsilon_{1x} > \varepsilon_{1y} > \varepsilon_{1z}$. The calculated static linear refractive indices of n_x, n_y, and n_z are 1.9553, 1.9541, and 1.9249, individually. The space

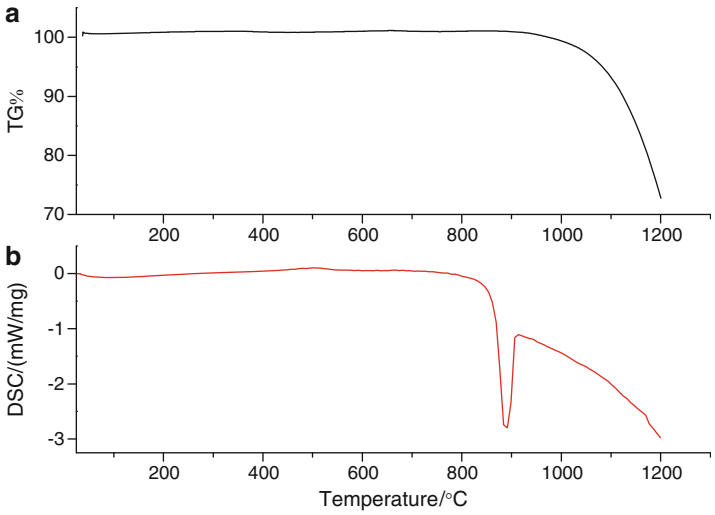

Fig. 28 (**a**) Thermogravimetric analyses and (**b**) differential thermal analyses diagrams for $Cd_4BiO(BO_3)_3$

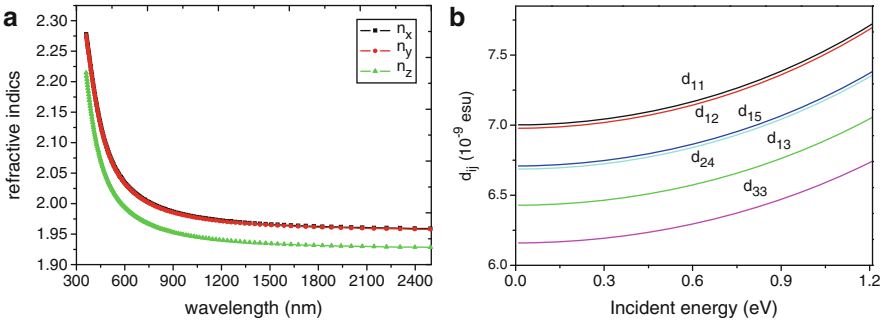

Fig. 29 (**a**) The calculated linear refractive indices and (**b**) frequency-dependent second-harmonic generation coefficients of $Cd_4BiO(BO_3)_3$ crystal

group of CBOB belongs to class *m* and has ten nonvanishing tensors of second-order susceptibility. Under the restriction of Kleinman's symmetry, only six independent SHG tensor components (d_{11}, d_{12}, d_{13}, d_{15}, d_{24}, and d_{33}) were considered. The frequency-dependent SHG tensor components of the CBOB were plotted in Fig. 29b. The calculated largest and smallest tensor components, d_{11} and d_{33}, are 3.21 pm/V (7.67×10^{-9} esu) and 2.81 pm/V (6.70×10^{-9} esu) at a wavelength of 1064 nm (1.165 eV), respectively. These values are close to our experimental value [29], which is six times that of KDP ($d_{36} = 1.1 \times 10^{-9}$ esu). Often, the performance of a NLO crystal or device is characterized by the FOM, which is defined as the FOM $= d_{\text{eff}}^2/(n_\omega^2 n_{2\omega})$ [16, 75]. It states that a large NLO coefficient combined with a low refractive index is desirable. As is evident from formula [16]

$$I(2\omega, l) = \frac{2\omega^2}{c^3 \varepsilon_0} \frac{d_{\text{eff}}^2 l^2}{n_{2\omega} n_\omega^2} \left(\frac{\sin(\Delta k l/2)}{\Delta k l/2} \right)^2 I^2(\omega), \tag{3}$$

where the intensity of doubling frequency light $I(2\omega,l)$ is directly proportional to the effective nonlinear coefficient d_{eff} while, at the same time, it has an inverse-square-root dependence on the refractive indexes. It is often customary to describe the efficiency of the nonlinear material from formula (3) in terms of a FOM. The calculated FOM of CBOB is 1.232 while $d_{ij} \approx d_{\text{eff}}$ with a theoretical estimation. By the comparisons with the available experiment data of β-BBO and LBO crystals [16], it is found that the FOM of CBOB is larger than those of β-BBO and LBO crystals.

5.3.3 Electronic Origination of SHG

We can gain an insight into the relation between electronic structures and NLO properties according to the above calculations of the band structures and densities of states as well as electronic density differences. It is found from Fig. 23b that the band just above the Fermi level is predominately derived from Bi-6p, but with

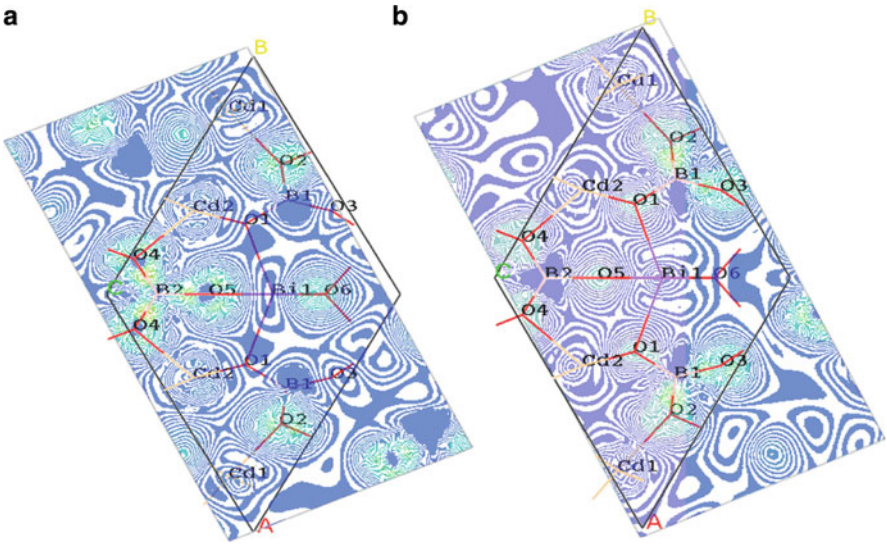

Fig. 30 The plots of electron-density difference maps containing (**a**) Cd2–O5 plane and containing (**b**) Cd1–O2 plane in $Cd_4BiO(BO_3)_3$, charges increasing from *blue* to *red color*

mixings of B-2p and Cd-5s, and much less unoccupied O-2p states and least unoccupied Bi-6s states. However, the band just below the Fermi level is mostly composed of O-2p states, and less mixed Bi-6s and Bi-6p states. The findings show that the charge transfers cross the band-gap edge are contributions from the O-2p state to the B-2p and Bi-6p and Cd-5s states. That is, the charge transfers within the 3-chromophores including BO_3, BiO_6, and CdO_n groups lead to a large SHG for the CBOB compound. The evidence is also found in the electron-density difference map of Fig. 30, for example, a decrease of O charges and an increase of cation charges in the B1–O1, Cd2–O4, Cd1–O2, and Bi–O1 linker zones. The compound $A_4M^{(III)}O(BO_3)_3$ (A = Ca; M = Nd, Gd, Sc, and Y) are isostructural with CBOB; however, the SHG response of CBOB is obviously larger than theirs [76–78]. By the above analyses, the strong SHG response of CBOB can be attributed to cooperation effects of the polarizations of the BiO_6 octahedra due to the Bi^{3+} cation SCALP, the asymmetric π-delocalization BO_3 groups, and the CdO_n polyhedra with polar displacement of d^{10} cation Cd^{2+}.

6 Conclusions

Following the idea of structural designs, we employed (1) 2-carboxylic acid-4-nitropyridine-1-oxide (POA) with π-charge asymmetrical distortion as chromophore to control packing of these chromophores to obtain two SHG crystals, (2) the distortion structure from a SCALP of cation Bi^{3+} as the building blocks to obtain

the eulytite-like $A_3^{II}M^{III}(PO_4)_3$ compounds crystallized in the acentric space group, (3) the ZnO with lacking a center of inversion as reaction precursor to synthesize SHG compounds of KZn_4SbO_7 and $KZn_4(SbO_4)_3$, and(4) three asymmetrical building units of polar displacement of the d^{10} Cd^{2+} ion, SCALP effect of Bi^{3+}, and π-delocalization of BO_3 to obtain strong SHG material of $Cd_4BiO(BO_3)_3$. The single-crystal structures were characterized, and physical properties, in particular, SHG responses, were measured for the obtained compounds. The electronic structures and DOS were calculated by DFT method, and the SHG properties are simulated to gain an insight into the relations between structure and NLO properties for the materials. The electronic origination of large SHG responses was assigned in terms of the calculated results.

References

1. Jechow A, Menzel R, Paschke K, Erbert G (2010) Laser Photon Rev 4:633–655
2. Lin C, Grau M, Dier O, Amann MC (2004) App Phys Lett 84:5088–5090
3. Campagnola PJ, Clark HA, Mohler WA, Lewis A, Loew LM (2001) J Biomed Opt 6:277–286
4. Campagnola PJ, Clark HA, Mohler WA, Lewis A, Loew LM (2003) Nat Biotech 21:1356–1360
5. Pantazis P, Maloney J, Wu D, Fraser S (2010) Proc Natl Acad Sci USA 107:14535–14540
6. Ramón C, Dawn N, Schafer KE, Sheetz FJF, Cisek R, Barzda V, Sylvester AW, Squier JA (2009) Rev Sci Instrum 80:081101–23
7. Cheng W-D, Wu D-S, Zhang H, Li X-D, Chen D-G, Lang Y-Z, Zhang Y-C, Gong Y-J (2004) J Phys Chem B 108:12658–12664
8. Segall MD, Lindan PLD, Probert MJ, Pickard CJ, Hasnip PJ, Clark SJ, Payne MC (2002) J Phys Condens Matter 14:2717–2744
9. Franken PA, Hill AE, Peters CW, Weinreich G (1961) Phys Rev Lett 7:118–119
10. Chen C-Z, Gao D-S, Chen C-T (1979) Acad Thesis Conf Cryst Growth Mater (China) B 44:197–199
11. Chen CT, Wu B, Jian A, You G (1985) Sci Sin B 28:235–243
12. Chen C-T, Wu Y-C, Jiang A-D, Wu B-C, You G-M, Li R-K, Lin S-J (1989) J Opt Soc Am B 6:616–621
13. Haidar S, Sasaki Y, Niwa E, Masumoto K, Ito H (2004) Opt Commun 229:325–330
14. Myers LE, Eckardt RC, Fejer MM, Byer RL, Bosenberg WR, Pierce JW (1995) J Opt Soc Am B 12:2102–2116
15. Li S-T, Zhang X-Y, Wang Q-P, Zhang X-L, Cong Z-H, Zhang H-J, Wang J-Y (2007) Opt Lett 32:2951–2953
16. Nie W (1993) Adv Mater 5:520–545
17. Ra HS, Ok KM, Halasyamani PS (2003) J Am Chem Soc 125:7764–7765
18. Sykora RE, Ok KM, Halasyamani PS, Albrecht-Schmitt TE (2002) J Am Chem Soc 124:1951–1957
19. Chi EO, Ok KM, Porter Y, Halasyamani PS (2006) Chem Mater 18:2070–2074
20. Inaguma Y, Yoshida M, Katsumata T (2008) J Am Chem Soc 130:6704–6705
21. Kim SH, Yeon J, Halasyamani PS (2009) Chem Mater 21:5335–5342
22. Phanon D, Gautier-Luneau I (2007) Angew Chem Int Ed 46:8488–8491
23. Sasaki T, Mori Y, Yoshimura M, Yap YK, Kamimura T (2000) Mater Sci Eng R Rep 30:1–54
24. Kong F, Huang S-P, Sun Z-M, Mao J-G, Cheng W-D (2006) J Am Chem Soc 128:7750–7751

25. Pan S, Smit JP, Watkins B, Marvel MR, Stern CL, Poeppelmeier KR (2006) J Am Chem Soc 128:11631–11634
26. Goodey J, Ok KM, Hofmann C, Broussard J, Escobedo FV, Halasyamani PS (2003) J Solid State Chem 175:3–12
27. Cohen RE, Krakauer H (1992) Ferroelectrics 136:65–83
28. Yang T, Sun J-L, Yeon J, ShivHalasyamani P, Huang S-L, Hemberger J, Greenblatt M (2010) Chem Mater 22:4814–4820
29. Zhang W-L, Cheng W-D, Zhang H, Geng L, Lin C-S, He Z-Z (2010) J Am Chem Soc 132:1508–1509
30. Wu W-S, Wu D-S, Cheng W-D, Zhang H, Dai J-C (2007) Cryst Growth Des 7:2316–2323
31. Zhang W-L, Lin X-S, Zhang H, Wang J-Y, Lin C-S, He Z-Z, Cheng W-D (2010) Dalton Trans 39:1546–1551
32. Brammer L (2004) Chem Soc Rev 33:476–489
33. Evans OR, Lin W-B (2002) Acc Chem Res 35:511–522
34. Evans OR, Lin W-B (2001) Chem Mater 13:2705–2712
35. Li SX, Liu SX, Wu WS (1987) Chin J Struct Chem 6:20–22
36. Baert F, Schweiss P, Heger G, More M (1988) J Mol Struct 178:29–48
37. Hartmann M, Wetmore SD, Random L (2001) J Phys Chem A 105:4470–4479
38. Becke AD (1993) J Chem Phys 98:5648–5652
39. Thalladi VR, Brasselet S, Weiss H-C, Bläser D, Katz AK, Carrell HL, Boese R, Zyss J, Nangia A, Desiraju GR (1998) J Am Chem Soc 120:2563–2577
40. Becke AD (1988) Phy Rev A 38:3098–3100
41. Perdew JP (1986) Phy Rev B 33:8822–8824
42. Pierre M, Baldeck PL, Block D, Georges R, Trommsdorff HP, Zyss J (1991) Chem Phys 156:103–111
43. Orr BJ, Ward JF (1971) Mol Phys 20:513–526
44. Bishop DM (1994) J Chem Phys 100:6535–6542
45. Zyss J, Nicoud JF, Conquillary M (1984) J Chem Phys 81:4160–4167
46. Kurtz SK, Jerphagnon J, Choy MM (1979) Landolt Bornstein Data Ser 11:671–674
47. Zyss J, Oudar JL (1982) Phys Rev A 26:2028–2048
48. Zyss J, Ledoux-Rak I, Weiss H-C, Blaser D, Boese R, Thallapally PK, Thalladi VR, Desiraju GR (2003) Chem Mater 15:3063–3073
49. Zhu W, Wu G-S (2001) J Phys Chem A 105:9568–9574
50. Sheldrick GM (1997) SHELXTL-97 Program for the refinement of crystal structure, University of Göttingen, Göttingen, Germany
51. Spek AL (2003) J Appl Crystallogr 36:7–13
52. Arbib EH, Elouadi B, Chaminade JP, Darriet J (2000) Mat Res Bull 35:761–773
53. Leclaire A, Borel MM, Raveau B (2001) J Solid State Chem 162:354–357
54. Roussel P, Giraud S, Suard E, Wignacourt JP, Steinfink H (2002) Solid State Sci 4:1143–1152
55. Perdew JP, Burke K, Ernzerhof M (1996) Phys Rev Lett 77:3865–3868
56. Chang HY, Kim SH, Ok KM, Halasyamani PS (2009) Chem Mater 21:1654–1662
57. Watson GW, Parker SC (1999) J Phys Chem B 103:1258–1262
58. Lefebvre I, Szymanski MA, Olivier-Fourcade J, Jumas JC (1998) Phys Rev B 58:1896–1906
59. Kurtz SW, Perry TT (1968) J Appl Phys 39:3798–3813
60. Klingshirn C (2007) Phys Stat Sol B 244:3027–3073
61. Yang S-L, Cheng W-D, Zhang H, Lin C-S, Zhang W-L, He Z-Z (2010) Dalton Trans 39:9547–9553
62. Kisi EH, Elcombe MM (1989) Acta Crystallogr C 45:1867–1870
63. Bates CH, White WB (1962) Science 137:993
64. Bates CH, White WB (1991) Mater Sci Forum 79:419–426
65. Boyd RW (1992) Nonlinear optics. Academic, New York, pp 21–52
66. Segall M, Probert M, Pickard C, Hasnip P, Clark S, Refson K, Payne M. Materials Studio CASTEP, Version 4.4

67. Jansen M (1979) Acta Crystallogr Sect B 35:539–542
68. Zhou S, Zhang X, Meng X, Fan X, Wu S, Zou K, Lee S (2004) Nanotechnology 15:1152–1155
69. Karazhanov S, Ravindran P, Kjekshus A, Fjellvag H, Svensson B (2007) Phys Rev B Condens Matter Mater Phys 75:155104–155106
70. Godby RW, Schluther M, Sham LJ (1987) Phy Rev B Condens Matter 36:6497–6500
71. Okoye CMI (2003) J Phys Condens Matter 15:5945–5958
72. Zhu J, Cheng W-D, Wu D-S, Zhang H, Gong Y-J, Tong H-N, Zhao D (2007) Eur J Inorg Chem 285–290
73. Yang T, Sun J, Yeon J, Halasyamani PS, Huang S, Hemberger J, Greenblatt M (2010) Chem Mater 22:4814–4820
74. Wendlandt WM, Hecht HG (1966) Reflectance spectroscopy. Interscience, New York
75. Yokoyama T, Nakayama K, Kurozuka KA, Mizushima T, Itoh T, Mizuuchi K, Yamamoto K (2008) Rev Laser Eng, Supplemental Volume: 1046–1048
76. Aka G, Mougel F, Augé F, Kahn-Harari A, Vivien D, Bénitez JM, Salin F, Pelenc D, Balembois F, Georges P, Brun A, Le Nain N, Jacquet M (2000) J Alloys Compd 401:303–304
77. Gheorghe L, Loiseau P, Aka G, Lupei V (2006) J Cryst Growth 294:442–446
78. Aka G, Brenier A (2003) Opt Mater 22:89–94

Struct Bond (2012) 144: 43–104
DOI: 10.1007/430_2011_65
© Springer-Verlag Berlin Heidelberg 2012
Published online: 3 March 2012

Second-Order Nonlinear Optical Materials Based on Metal Iodates, Selenites, and Tellurites

Fang Kong, Chuan-Fu Sun, Bing-Ping Yang, and Jiang-Gao Mao

Abstract In this chapter, the syntheses, structures, and Second Harmonic Generation (SHG) properties of metal iodates, selenites, and tellurites all of which contain a lone pair cation in an asymmetric coordination geometry were reviewed. A second asymmetric building unit such as distorted octahedra of the d^0 transition-metal (TM) cations such as V^{5+}, Mo^{6+}, other cations with a stereochemically active lone pair such as Pb^{2+} and Bi^{3+}, and tetrahedral groups such as BO_4^{5-} and PO_4^{3-}, can be introduced into metal iodates, selenites, and tellurites. The combination of d^0 transition-metal cations with the iodate groups afforded a large number of new metal iodates, a number of which display excellent SHG properties due to the additive effects of polarizations from both types of the asymmetric units. Introducing other lone-pair cations such as Pb^{2+} and Bi^{3+} into the metal iodates is also an effective strategy to design new SHG materials. With respect to the metal selenite or tellurite systems, many compounds in the alkali or alkaline earth-d^0 TM–Se(IV)/Te(IV)–O systems can also exhibit excellent SHG properties due to the additive effects of polarizations from both types of asymmetric units. Lanthanide or posttransition metal main group element-d^0 TM–Se(IV)/Te(IV)–O compounds are usually structurally centrosymmetric and not SHG active, but they can also display abundant structural diversities and interesting magnetic or luminescent properties. Metal tellurites and selenites containing tetrahedral groups of the main group elements such as BO_4 and PO_4 may also form NCS structures with excellent SHG properties.

F. Kong, C.-F. Sun, B.-P. Yang, and J.-G. Mao (✉)
State Key Laboratory of Structural Chemistry, Fujian Institute of Research on the Structure of Matter, Chinese Academy of Sciences, Fuzhou 350002, People's Republic of China
e-mail: mjg@fjirsm.ac.cn

Keywords Iodates · Lone pairs · Noncentrosymmetric structures · Second harmonic generation · Selenites · Tellurites

Contents

1 Introduction 44
2 Metal Iodates Containing d^0 Transition Metal Ions or Other Lone-Pair Cations 47
2.1 Combination of d^0 Transition Metal Ions with Iodate Group 48
2.2 Combination of Other Lone-Pair Cations with Iodate Groups 60
2.3 Other Mixed Metal Iodates 62
3 Selenites or Tellurites Containing d^0 Transition Metal Ions or Halogen Anions or Tetrahedral Groups of Main Group Elements 65
3.1 Combination of d^0 Transition Metal Ions with Selenites or Tellurites 66
3.2 Metal Selenites or Tellurites Containing Halogen Anions 92
3.3 Metal Tellurites and Selenites Containing Tetrahedral Groups of Main Group Elements 96
4 Conclusions and Outlook 98
References 100

1 Introduction

The search for new Second Harmonic Generation (SHG) or Second-Order Non-Linear Optical (NLO) materials is of current interest and great importance due to their applications in photonic technologies, such as laser frequency conversion, optical parameter oscillator (OPO), and signal communication [1–4]. At present, the most widely used and commercially manufactured such materials are mainly inorganic materials based on borates such as α-BaB_2O_4 (BBO) and LiB_3O_5 (LBO), phosphates such as KH_2PO_4 (KDP) and $KTiOPO_4$ (KTP), niobates such as $LiNbO_3$, iodates such as $LiIO_3$, and metal chalcogenides such as $AgGaS_2$ and $AgGaSe_2$ [5–10]. As we all know, an important prerequisite for a material to be SHG active is that it should be structurally noncentrosymmetric (NCS). In inorganic materials, the macroscopic acentricity is often a manifestation of the asymmetric coordination environments of the cations. The above four types of most widely used inorganic NLO oxides contain four different types of asymmetric units that are responsible for their NCS structures: π-conjugated planar (e.g., BO_3^{3-}) [10–12], rigid tetrahedral groups (e.g., PO_4^{3-}, BO_4^{5-}, BeO_4^{4-}) [13–15], d^0 transition-metal (TM) cations in an octahedral geometry (e.g., Nb^{5+}, V^{5+}, Mo^{6+}) [16, 17], and cations with a stereochemically active lone pair (e.g., SeO_3^{2-}, IO_3^{3-}, Pb^{2+}, Bi^{3+}) [18–21]. The last two types of cations are both susceptible to Second-Order Jahn–Teller (SOJT) distortion which will be discussed in more details later. During the early days, lots of efforts have been made to explore Second-Order NLO materials just containing one type of asymmetric building unit. Such compounds often exhibit simple structural features, which allow us to synthesize and grow large their single crystals easily. However, with the fast developments of the science and technique, they also

have various shortcomings. Firstly, the possibilities to discover new SHG materials in such systems are rather limited. Furthermore, many of the NLO materials that are in current use still have shortcomings of one kind or another and improvements should be made. For example, KDP shows a low SHG effect and it is also very moisture sensitive, and it is still a great challenge to grow high-quality large-single crystals of $KBe_2BO_3F_2$ (KBBF) [22]. Therefore, searching for better SHG materials is still a hot research topic and a great challenge. It has been demonstrated that the combination of two or more types of asymmetric inorganic building units into a same compound is an effective synthetic route for new inorganic solids with excellent SHG properties if polarizations of those asymmetric units can be properly aligned [15, 17].

SOJT distortion is a very important concept in second order NLO materials, it occurs in two different types of cations: d^0 transition metals (Mo^{6+}, W^{6+}, etc) in an octahedral coordination geometry and cations with stereoactive lone pairs (I^{5+}, Se^{4+}, Te^{4+}, etc). The d^0 transition metal cation can be distorted toward either a face (local C_3 direction), an edge (local C_2 direction), or a corner (local C_4 direction) of the MO_6 octahedron [7]. The situation with the lone-pair cations is more complex. The structural distortion and polarization was thought to be through the mixing of the metal cation *s* and *p* orbitals. Recently, it is believed that the oxide anion also plays an important role in the lone-pair formation. The interaction of the *s* and *p* orbitals of the metal cation with the oxide anion *p* states is critical for lone-pair formation. No matter how the lone pair is created, its structural consequences are profound, as the lone pair "pushes" the oxide ligands toward one side of the cation, resulting in a highly asymmetric coordination environment [14].

Metal iodates are one class of very important materials [18–20]. Many of them such as α-$LiIO_3$ [10] and α-$Cs_2I_4O_{11}$ [19], have been reported to be promising new SHG materials with wide transparent wavelength regions, large SHG coefficients and high optical-damage thresholds as well as high thermal stabilities. Furthermore, it is reported when iodate anion is combined with a transition metal ion with d^0 electronic configuration such as Mo^{6+} and W^{6+}, the chances to obtain materials with noncentrosymmetric structures and excellent SHG properties can be greatly increased due to the "constructive" addition of the polarizations from both types of asymmetric units [23–30].

Likewise, metal selenites and tellurites are also able to form a diversity of unusual structures because of the presence of the stereochemically active lone-pair electrons which could serve as a structure-directing agent [13, 14]. The asymmetric coordination polyhedron of the Se(IV) or Te(IV) atom caused by the so-called SOJT distortion may also result in noncentrosymmetric (NCS) structures with consequent interesting physical properties, such as SHG. Transition metal ions with d^0 electronic configuration such as V^{5+}, W^{6+}, Mo^{6+}, etc. have been also introduced into the selenite or tellurite systems to obtain new SHG materials by means of the additive polarizations of both types of bonds [31–33]. Most of these research efforts have been focused on alkali, alkaline earth, and NH_4^+ compounds which show potential application in SHG materials because of their broad

Table 1 Metal iodates with NCS structures and SHG properties

Compounds	Space group	SHG efficiency	Ref.
α-HIO_3	$P2_12_12_1$	300 × α-SiO_2	[19]
α-$LiIO_3$	$P6_3$	300 × α-SiO_2	[19, 20]
NaI_3O_8	$P\bar{4}$	300 × α-SiO_2	[10]
$Cs_2I_4O_{11}$	$P6_3$	300 × α-SiO_2	[19]
$La(IO_3)_3$	Cc	400 × α-SiO_2	[42]
$NaY(IO_3)_4$	Cc	300 × α-SiO_2	[42]
$K_2Zn(IO_3)_4(H_2O)_2$	$I2$	2.3 × KDP	[43]
$K_2Mg(IO_3)_4(H_2O)_2$	$I2$	1.4 × KDP	[43]
$K_2Co(IO_3)_4(H_2O)_2$	$I2$	0.3 × KDP	[43]
α-$K_3In(IO_3)_6$	$Fdd2$	1 × KDP	[44]
$BaPd(IO_3)_4$	$P1$	0.4 × KTP	[45]
$La_3Pb_3(IO_3)_{13}(\mu^3$-O)	$R3c$	2 × KDP	[46]
$Pr_3Pb_3(IO_3)_{13}(\mu^3$-O)	$R3c$	1 × KDP	[46]
$Nd_3Pb_3(IO_3)_{13}(\mu^3$-O)	$R3c$	0.8 × KDP	[46]
$Li_2Ti(IO_3)_6$	$P6_3$	500 × α-SiO_2	[26]
$Na_2Ti(IO_3)_6$	$P6_3$	400 × α-SiO_2	[27]
$NaVO_2(IO_3)_2(H_2O)$	$P2_1$	20 × KDP	[29]
$K(VO)_2O_2(IO_3)_3$	$Ima2$	3.6 × KTP	[30]
$LaVO_2(IO_3)_4{\cdot}H_2O$	$P2_1$	0.2 × KDP	[47]
$Cs(VO)_2O_2(IO_3)_3$	$Ima2$	500 × α-SiO_2	[24]
$BaNbO(IO_3)_5$	Cc	14 × KDP	[28]
$ThCrO_4(IO_3)_2$	$P2_12_12_1$	1 × α-SiO_2	[48]
$LiMoO_3(IO_3)$	$P2_1$	4 × KDP	[49]
$RbMoO_3(IO_3)$	$Pna2_1$	400 × α-SiO_2	[23]
$CsMoO_3(IO_3)$	$Pna2_1$	400 × α-SiO_2	[23]
$NdMoO_2(OH)(IO_3)_4$	$P2_1$	350 × α-SiO_2	[25]

transparency range and high transmittance in the ultraviolet and visible region [34–39]. Recently, similar phases of transition metal as well as the posttransition metal main group cations have also been prepared [40, 41]. Furthermore, boroselenites which contain both borate anion and selenium(IV) with a lone pair may also possess good SHG properties due to the presence of two types of SHG active groups. So far, such compounds are still rather scarce and $B_2Se_2O_7$ prepared by our group represents the only example. Its structure is built from B_2O_7 dimers composed of two corner-sharing BO_4 tetrahedra and SeO_3^{2-} groups. It exhibits a SHG efficiency of about 2.3 times that of KDP [13].

Our group and others have been exploring new NCS compounds in these systems during the past few years (Tables 1 and 2). In this chapter, our discussions will be mainly focused on metal iodates, selenites, or tellurites that contain d^0 transition metal (TM) ions; or additional lone-pair cations such as Pb^{2+}, Bi^{3+} etc, or tetrahedral groups of main group elements such as GeO_4 and PO_4. A brief description of some ternary compounds that exhibit SHG response will also be given when necessary. The discussions on metal selenites and tellurites will be mainly focused on those reported after 2008 since we had reviewed them in 2008 [14].

Table 2 Metal selenites or tellurites show NCS structures and SHG properties

Compounds	Space group	SHG efficiency	Ref.
TeO_2	$P4_12_12$	5 × α-SiO_2	[32]
Te_2O_5	$P2_1$	400 × α-SiO_2	[32]
$TeSeO_4$	Ia	400 × α-SiO_2	[31, 32]
Te_2SeO_7	$Pmn2_1$	200 × α-SiO_2	[32]
Bi_2TeO_5	$Abm2$	300 × α-SiO_2	[33]
$K(VO_2)_3(SeO_3)_2$	$P6_3$	45 × α-SiO_2	[50]
$Tl(VO_2)_3(SeO_3)_2$	$P6_3$	50 × α-SiO_2	[51]
$A(VO_2)_3(SeO_3)_2$(A = NH_4, Rb, Cs)	$P6_3$	40 × α-SiO_2	[50, 51]
$Cs(VO_2)_3(TeO_3)_2$	$P6_3$	40 × α-SiO_2	[50, 52]
$Rb_2(MoO_3)_3(SeO_3)$	$P6_3$	300 × α-SiO_2	[50]
$Cs_2(MoO_3)_3(SeO_3)$	$P6_3$	350 × α-SiO_2	[53]
$Tl_2(MoO_3)_3(SeO_3)$	$P31c$	400 × α-SiO_2	[50]
$(NH_4)_2(MoO_3)_3(SeO_3)$	$P6_3$	400 × α-SiO_2	[53]
$A_2(MoO_3)_3(TeO_3)$ (A = NH_4, Cs)	$P6_3$	400 × α-SiO_2	[54]
$A_2(WO_3)_3(SeO_3)$ (A = NH_4, Cs)	$P6_3$	200 × α-SiO_2	[55]
$Rb_2W_3TeO_{12}$	$P31c$	200 × α-SiO_2	[56]
$Cs_2W_3TeO_{12}$	$P6_3$	400 × α-SiO_2	[56]
$Na_2Mo_3Te_3O_{16}$	$I2$	500 × α-SiO_2	[57]
$Ag_2Mo_3Te_3O_{16}$	$I2$	8.0 × KDP	[58]
$(NH_4)_2WTe_2O_8$	$P2_1$	250 × α-SiO_2	[59]
Na_2MoSeO_6	$P2_13$	10 × α-SiO_2	[60]
$Na_2W_2TeO_9$	Ia	500 × α-SiO_2	[39]
$BaMo_2TeO_9$	$P2_1$	600 × α-SiO_2	[34]
BaW_2TeO_9	$P2_1$	500 × α-SiO_2	[34]
$Cd_4V_2Te_3O_{15}$	$P2_12_12_1$	1.4 × KDP	[61]
$Zn_2(MoO_4)(SeO_3)$	$P2_1$	100 × α-SiO_2	[62]
$Zn_2(MoO_4)(TeO_3)$	$P2_1$	80 × α-SiO_2	[62]
$TlSeVO_5$	$Pna2_1$	40 × α-SiO_2	[63]
$TlTeVO_5$	$Pna2_1$	40 × α-SiO_2	[63]
$InVSe_2O_8$	Pm	30 × α-SiO_2	[64]
$Te_2O(PO_4)_2$	Cc	50 × α-SiO_2	[65]
$Mn(MoO_3)(SeO_3)(H_2O)$	$Pmc2_1$	3.0 × KDP	[66]
α-$Ga_2(TeO_3)_3$	I-43d	1.0 × KDP	[67]
$B_2Se_2O_7$	$P2_12_12_1$	2.2 × KDP	[13]

2 Metal Iodates Containing d^0 Transition Metal Ions or Other Lone-Pair Cations

Metal iodates are a very important class of SHG materials. Even simple alkali metal iodates such as $LiIO_3$, have become standard materials exploited for laser frequency-doubling applications [10]. Metal iodates that display SHG properties are listed in Table 1. In this section, our discussion will be focused on two systems: combination of d^0 transition metal (TM) ions or other lone pair-containing cations with iodate anions.

Metal iodates containing IIIA group elements such as In(III) and divalent metal ions such as Pd^{2+}, Mn^{2+}, Co^{2+}, Zn^{2+}, and Mg^{2+} will also be described.

2.1 Combination of d^0 Transition Metal Ions with Iodate Group

A large number of compounds with abundant structural types have been reported in this system, many of which exhibit excellent SHG properties (Table 1). The transition metals with d^0 electronic configuration are mostly Mo(VI) and V(V) ions but there are also some examples involving Ti(IV), Zr(IV), Nb(V) and Cr(VI). The counterions include alkali(I), alkaline earth(II), lanthanide(III), and silver(I).

2.1.1 Mo(VI)–I(V)–O System

Such types of compounds are dominantly alkali(I) and silver(I) compounds but some alkaline earth(II) and lanthanide(III) compounds are also reported. Studies revealed that the ionic size of the counterions has also a great influence on the compositions, structures, and SHG properties of the materials formed.

Eight compounds, namely, $A_2MoO_2(IO_3)_4$ ($A = K^+$, Ag^+), $Rb_2Mo(IO_3)_6$, α- and β-$KMoO_3(IO_3)$, $LiMoO_3(IO_3)$ and $AMoO_3(IO_3)$ ($A = Rb^+$, Cs^+) were reported in A(I)–Mo(VI)–I(V)–O systems [23, 49, 68–70]. They exhibit six different structural types.

Colorless rhombohedra $K_2MoO_2(IO_3)_4$ crystals were obtained by hydrothermal reactions of MoO_3 (0.731 mmol), KIO_4 (1.46 mmol), NH_4Cl (1.10 mmol), and 1 mL H_2O at 180°C. $Ag_2MoO_2(IO_3)_4$ was synthesized by heating a mixture of $AgNO_3$ (1.0 mmol), MoO_3 (0.50 mmol), I_2O_5 (3.0 mmol), and 2 mL H_2O at 200°C. $A_2MoO_2(IO_3)_4$ ($A = Ag^+$, K^+) are isostructural and crystallized in the centrosymmetric (CS) space group *C*2/c [68, 69]. Their structures exhibit a zero-dimensional (0D) $[MoO_2(IO_3)_4]^{2-}$ anionic unit consisting of a Mo^{6+} cation bonded to two terminal oxo and four iodate anions, with the K^+ or Ag^+ cations acting as spacers to keep charge balance.

Orange rhombohedral crystals of $Rb_2Mo(IO_3)_6$ were prepared by hydrothermal reactions of MoO_3 (0.597 mmol), H_5IO_6 (1.202 mmol), Rb_2CO_3 (0.602 mmol), and 1 mL H_2O at 200°C. Its structure (*R*-3, CS) exhibits a 0D $[Mo(IO_3)_6]^{2-}$ anionic unit consisting of a nondistorted d^0-TM cation linked to six IO_3^- anions. These 0D anionic units are separated by the Rb^+ cations [70].

Colorless rods of β-$KMoO_3(IO_3)$ were obtained in a similar method to that of $K_2MoO_2(IO_3)_4$ by using more amount of MoO_3 [69]. Crystals of α-$KMoO_3(IO_3)$, $AMoO_3(IO_3)$ ($A = Rb^+$, Cs^+) can be produced in high yield with a 1:2 molar ratio of MoO_3:AIO_4 (A = K, Rb, Cs) in the absence of NH_4Cl [23]. Very pale yellow plate-like crystals of $LiMoO_3(IO_3)$ were synthesized by heating a mixture of MoO_3

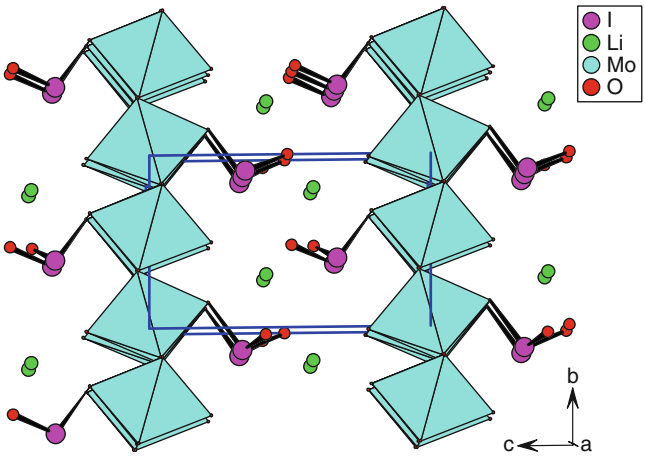

Fig. 1 View of the structure of $LiMoO_3(IO_3)$ along the *a*-axis

(2.529 mmol), H_5IO_6 (2.518 mmol), Li_2CO_3 (1.245 mmol), and 2 mL H_2O at 170°C [49]. Although α-$KMoO_3(IO_3)$, β-$KMoO_3(IO_3)$, $LiMoO_3(IO_3)$, and $AMoO_3(IO_3)$ ($A = Rb^+$, Cs^+) have a similar chemical formula, their structures are totally different. α-$KMoO_3(IO_3)$ (*P*bca) and β-$KMoO_3(IO_3)$ ($P2_1/n$) are centrosymmetric. Their structures exhibit a similar 2D $[MoO_3(IO_3)]^-$ anionic layer composed of the 1D chains of corner sharing MoO_6 octahedra further bridged by the iodate anions. The K^+ cations are located at the interlayer region to maintain the charge balance. The difference between these two compounds is that the $[MoO_3(IO_3)]^-$ layers in the α-phase are corrugated whereas those in the β-phase are regular.

$LiMoO_3(IO_3)$ [49] and $AMoO_3(IO_3)$ ($A = Rb^+$, Cs^+) [23] are NCS and SHG-active. $LiMoO_3(IO_3)$ ($P2_1$, NCS) exhibits a layered structure composed of $[MoO_3(IO_3)]^-$ anionic layers that are separated by Li^+ cations. Such a $[MoO_3(IO_3)]^-$ layer is totally different from those described above. Within the layer, the MoO_6 octahedra are interconnected into a WO_3-type sheet via corner-sharing with quadrangular windows along *c*-axis. The unidentate IO_3 groups are appended on both sides of the 2D layer (Fig. 1). Each Mo^{6+} cation undergoes intraoctahedral distortion toward a face (local C_3 direction), resulting in three short and three long Mo–O bonds, but the polarizations from neighboring MoO_6 octahedra are partially cancelled out. The large dipole moment of the compound is produced by IO_3^- groups because all of the lone pairs of the iodate groups are almost aligned in the same direction. SHG measurements revealed that $LiMoO_3(IO_3)$ shows a large SHG response of about 4×KDP [49].

$AMoO_3(IO_3)$ ($A = Rb^+$, Cs^+) are isostructural and crystallized in the polar space group $Pna2_1$. Their structures feature a three-dimensional (3D) network composed of 1D chains of corner-sharing MoO_6 octahedra that are bridged by iodate groups with the Rb^+ or Cs^+ cations filling in the voids of the structure and keeping charge

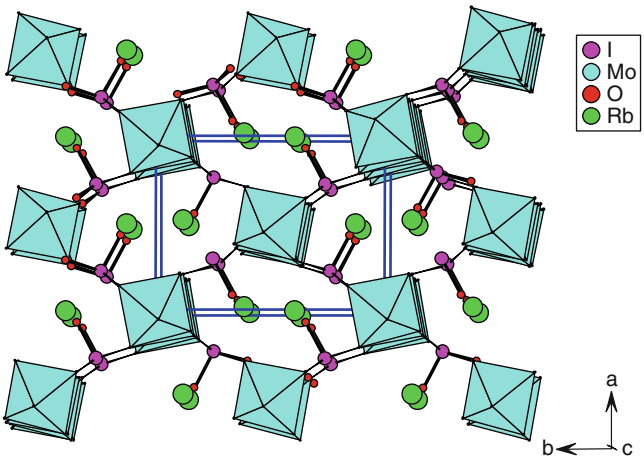

Fig. 2 View of the structure of $RbMoO_3(IO_3)$ along the *a*-axis

balance (Fig. 2). Each Mo^{6+} cation is octahedrally coordinated by two bridging and two terminal oxoanions as well as two unidentate iodate groups, displaying two short, two long, and two normal Mo–O bonds. Therefore the MoO_6 octahedron is distorted toward an edge (local C_2 direction). The polarizations of neighboring MoO_6 octahedra are partially cancelled out whereas those of the iodate groups are almost aligned along the *c*-axis to produce a large net dipole moment. SHG measurements reveal that $AMoO_3(IO_3)$ ($A = Rb^+$, Cs^+) display strong SHG responses of about 400 × α-SiO_2 and they are phase-matchable [23].

Only two alkaline earth molybdenum(VI) iodates were reported, namely, $BaMoO_2(IO_3)_4(H_2O)$ and $Ba(MoO_2)_6(IO_4)_2O_4(H_2O)$ [71, 72]. $BaMoO_2(IO_3)_4(H_2O)$ was synthesized by hydrothermal reactions of a mixture of $Ba(OH)_2{\cdot}8H_2O$ (1.58 mmol), MoO_3 (3.47 mmol), and HIO_3 (28.4 mmol) in 10 mL of H_2O at 230°C whereas $Ba(MoO_2)_6(IO_4)_2O_4(H_2O)$ was obtained by reactions of a mixture of MoO_3 (0.599 mmol) and BaH_3IO_6 (0.371 mmol) in 1 mL H_2O at 180°C. Both of them crystallized in centrosymmetric space groups. $BaMoO_2(IO_3)_4(H_2O)$ ($P2_1/n$, CS) exhibits a 0D $[MoO_2(IO_3)_4]^{2-}$ anionic unit consisting of a Mo^{6+} cation linked to four IO_3^- groups and two terminal oxoanions, such anionic units are separated by water molecules and Ba^{2+} cations. The structure of $Ba(MoO_2)_6(IO_4)_2O_4(H_2O)$ ($C2/c$, CS) consists of 2D $[(MoO_2)_3(IO_4)O_2]^-$ layers that are separated by Ba^{2+} cations and water molecules. There are three crystallographically unique Mo(VI) and one unique I(V) atoms in its asymmetric unit. Two $Mo(1)O_6$ octahedra form a $[Mo(1)_2O_{10}]$ dimer via edge sharing, likewise $[Mo(3)_2O_{10}]$ dimers. The above two types of dimers are further condensed into a 1D chain along *a*-axis via corner sharing, and neighboring 1D chains are further bridged by $Mo(2)O_6$ octahedra via corner sharing into a 2D layer with 1D tunnels of 6 MRs along *a*-axis. The IO_4^{3-} group are located at above tunnels and each forming six I–O–Mo bridges with five Mo(VI) centers.

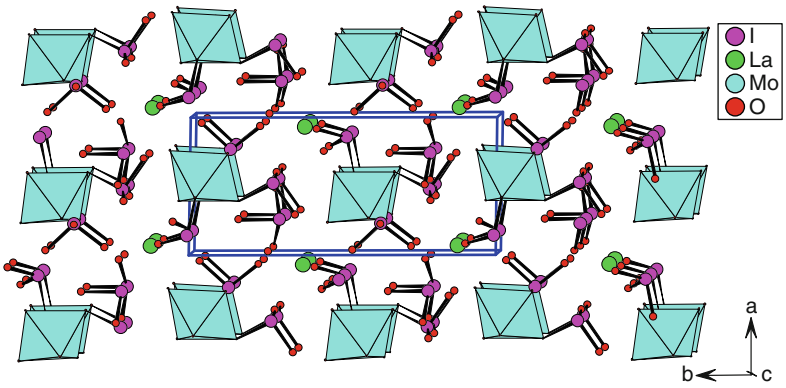

Fig. 3 View of structure of $LaMoO_2(OH)(IO_3)_4$ down the *c*-axis

$LnMoO_2(OH)(IO_3)_4$ (Ln = La, Nd, Sm, Eu) are the only lanthanide molybdenum (VI) iodates reported [25, 73]. They are isostructural and crystallized in the polar space group $P2_1$. $LaMoO_2(OH)(IO_3)_4$ was synthesized by heating a mixture of $La(NO_3)_3{\cdot}6H_2O$ (0.734 mmol), MoO_3 (1.480 mmol), H_5IO_6 (2.198 mmol), and I_2O_5 (1.474 mmol) in 9 mL H_2O at 170°C, whereas $LnMoO_2(OH)(IO_3)_4$ (Ln = Sm, Eu) were isolated by hydrothermal reactions of a mixture of MoO_3 (0.490 mmol), I_2O_5 (0.490 mmol), and $Ln(IO_3)_3$ (0.245 mmol) (Ln = Sm, Eu) in 1.0 mL H_2O at 200°C. For $NdMoO_2(OH)(IO_3)_4$, the loads are different: MoO_3 (0.616 mmol), I_2O_5 (0.616 mmol), $Ln(IO_3)_3$ (0.308 mmol), and 1.5 mL H_2O. Their structures feature a 0D $[MoO_2(OH)(IO_3)_3]^{2-}$ anionic unit composed of a Mo^{6+} cation linked to one hydroxyl, two terminal oxoanions, and three unidentate IO_3^- groups, these anionic units are separated by the Ln^{3+} cations and other "isolated" IO_3^- anions (Fig. 3). The Mo^{6+} cation undergoes an out-of-center distortion toward a face (local C_3 direction), exhibiting three short and three long Mo–O bonds. The Nd(III) compound displays a large SHG efficiency of about 350 × α-SiO_2 and it is also phase matchable.

2.1.2 V(V)–I(V)–O System

Such compounds are mostly focused in the A(I)–V(V)–I(V)–O system besides one Ba(II) and three La(III) compounds. Only six compounds were reported before our group's work in A(I)–V(V)–I(V)–O system, namely, $LiVO_2(IO_3)_2$, $KVO_2(IO_3)_2$, $RbVO_2(IO_3)_2$, $A(VO)_2O_2(IO_3)_3$ (A = NH_4^+, Rb^+, Cs^+) [24, 74]. Seven new compounds, namely, $NaVO_2(IO_3)_2(H_2O)$, α-$KVO_2(IO_3)_2(H_2O)$, β-$KVO_2(IO_3)_2(H_2O)$, $K_4[(VO)(IO_3)_5]_2(HIO_3)(H_2O)_2{\cdot}H_2O$, $K(VO)_2O_2(IO_3)_3$, $Ag_2VO_2(IO_3)_3$, and $Ag_2(V_2O_4)(IO_3)_4$, were prepared in our group through hydrothermal syntheses [29, 30, 68].

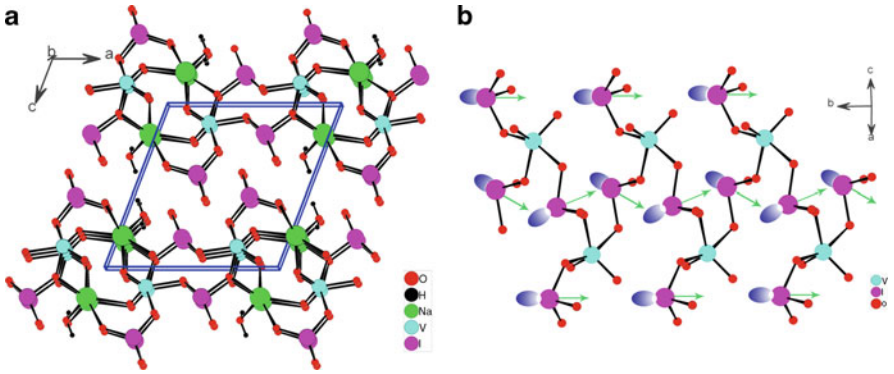

Fig. 4 (**a**) View of structure of $NaVO_2(IO_3)_2(H_2O)$ down the *b*-axis; (**b**) a 1D helical anionic chain with the macroscopic polarity indicated by *small green arrows* in $NaVO_2(IO_3)_2(H_2O)$

Yellow block-like crystals of $LiVO_2(IO_3)_2$ were obtained by heating a mixture of Li_2CO_3 (0.487 mmol), V_2O_5 (0.489 mmol), I_2O_5 (0.983 mmol), and H_2O (2 mL) at 170°C. $LiVO_2(IO_3)_2$ crystallized in the centrosymmetric space group $P2_1/c$ and its structure exhibits a 2D $[VO_2(IO_3)_2]^-$ anionic layer consisting of VO_6 octahedra bridged by IO_3 groups with the Li^+ cations being located at the interlayer space [74]. Bright yellow prisms of $KVO_2(IO_3)_2$ and yellow prisms of $RbVO_2(IO_3)_2$ were prepared by the hydrothermal reactions of a mixture of V_2O_5, KIO_4, I_2O_5, and 1 mL H_2O at 180°C. The loads are: V_2O_5 (0.51 mmol), KIO_4 (1.02 mmol), and I_2O_5 (0.51 mmol) for $KVO_2(IO_3)_2$; V_2O_5 (0.47 mmol), $RbIO_4$ (0.94 mmol), and I_2O_5 (0.47 mmol) for $RbVO_2(IO_3)_2$. Both $KVO_2(IO_3)_2$ ($P2_1/n$, CS) and $RbVO_2(IO_3)_2$ (P-1, CS) contain 1D $[VO_2(IO_3)_2]^-$ chains that are separated by K^+ or Rb^+ cations. These 1D chains are constructed by distorted VO_5 square pyramids interconnected by bidentate bridging $I(1)O_3$ groups with the $I(2)O_3$ groups being attached unidentately on the same side of the 1D chain. The difference is that the chains in $KVO_2(IO_3)_2$ are running down the *b*-axis, whereas the chains in $RbVO_2(IO_3)_2$ are along the *a*-axis [24]. We are awared that although $AVO_2(IO_3)_2$ ($A = Li^+, K^+, Rb^+$) have similar chemical formulae, their structures are very different.

Single crystals of $NaVO_2(IO_3)_2(H_2O)$ were synthesized by the hydrothermal reactions of a mixture of $NaVO_3{\cdot}2H_2O$ (1 mmol), I_2O_5 (3 mmol), Ga_2O_3 (0.25 mmol), and 5 mL of water at 200°C. It crystallized in the polar space group $P2_1$, and its structure features a unique 2D layer, which is composed of 1D right-handed helical $[VO_2(IO_3)_2]^-$ chains further bridged by Na^+ ions (Fig. 4a). The vanadium(V) cation is in a strongly distorted trigonal bipyramidal geometry, coordinated with two terminal oxoanions and three iodate anions, resulting in two short and three elongated V–O bonds. Both I(V) cations are in the asymmetric coordination environment, coordinated with three oxygen atoms in a distorted trigonal-pyramidal geometry. The VO_5 polyhedra are interconnected by the bidentate bridging $I(1)O_3$ groups into a 1D right-handed helical chain with $I(2)O_3$

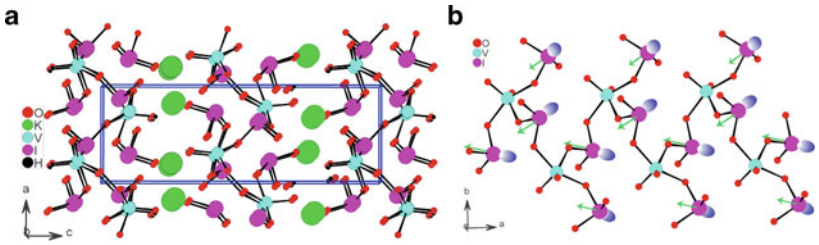

Fig. 5 (**a**) View of structure of β-$KVO_2(IO_3)_2(H_2O)$ down the *b*-axis; (**b**) a 1D $[VO_2(IO_3)_2]^-$ right-handed helical anionic chain with the macroscopic polarity indicated by *small green arrows* in β-$KVO_2(IO_3)_2(H_2O)$

groups being grafted unidentately on both sides of the helical chain. Within the 1D helical chain, all of the lone pairs of the IO_3 groups are aligned in the same direction to produce a large net dipole moment along the *b*-axis (Fig. 4b). SHG measurements revealed that $NaVO_2(IO_3)_2(H_2O)$ displays a very large SHG response of about 20 ×KDP and it is also phase matchable [29].

Yellow needle-shaped α-$KVO_2(IO_3)_2(H_2O)$ crystals were prepared by hydrothermal reactions of a mixture of K_2CO_3 (0.75 mmol), V_2O_5 (0.50 mmol), I_2O_5 (2.00 mmol), and H_2O (2.0 mL) at 155°C whereas yellow plate-shaped β-$KVO_2(IO_3)_2(H_2O)$ crystals were obtained by reactions of a mixture of K_2CO_3 (0.50 mmol), V_2O_5 (0.25 mmol), I_2O_5 (2.00 mmol), Bi_2O_3 (0.01 mmol), and H_2O (3.0 mL) at 230°C. When the reactions were carried out in the absence of Bi_2O_3, only unknown amorphous phase could be isolated. It is still not clear what kind of role Bi_2O_3 played in the formation of β-$KVO_2(IO_3)_2(H_2O)$.

α-$KVO_2(IO_3)_2(H_2O)$ (*P*bca, CS) exhibits a novel 2D layered structure composed of 1D $[VO_2(IO_3)_2]^-$ anionic chains bridged by K^+ cations. β-$KVO_2(IO_3)_2(H_2O)$ crystallizes in the chiral space group $P2_12_12_1$ and its structure features 1D $[VO_2(IO_3)_2]^-$ right-handed helical anionic chains along the *a*-axis which are separated by K^+ cations (Fig. 5a). In β-$KVO_2(IO_3)_2(H_2O)$, the V(V) cations are in a strongly distorted trigonal bipyramidal geometry composed of two terminal oxide anions and three iodate groups, resulting in two short and three long V–O bonds. Neighboring VO_5 polyhedra are further interconnected by bidentate bridging I(2)O_3 groups into a 1D right-handed helical chain along the *a*-axis with the I(1)O_3 groups being attached unidentately on both sides of the helical chain, which is similar to that in $NaVO_2(IO_3)_2(H_2O)$. Within a $[VO_2(IO_3)_2]^-$ helical chain, all of the lone pairs on the IO_3 groups are almost aligned in the same direction, producing a large dipole moment toward the *a*-axis (Fig. 5b). However, the lone pairs of the IO_3 groups from two neighboring helical chains are nearly aligned in opposite directions; hence, their local dipole moments are mostly cancelled out, which is confirmed by a very weak SHG response detected for the compound [30].

Orange brick-shaped $K_4[(VO)(IO_3)_5]_2(HIO_3)(H_2O)_2{\cdot}H_2O$ crystals were obtained by hydrothermal reactions of a mixture of K_2CO_3 (1.50 mmol), V_2O_5 (0.50 mmol),

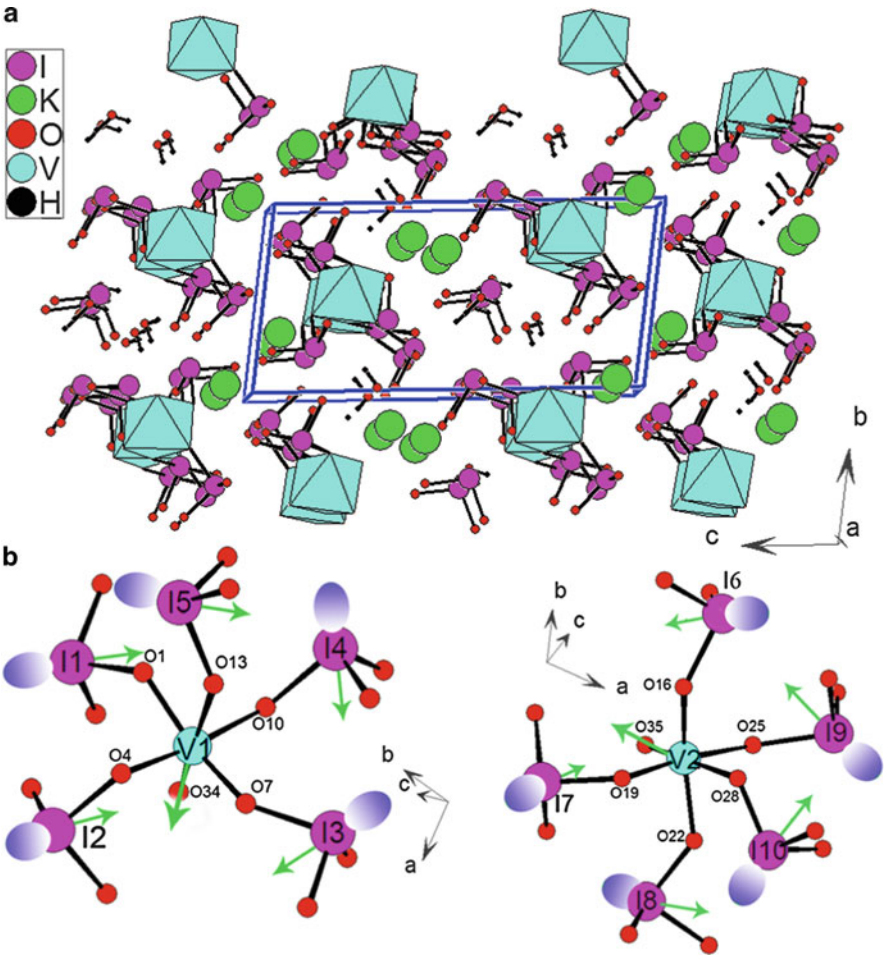

Fig. 6 (**a**) View of structure of $K_4[(VO)(IO_3)_5]_2(HIO_3)(H_2O)_2{\cdot}H_2O$ down the *a*-axis; (**b**) two 0D $[(VO)(IO_3)_5]^{2-}$ anions in the asymmetric unit showing the lone pairs (*purple ellipsoids*) and local moments (*green arrows*). VO_6 octahedra are shaded in *cyan*

I_2O_5 (9.00 mmol), and H_2O (5.0 mL) at 160°C. $K_4[(VO)(IO_3)_5]_2(HIO_3)(H_2O)_2{\cdot}H_2O$ crystallizes in the polar space group *P*1 and its structure features novel 0D $[(VO)(IO_3)_5]^{2-}$ anionic units composed of one VO_6 octahedron corner sharing with five IO_3 groups (Fig. 6a). The K^+ cations, water molecules, and "isolated" HIO_3 groups are located in-between these 0D units. Both V(V) cations in the asymmetric unit undergo an intraoctahedral distortion toward the terminal oxoanions, that is, local C_4 distortion, exhibiting one short, one long, and four normal V–O bonds. Although the 0D $[(VO)(IO_3)_5]^{2-}$ units in the asymmetric unit are polar, the polarization directions of VO_6 and IO_3 groups in the 0D units are almost opposite each other

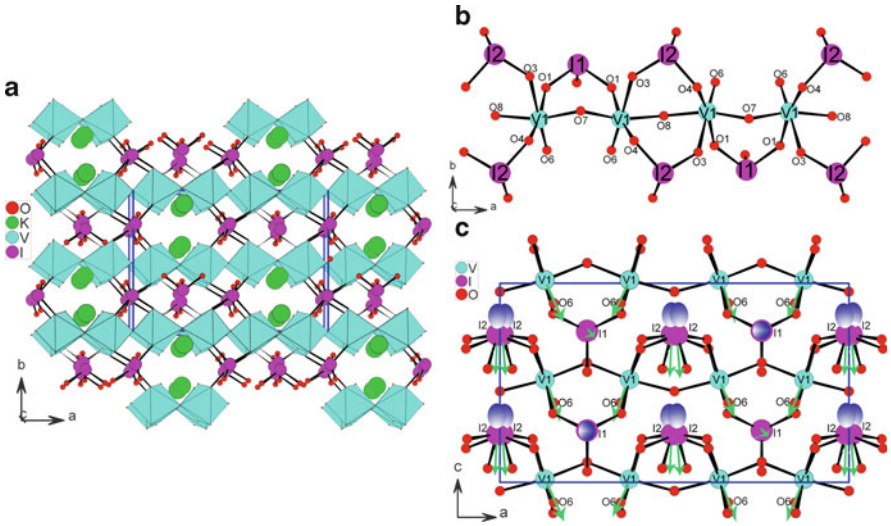

Fig. 7 (**a**) View of structure of $K(VO)_2O_2(IO_3)_3$; (**b**) a 1D $[(VO)_2O_2(IO_3)_3]^-$ chain along the *a*-axis; (**c**) 1D $[(VO)_2O_2(IO_3)_3]^-$ chains along the *a*-axis showing the lone pairs (*purple ellipsoids*) and local moments (*green arrows*)

(Fig. 6b), resulting in partial cancellation of the local dipole moments, which is also confirmed by its very weak SHG response [30].

Red brick-shaped crystals of $K(VO)_2O_2(IO_3)_3$ were prepared by heating a mixture of K_2CO_3 (0.40 mmol), V_2O_5 (0.50 mmol), I_2O_5 (2.00 mmol), and H_2O (2.0 mL) at 160°C, whereas $A(VO)_2O_2(IO_3)_3$ ($A = Rb^+, Cs^+, NH_4^+$) were prepared from the hydrothermal reactions of V_2O_5, AIO_4 ($A = Rb^+, Cs^+, NH_4^+$), and I_2O_5 at 180°C. $A(VO)_2O_2(IO_3)_3$ ($A = K^+, Rb^+, Cs^+, NH_4^+$) are isostructural and crystallized in the polar space group *I*ma2. Their structures features a 1D $[(VO)_2O_2(IO_3)_3]^-$ chain formed by 1D corner-sharing VO_6 octahedral chain which is further decorated by the bidentate bridging IO_3 groups from both sides (Fig. 7). These 1D chains are separated by the alkali or ammonium cations. The V(V) cation is distorted toward a corner (local C_4 direction), resulting in one long, one short, and four normal V–O bonds. Within the 1D chain, the lone pairs from $I(1)O_3$ groups are nearly aligned in the opposite directions, which makes their polarizations cancelled out. The polarizations of these compounds mainly come from $I(2)O_3$ groups and VO_6 octahedra. As shown in Fig. 7c, the polarizations of $I(2)O_3$ groups and VO_6 octahedra are almost aligned along the *c*-axis. Hence, the polarizations associated with $I(2)O_3$ and VO_6 octahedra constructively add, resulting in a large net dipole moment. SHG measurements showed that all four compounds display strong SHG responses, corresponding to 3.6, 2.2, 1.3, and 0.4 times of KTP ($KTiOPO_4$) for the potassium, rubidium, cesium, and ammonium phases, respectively. It is apparent that the SHG responses follow a sequence of K> Rb> Cs> NH_4. The SHG response of $K(VO)_2O_2(IO_3)_3$ is the strongest one,

being about 1.6 times as large as that of the rubidium phase. It is concluded that the different ionic sizes of K^+, Rb^+, Cs^+, and NH_4^+ produce different net polarizations for the four materials, and eventually led to different SHG responses [24, 30].

$Ag_2VO_2(IO_3)_3$ (*P*bca, CS) and $Ag_2(V_2O_4)(IO_3)_4$ (*P*ccn, CS) exhibit 1D $[VO_2(IO_3)_2]^{2-}$ and $[(V_2O_4)(IO_3)_3]^{2-}$ anionic chains, respectively, both based on 1D chains of corner-sharing VO_6 octahedra. Such 1D anionic chains are separated by the Ag^+ cations and "isolated" IO_3 groups. The IO_3 groups in the 1D $[VO_2(IO_3)_2]^{2-}$ chains are attached on both sides of the 1D vanadium oxide chain in unidentate or bidentate fashions, whereas all the IO_3 groups in $[(V_2O_4)(IO_3)_3]^{2-}$ anionic chains are grafted from both sides of the 1D vanadium oxide chain in a bidentate bridging fashion. Both compounds were prepared by heating a mixture of $AgNO_3$, V_2O_5, I_2O_5 in water at 200°C. The loaded compositions are $AgNO_3$, (1 mmol), V_2O_5 (0.3 mmol), and I_2O_5 (3.0 mmol) in 2 mL of H_2O for $Ag_2(VO_2)(IO_3)_3$; and $AgNO_3$ (0.25 mmol), V_2O_5 (0.25 mmol), and I_2O_5 (1.0 mmol) in 1 mL of H_2O (1 mL) for $Ag_2(V_2O_4)(IO_3)_4$ [68].

$Ba_2VO_2(IO_3)_5$ was prepared by heating a mixture of $Ba(OH)_2{\cdot}8H_2O$ (1.58 mmol), V_2O_5 (1.10 mmol), HIO_3 (28.4 mmol), and 10 mL H_2O at 230°C. It crystallized in CS space group $P2_1/c$, its structure features a 0D $[VO_2(IO_3)_4]^{3-}$ anionic unit that consists of a V^{5+} cation bonded to two terminal oxoanions and four IO_3 groups. These 0D anions are separated by the Ba^{2+} cations and "noncoordination" IO_3 groups [71].

Three compounds in the La(III)–V(IV)/V(V)–I(V)–O systems, namely, $LaVO^{IV}(IO_3)_5$, $LaV_2O_6(IO_3)$, and $LaVO_2(IO_3)_4{\cdot}H_2O$ were prepared by our group [47]. Green needle-shaped crystals of $LaVO(IO_3)_5$ were obtained by heating a mixture of La_2O_3 (0.25 mmol), V_2O_5 (0.75 mmol), and I_2O_5 (4.0 mmol) and H_2O (2 mL) at 250°C. It was found that V^{5+} ion was reduced to V^{4+} ion during the reactions. Yellow needle-shaped crystals of $LaV_2O_6(IO_3)$ were prepared by the hydrothermal reactions of $La(NO_3)_3{\cdot}6H_2O$ (0.45 mmol), V_2O_5 (0.25 mmol), I_2O_5 (1.5 mmol), and H_2O (2 mL) at 250°C. Orange brick-shaped single crystals of $LaVO_2(IO_3)_4{\cdot}H_2O$ were obtained by heating a mixture of $La(NO_3)_3{\cdot}6H_2O$ (0.35 mmol), VO_2 (0.5 mmol), I_2O_5 (2.0 mmol), and H_2O (2 mL) at 180°C. V^{4+} ion was oxidized to V^{5+} ion during the reactions.

$LaV^{IV}O(IO_3)_5$ ($P2_1/n$, CS) contains a 0D $[VO(IO_3)_5]^{3-}$ anionic unit in which a VO_6 octahedron is corner sharing with five IO_3 groups. Such 0D units are separated by the La^{3+} ions. $LaV_2O_6(IO_3)$ (*P*bcm, CS) exhibits a unique 1D ladder-like $[V_2O_6]^{2-}$ anionic chain which is not directly connected to any IO_3 groups, the La^{3+} ions and the "isolated" iodate groups are located between these anionic chains. $LaVO_2(IO_3)_4{\cdot}H_2O$ ($P2_1$) is isostructural with $LnMoO_2(IO_3)_4(OH)$ (Ln = La, Nd, Sm, Eu) and its structure contains a 0D $[VO_2(IO_3)_4]^{3-}$ anionic unit in which the V^{5+} cation is octahedrally coordinated by four unidentate IO_3 groups and two terminal oxoanions, and such anionic units are separated by La^{3+} cations and lattice water molecules (Fig. 8). The V^{5+} cation undergoes a SOJT distortion toward an edge (local C_2 direction), displaying two short, two normal, and two long V–O bonds. $LaVO_2(IO_3)_4{\cdot}H_2O$ displays a weak SHG response of 0.2 ×KDP since the polarizations from VO_6 octahedra and iodate groups have been largely cancelled out.

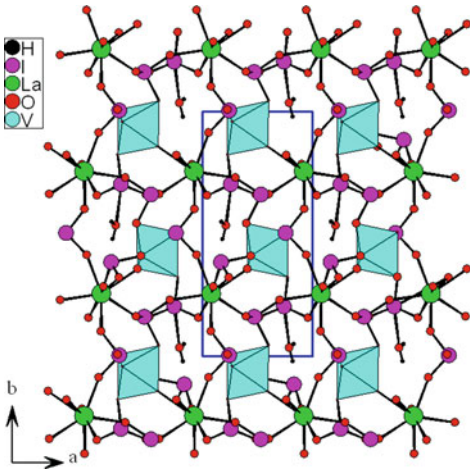

Fig. 8 View of the structure of $LaVO_2(IO_3)_4{\cdot}H_2O$ down the *c*-axis

2.1.3 Other d^0-TM–I(V)–O Systems

So far, only three Ti(IV), one Zr(IV), one Nb(IV), and two Cr(VI) iodates have been reported.

$A_2Ti(IO_3)_6$ ($A = Li^+$, Na^+) (space group $P6_3$) are isostructural and NCS. They revealed very strong SHG responses of about 500 and 400 × α-SiO_2, respectively, and both are phase matchable [26, 27]. $A_2Ti(IO_3)_6$ ($A = K^+$, Rb^+, Cs^+, Tl^+, Ag^+), $BaTi(IO_3)_6$, and $A_2Zr(IO_3)_6$ ($A = Rb^+$, Cs^+) are isostructural and crystallize in the centrosymmetric (CS) space group *R*-3; hence, they are not SHG active [27, 68, 70, 71].

$A_2Ti(IO_3)_6$ ($A = Li^+$, Na^+, K^+, Rb^+, Cs^+, Tl^+) were synthesized by hydrothermal reactions of a mixture of A_2CO_3 ($A = Li^+$, Na^+, K^+, Rb^+, Cs^+, Tl^+), TiO_2, and HIO_3 in 10 mL water at 230°C for 4 days [26, 27]. The loads are: for $Li_2Ti(IO_3)_6$, Li_2CO_3 (4.06 mmol), TiO_2 (3.76 mmol), and HIO_3 (28.4 mmol); for $Na_2Ti(IO_3)_6$, Na_2CO_3 (4.7 mmol), TiO_2 (3.8 mmol), and HIO_3 (28 mmol); for $K_2Ti(IO_3)_6$, K_2CO_3 (1.7 mmol), TiO_2 (1.3 mmol), and HIO_3 (17 mmol); for $Rb_2Ti(IO_3)_6$, Rb_2CO_3 (1.7 mmol), TiO_2 (1.3 mmol), and HIO_3 (17 mmol); for $Cs_2Ti(IO_3)_6$, Cs_2CO_3 (1.4 mmol), TiO_2 (1.3 mmol), and HIO_3 (17 mmol); for $Tl_2Ti(IO_3)_6$, Tl_2CO_3 (1.4 mmol), TiO_2 (1.3 mmol), and HIO_3 (28 mmol). $Ag_2Ti(IO_3)_6$ was obtained by heating a mixture of $AgNO_3$ (0.5 mmol), TiO_2 (0.25 mmol), I_2O_5 (1.0 mmol), and 1 mL water at 200°C. $BaTi(IO_3)_6$ was prepared by heating $Ba(OH)_2{\cdot}8H_2O$ (1.58 mmol), TiO_2 (2.50 mmol), HIO_3 (28.4 mmol), and 10 mL H_2O at 230°C. $A_2Zr(IO_3)_6$ ($A = Rb^+$, Cs^+) were synthesized by hydrothermal reactions of a mixture of AIO_4 ($A = Rb^+$, Cs^+), I_2O_5, $ZrOCl_2$, and 1.5 mL H_2O at 200°C. The loaded compositions are: $RbIO_4$ (0.829 mmol), I_2O_5 (0.414 mmol), and $ZrOCl_2$ (0.425 mmol) for $RbZr(IO_3)_6$; $CsIO_4$ (0.772 mmol), I_2O_5 (0.380 mmol), and $ZrOCl_2$ (0.382 mmol) for $CsZr(IO_3)_6$. These compounds mentioned above are topologically similar and exhibit a 0D $[Ti(IO_3)_6]^{2-}$ or $[Zr(IO_3)_6]^{2-}$ anionic unit consisting of a nondistorted d^0-TM cation linked to six IO_3^- anions (Fig. 9). These 0D anionic units are separated by the A^+ cations. In $A_2Ti(IO_3)_6$ ($A = Li^+$, Na^+), all of

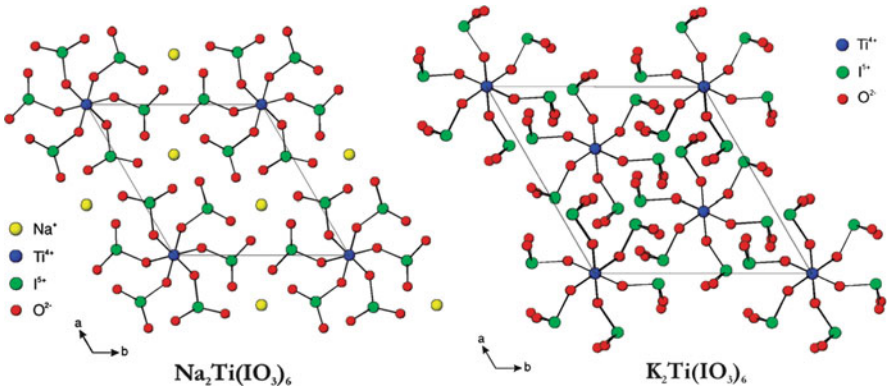

Fig. 9 View of the structure of $Na_2Ti(IO_3)_6$ and $K_2Ti(IO_3)_6$ along *c*-axis

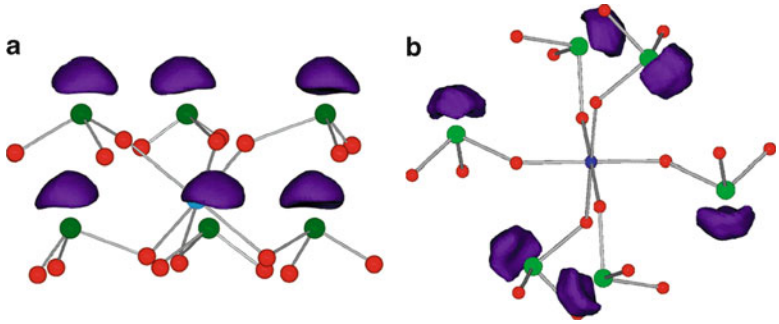

Fig. 10 A 0D $[Ti(IO_3)_6]^{2-}$ unit for $A_2Ti(IO_3)_6$ (A = Li^+, Na^+) (**a**) and $A_2Ti(IO_3)_6$ (A = K^+, Rb^+, Cs^+, Tl^+, Ag^+) (**b**)

the lone pairs on the I^{5+} cations are aligned in a parallel manner, producing a macroscopic dipole moment and thereby creating a polar material (Fig. 10a). In other compounds, the lone pairs on the I^{5+} cations are located *trans* to each other, which resulted in cancellation of the local dipole moments and they are nonpolar (Fig. 10b). It is obvious that the different ionic radii of A cations have a strong effect on the structures and properties of the materials formed.

$LaTiO(IO_3)_5$ was obtained by hydrothermal reactions of La_2O_3 (0.921 mmol), TiO_2 (2.50 mmol), and HIO_3 (28.4 mmol) in 10 mL of H_2O at 230°C. $LaTiO(IO_3)_5$ ($P2_1/n$) represents the third structural type in this system and its structure features a 0D $[TiO(IO_3)_5]^{3-}$ anionic unit composed of a Ti^{4+} ion surrounded by five IO_3 anions and one terminal oxoanion. Such 0D units are separated by the La^{3+} ions [71]. Each Ti^{4+} cation is in a distorted octahedral environment with one short, four normal, and one elongated Ti–O bonds; therefore, the Ti^{4+} undergoes an out-of-center distortion toward a corner of the octahedron (C_4 distortion).

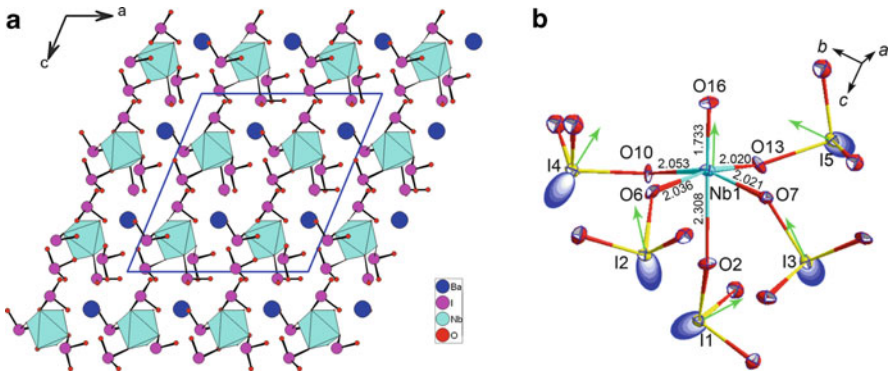

Fig. 11 (**a**) Ball-and-stick packing diagram of $BaNbO(IO_3)_5$ down the *b*-axis, NbO_6 octahedra are shaded in blue; (**b**) ORTEP drawing showing the 0D $[NbO(IO_3)_5]^{2-}$ anion, lone pairs (*blue ellipsoids*) as well as the local moments (*green arrows*)

$BaNbO(IO_3)_5$ was synthesized by the hydrothermal reaction of $Ba(IO_3)_2{\cdot}H_2O$ (1.0 mmol), Nb_2O_5 (0.6 mmol), and I_2O_5 (9 mmol) in 5 mL of water at 230°C for 4 days. $BaNbO(IO_3)_5$ is the only niobium(V) iodate reported. It crystallizes in the polar space group *Cc* and its structure features a 0D $[NbO(IO_3)_5]^{2-}$ anionic unit composed of a Nb^{5+} ion linked to five iodate groups and one terminal oxoanion (Fig. 11a) [28]. The Ba^{2+} cations act as spacers between these anionic units. Both the Nb^{5+} and I^{5+} cations are in asymmetric coordination environments attribute to SOJT effects. The Nb^{5+} cation undergoes intraoctahedral distortion toward the terminal oxide ligand, that is, a corner (C_4) distortion, resulting in one short, one long, and four normal Nb–O bonds. More interestingly, the polarizations associated with IO_3 and NbO_6 polyhedra are almost toward the same direction and therefore constructively add, resulting in a large local dipole moment (Fig. 11b). $BaNbO(IO_3)_5$ displays a very large SHG response of about 14 × KDP. Furthermore, it is phase matchable.

$KCrIO_6$ was prepared by reactions of 7.5 g $K_2Cr_2O_7$ dissolved in 40 mL H_2O and 6.5 g HIO_3. $KCrIO_6$ ($P2_1/c$, CS) can also be formulated as $KCrO_3(IO_3)$ and its structure features a 0D $[CrO_3(IO_3)]$ anionic unit composed of a CrO_4 tetrahedron corner sharing with an IO_3 group. These 0D units are separated by the K^+ cations [75]. $ThCrO_4(IO_3)_2$ was obtained by the hydrothermal reactions of $Th(NO_3)_4{\cdot}xH_2O$ (0.435 mmol), H_5IO_6 (0.451 mmol), $Cr(NO_3)_3{\cdot}9H_2O$ (0.451 mmol), and 1.0 mL of water at 200°C. $ThCrO_4(IO_3)_2$ crystallizes in the NCS space group $P2_12_12_1$ and its structure contains "isolated" IO_3 groups and CrO_4 tetrahedra; that is, the CrO_4 tetrahedron is not directly connected to any IO_3 groups. Each Th(IV) center is connected to six IO_3 and three CrO_4 groups. The SHG efficiency of $ThCrO_4(IO_3)_2$ is very weak and comparable to that of α-SiO_2 [48].

No Hf(IV), Ta(V) and W(VI) iodates has been reported; therefore, still a lot of synthetic explorations are needed. Furthermore, there are also many opportunities and challenges to find new phases in the A–Ti(IV)/Zr(IV)/Nb(V)/Cr(VI)–I(V)–O

systems, especially the Zr(IV), Nb(V), and Cr(VI) iodates. Studies also revealed that the size of the counterions has also a great influence on the compositions, structures, and SHG properties of the materials formed.

2.2 Combination of Other Lone-Pair Cations with Iodate Groups

So far, little is known about the metal iodates that contain two different types of lone pair cations. Such metal iodates reported are limited to bismuth(III), lead(II), or thallium(I) iodates, including $Tl^{I}IO_3$, $Tl_2{}^{I}Tl^{III}(IO_3)_6$, $Bi(IO_3)_3$, $Bi(IO_3)_3(H_2O)_2$, $Pb(IO_3)_2$, $Pb_3(IO_3)_2Cl_4$, and $Pb_3(IO_3)OCl_3$ [76–82]. Our recent research efforts in such systems afford four new lanthanide(III) lead(II) iodates, namely, $Ln_3Pb_3(IO_3)_{13}(\mu^3\text{-O})$ (Ln = La–Nd) [46].

$Tl^{I}IO_3$ crystallizes in the polar space group *R*3m and its structure contains isolated IO_3 groups separated by Tl^+ cations. The polarity in these structures is imparted by the alignment of the stereochemically active lone pairs of the iodate anions along the *c*-axis [76]. $Tl_4(IO_3)_6$ (*P*-1, CS) features a 0D $[Tl^{III}(IO_3)_6]^{2-}$ anions composed of a TlO_6 octahedron connected with six unidentate IO_3 groups. These 0D units are separated by the Tl^+ cations [77].

$Bi(IO_3)_3$ ($P2_1/n$, CS) exhibits a layered structure in which the Bi^{3+} cation is coordinated by seven unidentate iodate groups and each BiO_7 polyhedron is further interconnected to six neighboring ones by bridging iodate groups into a 2D layer [78]. $Bi(IO_3)_3(H_2O)_2$ (*P*-1, CS) also exhibits a layered structure in which the Bi^{3+} cation is eight coordinated by seven iodate groups in a unidentate fashion and an aqua ligand, one BiO_8 polyhedron is further connected with five neighboring ones by bridging iodate groups into a 2D layer [79]. The structure of $Pb(IO_3)_2$ (*P*bcn, CS) features a 1D chain in which neighboring asymmetric PbO_4 polyhedra are further interconnected by edge sharing into a chain with the iodate groups attached on both sides of the chain in a unidentate fashion [80].

$Pb_3(IO_3)_2Cl_4$ (*C*2/c, CS) exhibits a 3D network structure constructed by $[Pb_3Cl_4]^{2+}$ layers further interconnected by bridging iodate groups [81]. $Pb_3(IO_3)OCl_3$ crystallizes in NCS space group *C*mm2 and its structure features a thick quadruple layer composed of one $[IO_2]^+$, one $[Pb_2IO_4Cl_2]^-$, one $[Pb_3O_2Cl_3]^-$, and one $[Pb_4IO_4Cl_4]^+$ layers. It should be mentioned that the I^{5+} cation of the $[IO_2]^+$ layer is coordinated by four oxygen atoms in a square planar geometry, whereas the remaining I^{5+} cations are also four coordinated with a square pyramidal environment [82].

Single crystals of $Ln_3Pb_3(IO_3)_{13}(\mu^3\text{-O})$ (Ln = La–Nd) were prepared by the hydrothermal reactions of a mixture of lanthanide(III) oxide or nitrate (for the Ce compound), $PbCl_2$, and I_2O_5 in 10 mL (for La and Ce phases) or 4 mL (for Pr and Nd phases) H_2O in a 23 mL Teflon-lined stainless steel vessel at 200°C for 4 (for the La and Pr compounds) or 5 (for the Ce and Nd compounds) days. The loaded

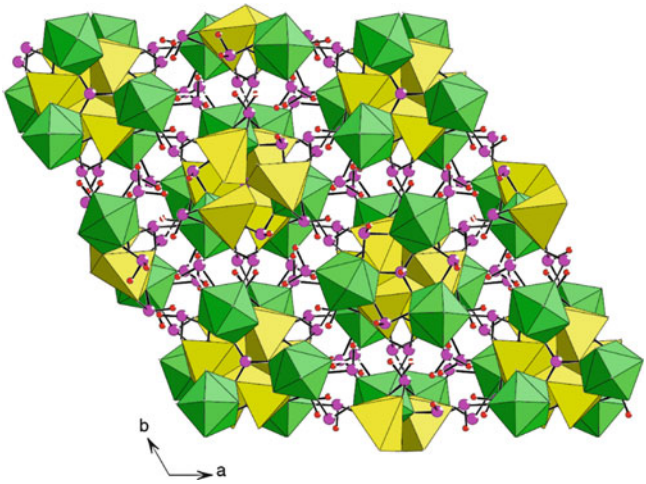

Fig. 12 View of the structure of $Ln_3Pb_3(IO_3)_{13}(\mu^3\text{-}O)$ (Ln = La–Nd) down the *c*-axis. LaO9 and PbO6 polyhedra are shaded in *green* and *yellow*, respectively. I and O atoms are drawn as *pink* and *red circles*, respectively

compositions are: La_2O_3 (0.613 mmol), $PbCl_2$ (0.719 mmol), I_2O_5 (2.4 mmol) for La compound; $Ce(NO_3)_3{\cdot}6H_2O$ (0.645 mmol), $PbCl_2$ (0.576 mmol), I_2O_5 (1.25 mmol) for Ce compound; Pr_2O_3 (0.303 mmol), $PbCl_2$ (0.719 mmol), I_2O_5 (1.35 mmol) for Pr compound; Nd_2O_3 (0.297 mmol), $PbCl_2$ (0.719 mmol), I_2O_5 (1.35 mmol) for Nd compound.

$Ln_3Pb_3(IO_3)_{13}(\mu^3\text{-}O)$ (Ln = La–Nd) crystallized in the polar space group *R*3c and their structures exhibit a complicated 3D network structure composed of LnO_9, asymmetric PbO_6 and IO_3 polyhedra that are interconnected via corner- or/and edge sharing (Fig. 12) [46]. SHG measurements revealed that $Ln_3Pb_3(IO_3)_{13}(\mu^3\text{-}O)$ (Ln = La, Pr, Nd) display SHG responses that about 2.0, 1.0, and 0.8 times of KDP, respectively. The SHG signal for the cerium compound is very weak. On the basis of structural data, the polarizations from the Pb(II) ions and $I(1)O_3$, $I(2)O_3$, and $I(4)O_3$ groups are expected to be small since their dipole moments are mainly aligned in the *ab* plane and cancelled each other. The main contributions are from $I(3)O_3$ and $I(5)O_3$ groups since their dipole moments are aligned in the same direction (along the *c*-axis).

For the metal iodates containing other lone-pair cations, there are also several opportunities and challenges. So far, there is no metal iodates with lone pair-containing Sb(III), Se(IV), Te(IV), or Sn(II) reported, and little is known about the bismuth iodates except centrosymmetric $Bi(IO_3)_3$ and $Bi(IO_3)_3(H_2O)_2$. The greatest challenge is that Sb(III), Se(IV), Te(IV), and Sn(II) are very apt to be oxidized by the I(V) cations and then the stereochemically active lone pairs may be lost.

2.3 Other Mixed Metal Iodates

From the above discussions, the combination of two types of asymmetric units (d^0 TM and iodate groups, other lone-pair cations, and iodate groups) affords many NCS compounds with rich structural types and excellent SHG properties. But it is still a great challenge to summarize the relationships between structures or chemical compositions of the materials and their second-order NLO properties. To better understand the relationships between the structures and SHG properties, we have also made a systematic exploration in the alkali metal indium iodates, palladium(II) iodates, and mixed metal iodates in the K–M(II)–IO_3 system.

Seven alkali metal indium iodates were reported in the alkali metal indium iodates, namely, $AIn(IO_3)_4$ (A = Li, Na), α-$K_3In(IO_3)_6$, β-$K_3In(IO_3)_6$, $Rb_3In(IO_3)_6$, and $A_2HIn(IO_3)_6$ (A = Rb, Cs). The seven compounds except the two potassium compounds were synthesized by a similar method of alkali metal salts In_2O_3 and H_5IO_6 in water at 200°C for 4 days. α-$K_3In(IO_3)_6$ was synthesized from a mixture containing KIO_4(1.5 mmol), $In(NO_3)_3{\cdot}20.5H_2O$ (1 mmol), 2,2′-bipy (0.5 mmol), and 0.4 mL of HCl (38%) in the presence of water (5 mL) at 120°C for 4 days, whereas β-$K_3In(IO_3)_6$ was synthesized from a mixture containing KIO_4 (1 mmol), $In(NO_3)_3{\cdot}20.5H_2O$ (1 mmol), imidazole (1 mmol), 0.4 mL of HCl (38%), and water (5 mL) at 100°C for 7 days [44, 83].

Although $LiIn(IO_3)_4$ (*P*-1, CS) and $NaIn(IO_3)_4$ ($P2_1/c$, CS) are not isostructural, both of them feature 1D $[In(IO_3)_4]^-$ chains that are separated by Li^+ or Na^+ cations. The In^{3+} ion is in a slightly distorted octahedral geometry, being coordinated by six iodate anions in a unidentate fashion. These InO_6 octahedra are further interconnected by bridging iodate groups into a 1D chain with the remaining iodate groups, which are attached monodentately on both sides of the 1D chain. The chains in $LiIn(IO_3)_4$ are propagated along the *a*-axis, whereas the chains in $NaIn(IO_3)_4$ are along the *b*-axis.

$Rb_3In(IO_3)_6$ is isostructural to α-$K_3In(IO_3)_6$ and crystallized in the CS space group *P*-1. Its structure features a 0D isolated $[In(IO_3)_6]^{3-}$ anion consisting of a InO_6 octahedron corner sharing with six iodate groups. These isolated anions are separated by Rb^+ cations. In these structures, the polarizations of IO_3 groups have cancelled out each other; hence, these three compounds are non-polar.

$A_2HIn(IO_3)_6$ (A = Rb^+, Cs^+) (*P*-1, CS) are isostructural and their structures also exhibit isolated $[In(IO_3)_6]^{3-}$ anions as in $A_3In(IO_3)_6$ (A = K^+, Rb^+). However, one of three alkali metal cations lying on an inversion center is replaced by a proton. Since the lone pairs on IO_3 polyhedra are oriented *trans* to each other, their local dipole moments cancelled out each other. Hence, these materials are nonpolar [83].

β-$K_3In(IO_3)_6$ crystallized in the polar space group *F*dd2 and exhibits a 0D isolated $[In(IO_3)_6]^{3-}$ anion consisting of a slightly distorted InO_6 octahedron corner sharing with six iodate groups. These isolated anionic units are separated by K^+ cations. Different from that in α-$K_3In(IO_3)_6$, the isolated $[In(IO_3)_6]^{3-}$ anion in β-$K_3In(IO_3)_6$ is polar and β-$K_3In(IO_3)_6$ displays an SHG efficiency of about 1 × KDP. Hence, the local asymmetric environment is a necessary, but not a sufficient condition for creating macroscopic NCS structures. In other words,

once the local acentric units are aligned in an antiparallel fashion, a material may crystallize in a centrosymmetric structure and is nonpolar [44].

Only four palladium(II) iodates have been reported so far, namely, $Pd(IO_3)_2$, $K_{2.5}Pd(IO_3)_4(H_{0.5}IO_3)$, $AgPd(IO_3)_3$, and $BaPd(IO_3)_4$ [45, 84]. Red plate-shaped crystals of $Pd(IO_3)_2$ were obtained by the hydrothermal reactions of aqueous solution of $Pd(NO_3)_2{\cdot}2H_2O$ (0.10 mmol), I_2O_5 (2.00 mmol), and H_2O (2.0 mL) with Li_2CO_3 (0.50 mmol) used as the pH adjuster at 200°C. Dark orange plates of $K_{2.5}Pd(IO_3)_4(H_{0.5}IO_3)$ were prepared by hydrothermal reactions of $Pd(NO_3)_2{\cdot}2H_2O$ (0.397 mmol), KIO_4 (1.236 mmol), and 0.5 mL H_2O at 200°C. Red plate-shaped crystals of $AgPd(IO_3)_3$ were synthesized by heating a mixture of Ag_2O (0.05 mmol), $Pd(CH_3COO)_2$ (0.102 mmol), I_2O_5 (2.00 mmol), and H_2O (2.0 mL) at 200°C. Red block-shaped crystals of $BaPd(IO_3)_4$ were obtained by the hydrothermal reactions of $BaCO_3$ (0.10 mmol), $Pd(CH_3COO)_2$ (0.103 mmol), I_2O_5 (2.00 mmol), and H_2O (2.0 mL) at 200°C.

$Pd(IO_3)_2$ (*P*bca, CS) exhibits a 2D layered structure in which each PdO_4 square is further interconnected with four neighboring ones through four bridging iodate groups. The Pd^{2+} ion is bonded to four iodate anions in a slightly distorted square planar environment. The lone pairs of IO_3 groups are aligned *trans* to each other (oriented in opposite directions), resulting in the cancellation of their local dipole moments; hence, $Pd(IO_3)_2$ is nonpolar [45].

The structure of $K_{2.5}Pd(IO_3)_4(H_{0.5}IO_3)$ (*C*2/m, CS) features a 0D $[Pd(IO_3)_4]^{2-}$ anionic unit which is composed of a PdO_4 square unit corner sharing with four iodate groups; such anionic units are separated by the K^+ cations and "isolated" HIO_3 groups. It is interesting to note that all of the four iodate anions in the $[Pd(IO_3)_4]^{2-}$ anionic unit are aligned on the same side of the PdO_4 square plane; therefore, such anionic unit is polar [84]. However, there is no macroscopic polarization for the overall structure since the polarizations of neighboring $[Pd(IO_3)_4]^{2-}$ units cancelled out each other due to its centrosymmetric space group.

$AgPd(IO_3)_3$ crystallizes in the space group *P*-1 and its structure features 1D $[Pd(IO_3)_3]^-$ anionic chains along the *c*-axis which are separated by Ag^+ cations. The Pd^{2+} cation is also in a slightly distorted square planar geometry, being coordinated by four iodate groups. The PdO_4 squares are further interconnected by bridging I(1)O_3 groups into a 1D chain with I(2)O_3 and I(3)O_3 groups alternately attached on both sides of the chain in a unidentate fashion, forming a 1D $[Pd(IO_3)_3]^-$ anionic chain. Similar to those in $Pd(IO_3)_2$, the lone pairs of the IO_3 groups are aligned *trans* to each other, resulting in the cancellation of the local dipole moments and rendering the $[Pd(IO_3)_3]^-$ chain nonpolar [45].

$BaPd(IO_3)_4$ is isostructural with $KAu(IO_3)_4$ and crystallized in polar space group *P*1. Their structures contain a 0D $[TM(IO_3)_4]^{2-}$ (TM = Au, Pd) consisting of a TMO_4 square corner sharing with four unidentate iodate groups, with the K^+ or Ba^{2+} cations acting as the spacers. The MO_4 square plane is much more distorted than those in $Pd(IO_3)_2$ and $AgPd(IO_3)_3$. All four iodate groups in the $[M(IO_3)_4]$ unit are aligned on the same side of the square plane; hence, all of the lone pairs of I(V) cations are almost oriented toward the same direction (Fig. 13). Such a special

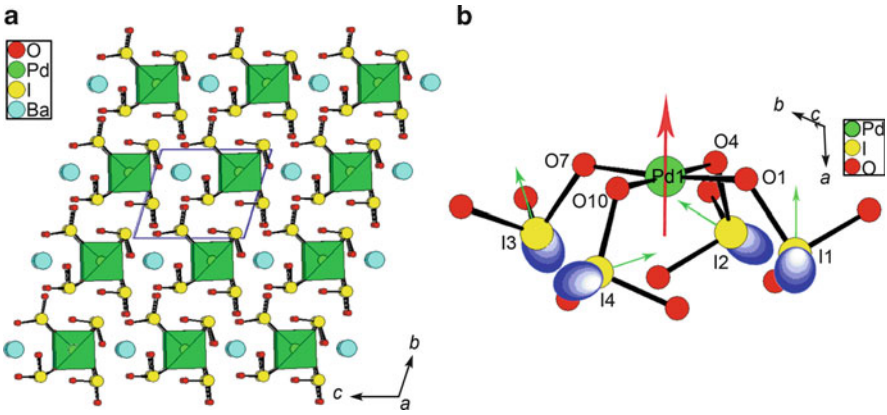

Fig. 13 (**a**) View of structure of $BaPd(IO_3)_4$ down the *a*-axis. PdO_4 squares are shaded in *green*; (**b**) a 0D $[Pd(IO_3)_4]^{2-}$ unit of $BaPd(IO_3)_4$

arrangement resulted in a large net dipole moment. SHG measurements on a 2.05 μm Q-switch laser revealed that $BaPd(IO_3)_4$ displays a moderate SHG efficiency of about 0.4 × KTP. So far, little is known about the gold(III) and platinum (II) iodates in which the metal ions may also have a square-planar geometry [45].

Most of the compounds reported in the alkali–M(II)–IO_3 system are mostly centrosymmetric except for $K_2M(IO_3)_4(H_2O)_2$ ($M = Mn^{2+}$, Co^{2+}, Zn^{2+}, Mg^{2+}) [43]. These four compounds were hydrothermally synthesized by the hydrothermal reactions of a mixture containing hexahydrated metal chloride (for Co and Mg compounds) or metal acetate (for Mn and Zn compounds) and potassium iodate in 10 mL of distilled water at 100°C. The K/M molar ratios are equal to 4/1 (5/1 for the Mn compound) for $K_2M(IO_3)_4(H_2O)_2$ ($M = Co^{2+}$, Zn^{2+}, Mg^{2+}). Furthermore, $NH_4H_2PO_4$ was used during the growth of the single crystals for $K_2Mn(IO_3)_4(H_2O)_2$.

These four compounds are isostructural and crystallized in the space group *I*2. Their structures feature 0D $[M(IO_3)_4(H_2O)_2]^{2-}$ ($M = Mn^{2+}$, Co^{2+}, Zn^{2+}, Mg^{2+}) anions that are separated by K^+ cations. The central transitional metal or Mg^{2+} cation is in a slightly distorted octahedral geometry composed of four unidentate iodate groups and two aqua ligands. The polarizations of the $I(2)O_3$ groups almost cancelled out each other, whereas those of $I(1)O_3$ groups are aligned in a parallel manner which produces a net dipole moment along the *b*-axis (Fig. 14). Neighboring 0D $[TM(IO_3)_4(H_2O)_2]^{2-}$ anions are packed in such a way that they produce a large macroscopic dipole moment along the *b*-axis. SHG measurements revealed that $K_2TM(IO_3)_4(H_2O)_2$ ($TM = Co^{2+}$, Zn^{2+}, Mg^{2+}) display SHG responses of 0.3, 2.3, and 1.4 times that of KDP, respectively, whereas no obvious SHG signal was detected for the Mn phase. Furthermore, the Zn and Mg compounds are found to be phase matchable.

One compound in the A–Ln(II)–IO_3 system is reported by Prof. Halasyamani, namely, $NaY(IO_3)_4$ [42]. Colorless crystals of $NaY(IO_3)_4$ were obtained by the reactions of Na_2CO_3 (2 mmol), Y_2O_3 (1 mmol), and HIO_3 (22.7 mmol) combining

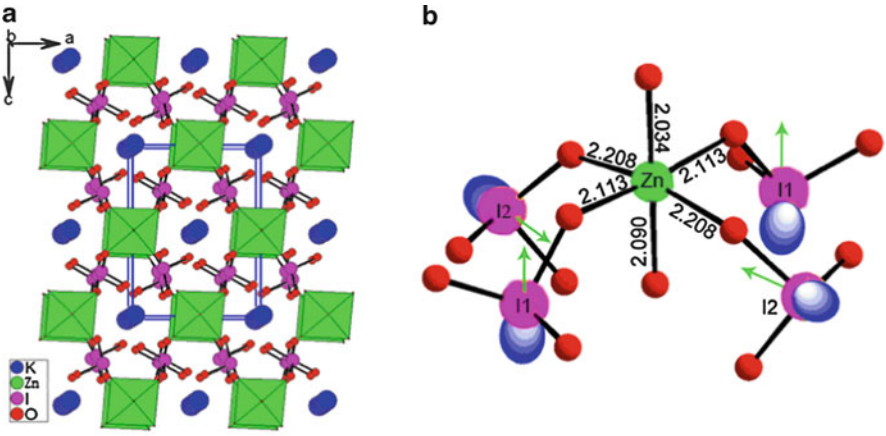

Fig. 14 (**a**) View of structure of $K_2Zn(IO_3)_4(H_2O)_2$ down the *b*-axis; (**b**) a 0D $[Zn(IO_3)_4(H_2O)_2]^{2-}$ unit, lone pairs (*blue ellipsoids*) as well as the local moments (*green arrows*), ZnO_6 octahedra are shaded in *green*

with 10 mL of H_2O at 220°C for 4 days. $NaY(IO_3)_4$ crystallizes in polar space group *Cc* and exhibits a two-dimensional (2D) layered structure consisting of YO_8 polyhedra linked to asymmetric IO_3 and IO_4 polyhedra. The connectivity of YO_8 and iodate polyhedra within each 2D layer generates 1D tunnels of eight-membered-ring (8-MRs) along the [010] direction which are occupied by the Na^+ cations. SHG measurements indicate that $NaY(IO_3)_4$ shows a large SHG response of about 300 × α-SiO_2.

Compounds with just IO_3 groups as the asymmetric inorganic building unit can also afford new NLO materials with SHG properties, but they trend to display a weak SHG response and most of such compounds are more prone to be centrosymmetric.

3 Selenites or Tellurites Containing d^0 Transition Metal Ions or Halogen Anions or Tetrahedral Groups of Main Group Elements

Metal selenites and tellurites are also a class of very important compounds, especially in nonlinear optical applications [34, 39]. Metal selenites and tellurites that display SHG properties are listed in Table 2. Recently, Tao and Halasyamani groups have also grown the large single crystals for several metal tellurites [35, 36, 85, 86]. In this part, our discussion will be focused on three systems: metal selenites and tellurites containing either d^0 transition metal (TM) ions, or halogen anions, or tetrahedral units of p-block main group elements.

3.1 Combination of d^0 Transition Metal Ions with Selenites or Tellurites

The number of compounds in these systems is much more than that of corresponding metal iodates. Different from metal iodates, the counterions in these compounds have much stronger effects on the SHG properties of the compounds formed. For example, alkali (or alkaline earth) compounds can display excellent second order NLO properties but lanthanide(III) compounds are usually not SHG active due to the high coordination number of Ln(III) ions. Hence, we will classify these compounds in terms of the counterions [15].

3.1.1 Alkali (or Alkaline Earth)-d^0 TM–Se(IV)/Te(IV)–O System

A large number of compounds in the Alkali (or Alkaline Earth)-d^0 TM–Se(IV)/Te(IV)–O systems were reported, some of which possess good SHG properties (Table 2). The transition metal ions with d^0 electronic configuration are mostly Mo^{6+}, W^{6+}, and V^{5+}, although some examples of Nb^{5+} and Ta^{5+} have also been isolated.

Seven compounds with five different structural types were reported in alkali metal-molybdenum(VI)–selenium(IV) oxide systems, A_2MoSeO_6 (A = Na^+, K^+, Rb^+), and $A_2(MoO_3)_3(SeO_3)$ (A = NH_4^+, Cs^+, Rb^+ and Tl^+) [50, 53, 60].

Colorless crystals of the first three compounds were synthesized by solid-state reactions of stoichiometric amounts of SeO_2 and A_2MoO_4 (A = Na^+, K^+, or Rb^+) at 370°C for 1 day. Na_2MoSeO_6 crystallized in an NCS space group $P2_13$, its structure features a 3D anionic network based on alternative linkage of MoO_6 octahedra (distorted toward a face) and SeO_3 groups, forming tunnels of Mo_2Se_2 four-member rings, and Mo_4Se_4 eight-member rings. The sodium cations are located at the larger tunnels. Na_2MoSeO_6 revealed a weak SHG intensity of about 10 × α-SiO_2. The SHG intensity can be attributed to the polarizations from the SeO_3 and MoO_6 groups. K_2MoSeO_6 ($P2_1/c$) and Rb_2MoSeO_6 ($Pnma$) crystallized in CS space group and are not SHG active [60].

Light yellow crystals of $A_2(MoO_3)_3(SeO_3)$ (A = NH_4^+ Cs^+, Rb^+ and Tl^+) were obtained by hydrothermal reactions of $(NH_4)_6Mo_7O_{24}{\cdot}4H_2O$ and SeO_2 at 200°C or Cs_2CO_3 (or Rb_2CO_3, Tl_2CO_3), SeO_2 and MoO_3 at 230°C for 2–3 days. $A_2(MoO_3)_3(SeO_3)$ (A = NH_4^+ Cs^+ and Rb^+) ($P6_3$, NCS) and $Tl_2(MoO_3)_3(SeO_3)$ ($P3_1c$, NCS) are polar and their structures all feature a 2D hexagonal tungsten bronze-like anionic layer of MoO_6 octahedra capped on one side by SeO_3^{2-} anions (Fig. 15). The lone pairs of the selenite groups are aligned in the same direction to produce a large macroscopic dipole moment along the *c*-axis. SHG measurements revealed that $A_2(MoO_3)_3(SeO_3)$ (A = NH_4^+ Cs^+, Rb^+, and Tl^+) display a large SHG response of about 400, 350, 300, and 400 × α-SiO_2, respectively [50, 53].

Five compounds with three different structural types have been isolated in the alkali metal–molybdenum(VI)–tellurium(IV) oxide systems, namely, $Na_2Mo_3Te_3O_{16}$, $A_2Mo_3TeO_{12}$ (A = NH_4, Cs), and $A_4Mo_6Te_2O_{24}{\cdot}6H_2O$ (A = Rb, K) [54, 57]. Colorless bar-shaped crystals of $Na_2Mo_3Te_3O_{16}$ were synthesized hydrothermally from a

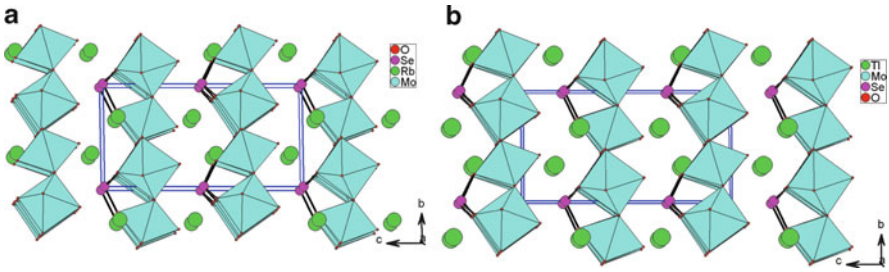

Fig. 15 View of structure of $Rb_2(MoO_3)_3(SeO_3)$ (**a**) and $Tl_2(MoO_3)_3(SeO_3)$ (**b**) along *a*-axis

mixture of Na_2TeO_3 and MoO_3 in H_2O at 220°C for 2 days. $Na_2Mo_3Te_3O_{16}$ crystallized in *NCS* space group *I*2 and its structure exhibits a quasi-one-dimensional crystal structure. Within the chain Mo_3O_{14} trimers composed of three edge-shared MoO_6 octahedra are interconnected by $Te_3O_8^{4-}$ anions each consisted of one TeO_4 group corner-sharing with two TeO_3 groups (Scheme 1a). Both Mo^{6+} and Te^{4+} cations are in the asymmetric coordination environments attributable to SOJT effects. The Mo^{6+} cations are distorted toward an edge of the MoO_6 octahedron (local C_2 direction). The polarization directions of the two TeO_3 groups are opposite but the lone pairs of the TeO_4 groups are aligned in the same direction to produce a large macroscopic dipole moment along the *b*-axis (Fig. 16). SHG measurements revealed that $Na_2Mo_3Te_3O_{16}$ displays a very large SHG response of about 500 × α-SiO_2 and is phase matchable. The strong SHG efficiency is maintained up to the melting temperature (around 450°C) [57].

Use of other alkali metal ions led to the discovery of two other structural types. $A_2Mo_3TeO_{12}$ (A = NH_4^+ and Cs^+) and $A_4Mo_6Te_2O_{24}{\cdot}6H_2O$ (A = Rb, K) were obtained by hydrothermal reactions of $(NH_4)_6Mo_7O_{24}{\cdot}4(H_2O)$ (or K_2CO_3, Rb_2CO_3, Cs_2CO_3, and MoO_3) and TeO_2 at 225°C. $A_2Mo_3TeO_{12}$ (A = NH_4^+ and Cs^+) ($P6_3$, NCS) are isostructural to $A_2(MoO_3)_3(SeO_3)$ (A = NH_4^+ and Cs^+), and their structures feature a 2D hexagonal tungsten oxide related $(Mo_3TeO_{12})^{2-}$ anionic layers that are separated by NH_4^+ or Cs^+ ions. The TeO_3 groups caps on the same side of the anionic layer in the same direction, resulting in a large macroscopic dipole moment along the *c*-axis. SHG measurements revealed that they display a large SHG response of about 400 × α-SiO_2 [54]. It is worthy to mention that large single crystals of $Cs_2Mo_3TeO_{12}$ with dimensions up to 20 × 20 × 16 mm^3 were grown successfully through a top-seeded solution growth (TSSG) method using a TeO_2–MoO_3 mixture as a self-flux by Tao's group [85]. $A_4Mo_6Te_2O_{24}{\cdot}6H_2O$ (A = Rb and K) ($P2_1/c$, CS) composed of discrete centrosymmetric $(Mo_6Te_2O_{24})^{4-}$ anionic aggregates and alkali metal ions. The hexamolybdoditellurite anion is centrosymmetric and formed by six edge-sharing MoO_6 octahedra further capped by two tellurite groups from both sides [87].

Three types of compounds were found in the alkali metal–tungsten(VI)–tellurium (IV) oxide systems, namely, $(NH_4)_2WTe_2O_8$ [59], $Na_2W_2TeO_9$ [39], and $A_2W_3TeO_{12}$ (A = K^+, Rb^+ and Cs^+) [56]. These compounds were synthesized hydrothermally from a mixture of AOH (A = NH_4, Na, K, Rb, or Cs), WO_3, and TeO_2 at 230 or 470°C.

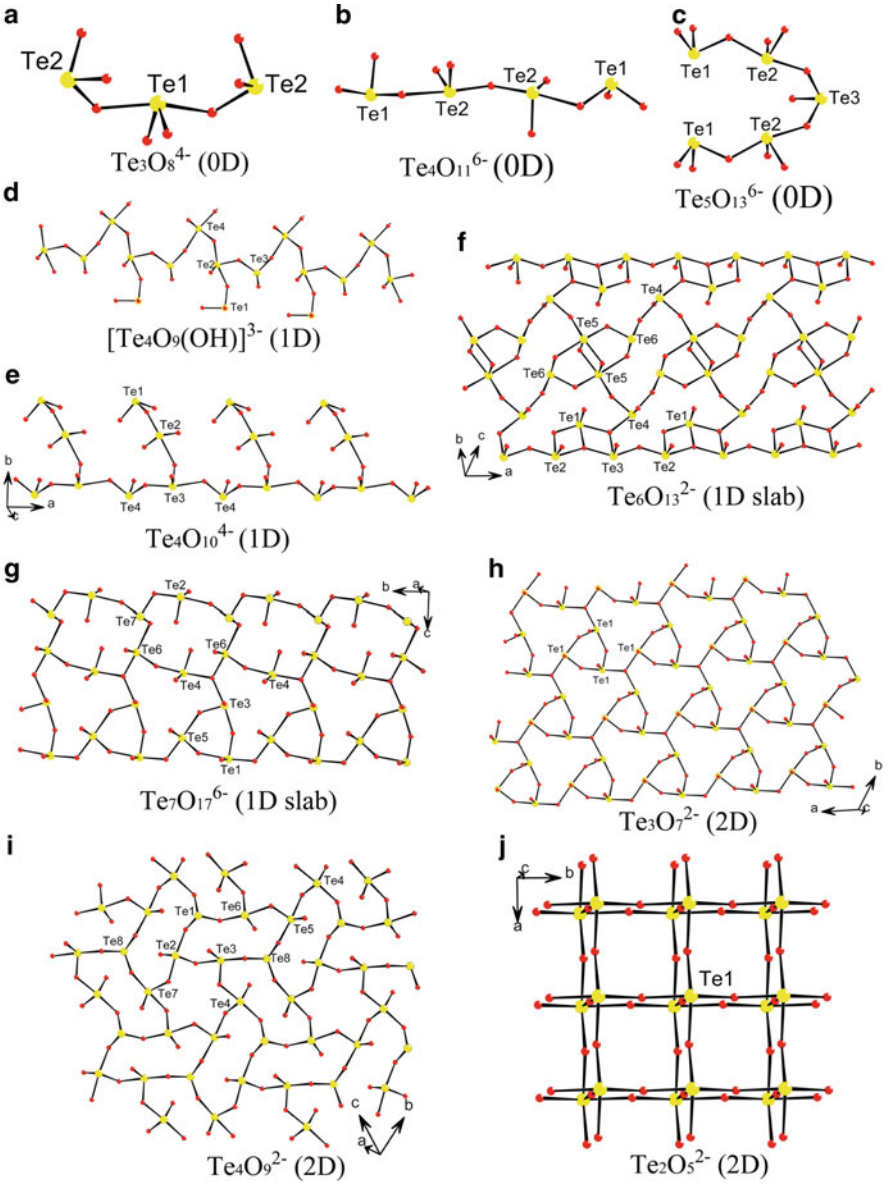

Scheme 1 Selected examples of tellurium(IV) oxide anions with polynuclear cluster units or extended structures

$(NH_4)_2WTe_2O_8$ crystallizes in the NCS polar space group $P2_1$. It exhibits a 2D layered structure consisting of WO_6 octahedra and TeO_4 polyhedra with the ammonium cations located at the interlayer region. Within the structure, the polarizations of

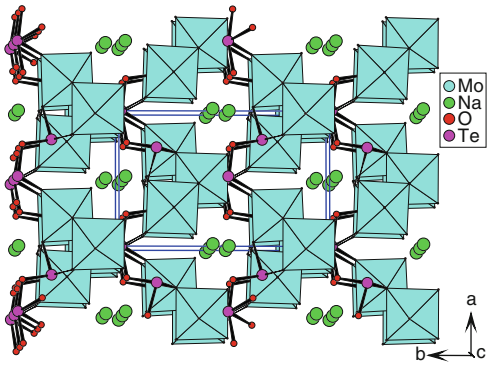

Fig. 16 View of structure of $Na_2Mo_3Te_3O_{16}$ along *c*-axis

$Te(1)O_4$ groups are toward almost opposite directions and cancel out each other but those of $Te(2)O_4$ and WO_6 polyhedra are almost aligned along the *b*-axis to produce a large net dipole moment. SHG measurements revealed that $(NH_4)_2WTe_2O_8$ displays a moderate SHG efficiency of approximately 250 × α-SiO_2 [59].

The NCS $Na_2W_2TeO_9$ (space group *Ia*) exhibits a 3D structure comprising distorted WO_6 octahedra linked by asymmetric TeO_3 groups (Fig. 17). The WO_6 octahedra form a corrugated 2D tungsten oxide layer through corner sharing, and these layers are further interconnected by bridging TeO_3 groups. Both Te(IV) and W(VI) cations are in local acentric environments attributable to the SOJT effects. Powder SHG measurements on polycrystalline $Na_2W_2TeO_9$ revealed a strong SHG intensity of approximately 500 × α-SiO_2 and the material is also phase matchable (Type I) [39].

$Cs_2W_3TeO_{12}$ ($P6_3$, NCS) is isostructural with $Cs_2Mo_3TeO_{12}$ [54]. Although $K_2W_3TeO_{12}$ ($P2_1/n$, CS) and $Rb_2W_3TeO_{12}$ ($P3_1c$, NCS) have a similar chemical formula to $Cs_2W_3TeO_{12}$, their structures are somehow different. All three compounds feature a same 2D tungsten oxide layer of corner-sharing WO_6 octahedra with W_3 and W_6 rings. The TeO_3 groups in $K_2W_3TeO_{12}$ act as interlayer linkers to form a 3D structure. In Rb and Cs phases, the TeO_3 groups only cap on the same side of the W_3 rings; therefore, they remain 2D. In the structure of $Rb_2W_3TeO_{12}$, the polarization directions of TeO_3 groups are almost aligned along the *c*-axis to produce a large net

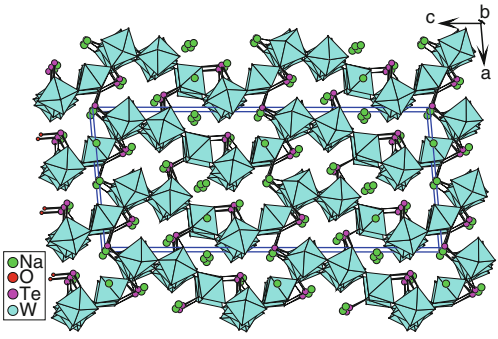

Fig. 17 View of structure of $Na_2W_2TeO_9$ along *b*-axis

dipole moment. SHG measurements revealed that the Rb and Cs compounds display strong SHG efficiencies of 200 and 400 × α-SiO_2, respectively [56]. Two tungsten (VI) selenite analog of $Cs_2W_3TeO_{12}$ were also reported, namely, $A_2(WO_3)_3(SeO_3)$ (A = NH_4, Cs), both of which show strong SHG efficiency of 200 × α-SiO_2 [55].

The Ae^{2+}–Mo^{6+}(W^{6+})–Se^{4+}(Te^{4+})–O systems are still less explored. Two compounds in the Ba–Mo(VI)–Se(IV)–O system were reported, namely, $BaMoO_3(SeO_3)$ and $BaMo_2O_5(SeO_3)_2$ [88]. Both compounds were synthesized hydrothermally from a solution of $BaCO_3$ or $Ba(OH)_2{\cdot}8H_2O$, MoO_3, and SeO_2 at 180°C for 4–5 days. $BaMoO_3(SeO_3)$ ($P2_1/c$, CS) exhibits a layered structure in which MoO_6 octahedra (distorted toward a face) are bridged by SeO_3 groups, forming Mo_2Se_2 four-member rings and Mo_3Se_3 six-member rings. $BaMo_2O_5(SeO_3)_2$ is polar ($Cmc2_1$) and features a 3D network composed of pairs of corner-sharing MoO_6 octahedra bridged by SeO_3 groups. The MoO_6 octahedron is distorted toward an edge (the local C_2 direction). Although $BaMo_2O_5(SeO_3)_2$ crystallizes in a polar space group, the polarizations from SeO_3 and MoO_6 polyhedra are almost cancel out each other [88].

$BaMo_2TeO_9$ and BaW_2TeO_9 were synthesized by solid-state reactions of stoichiometric amounts of Ba_2CO_3, MoO_3 (or WO_3), and TeO_2 at 560 or 760°C [34]. The two compounds are isostructural and crystallized in the polar space group $P2_1$. Their structures feature an anionic layer composed of MO_6 octahedra linked by the asymmetric TeO_3 polyhedra (Fig. 18). The MoO_6 octahedra in $BaMo_2TeO_9$ are distorted toward a face (along the local C_3 direction) with three short and three long Mo–O distances, whereas the WO_6 octahedra in BaW_2TeO_9 exhibit two types of distortions: toward a face as discussed above as well as toward an edge with two short, two normal, and two long W–O bonds. A pairs of MO_6 octahedra form a dimer via an M–O–M bridge and such dimeric units are further interconnected by TeO_3 groups via M–O–Te bridges. $BaMo_2TeO_9$ and BaW_2TeO_9 revealed extremely strong SHG responses of 600 and 500 × α-SiO_2, respectively [34]. Large crystals of $BaTeMo_2O_9$ with size up to 30 × 23 × 18 mm^3 and good optical quality were grown from the TeO_2–MoO_3 flux system, and their physical properties such as refractive indices, the principal thermal expansion, and thermal conductivity coefficients have been measured by the Tao's group [35, 36].

Several phases were reported in A–V^{5+}–Se^{4+}–O system, namely, $A(VO_2)_3(SeO_3)_2$ (A = K^+, Rb^+, Cs^+, Tl^+, NH_4^+), $AVSeO_5$ (A = Rb, Cs) and a V^{5+}/V^{4+} mixed valent

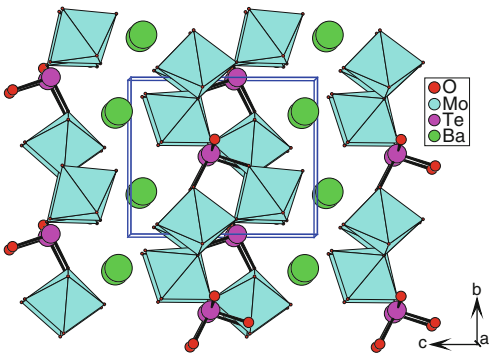

Fig. 18 View of structure of $BaMo_2TeO_9$ along *a*-axis

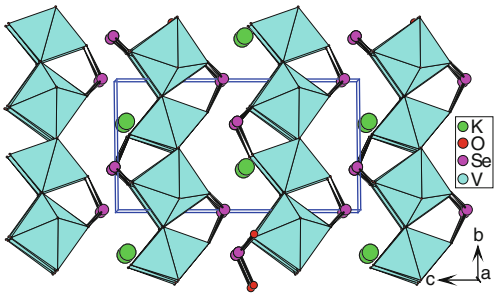

Fig. 19 View of structure of $K(VO_2)_3(SeO_3)_2$ along *a*-axis

KV_2SeO_7 [51, 89–91]. All of them were obtained by hydrothermal reactions. $A(VO_2)_3(SeO_3)_2$ ($A = K^+$, Rb^+, Cs^+, Tl^+, NH_4^+) ($P6_3$, NCS) are isostructural and exhibit layered hexagonal tungsten oxide (HTO)-type topologies consisting of corner-shared VO_6 octahedra that are capped by SeO_3 polyhedra on both sides [51, 89, 90]; such HTO layers are similar to those in $A_2(MoO_3)_3(SeO_3)$ ($A = NH_4^+$, Rb^+ and Cs^+) [53]. However, the 2D layer in the latter only capped by the SeO_3 groups on one side of the layer. Furthermore, the interlayer distances in the vanadium phases are much shorter than those of the corresponding molybdenum(VI) compounds due to the fact that much fewer countercations are needed to balance the charge. Different from those in the Mo(VI) selenites, the polarization directions of the SeO_3 groups in $A(VO_2)_3(SeO_3)_2$ ($A = K^+$, Rb^+, Cs^+, NH_4^+) are almost opposite each other and their local moments are mostly cancelled out (Fig. 19). SHG measurement revealed that $A(VO_2)_3(SeO_3)_2$ ($A = K^+, Rb^+, Cs^+, NH_4^+$) display weak SHG efficiencies of about 45, 40, 40, and 40 × α-SiO_2, respectively [50]. Only one tellurite analog of $A(VO_2)_3(SeO_3)_2$ was also reported, namely, $Cs(VO_2)_3(TeO_3)_2$, which shows a weak SHG efficiency of 40 × α-SiO_2 [50, 52].

The structure of the polar $AVSeO_5$ (A = Rb, Cs) (space group $P2_1$) is a 3D anionic network formed by alternative linkage of VO_5 square pyramids and SeO_3 groups via corner sharing, forming two types of helical tunnels along *b*-axis composed of four-member rings and eight-member rings, respectively. The alkali metal ions are located at the large tunnels. KV_2SeO_7 contains both V^{5+} and V^{4+} ions, with an octahedral and tetrahedral coordination environment, respectively. Its structure features a double layer of $\{V_2SeO_7\}^-$ composed of corner-sharing VO_6 octahedra, VO_4 tetrahedra, and SeO_3 groups [91].

Only three compounds were reported for the alkaline earth–V(V)–Se(IV)/Te(IV)–O family before our group's further explorations of these systems, namely, BaV_2TeO_8 [92], $Ba_{2.5}(VO_2)_3(SeO_3)_4{\cdot}3H_2O$ [93], and $Ba(VO_2)(SeO_3)_2(HSeO_3)$ [94]. Our efforts in alkaline earth–V^V/V^{IV}–Se^{IV}/Te^{IV}–O systems afforded six new compounds, namely, $Sr_2(VO)_3(SeO_3)_5$, $Sr(V_2O_5)(TeO_3)$, $Sr_2(V_2O_5)_2(TeO_3)_2(H_2O)$, $Ba_3(VO_2)_2(SeO_3)_4$, $Ba_2(VO_3)Te_4O_9(OH)$, $Ba_2V_2O_5(Te_2O_6)$ [95]. They exhibit six different types of structures.

The six alkaline earth metal vanadium selenites or tellurites were prepared by hydrothermal reactions of $SrCO_3$ (or $Ba(OH)_2{\cdot}8H_2O$ or $BaCO_3$), SeO_2 (or TeO_2), and V_2O_5 in different molar ratios at 230°C. During the preparation of

$Sr_2(VO)_3(SeO_3)_5$, the V^{5+} ion in V_2O_5 was reduced to an oxidation state of +4 by excess SeO_2. The structure of $Sr_2(VO)_3(SeO_3)_5$ (*P*nma, CS) features a 3D anionic network of $[(VO)_3(SeO_3)_5]^{4-}$ with 1D 8-MR tunnels along the *b*-axis, half of which are filled by Sr^{2+} ions. Within the structure, both $V(1)O_6$ and $V(2)O_6$ octahedra are distorted toward a corner (local C_4 direction) resulting one "short," four "normal," and one "long" V–O bonds. Neighboring $V(1)O_6$ octahedra are bridged by the $Se(2)O_3$ group via edge- and corner-sharing into a 1D zigzag chain along the *c*-axis, whereas two neighboring $V(2)O_6$ octahedra are bridged by a pair of $Se(1)O_3$ groups via corner sharing into a 1D chain along the *b*-axis with the $Se(3)O_3$ hanging on the chain. The intergrowth of the above two types of 1D chains resulted in a 3D anionic framework with two types of 1D 8-MR tunnels running along the *b*-axis. Half of these tunnels are occupied by the lone pairs of Se(IV) atoms, whereas the remaining tunnels are filled by Sr^{2+} ions.

Single crystals of $Sr(V_2O_5)(TeO_3)$ (as minor phase) and $Sr_2(V_2O_5)_2(TeO_3)_2(H_2O)$ (as main phase) were isolated from the same reaction. The structure of $Sr(V_2O_5)(TeO_3)$ (*P*-1, CS) features novel vanadium(V) tellurite chains in which V_2O_7 and V_2O_8 dimers are bridged by both TeO_4 and TeO_3 groups. Such structure differs from that of BaV_2TeO_8 with a similar chemical formula. BaV_2TeO_8 features a 1D chain composed of VO_4 tetrahedra and dimers of edge-sharing VO_5 square pyramids bridged by solely TeO_4 groups, forming 1D tunnels of 8-MRs each composed of two VO_4 tetrahedra, two VO_5 square pyramids, and four TeO_4 groups. The structure of $Sr_2(V_2O_5)_2(TeO_3)_2(H_2O)$ (*C*2/c, CS) features a 2D layer consisting of linear $[V_4O_{14}]$ tetramers bridged by TeO_3^{2-} anions with Sr^{2+} ions and water molecules located at the interlayer space. A pair of the $V(1)O_5$ form a V_2O_8 dimer via edge sharing. The V_2O_8 dimer is further attached by a $V(2)O_4$ tetrahedron via corner sharing on each side so as to form a linear $[V_4O_{14}]$ tetramer. Neighboring $[V_4O_{14}]$ clusters are bridged by TeO_3^{2-} groups via V–O–Te bridges into a 2D layer parallel to the *bc* plane. The structures of $Sr(V_2O_5)(TeO_3)$ and $Sr_2(V_2O_5)_2(TeO_3)_2(H_2O)$ are totally different; therefore, we failed to convert $Sr_2(V_2O_5)_2(TeO_3)_2(H_2O)$ into $Sr(V_2O_5)(TeO_3)$ by removal of a H_2O molecule.

When $Ba(OH)_2{\cdot}8H_2O$ (or $BaCO_3$) was used instead of $SrCO_3$ as the counter ions, three barium vanadium selenites or tellurites were isolated. $Ba_3(VO_2)_2(SeO_3)_4$ was obtained by hydrothermal reactions of $Ba(OH)_2{\cdot}8H_2O$ (1.0 mmol), V_2O_5 (0.4 mmol), and SeO_2 (1.0 mmol) at 230°C for 4 days. The structure of $Ba_3(VO_2)_2(SeO_3)_4$ ($P2_1$/n, CS) exhibits 0D $[(VO_2)(SeO_3)_2]^{3-}$ anions that are separated by Ba^{2+} ions. Each VO_5 square pyramid is connected to one SeO_3^{2-} anion via edge sharing and another selenite group via corner sharing, resulting in the formation of a 0D $[(VO_2)(SeO_3)_2]^{3-}$ anion. It is interesting to note that both $Ba_3(VO_2)_2(SeO_3)_4$ and $Ba_{2.5}(VO_2)_3(SeO_3)_4{\cdot}3H_2O$ are structurally based on VO_5 and SeO_3 polyhedra, but their structures are quite different. $Ba_{2.5}(VO_2)_3(SeO_3)_4{\cdot}3H_2O$ features a layered structure in which VO_5 polyhedra are interconnected by both bidentate and tridentate SeO_3 groups, forming tunnels of V_4Se_4 8-MRs and V_6Se_6 12-MRs. In $Ba_3(VO_2)_2(SeO_3)_4$, two selenite anions are bidentate chelating whereas the other two are unidentate; hence, the compound displays a much lower dimensionality.

$Ba_2(VO_3)Te_4O_9(OH)$ was obtained by heating a mixture of $Ba(OH)_2{\cdot}8H_2O$ (0.5 mmol), V_2O_5 (0.2 mmol) and TeO_2 (1.0 mmol) at 230°C for 4 days. The structure of $Ba_2(VO_3)Te_4O_9(OH)$ ($P2_1/n$, CS) exhibits a novel 1D $[Te_4O_9(OH)]^{3-}$ chain decorated by VO_4 tetrahedra with the Ba^{2+} located at the interchain space. $Te(2)O_4$ and $Te(4)O_4$ groups form a Te_2O_7 dimer via corner sharing; such dimers are further bridged by $Te(3)O_3$ polyhedra via corner sharing into a 1D tellurium(IV) oxide chain along the *b*-axis. The $Te(1)O_3$ groups are hanging on the same side of the chain through Te(1)–O(3)–Te(2) bridges, resulting in a 1D $[Te_4O_9(OH)]^{3-}$ chain (Scheme 1d). The discrete VO_4 tetrahedra are attached on the $Te(1)O_3$ groups via corner sharing.

$Ba_2V_2O_5(Te_2O_6)$ was obtained by heating a mixture of $Ba(OH)_2{\cdot}8H_2O$ (0.3 mmol), $NaVO_3{\cdot}2H_2O$ (1.0 mmol), and TeO_2 (1.0 mmol) at 230°C for 4 days. The structure of $Ba_2V_2O_5(Te_2O_6)$ ($P2_1/m$, CS) features a 1D vanadium (V) tellurites chain in which the VO_4 tetrahedra are interconnected by the $[Te_2O_6]^{4-}$ dimers with the Ba^{2+} ions acting as the counter ions. A pair of TeO_4 tetrahedra are interconnected into a $[Te_2O_6]^{4-}$ anion via edging sharing. $V(1)O_4$ tetrahedra are bridged by $[Te_2O_6]^{4-}$ anions into a 1D zigzag chain along the *b*-axis. The $V(2)O_4$ tetrahedra are grafted into the chain on the same side. Each $[Te_2O_6]^{4-}$ anion acts as a tridentate ligand and bridges to three $V(1)O_4$ tetrahedra.

These compounds display six different types of anionic structures, including 0D $[(VO_2)(SeO_3)_2]^{3-}$ anion, three different types of 1D vanadium(V) tellurite chains, 2D $[(V_2O_5)_2(TeO_3)_2]^{4-}$ layer, and 3D $[(VO)_3(SeO_3)_5]^{4-}$ (Fig. 20). The richness of

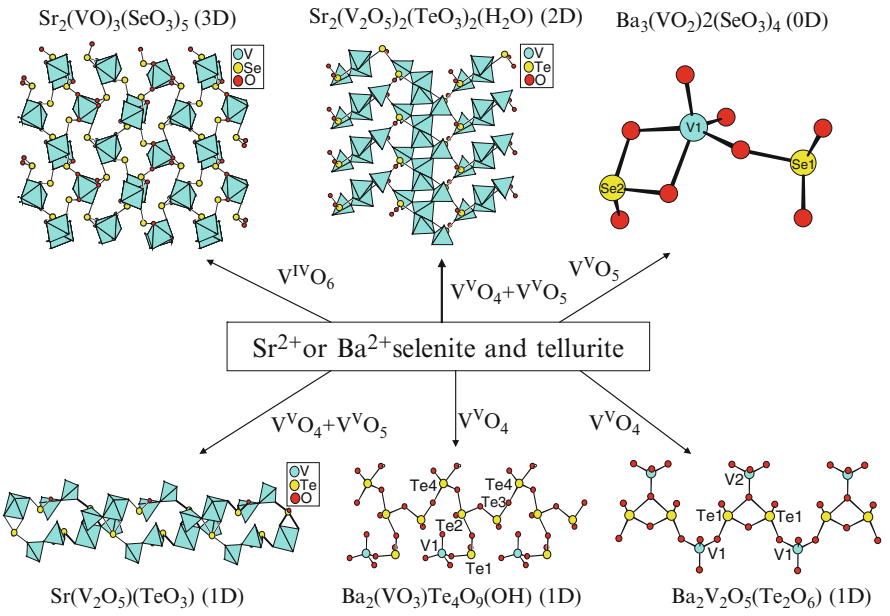

Fig. 20 View of the six different types of anionic structures in Ba^{II}/Sr^{II}–V^{V}/V^{IV}–Se^{IV}/Te^{IV}–O systems

the structure type for the vanadium tellurites or selenites can be attributed to the various coordination geometries available for the vanadium(V) cation and various coordination modes the tellurite and selenite anions can adopt [95].

Reports on A(Ae)–Nb^{5+}(or Ta^{5+})–Se^{4+}(or Te^{4+}) oxides are still rare. Only four types of structures were reported before our group's work, namely, $Na_{1.4}Nb_3Te_{4.9}O_{18}$, $NaNb_3Te_4O_{16}$, $Ba_2M_6Te_2O_{21}$ (M = Nb, Ta), and $BaMTeO_4(PO_4)$ (M = Nb, Ta) [96–98]. Our exploratory efforts in the alkali metal–Nb^V/Ta^V–Se^{IV}/Te^{IV}–O systems afford six new compounds with two different types of structures, namely, $KNb_3O_6(TeO_3)_2$, $KTa_3O_6(TeO_3)_2$, $RbNb_3O_6(TeO_3)_2$, $RbTa_3O_6(TeO_3)_2$, $KNb_3O_6(SeO_3)_2$, and $Cs_3Nb_9O_{18}(TeO_3)_2(TeO_4)_2$ [99]. These compounds were synthesized by standard solid-state reactions of KBr (or Rb_2CO_3 or Cs_2CO_3), Nb_2O_5 (or Ta_2O_5) and TeO_2 (or SeO_2) at 720–840°C for 4–6 days.

$KNb_3O_6(TeO_3)_2$, $KTa_3O_6(TeO_3)_2$, $RbNb_3O_6(TeO_3)_2$, $RbTa_3O_6(TeO_3)_2$, and $KNb_3O_6(SeO_3)_2$ are isostructural. Their structures (*P*bcm, CS) feature a novel 3D anionic network based on 2D layers of the corner-sharing NbO_6 or TaO_6 octahedra further bridged by TeO_3 or SeO_3 polyhedra, forming 1D tunnels of 4- and 6-MRs along the *a*-axis. The lone pair of the Te(IV) or Se(IV) atoms are orientated toward the center of the 4-MR tunnels, whereas the alkali cations are located at the 6-MR tunnels. Let us take $KNb_3O_6(TeO_3)_2$ as a representative to discuss the 3D network in more detail. Nb(2)O_6 octahedra are interconnected via corner sharing into a double chain along the *a*-axis, whereas Nb(1)O_6 octahedra are interconnected via corner sharing into a single chain along the *a*-axis. The above two types of 1D chains are alternate and interconnected via corner sharing along the *c*-axis, resulting in the formation of a corrugated niobium oxide layer parallel to the *ac* plane. Neighboring niobium oxide layers are bridged by TeO_3 groups into a 3D anionic network, forming 1D tunnels of 4- and 6-MRs along the *a*-axis. There are two types of 4-MRs tunnels, based on Te_2Nb_2 rings and Nb_3Te rings, respectively. The 6-MR tunnels are based on solely Nb_4Te_2 rings.

It is interesting to compare the structure of $ANb_3O_6(TeO_3)_2$ (A = K, Rb) with those of $Na_{1.4}Nb_3Te_{4.9}O_{18}$ and $NaNb_3Te_4O_{16}$ [96]. All three structures are based on NbO_6 octahedra connected by TeO_3 groups (or/and TeO_4 groups). Both $Na_{1.4}Nb_3Te_{4.9}O_{18}$ and $NaNb_3Te_4O_{16}$ feature 1D chains of corner sharing NbO_6 octahedra, whereas the structure of $KNb_3O_6(TeO_3)_2$ is based on 2D layers of corner-sharing NbO_6 octahedra. The Te(IV) cations in $KNb_3O_6(TeO_3)_2$ are all in distorted trigonal pyramidal environments, whereas additional TeO_4 groups with a "seesaw" geometry are present in $Na_{1.4}Nb_3Te_{4.9}O_{18}$, and $NaNb_3Te_4O_{16}$.

$Cs_3Nb_9O_{18}(TeO_3)_2(TeO_4)_2$ exhibits a different structure from those of the above five compounds. The structure of $Cs_3Nb_9O_{18}(TeO_3)_2(TeO_4)_2$ (*C*mcm, CS) features a novel 2D Nb–Te–O layer in which layer of corner-sharing NbO_6 octahedra is further decorated by asymmetric TeO_3 groups and 1D chains of corner-sharing TeO_4 polyhedra. Nb(1)O_6 octahedra are interconnected via corner sharing into a 1D chain along the *c*-axis, so are Nb(3)O_6 and Nb(5)O_6 octahedra. Nb(4)O_6 and Nb(2)O_6 octahedra form a linear Nb_4O_{21} tetramer via corner sharing. The above corner-sharing NbO_6 octahedral chains were interconnected by the linear Nb_4O_{21} tetramers via corner sharing into a thick Nb–O layer parallel to the *bc*-plane, forming 1D

tunnels of 6-MRs along the *c*-axis. The thickness of the niobium oxide layer is about 19.3 Å. The TeO_3 polyhedra and the 1D chains of corner-shared TeO_4 groups are grafted on the thick 2D Nb–O layer to form a Nb–Te–O layer, leaving virtually no free interlayer space. The Cs^+ cations are located at the 1D 6-MR tunnels. It is interesting to compare the structure of $Cs_3Nb_9O_{18}(TeO_3)_2(TeO_4)_2$ with that of $BaNbO_4Te(PO_4)$ [98]; both have layered anionic structures. The niobium oxide skeleton in $Cs_3Nb_9O_{18}(TeO_3)_2(TeO_4)_2$ is a 2D, whereas that in $BaNbO_4Te(PO_4)$ is a simple 1D chain.

These results indicate that metal selenites or tellurites containing V^{5+}, Nb^{5+}, or Ta^{5+} also display rich structure chemistry as those of Mo^{6+} and W^{6+}.

3.1.2 Ln-d^0 TM–Se(IV)/Te(IV)–O System

A lot of works have been done in Ln-d^0 TM–Se(IV)/Te(IV)–O system, mainly by the Halasyamani group and our group. The transition metal ions with d^0 electronic configuration used include Mo(VI), W(VI), and V(V) ions. The Halasyamani group reported three compounds, namely, $LaNbTeO_6$ and $La_4M_2Te_6O_{23}$ (M = Nb or Ta) [100]. We systematically explored the lanthanide selenium(IV) or tellurium(IV) oxides with additional transition metal ions with d^0-electronic configuration in our attempts to find new lanthanide SHG materials. Solid-state reactions of lanthanide(III) oxide (or/and lanthanide(III) oxychloride), MoO_3 (or WO_3) and TeO_2 at high temperature led to twelve new compounds with eight different types of structures, namely, $Nd_2MoSe_2O_{10}$, $Gd_2MoSe_3O_{12}$, $La_2MoTe_3O_{12}$, $Nd_2MoTe_3O_{12}$, $Ln_2MoTe_4O_{14}$ (Ln = Pr, Nd), $La_2WTe_6O_{18}$, $Nd_2W_2Te_2O_{13}$, and $Ln_5MTe_7O_{23}Cl_3$ (Ln = Pr, Nd; M = Mo, W) [101, 102]. Hydrothermal reactions of lanthanide(III) oxide (or/and lanthanide(III) chloride), MoO_3 (or V_2O_3) and SeO_2 at 200 or 230°C led to nine new compounds with four different types of structures, namely, $Nd_2(V_2O_4)(SeO_3)_4{\cdot}H_2O$, $Ln(VO_2)(SeO_3)_2$ (Ln = Eu, Gd, Tb), $H_3Ln_4Mo_{9.5}O_{32}(SeO_3)_4(H_2O)_2$ (Ln = La, Nd,), and $Ln_2Mo_3O_{10}(SeO_3)_2(H_2O)$ (Ln = Eu, Dy, Er) [103, 104].

Light purple phase of $Nd_2MoSe_2O_{10}$ was obtained by heating a mixture of Nd_2O_3 (0.6 mmol), MoO_3 (0.6 mmol), and SeO_2 (1.2 mmol) at 700°C for 6 days. $Nd_2MoSe_2O_{10}$ (*P*-1, CS) can also be formulated as $Nd_2(MoO_4)(SeO_3)_2$. Its structure features a 3D network in which the Nd(III) ions are interconnected by SeO_3^{2-} anions and MoO_4 tetrahedra. The interconnection of Nd(1) atoms via bridging selenite groups lead to a ⟨001⟩ layer, whereas Nd(2) atoms are bridged by MoO_4 tetrahedra to form a ⟨002⟩ layer. The above two types of layers are further interconnected via Nd–O–Se bridges into a 3D network. The lone pairs of the selenium(IV) cations are orientated to the cavities of the structure.

When Gd_2O_3 was used instead of Nd_2O_3, light yellow single crystals of $Gd_2MoSe_3O_{12}$ with a different structure were obtained. $Gd_2MoSe_3O_{12}$ (*P*-1, CS) can also be formulated as $Gd_2(MoO_3)(SeO_3)_3$, which can be considered as one O^{2-} anion of $Nd_2MoSe_2O_{10}$ being replaced by the third selenite group. The structure of $Gd_2MoSe_3O_{12}$ features a 3D network of gadolinium(III) selenite with the MoO_6 octahedra occupying the cavities of the network (Fig. 21). Unlike that in

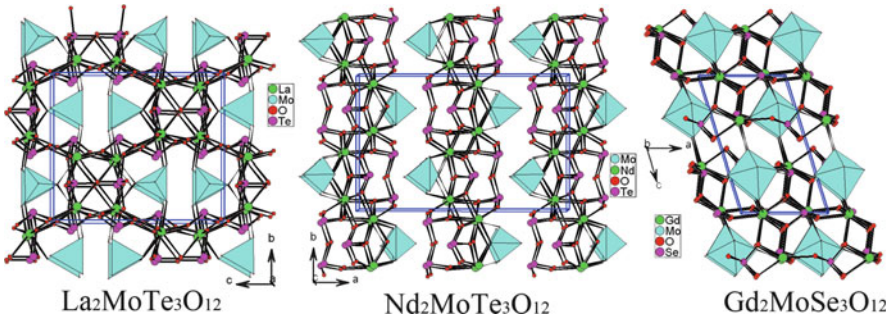

Fig. 21 View of the different structure types of $Ln_2MoTe_3O_{12}$ (Ln = La, Nd, Gd) with a similar formula

$Nd_2MoSe_2O_{10}$, the molybdenum(VI) atom in $Gd_2MoSe_3O_{12}$ is octahedrally coordinated by three oxygen atoms from three selenite groups and three O^{2-} anions. The MoO_6 octahedron is distorted toward a face (local C_3 direction), exhibiting three "long" and three "short" Mo–O bonds. The magnitude of the distortion (Δd) is calculated to be 1.492. The interconnection of the gadolinium(III) ions by selenite groups results in a 3D network with tunnels running along the *b*-axis. The MoO_6 octahedra are located at the tunnels formed by the gadolinium(III) selenite, forming Mo–O–Gd and Mo–O–Se bridges.

Colorless crystals of $La_2MoTe_3O_{12}$ were obtained by solid-state reaction of La_2O_3 (0.3 mmol), MoO_3 (0.6 mmol), and TeO_2 (1.5 mmol) in an evacuated quartz tube at 750°C for 7 days. The structure of $La_2MoTe_3O_{12}$ (*P*nma, CS) is composed of two La^{3+} ions, one MoO_4^{2-} anion, and one $Te_3O_8^{4-}$ anion. It can be considered as two selenite anions in $Nd_2MoSe_2O_{10}$ being replaced by a $Te_3O_8^{4-}$ anion. The trinuclear $Te_3O_8^{4-}$ anion is formed by one TeO_4 group corner sharing with two TeO_3 groups (Scheme 1a). The Mo(VI) cation is in a slightly distorted tetrahedral coordination geometry with the Mo–O distances ranging from 1.754(8) to 1.793(11) Å. The interconnection of the lanthanum(III) by chelating and bridging $Te_3O_8^{4-}$ anions led to a 3D network with 1D tunnels of La_6Te_4 MRs along *a*-axis. The MoO_4 polyhedra filled in the above tunnels and connected with the La^{3+} ions via Mo–O–La bridges (Fig. 21).

Light purple crystals of $Nd_2MoTe_3O_{12}$ were obtained by the solid-state reaction of a mixture of Nd_2O_3 (0.2 mmol), MoO_3 (0.6 mmol), and TeO_2 (1.2 mmol) in an evacuated quartz tube at 700°C for 6 days. $Nd_2MoTe_3O_{12}$ (*P*nma, CS) can be formulated as $Nd_2(MoO_4)(TeO_3)(Te_2O_5)$, it can also be considered as the $Te_3O_8^{4-}$ anion in $La_2MoTe_3O_{12}$ being replaced by a tellurite and a ditellurite anions. The structure of $Nd_2MoTe_3O_{12}$ features a 2D layer built by the lanthanide ions interconnected by tellurite groups and ditellurite groups, with the MoO_4 tetrahedra acting as the interlayer pendant groups (Fig. 21). The interlayer distance is about 8.85 Å [101].

Light green single crystals of $Pr_2MoTe_4O_{14}$ were obtained by the solid-state reaction of a mixture containing Pr_2O_3 (0.25 mmol), MoO_3 (0.25 mmol), and TeO_2

(1.5 mmol) in an evacuated quartz tube at 750°C for 6 days whereas light purple single crystals of $Nd_2MoTe_4O_{14}$ were prepared by heating the mixture of Nd_2O_3 (0.18 mmol), MoO_3 (0.35 mmol) and TeO_2 (1.4 mmol) at 720°C for 6 days. $Ln_2MoTe_4O_{14}$ (Ln = Pr, Nd) (*P*-1, CS) are isostructural and feature a 3D network in which the Ln(III) ions are interconnected by 1D $Te_4O_{10}^{4-}$ chains and MoO_4 tetrahedra. Therefore, $Ln_2MoTe_4O_{14}$ (Ln = Pr, Nd) can also be formulated as $Ln_2(MoO_4)(Te_4O_{10})$ (Ln = Pr, Nd). The TeO_3 and TeO_4 groups are interconnected via corner sharing into a novel 1D $Te_4O_{10}^{4-}$ anionic chain. Te(3)O_4 and Te(4)O_3 groups are interconnected via corner sharing, leading to a linear chain. Te(1)O_3 and Te(2)O_4 groups form a dimer by corner sharing. The dimers are hanging on the same side of the linear chain through corner sharing (Scheme 1e). Such 1D $[Te_4O_{10}]^{4-}$ anionic chain is very different from the 1D $[Te_4O_9(OH)]^{3-}$ anionic chain in $Ba_2(VO_3)Te_4O_9(OH)$ we discussed earlier. It is worthy to compare the structures of $Ln_2MoTe_4O_{14}$ (Ln = Pr, Nd) with those of $La_2MoTe_3O_{12}$ and $Nd_2MoTe_3O_{12}$. All four compounds contain MoO_4 tetrahedra; however, their Te–O architectures are completely different: $La_2MoTe_3O_{12}$ features discrete $Te_3O_8^{4-}$ anions, whereas $Nd_2MoTe_3O_{12}$ contains both TeO_3^{2-} anion and dimeric $Te_2O_5^{2-}$ anions, and 1D $Te_4O_{10}^{4-}$ anions are formed in $Ln_2MoTe_4O_{14}$ (Ln = Pr, Nd). $Nd_2MoTe_3O_{12}$ features a layered structure with MoO_4 tetrahedra hanging between two neighboring layers, whereas the MoO_4 tetrahedra in $La_2MoTe_3O_{12}$ are located at the tunnels of lanthanum (III) tellurium(IV) oxide. In $Ln_2MoTe_4O_{14}$ (Ln = Pr, Nd), the MoO_4 tetrahedron serves as a pillar between two lanthanide(III) tellurium(IV) oxide layers.

Colorless plate-shaped single crystals of $La_2WTe_6O_{18}$ were obtained by solid-state reaction of a mixture of La_2O_3 (0.30 mmol), WO_3 (0.60 mmol), and TeO_2 (1.5 mmol) in an evacuated quartz tube at 750°C for 6 days. $La_2WTe_6O_{18}$ (*P*-3*c*1, CS) can also be formulated as $La_2(WO_4)(Te_3O_7)_2$. The TeO_4 groups are interconnected into a $Te_3O_7^{2-}$ layer via corner sharing. Within the layer, three-member rings and "pear-shaped" six-member rings are found (Scheme 1h). The interconnection of La^{3+} ions by bridging WO_4^{2-} anions led to a 2D $[La_2WO_4]^{4+}$ layer along the *ab* plane. One $[La_2WO_4]^{4+}$ layer is sandwiched by two $Te_3O_7^{2-}$ layers into a thick layer in the *ab* plane via La–O–Te bridges. The thickness of the layer is about 7.65 Å and the width of the interlayer opening is about 3.0 Å. The lone-pair electrons of Te(IV) atoms are orientated toward the interlayer space.

Light purple single crystals of $Nd_2W_2Te_2O_{13}$ was obtained by solid-state reactions of a mixture of Nd_2O_3 (0.25 mmol), WO_3 (0.50 mmol), and TeO_2 (1.25 mmol) in an evacuated quartz tube at 720°C for 6 days. $Nd_2W_2Te_2O_{13}$ (*P*-1, CS) features a 3D network structure in which the W_2O_{10} dimers occupy the large apertures formed by neodymium tellurite. Among two unique Nd^{3+} ions in the asymmetric unit, one is 8-coordinated whereas the other one is 9-coordinated. Unlike that in $La_2WTe_6O_{18}$, both the W(VI) cations in $Nd_2W_2Te_2O_{13}$ are octahedrally coordinated. A pairs of WO_6 octahedra are interconnected via edge sharing into a $W_2O_{10}^{8-}$ dimer. One W atom is distorted toward a face (local C_3 direction) with three "short" and three "long" W–O bonds, whereas W(2) atom is distorted toward an edge (C_2) with two "short," two "normal," and two "long" W–O bonds. The magnitudes of the distortion (Δd) is 1.118 and 0.945 Å, respectively, for W(1)O_6

and $W(2)O_6$. The interconnection of the Nd(III) ions by the tellurite groups resulted in a 3D network with two types of apertures along the *a*-axis. The large apertures with a narrow-long shape are formed by 10-member rings composed of 4 TeO_3 groups and 6 Nd(III) ions, whereas the small ones are formed by four-member rings composed of 2 Nd(1) and two $Te(1)O_3$ groups. The W_2O_{10} dimers are located at the large apertures. In $Nd_2W_2Te_2O_{13}$, each W_2O_{10} dimer connects with two TeO_3 groups (one in a unidentate fashion and the other in a bidentate bridging fashion) to form a $[W_2Te_2O_{13}]^{6-}$ anion. Therefore, the structure of $Nd_2W_2Te_2O_{13}$ also can be viewed as the Nd^{3+} ions being interconnected by $[W_2Te_2O_{13}]^{6-}$ anions via Nd–O–Te and Nd–O–W bridges.

Isostructural $Ln_5MTe_7O_{23}Cl_3$ (Ln = Pr, Nd; M = Mo, W) (*C*2/m, Cs) were obtained by solid-state reactions of a mixture containing LnOCl (Ln = Pr, Nd), WO_3 (or MoO_3), and TeO_2 in an evacuated quartz tube at 750 or 720°C for 6 days. These compounds feature a 3D network of lanthanide(III) molybdenum(VI) tellurium(IV) oxychloride with large apertures occupied by isolated Cl anions and the lone-pair electrons of Te(IV). $Ln_5MTe_7O_{23}Cl_3$ can be also formulated as $Ln_5(MO_4)(Te_5O_{13})(TeO_3)_2Cl_3$. 2 $Te(1)O_3$, 2 $Te(2)O_4$, and 1 $Te(3)O_3$ groups are corner sharing to form a novel $Te_5O_{13}^{6-}$ pentamer in a "semi-cycle" shape (Scheme 1c). The interconnection of Ln(III) ions via $Te_5O_{13}^{6-}$ and TeO_3^{2-} anions resulted in a thick layer parallel to the *ab* plane. Neighboring lanthanide tellurium(IV) oxide layers are bridged by Cl(2) atoms into a complicated 3D network, forming two different types of apertures. The small $Ln_4O_2Cl_2$ ring was capped by the MO_4 polyhedra on both sides, whereas the large apertures formed by eight-member rings are filled by the isolated Cl^- anions and the lone-pair electrons of Te(IV) atoms of the $Te_5O_{13}^{6-}$ groups [102].

The solid-state luminescent properties of $Nd_2MoSe_2O_{10}$, $Nd_2MoTe_3O_{12}$, $Nd_2MoTe_4O_{14}$, and $Nd_2W_2Te_2O_{13}$ were investigated at both room temperature and 10 K, and the solid-state luminescent properties of $Nd_5MoTe_7O_{23}Cl_3$ and $Nd_5WTe_7O_{23}Cl_3$ were studied at room temperature. Under excitation at 514 nm, the room temperature emission spectra for all six Nd(III) compounds display three sets of characteristic emission bands for the Nd(III) ion in the near IR region: $^4F_{3/2} \rightarrow {}^4I_{9/2}$, $^4F_{3/2} \rightarrow {}^4I_{11/2}$, and $^4F_{3/2} \rightarrow {}^4I_{13/2}$. $Nd_2MoTe_3O_{12}$ contains only one independent Nd (III) site, whereas $Nd_2MoSe_2O_{10}$, $Nd_2MoTe_4O_{14}$, and $Nd_2W_2Te_2O_{13}$ each contains two unique Nd(III) sites with C_1 symmetry. Due to the crystal field effect, each transition band was split into several subbands. $Pr_5MoTe_7O_{23}Cl_3$ and $Pr_5WTe_7O_{23}Cl_3$ display four sets of emission bands at 491 nm (very strong, $^3P_0 \rightarrow {}^3H_4$), 534 nm (moderate, $^3P_0 \rightarrow {}^3H_5$), 619 nm (moderate, $^3P_0 \rightarrow {}^3H_6$), 649 nm (strong, $^3P_0 \rightarrow {}^3F_2$) and 735 nm (weak, $^3P_0 \rightarrow {}^3F_4$) under $\lambda_{ex} = 448$ nm. Under the same experimental conditions, the corresponding emission bands for $Pr_2MoTe_4O_{14}$ are much weaker. Due to the so called "crystal field effect" as well as multiple Pr^{3+} sites, a few emission bands were split into several subbands [101, 102].

It is noticed that most of MoO_x ($x = 4$ or 6) polyhedra in the above compounds are not polymerized because of small Mo/Ln (≤ 1) ratios. We deem that these MoO_4 or MoO_6 may polymerize into novel polynuclear clusters or extended structures through corner- or edge sharing if the Mo/Ln ratios are larger (>1).

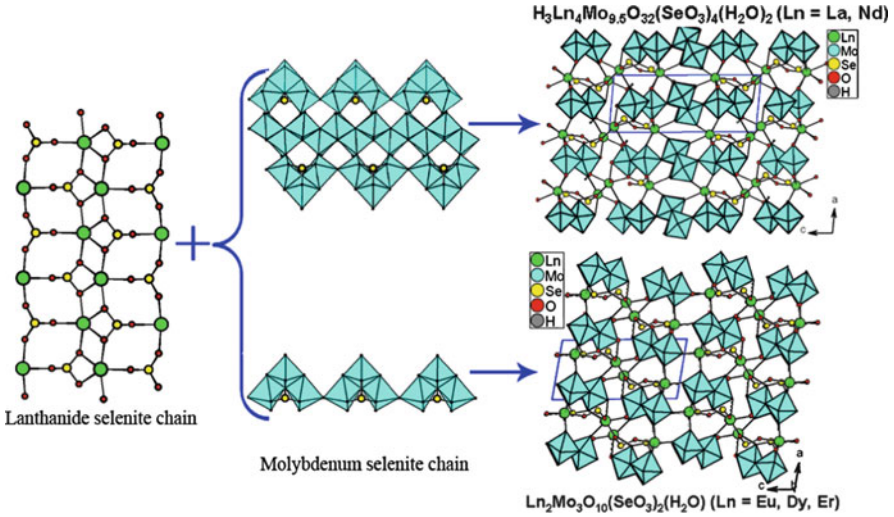

Fig. 22 View of the structure of $H_3Ln_4Mo_{9.5}O_{32}(SeO_3)_4(H_2O)_2$ (Ln = La, Nd) and $Ln_2Mo_3O_{10}(SeO_3)_2(H_2O)$ (Ln = Eu, Dy, Er)

Our explorations of Mo-rich Ln^{III}–Mo^{VI}–Se^{VI}–O phases led to five new lanthanide selenites containing MoO_6 octahedra, namely, $H_3Ln_4Mo_{9.5}O_{32}(SeO_3)_4(H_2O)_2$ (Ln = La, Nd,) and $Ln_2Mo_3O_{10}(SeO_3)_2(H_2O)$ (Ln = Eu, Dy, Er) [103]. The MoO_6 octahedra in the above two classes of compounds are interconnected into two types of novel molybdenum oxide chains.

The above five compounds were initially synthesized by the hydrothermal reactions of a mixture of lanthanide oxide (0.1 mmol), molybdenum oxide (0.5 mmol), and selenium dioxide (1.0 mmol) in 5 mL of distilled water at 230°C for 4 days. $H_3Ln_4Mo_{9.5}O_{32}(SeO_3)_4(H_2O)_2$ (Ln = La, Nd,) (*P*-1, CS) features a complicated 3D network in which the molybdenum selenite chains are further interconnected by lanthanide selenite chains (Fig. 22). The interconnection of La (1) and La(2) ions by bridging SeO_3^{2-} groups resulted in a lanthanide selenite chain along the *b*-axis. $Mo(1)O_6$, $Mo(2)O_6$, and $Mo(3)O_6$ octahedra are interconnected by edge-sharing bonds forming a $[Mo_3O_{14}]^{10-}$ trimer. The $Se(2)O_3^{2-}$ group capped on the trimer via Se–O–Mo bridges to form a $[Mo_3SeO_{14}]^{6-}$ unit. Such units are further condensed into a molybdenum selenite chain of $[Mo_3SeO_{13}]^{4-}$ via corner sharing along the *b*-axis. A pair of $Mo(4)O_6$ octahedra are edge shared into a $[Mo(4)_{1.5}O_{11}]^{13-}$ dimer; so are pairs of $Mo(5)O_6$ octahedra. The interconnection of $[Mo(4)_{1.5}O_{11}]^{13-}$ and $[Mo(5)_2O_{11}]^{10-}$ via edge sharing resulted in a double strand polymer of $[Mo_{1.75}O_8]^{5.5-}$. A pair of $[Mo_3SeO_{13}]^{4-}$ chains are sandwiched by two $[Mo_{1.75}O_8]^{5.5-}$ chains into a thick 1D slab of $[Mo_{4.75}SeO_{19}]^{5.5-}$ through Mo–O–Mo bridges.

$Ln_2Mo_3O_{10}(SeO_3)_2(H_2O)$ (Ln = Eu, Dy, Er) ($P2_1/m$, CS) with lower Ln/Mo molar ratio was obtained for the heavier lanthanide elements. Their structures feature a 3D framework also constructed by the intergrowth of the molybdenum selenite

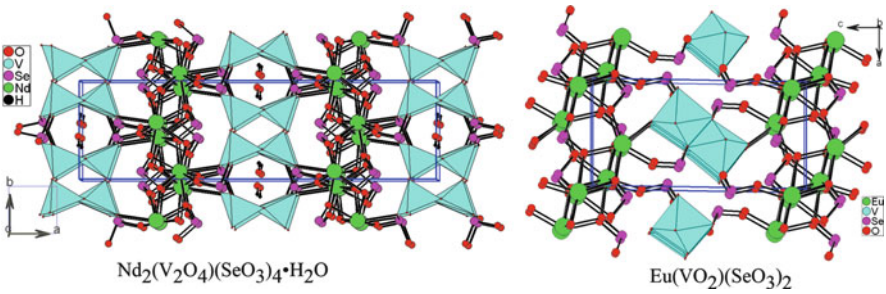

Fig. 23 View of the different structure types of $Nd_2(V_2O_4)(SeO_3)_4{\cdot}H_2O$ and $Eu(VO_2)(SeO_3)_2$

chains and the lanthanide selenites chains (Fig. 22). The interconnection of $Ln(1)^{3+}$ and $Ln(2)^{3+}$ ions through bridging $Se(1)O_3^{2-}$ and $Se(2)O_3^{2-}$ groups led to a lanthanide selenite chain along the *b*-axis. Two $Mo(1)O_6$ and one $Mo(2)O_6$ octahedra are interconnected by edge sharing into a $[Mo_3O_{14}]^{10-}$ trimer. This $[Mo_3O_{14}]^{10-}$ trimer is further capped by Se(2) atoms into a $[Mo_3SeO_{14}]^{6-}$ unit. Neighboring $[Mo_3SeO_{14}]^{6-}$ units are further interconnected via corner sharing into a molybdenum selenite chain as in $H_3Ln_4Mo_{9.5}O_{32}(SeO_3)_4(H_2O)_2$ (Ln = La, Nd,). The interconnection of the alternating lanthanide selenite and molybdenum selenite chains along the *a*-axis via Mo–O–Ln bridges resulted in a novel 3D network.

We had also isolated four lanthanide vanadium selenites with two types of structures, namely, $Nd_2(V_2O_4)(SeO_3)_4{\cdot}H_2O$ and $Ln(VO_2)(SeO_3)_2$ (Ln = Eu, Gd, Tb) [104]. They were hydrothermally synthesized by reactions of a mixture of $LnCl_3{\cdot}6H_2O$ (Ln = Nd, Eu, Gd, Tb), V_2O_3, and selenium dioxide in 5.0 or 8.0 mL of distilled water at 200°C for 4 days. During the reactions, V^{3+} ion has been oxidized to V^{5+}.

The structure of compound $Nd_2(V_2O_4)(SeO_3)_4{\cdot}H_2O$ features a 3D network composed of the 2D layers of $[Nd(SeO_3)]^+$ that are bridged by 1D $[V_2O_4(SeO_3)_2]^{2-}$ chains with the lattice water molecules located at the small 6-membered ring tunnels thus formed (Fig. 23). The two VO_5 tetragonal pyramids are interconnected by edge sharing to form a $[V_2O_8]^{6-}$ binuclear cluster unit. The $[V_2O_8]^{6-}$ dinuclear cluster units are further bridged by $Se(2)O_3^{2-}$ groups via corner sharing into a 1D chain along the *c*-axis. The Nd^{3+} ions are interconnected by bridging $Se(1)O_3$ groups into a neodymium(III) selenites layer parallel to the *bc* plane. The above two building units are further interconnected via Nd–O–Se(2) –O–V bridges into a 3D architecture with two types of narrow-long shaped 6-MR and 10-MR tunnels along the *c*-axis. The lattice water molecules are located at 6-MR tunnels composed of four VO_5 and two SeO_3 groups. The lattice water molecules also form a few hydrogen bonds with oxoanion and selenite oxygen atoms, which further increases the stability of the 3D structure. The structure of $Ln(VO_2)(SeO_3)_2$ (Ln = Eu, Gd, Tb) ($P2_1/m$, CS) also features a 3D network composed of 2D $[Ln(SeO_3)]^+$ layers which are bridged by 1D $[(VO_2)(SeO_3)]^-$ chains (Fig. 23). The two VO_6 octahedra are interconnected by edge sharing to form a $[V_2O_{10}]^{10-}$ dimer. These dimers are further interconnected though the corner sharing oxoanions into a double chain along the *b*-axis, $Se(1)O_3$ groups are grafted on both sides of the double chain in a bidentate bridging fashion, whereas

$Se(3)O_3$ groups capped on V_4 rings of the 1D chain. The Ln(III) ions are bridged by $Se(2)O_3$ and $Se(4)O_3$ groups into a double layer perpendicular to the *c*-axis. The above two building units are further interconnected via Ln–O–Se–O–V bridges into a 3D architecture with narrow-long shaped 10-MR tunnels along the *b*-axis.

It should be mentioned that these lanthanide selenites and tellurites containing V^{5+}, Mo^{6+}, and W^{6+} are not SHG active since they are all structurally centrosymmetric. This is very different from the corresponding metal iodates some of which are SHG active, as discussed earlier.

3.1.3 TM-d^0 TM–Se(IV)/Te(IV)–O System

A number of compounds in the translation metal (TM)-d^0 TM–Te(IV)/Se(IV)–O systems have been reported, a few of which exhibit moderate SHG efficiency (Table 2).

Four new transition metal vanadium selenites or tellurites with different types of structures were isolated by our group, namely, $ZnVSe_2O_7$, $Cd_6V_2Se_5O_{21}$, $Zn_3V_2TeO_{10}$, and $Cd_4V_2Te_3O_{15}$ [61, 105].

Dark-cyan crystals of $ZnVSe_2O_7$ was prepared by hydrothermal reactions of a mixture of $Zn(CH_3COO)_2{\cdot}2H_2O$ (0.84 mmol), V_2O_5 (0.28 mmol), SeO_2 (1.08 mmol), and H_2O (5 mL) at 200°C for 4 days. V^{5+} ion was reduced to V^{4+} ion during the reactions. The structure of $ZnVSe_2O_7$ ($P2_1/n$, CS) features a 3D network composed of 3D anionic framework of $[VSe_2O_7]^{2-}$ with the zinc(II) cations located at the six MR tunnels along *a*-axis. $ZnVSe_2O_7$ can also be formulated as $Zn(VO)(SeO_3)_2$. The VO_6 octahedra are interconnected via corner sharing into a 1D vanadium oxide chain along the $\langle 101 \rangle$ direction. These chains are further bridged by $Se(1)O_3$ groups into a 2D layer parallel to the *ac* plane. Such 2D layers are further interconnected by bridging $Se(2)O_3$ groups into pillar layers $[VSe_2O_7]^{2-}$ with two types of 6-MRs tunnels along the *a*-axis. Both 6-MRs are composed of four VO_6 octahedra and two SeO_3 groups, one is wider whereas the other is narrower. The lone pairs of the selenium(IV) point toward the center of the narrow ones, whereas the zinc(II) cations are located at the wider tunnels.

Red needle-shaped single crystals of $Cd_6V_2Se_5O_{21}$ were obtained by the solid-state reaction of a mixture of CdO, V_2O_5, and SeO_2 in a molar ratio of 2:1:1 or 1:1:1 at 680°C for 6 days. $Cd_6V_2Se_5O_{21}$ can also be formulated as $Cd_6(V_2O_6)(SeO_3)_5$. The structure of $Cd_6V_2Se_5O_{21}$ ($P2_1/c$, CS) features a novel 3D network composed 3D $\{Cd_6(SeO_3)_5\}^{2+}$ with 1D 16-MR tunnels along the *b*-axis, 1D $\{V_2O_6\}^{2-}$ anionic chains are located at the big tunnels and form Cd–O–V bridges. There are six unique cadmium(II) ions, two vanadium(V) cations, and five selenites in its asymmetric unit. The cadmium(II) ions are interconnected by bridging and chelating selenite groups into a 3D framework of $\{Cd_6(SeO_3)_5\}^{2+}$ with 1D 16-MRs tunnels along the *b*-axis. The size of the tunnel is estimated to be 3.0×12.0 Å^2 based on the structural data (the atomic radii of the ring atoms have been deducted). The 16-MRs tunnels are constructed by six SeO_3 groups and ten cadmium atoms. The lone pairs of the selenite anions are pointing toward the center of the tunnels. $V(1)O_4$ and

$V(2)O_4$ tetrahedra are interconnected alternately via corner sharing into a 1D $\{V_2O_6\}^{2-}$ anionic chain along the *b*-axis. These vanadium oxide chains are inserted in the above tunnels of the cadmium(II) selenite and interact with the main skeleton via V–O–Cd bridges [105].

Solid-state reactions of zinc(II) or cadmium(II) oxide, V_2O_5, and TeO_2 at high temperature led to two novel quaternary compounds, namely, $Zn_3V_2TeO_{10}$ and $Cd_4V_2Te_3O_{15}$ [61].

$Zn_3V_2TeO_{10}$ ($P2_1/c$, CS) features a novel 3D network composed of 2D zinc tellurite layers bridged by $V(1)O_4$ tetrahedra with 8-MRs tunnels along the *c*-axis, and the $V(2)O_4$ tetrahedra are located at the above tunnels. In the structure, $Zn(1)O_6$ and $Zn(2)O_5$ polyhedra are interconnected via edge- and corner sharing into a 1D chain along the *a*-axis. $Zn(3)O_5$ polyhedra are interconnected via edge sharing to form a 1D chain along the *c*-axis. The two types of 1D chains are further interconnected via corner sharing into a zinc(II) oxide layer parallel to the *ac* plane. The TeO_4 groups are grafted into the layers through Te–O–Zn bridges to form a thick zinc(II) tellurite layer with 8-MRs tunnels along the *c*-axis. Neighboring such layers are bridged by $V(1)O_4$ tetrahedra via corner sharing along the *b*-axis into a 3D architecture. The $V(2)O_4$ tetrahedra are located at the eight-membered ring tunnels formed by two tellurite groups and six zinc atoms.

$Cd_4V_2Te_3O_{15}$ crystallizes in the NCS space group $P2_12_12_1$. Its structure features a 3D network composed of 2D cadmium tellurite layers bridged by discrete VO_4 tetrahedra and 1D vanadium oxide helical chains (Fig. 24). There are four Cd(II) ions, two V(V), and three tellurite groups in the asymmetric unit of $Cd_4V_2Te_3O_{15}$. It can also be formulated as $Cd_4(VO_3)_2(TeO_3)_3$. All four unique cadmium(II) ions are octahedrally coordinated by six oxygen atoms, and both vanadium(V) ions are in the tetrahedral geometry. $V(1)O_4$ tetrahedra are interconnected into a 1D right-handed helical chain via corner sharing, whereas the $V(2)O_4$ tetrahedra remain "isolated." The CdO_6 octahedra are interconnected into a 2D cadmium(II) oxide layer via corner- and edge sharing. The tellurite (TeO_3) anions capped on both sides

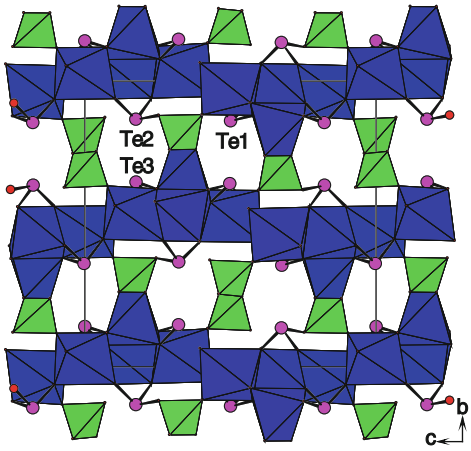

Fig. 24 View of the structure of $Cd_4V_2Te_3O_{15}$ down the *a*-axis. The CdO_6 and VO_4 polyhedra are shaded in *blue* and *green*, respectively. Te and O atoms are drawn as *pink* and *red circles*, respectively

of the cadmium(II) oxide layer to form a novel cadmium(II) tellurite layer parallel to the *ac* plane. Neighboring cadmium(II) tellurite layers are further bridged by the "isolated" $V(2)O_4$ tetrahedra and the V(1) oxide helical chains into a 3D architecture with two types of left-handed helical tunnels along the *a*-axis. The larger ones are formed by eight-membered rings composed of four cadmium(II) atoms, three vanadium(V) atoms, and a tellurium(IV) atom, whereas the smaller ones are based on six-membered rings containing four cadmium(II) and two vanadium(V) atoms. The lone-pair electrons of the tellurium(IV) atoms are orientated toward the tunnels above [61]. SHG measurements revealed that $Cd_4V_2Te_3O_{15}$ displays a moderately strong SHG signal about 1.4 times that of KDP. This SHG response could be attributed to both the lone pairs of the tellurite anions and the 1D vanadium(V) oxide helical chain. The DTA studies indicate that $Cd_4V_2Te_3O_{15}$ exhibits an endothermic peak at 751°C in the heating curve and an exothermic peak at 695°C in the cooling curve; hence, $Cd_4V_2Te_3O_{15}$ may melt congruently at about 751°C. This suggests that $Cd_4V_2Te_3O_{15}$ is a congruently melting compound, which was also confirmed by powder XRD studies under different temperatures. Therefore, in principle, large single crystals could be grown from the stoichiometric melts.

A large number of transition metal molybdenum(VI) (or tungsten(VI)) selenites or tellerites have been reported, some of them are SHG active [58, 62, 66, 106].

Polar $Zn_2(MoO_4)(QO_3)$ (Q = Se, Te) was reported by the Halasyamani group very recently [62]. Crystals of $Zn_2(MoO_4)(TeO_3)$ were grown by hydrothermal reactions of ZnO (2.0 mmol), TeO_2 (1.0 mmol), MoO_3 (1.00 mmol), and NH_4Cl/NH_3 1 M buffer solution (3 mL) at 230°C for 2 days, whereas Bulk polycrystalline and crystals of $Zn_2(MoO_4)(SeO_3)$ were prepared by solid-state reactions of a mixture of ZnO (2.0 mmol), SeO_2 (1.0 mmol), and MoO_3 (1.0 mmol) at 550°C for 48 h. $Zn_2(MoO_4)(QO_3)$ (Q = Se, Te) are isostructural and both crystallized in a polar space group $P2_1$. Their structures feature a 3D network composed of 2D zinc selenites (or tellurites) layers further bridged by MoO_4 tetrahedra. The ZnO_n ($n = 4$, 6) polyhedra are interconnected into a wave-like 2D layer via corner sharing with the SeO_3 (or TeO_3) groups capping from both sides of the layer. These zinc selenites (or tellurites) layers are further interconnected by the MoO_4 tetrahedra to a 3D framework via corner sharing. The polarities come mainly from the lone-pair cations since MoO_4 tetrahedra cannot undergo SOJT distortion. Powder SHG measurements using 1,064 nm radiation indicate the compounds exhibit moderate SHG efficiencies of 100 and 80 × α-SiO_2 for $Zn_2(MoO_4)(SeO_3)$ and $Zn_2(MoO_4)(TeO_3)$, respectively. Both of them are nonphase-matching materials [62].

Three new phases in Ag^{I}–Mo^{VI}/W^{VI}–Te^{IV}–O system, namely, $Ag_2Mo_3Te_3O_{16}$, $Ag_2MoTe_4O_{12}$, and $Ag_6W_3Te_4O_{20}$, were prepared by our group [58]. They were synthesized hydrothermally from a stoichiometric mixture of Ag_2O, TeO_2, MoO_3 or WO_3, and 10 mL of H_2O at 230°C. The loaded compositions are: Ag_2O (0.1 mmol), TeO_2 (0.3 mmol), and MoO_3 (0.3 mmol) for $Ag_2Mo_3Te_3O_{16}$; Ag_2O (0.1 mmol), TeO_2 (0.4 mmol), and MoO_3 (0.1 mmol) for $Ag_2MoTe_4O_{12}$; Ag_2O (0.3 mmol), TeO_2 (0.4 mmol), and WO_3 (0.3 mmol) for $Ag_6W_3Te_4O_{20}$.

$Ag_2Mo_3Te_3O_{16}$ is isostructural to $Na_2Mo_3Te_3O_{16}$ and crystallized in a polar space group *I*2 [57]. Its structure features a 1D $[Mo_3Te_3O_{16}]^{2-}$ anionic chain

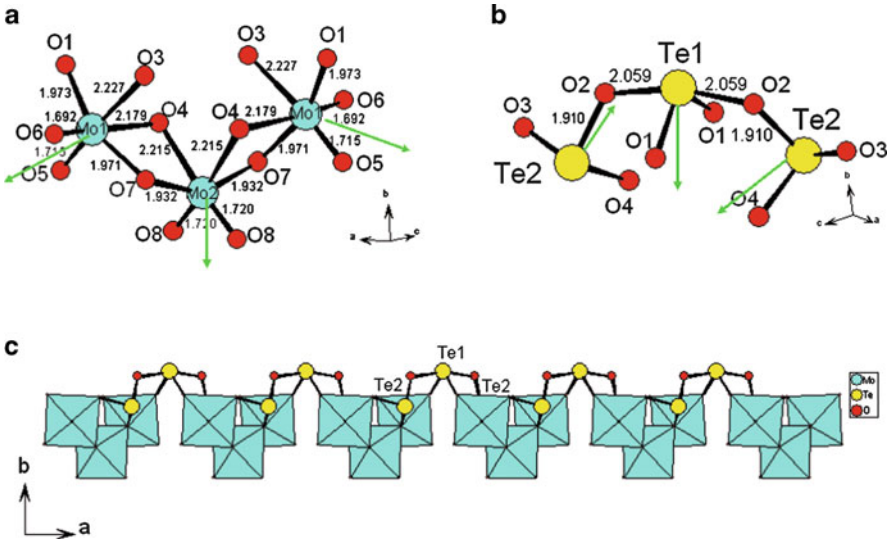

Fig. 25 The $[Mo_3O_{14}]^{12-}$ cluster (**a**), the $[Te_3O_8]^{4-}$ cluster (**b**) and a 1D $[Mo_3Te_3O_{16}]^{2-}$ anion (**c**) in $Ag_2Mo_3Te_3O_{16}$. The *green arrows* indicate the directions of the polarization of the cations

composed of $[Mo_3O_{14}]^{10-}$ clusters bridged by $[Te_3O_8]^{4-}$ anions via corner sharing. Neighboring chains are further bridged by the Ag^+ ions into a condensed 3D network. The $[Mo_3O_{14}]^{10-}$ cluster is formed by three edge-shared MoO_6 octahedra in which the Mo^{6+} cations are distorted toward an edge (local C_2 direction), resulting in two short, two normal, and two long Mo–O bonds. The magnitude of the distortion (Δd) was calculated to be 1.52 and 1.02 for Mo(1) and Mo(2), respectively. The $[Te_3O_8]^{4-}$ anion composes of one Te(1)O_4 and two Te(2)O_3 groups interconnected by corner sharing (Scheme 1a). In the molybdenum tellurite chains, the lone pairs of the TeO_3 groups are aligned on the same side to produce a large macroscopic dipole moment in the compound (Fig. 25). SHG measurements revealed that $Ag_2Mo_3Te_3O_{16}$ displays a large SHG response of about 8 × KDP. From Fig. 25, we can see that the polarization of the two Mo(1)O_6 octahedra in the $[Mo_3O_{14}]^{10-}$ cluster are almost cancelled out whereas the polarization of the central Mo(2)O_6 octahedron is approximately along the *b*-axis. As for the $[Te_3O_8]^{4-}$ anion, the contributions from Te(2)O_3 groups almost cancelled each other, and that of the Te(1)O_4 group is polarized along the *b*-axis. Hence, the polarizations of both types of asymmetric polyhedra within the 1D $[Mo_3Te_3O_{16}]^{2-}$ anionic chain are "constructive" add. Therefore, the molybdenum tellurite chains are polar.

$Ag_2MoTe_4O_{12}$ (*C*2/c, CS) is isostructural with $Na_2MTe_4O_{12}$ (M = Mo, W), and its structure features a 3D anionic $[MoTe_4O_{12}]^{2-}$ network with Ag^+ ions filling the cavities of the structure. The Te(1)O_5 and Te(2)O_3 groups are interconnected into a 2D $[Te_4O_{10}]^{4-}$ anionic double layer perpendicular to the *a*-axis via corner- and

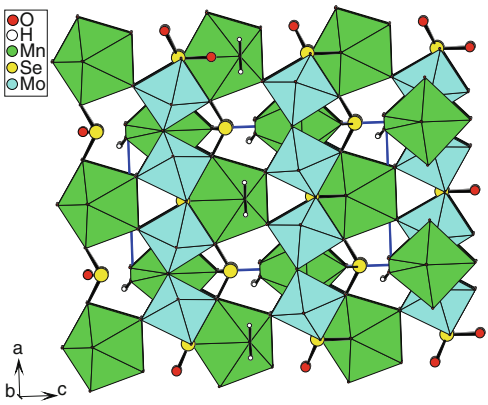

Fig. 26 View the structure of $Mn(MoO_3)(SeO_3)(H_2O)$ down the *b*-axis

edge sharing. These double layers are bridged by MoO_6 octahedra into a 3D anionic $[MoTe_4O_{12}]^{2-}$ network.

The structure of $Ag_6W_3Te_4O_{20}$ (*C*2/c, CS) exhibits a 3D anionic network composed of 2D W(2)–Te(1)–O layers being bridged by 1D W(1)–Te(2)–O chains with the silver(I) ions located at the cavities of the structure. Neighboring $W(1)O_6$ octahedra are bridged by pairs of $Te(2)O_4$ groups via corner sharing into a 1D anionic chain along the *c*-axis. Two $Te(1)O_4$ groups are interconnected to a Te_2O_6 dimer via edge sharing. $W(2)O_6$ octahedra are bridged by Te_2O_6 dimers to form a 2D layer parallel to the *bc* plane. The W(2)–Te(1)–O layers were further connected by the 1D W(1)–Te(2)–O chains to a 3D framework via Te(2)–O–W(2) bridges [58].

Our systematic explorations of new SHG materials in the divalent transition metal-Mo(VI)–Se(IV)/Te(IV)–O systems afforded seven new compounds, namely, $TM(MoO_3)(SeO_3)(H_2O)$ (TM = Mn, Co), $Fe_2(Mo_2O_7)(SeO_3)_2(H_2O)$, $Cu_2(MoO_4)(SeO_3)$, $Ni_3(MoO_4)(TeO_3)_2$, and $Ni_3(Mo_2O_8)(XO_3)$ (X = Se, Te) [66, 106].

Yellow brick-shaped crystals of $Mn(MoO_3)(SeO_3)(H_2O)$ were isolated by heating a mixture of 0.4 mmol MoO_3, 0.4 mmol $MnCO_3$, 1.2 mmol SeO_2, and 5 mL H_2O at 210°C. The structure of $Mn(MoO_3)(SeO_3)(H_2O)$ ($Pmc2_1$, NCS) features a complicated 3D network composed of MnO_7 polyhedra, MoO_6 octahedra, and SeO_3 polyhedra (Fig. 26). Its asymmetric unit contains two unique Mn atoms lying on mirror planes, one Mo in the general site, and two Se atoms sitting on mirror planes. Both Mn(1) and Mn(2) are seven coordinated by three selenite oxygens, one aqua ligand, and four oxoanions in a pentagonal bipyramid geometry. Mo(1) is octahedrally coordinated by two selenite oxygens, two terminal, and two bridging oxoanions. The MoO_6 octahedron is distorted toward an edge (local C_2 direction) with two "short," two "normal," and two "long" Mo–O bonds, and the magnitude of the distortion (Δd) was calculated to be 0.98. The MoO_6 octahedra are corner shared into a 1D Mo–O chain along the *a*-axis. MnO_7 polyhedra and SeO_3 groups are interconnected into a ladder-shaped 1D chain along the *a*-axis. The above two types of chains are further interconnected and alternating along *b* and *c*-axis, forming a complicated 3D network with 1D tunnels of Mn_2Mo_2Se 5-MRs and small tunnels of $MnMo_2$ 3-MR along the *b*-axis.

SHG measurements revealed that $Mn(MoO_3)(SeO_3)(H_2O)$ displays a moderate SHG signal of about three times of KDP [66].

Brown plate-shaped crystals of $Co(MoO_3)(SeO_3)(H_2O)$ were obtained by heating a mixture of 0.4 mmol MoO_3, 0.4 mmol $CoCl_2$, 1.2 mmol SeO_2, and H_2O (5 mL) at 210°C. Although $Co(MoO_3)(SeO_3)(H_2O)$ and $Mn(MoO_3)(SeO_3)(H_2O)$ have a similar formula, they display totally different structures. The structure of $Co(MoO_3)(SeO_3)(H_2O)$ (*P*-1, CS) features a 3D network composed of 1D molybdenum(VI) selenite chains bridged by CoO_6 octahedra with 1D 8-MR tunnels along the *a*-axis. The asymmetric unit of $Co(MoO_3)(SeO_3)(H_2O)$ is composed of two Co(II) atoms on inversion centers, one Mo(VI), one SeO_3^{2-} anion, and an aqua ligand on general sites. Both Co(1) and Co(2) are octahedrally coordinated by six oxygen atoms which is different from the seven-coordinated Mn(II) atoms in the $Mn(MoO_3)(SeO_3)(H_2O)$. The Mo(1) atom is octahedrally coordinated by two selenite oxygens, two terminal and two bridging oxoanions with three "short" and three "long" Mo–O bonds. Hence, the Mo(VI) cation is distorted toward a face (local C_3 direction) and the magnitude of the distortion (Δd) was calculated to be 1.248. The MoO_6 octahedra are interconnected into a 1D Mo–O chain along the *a*-axis via edge sharing, and the selenite anions are hanging on both sides of the chain. Within the molybdenum(VI) selenite chain, the polarization directions of the neighboring MoO_6 octahedra are opposite each other and the polarizations of the selenites are cancelled out. These centrosymmetric molybdenum(VI) selenite chains are further bridged by the CoO_6 octahedra into a 3D network with 1D 8-MR tunnels along the *a*-axis. The long narrow 8-MR tunnels are composed of 2 MoO_6 octahedra, 4 CoO_6 octahedra, and 2 selenites. The lone-pair electrons of the Se(IV) cations are orientated toward the center of the tunnels.

Red brick-shaped crystals of $Fe_2(Mo_2O_7)(SeO_3)_2(H_2O)$ were isolated by heating a mixture of 0.4 mmol MoO_3, 0.4 mmol Fe_2O_3, 1.2 mmol SeO_2, and H_2O (5 mL) at 230°C for 4 days. The structure of $Fe_2(Mo_2O_7)(SeO_3)_2(H_2O)$ (*C*2/c, CS) features a 3D architecture composed of iron(III) selenite layers interconnected by Mo_2O_{10} dimers. The asymmetric unit of $Fe_2(Mo_2O_7)(SeO_3)_2(H_2O)$ contains one FeO_6 octahedra, one MoO_6 octahedra, and one selenite anion. The MoO_6 octahedron is distorted toward an edge (local C_2 direction), displaying two "short," two "normal," and two "long" Mo–O bonds. The magnitude of the distortion (Δd) is calculated to be 1.45. Each pair of FeO_6 octahedra form a Fe_2O_{10} dimer via edge sharing, and such dimers are further bridged by selenite anions into a $\langle 100 \rangle$ layer. Two MoO_6 octahedra form a Mo_2O_{10} dimer by edge sharing. The above iron(III) selenite layers are further interconnected by the Mo_2O_{10} dimers via Mo–O–Fe bridges into a 3D framework with 1D 8-MR tunnels along the *b*-axis. The 8-MR is composed of 2 SeO_3, 2 FeO_6, and 4 MoO_6 groups. The lone pairs of the selenite groups are orientated toward the centers of the above tunnels.

$Cu_2(MoO_4)(SeO_3)$ was obtained by heating a mixture of 0.4 mmol MoO_3, 0.4 mmol CuO, 0.4 mmol SeO_2, and H_2O (5 mL) at 210°C for 4 days. The structure of $Cu_2(MoO_4)(SeO_3)$ ($P2_1/c$, CS) exhibits a 2D layer composed of 1D copper(II) oxide chains that are further bridged by SeO_3 groups and MoO_4 tetrahedra. Its asymmetric unit contains two CuO_5 square pyramids, one MoO_4 tetrahedron, and

one SeO_3 group. Two $Cu(2)O_5$ square pyramids are edge shared to $Cu(2)_2O_8$ dimers, and the latter are further bridged by the $Cu(1)O_5$ square pyramids to form a copper(II) oxide chain along the *c*-axis. Neighboring copper oxide chains are further bridged by SeO_3 anions and MoO_4 tetrahedra via corner sharing into a 2D layer parallel to the *bc* plane with 1D 5-MR tunnels along the *c*-axis. The unusual odd member ring is composed of 1 $Cu(1)O_5$ square pyramid, 2 $Cu(2)O_5$ square pyramids, 1 MoO_4 tetrahedron, and 1 SeO_3 group. The lone-pair electrons of the Se(IV) atoms are orientated toward the interlayer space. The interlayer *d*-spacing is about 8.15 Å [66].

Red prism-shaped crystals of $Ni_3(MoO_4)(TeO_3)_2$ were synthesized by solid-state reactions at 720°C: $3NiO + MoO_3 + 2TeO_2 \rightarrow Ni_3(MoO_4)(TeO_3)_2$. $Ni_3(MoO_4)(TeO_3)_2$ crystallizes in the NCS space group $P2_12_12_1$. Its structure features a novel 3D network of nickel(II) oxide with lager 1D tunnels along *a*-axis, the MoO_4 tetrahedra, and TeO_3 groups capped on walls of the tunnels. Among three unique nickel(II) ions in the asymmetric unit, Ni(1) and Ni(2) are octahedrally coordinated, whereas Ni(3) is in a square pyramidal geometry. $Ni(1)O_6$ and $Ni(2)O_6$ octahedra are alternately interconnected into a 2D layer parallel to the *ab* plane by edge sharing, whereas $Ni(3)O_5$ square pyramids are corner sharing into a 1D right-hand helical chain along the *a*-axis. The above 2D layers and the 1D chains are further interconnected via Ni(1)–O(4)–Ni(3) and Ni(2)–O(9)–Ni(3) bridges into a 3D network with large 12-MR tunnels along the *a*-axis. The tunnels are based on Ni_{12} rings. The MoO_4 tetrahedra and TeO_3 groups capped on walls of the tunnels [106]. SHG measurements indicate that the SHG signal of $Ni_3(MoO_4)(TeO_3)_2$ is much weaker than that of KDP. This is due to the fact that the Mo^{6+} in a tetrahedral geometry is not subject to SOJT distortion and the polarizations of the tellurite groups which capped on the walls of the large 12-MR tunnels have been mostly cancelled out.

Green brick-shaped crystals of $Ni_3(Mo_2O_8)(SeO_3)$ were initially prepared by the solid-state reaction of a mixture of Nd_2O_3 (0.35 mmol), MoO_3 (0.35 mmol), $NiCl_2$ (0.35 mmol), and SeO_2 (1.4 mmol) at 700°C for 5 days. Although Nd(III) is not present in the product, the addition of Nd_2O_3 helped the crystallization of $Ni_3(Mo_2O_8)(SeO_3)$, and the quality of the crystals is very poor when the synthesis was carried out in the absence of Nd_2O_3. The structure of $Ni_3(Mo_2O_8)(SeO_3)$ (*P*-1, CS) features a 3D network composed of $[Ni_6O_{22}]^{32-}$ cluster units that are interconnected by $[Mo_4O_{16}]^{8-}$ clusters and SeO_3^{2-} anions. There are three NiO_6 octahedra, two MoO_6 octahedra, and one SeO_3 group in the asymmetric unit. The Mo(VI) cations are distorted toward an edge (local C_2 direction) with two "short," two "normal," and two "long" Mo–O bonds. The magnitudes of the distortions (Δd) are calculated to be 1.18 and 1.29, respectively, for Mo(1) and Mo(2). Four MoO_6 octahedra are interconnected by edge sharing to form a cyclic $[Mo_4O_{16}]^{8-}$ tetranuclear cluster unit. Six NiO_6 octahedra are interconnected into ahexanuclear $[Ni_6O_{22}]^{32-}$ cluster unit through edge sharing. The $[Ni_6O_{22}]^{32-}$ cluster units are bridged by SeO_3^{2-} groups to form a 2D nickel selenite layer parallel to the *ab* plane. Neighboring nickel selenite layers are further interconnected by the $[Mo_4O_{16}]^{8-}$ clusters via Mo–O–Ni bridges into a 3D network structure. The lone pairs of the selenium(IV) atoms are orientated to the cavities of the structure.

Green brick-shaped crystals of $Ni_3(Mo_2O_8)(TeO_3)$ were prepared by the solid-state reaction of a mixture containing NiO (0.5 mmol), MoO_3 (0.5 mmol), and TeO_2 (1.5 mmol) at 720°C for 6 days. The structure of $Ni_3(Mo_2O_8)(TeO_3)$ is different from that of $Ni_3(Mo_2O_8)(SeO_3)$, although their chemical formulae are comparable. $Ni_3(Mo_2O_8)(TeO_3)$ (*C*2/m, CS) features a 3D structure in which the corrugated nickel-oxide anionic chains are bridged by $[Mo_4O_{16}]^{8-}$ cluster units and TeO_3^{2-} anions. As in $Ni_3(Mo_2O_8)(SeO_3)$, the Ni(II) and Mo(VI) cations are octahedrally coordinated by six oxygens. Similar to that in $Ni_3(Mo_2O_8)(SeO_3)$, the four MoO_6 octahedra in $Ni_3(Mo_2O_8)(TeO_3)$ are interconnected via edge sharing to form a $[Mo_4O_{16}]^{8-}$ tetranuclear cluster unit. Different is two $Ni(1)O_6$ and one $Ni(2)O_6$ octahedra are interconnected via edge sharing into a $[Ni_3O_{13}]^{20-}$ trinuclear unit. Neighboring such trinuclear units are further interconnected through edge sharing into a corrugated $[Ni_3O_{11}]^{16-}$ anionic chain along *b*-axis. This nickel oxide chain can also be viewed as $Ni(2)O_6$ octahedra being grafted onto the corrugated chain of $Ni(1)O_6$ through edge sharing. It is interesting to note that $[Ni_6O_{22}]^{32-}$ clusters are formed in $Ni_3(Mo_2O_8)(SeO_3)$, whereas corrugated $[Ni_3O_{11}]^{16-}$ anionic chains are observed in $Ni_3(Mo_2O_8)(TeO_3)$. Both nickel-oxide building units are based on Ni_3O triangles. The Ni_3O triangles in $[Ni_6O_{22}]^{32-}$ clusters are condensed via sharing Ni···Ni edges, whereas those in $[Ni_3O_{11}]^{16-}$ anionic chains are interconnected through pairs of Ni–O–Ni bridges. These different nickel(II) oxide architectures may result from the different coordination modes of the selenite and tellurite groups as well as the different ionic radii of Se(IV) and Te(IV). Neighboring corrugated nickel(II) oxide chains are bridged by TeO_3^{2-} anions to form a thick nickel(II) tellurite layer parallel to the *ab* plane. The thickness of the layer is about 12.1 Å. Such layers are further interconnected by the $[Mo_4O_{16}]^{8-}$ clusters via Mo–O–Ni bridges into a 3D network structure. The lone-pair electrons of the tellurium(IV) atoms are orientated to the tunnels of the structure [106].

3.1.4 p-Block Elements-d^0 TM–Se(IV)/Te(IV)–O System

The Tl^+, Pb^{2+}, and Bi^{3+} cations may also have stereoactive lone-pair electrons and can form asymmetric coordination environments. As for Ga^{3+}/In^{3+}, the cations of group IIIA, have an oxidation state of +3 as lanthanide(III) ions but their coordination geometries are more closer to those of transition metal ions. Thus, we deemed that these p-block main group cations in combinations with two other different kinds of SOJT cations may result in new compounds with new types of structures as well as different optical properties. So far such compounds are still rare.

Two NCS quaternary oxides, namely, $TlMVO_5$ (M = Se^{4+} or Te^{4+}) have been synthesized by hydrothermal techniques [63]. $TlMVO_5$ (M = Se^{4+} or Te^{4+}) crystallize in a polar space group $Pna2_1$, their structures feature a 3D framework composed of corner-shared VO_6 octahedra connected by asymmetric SeO_3 (or TeO_4) and TlO_8 polyhedra. Powder SHG measurements using 1,064 nm radiation revealed that $TlMVO_5$ (M = Se^{4+} or Te^{4+}) have SHG efficiencies of approximately 40 times of α-SiO_2, but they are nonphase matchable.

Four such tellurites, namely, $Bi_2WTe_2O_{10}$, $Bi_2W_3Te_2O_{16}$, $BiNbTe_2O_8$, $Pb_4M_{10}Te_6O_{41}$ (M = Nb^{5+} or Ta^{5+}) were reported in the Pb^{2+}/Bi^{3+}-d^0 TM–Se^{4+}/Te^{4+}–O systems [37, 107–109]. $Bi_2WTe_2O_{10}$ features 1D chains of $[WO_4(TeO_3)_2]^{4-}$ anions that are further interconnected by Bi^{3+} ions [107], whereas $Bi_2W_3Te_2O_{16}$ features triple-decker chains of $[W_3O_{10}(TeO_3)_2]^{4-}$, which are further interconnected by Bi^{3+} ions [108]. $BiNbTe_2O_8$ can be described as layers of corner-shared NbO_6 octahedra and fluorite-like sheets of BiO_8 distorted cubes capped by TeO_4 groups are further interconnected by TeO_3 pyramids via Nb–O–Te–O–Bi bridges [109]. $Pb_4M_{10}Te_6O_{41}$ (M = Nb^{5+} or Ta^{5+}) exhibits a 3D framework consisting of layers of corner-shared NbO_6 octahedra being further interconnected by TeO_3 and PbO_6 polyhedra [37].

Two new quaternary mixed metal oxide materials, namely, $InVTe_2O_8$ and $InVSe_2O_8$, have been synthesized by standard solid-state reactions in In^{3+}–V^{5+}–Se^{4+}/Te^{4+}–O systems [64]. $InVTe_2O_8$ crystallized in the centrosymmetric space group $P2_1/n$. Its structure is a 2D layer consisting of 1D chains of corner-shared InO_6 octahedra being further bridged by Te_4O_{12} tetramers and VO_4 tetrahedra. $InVSe_2O_8$ exhibits a totally different structure type although its formula is similar to that of $InVTe_2O_8$. $InVSe_2O_8$ crystallized in NCS polar space group *P*m, its structure is a 3D framework composed of 1D edge-shared InO_6 chains and 1D corner-shared VO_5 chains that are bridged by the SeO_3 anions. Powder SHG measurements, using 1,064-nm radiation, indicated that $InVSe_2O_8$ has a SHG efficiency ~30 times that of α-SiO_2 and it is nonphase matchable. The origin of the polarization in $InVSe_2O_8$ is thought to be from the local moments of the VO_5 square pyramids which were partly cancelled by the selenite groups [64].

Nine new quaternary phases in the p-block elements-d^0 TM–Se(IV)/Te(IV)–O systems, namely, $Pb_2V_2^{V}Se_2O_{11}$, $Pb_2V_3^{IV}Se_5O_{18}$, $Pb_2Nb_2^{V}Se_4O_{15}$, $Bi_2V_2^{V}Se_4O_{16}$, and $Bi_2Mo_2^{VI}Se_2O_{13}$, [110], and $Ga_2MoQ_2O_{10}$ (Q = Se, Te), $In_2Mo_2Se_2O_{13}(H_2O)$, and $In_2MoTe_2O_{10}$ [111], were isolated by our group. They exhibit eight different types of anionic structures.

$Pb_2V_2^{V}Se_2O_{11}$, $Pb_2V_3^{IV}Se_5O_{18}$, $Pb_2Nb_2^{V}Se_4O_{15}$, $Bi_2V_2^{V}Se_4O_{16}$, and $Bi_2Mo_2^{VI}Se_2O_{13}$ were hydrothermally synthesized by reactions of a mixture of PbO (or Bi_2O_3), V_2O_3 (or Nb_2O_5, MoO_3), and SeO_2 in 5–8 mL of distilled water, at 200 or 230°C for 4–5 days. It should be mentioned that the two vanadium(V) phases were formed through the oxidation of the V^{3+} ion. These compounds cannot be prepared by directly using the V_2O_5 as the V sources.

All five compounds contain three types of asymmetric building blocks: two types of cations with a lone pair and a distorted MO_6 (M = V, Nb, Mo) octahedron. Their structures belong to five different types. The structure of $Pb_2V_2^{V}Se_2O_{11}$ (*P*-1, CS) features 1D $[V_2O_5(SeO_3)_2]^{4-}$ chains that are further bridged by the Pb^{2+} cations into a 3D network. There are two PbO_5 square pyramids, two VO_6 octahedra, and two selenite anions in the asymmetric unit of $Pb_2V_2^{V}Se_2O_{11}$; hence, $Pb_2V_2^{V}Se_2O_{11}$ can also be formulated as $Pb_2V_2^{V}O_5(SeO_3)_2$. A pair of $V(1)O_6$ octahedra are interconnected by edge sharing to a $V(1)_2O_{10}$ dimer. Two $V(2)O_6$ octahedra are capping on the $V(1)_2O_{10}$ dimer to form a cyclic $[V_4O_{16}]^{12-}$ tetranuclear cluster unit. Neighboring $[V_4O_{16}]^{12-}$ tetranuclear cluster units are further interconnected by

$Se(2)O_3^{2-}$ groups via corner sharing into a 1D anionic chain of $[V_2O_5(SeO_3)_2]^{4-}$ along the *b*-axis, and the $Se(1)O_3^{2-}$ groups are hanging on both sides of the chain. Neighboring such chains are further bridged by lead(II) ions into a 3D network.

The structure of $Pb_2V_3^{IV}Se_5O_{18}$ (*P*nma, CS) features a 3D anionic framework of $[V_3Se_5O_{18}]^{4-}$ with the lead(II) cations being located at the 1D 8-MR tunnels along *b*-axis. There are two lead(II) ions located on the mirror plane, two V^{5+} ions with V(1) at a mirror plane and three selenite anions with Se(1) at a mirror plane in the asymmetric unit of $Pb_2V_3^{IV}Se_5O_{18}$; hence, $Pb_2V_3^{IV}Se_5O_{18}$ can also be formulated as $Pb_2(V^{IV}O)_3(SeO_3)_5$. The VO_6 octahedra are bridged by SeO_3 groups via corner sharing into a 3D anionic framework with two types of 1D 8-MR tunnels along the *b*-axis. One type of 1D 8-MR tunnel is based on 2 $V(1)O_6$ octahedra, 2 $V(2)O_6$ octahedra, 2 $Se(1)O_3$, and 2 $Se(3)O_3$ groups and the lone pairs of $Se(1)O_3$ and $Se(3)O_3$ groups are oriented toward its center. The other type of 1D 8-MR tunnel is based on 1 $V(1)O_6$ octahedra, 3 $V(2)O_6$ octahedra, 2 $Se(2)O_3$, 1 $Se(1)O_3$, and 1 $Se(3)O_3$ groups; the lone pair of $Se(2)O_3$ is oriented toward the center of the tunnel. The lead (II) ions are also located at the second type of 1D 8-MR tunnels.

The structure of $Pb_2Nb_2^{V}Se_4O_{15}$ (*C*2/c, CS) features novel niobium(V) oxy-selenite chains of $[Nb_2O_3(SeO_3)_4]^{4-}$ that are bridged by Pb^{2+} cations into a 3D network. The asymmetric unit of $Pb_2Nb_2^{V}Se_4O_{15}$ contains one severely distorted PbO_5 square pyramid, one NbO_6 octahedron, and two selenite anions. The NbO_6 octahedra are interconnected via corner sharing into a ladder-like double chain along the *c*-axis; $Se(2)O_3$ and $Se(1)O_3$ groups are grafted into the chain in a bidentate bridging and a unidentate fashion, respectively. The PbO_5 square pyramids are interconnected into a 2D layer parallel to the *bc* plane via corner- and edge sharing. The above two types of building units are further interconnected via Pb–O–Se–O–Nb bridges into a complicated 3D network with 1D tunnels of 8-MR along *c*-axis. The 1D 8-MR tunnels are based on 4 NbO_6 octahedra and 4 $Se(2)O_3$ groups, the lone pairs of the Se(2) atoms are oriented toward the center of the tunnel.

The structure of $Bi_2V_2^{V}Se_4O_{16}$ ($P2_1$/c, CS) features a 3D network composed of the 2D layer of $[Bi_2(SeO_3)_2]^{2+}$ and the 1D $[(VO_2)_2(SeO_3)_2]^{2-}$ chains. Its asymmetric unit contains two BiO_7 polyhedra, two VO_6 octahedra, and four selenite anions; hence, $Bi_2V_2^{V}Se_4O_{16}$ can also be formulated as $Bi_2(V^{V}O_2)_2(SeO_3)_4$. Neighboring $V(1)O_6$ and $V(2)O_6$ octahedra are interconnected via corner sharing into a 1D chain and a pair of such chains are further interconnected via edge sharing into a 1D double chain along the *b*-axis, $Se(3)O_3$, and $Se(4)O_3$ groups are grafted into the double chain in a bidentate bridging fashion. The BiO_7 polyhedra are interconnected to a 2D layer parallel to the *ac* plane via edge- and face sharing, $Se(1)O_3$ and $Se(2)O_3$ groups are capping on the both sides of the bismuth(II) oxide layer. The above two building units are further interconnected via Bi–O–Se bridges into a 3D architecture with narrow-long-shaped 10-MR tunnels along the *b*-axis.

$Bi_2Mo_2^{VI}Se_2O_{13}$ is isostructural to $Nd_2W_2Te_2O_{13}$ mentioned earlier [102], in which the two Nd^{3+} ions have been replaced by two Bi^{3+} ions and W^{6+} cations by Mo^{6+} cations. The structure of $Bi_2Mo_2^{VI}Se_2O_{13}$ (*P*-1, CS) features a 3D network of 3D bismuth selenite with the 10-MR tunnels along *a*-axis occupied by the Mo_2O_{10} clusters [110].

It should be mentioned that although the above compounds contain two types of lone-pair cations as well as d^0 transition metal ions, they are not SHG active due to their centrosymmetric structures.

Systematic explorations of new phases in the Ga^{III}/In^{III}–Mo^{VI}–Se^{IV}/Te^{IV}–O systems by hydrothermal reactions or solid-state reactions at high temperature led to four new quaternary compounds, namely, $Ga_2MoQ_2O_{10}$ (Q = Se, Te), $In_2Mo_2Se_2O_{13}(H_2O)$, and $In_2MoTe_2O_{10}$ [111].

$Ga_2MoQ_2O_{10}$ (Q = Se, Te) were obtained by heating a mixture of Ga_2O_3, MoO_3, SeO_2, (or TeO_2) at 200 or 230°C for 4 days. $Ga_2MoQ_2O_{10}$ (Q = Se, Te) (*P*nma, CS) are isostructural, and their features a novel 3D network in which 1D chains of the edge-shared GaO_6 octahedra are further interconnected by bridging QO_3^{2-} (Q = Se, Te) anions and MoO_6 octahedra. There are one GaO_6 octahedron, one MoO_6 octahedron and two QO_3 groups in the asymmetric unit. The GaO_6 octahedra are interconnected into a 1D chain along *b*-axis via edge sharing. Neighboring gallium oxide chains are further bridged by MoO_6 octahedra into a corrugated 2D layer passing through about 1/3 *c* and 2/3 *c* with $Q(2)O_3$ groups capping on the cavities of the layer. It should be noted that MoO_6 octahedra are bridged by $Q(2)O_3$ groups into a molybdenum tellurite chain parallel to *b*-axis via corner sharing. Hence, the corrugated 2D structure can also be described as a layer formed by gallium oxide chains and molybdenum tellurite chains that are alternating along *a*-axis. The above Ga–Mo–Te–O layers are further bridged by $Q(1)O_3$ groups into a 3D network with large 1D tunnels of $Ga_6Mo_2Q_4$ 12-member rings and small tunnels of Ga_2Q_2 four-member rings both along the *b*-axis. The lone pairs of the Q^{4+} cations are orientated toward the center of the large tunnels. Although the chemical compositions of $Ga_2MoQ_2O_{10}$ and $Nd_2MoSe_2O_{10}$ are comparable, their structures are quite different. In $Nd_2MoSe_2O_{10}$, the Nd^{3+} ions are eight-coordinated and the Mo^{6+} cation is tetrahedrally coordinated. $Nd_2MoSe_2O_{10}$ features a 3D network composed of alternating neodymium(III) selenite layers and neodymium(III) molybdate layers.

When the indium(III) oxide was used instead of gallium(III) oxide, $In_2Mo_2Se_2O_{13}(H_2O)$ and $In_2MoTe_2O_{10}$ were isolated. Rose-pink prism-shaped crystals of $In_2Mo_2Se_2O_{13}(H_2O)$ were obtained by heating a mixture of MoO_3 (0.5 mmol), In_2O_3 (0.5 mmol), SeO_2 (1.2 mmol), and H_2O (6 mL) at 200°C for 5 days. The structure of $In_2Mo_2Se_2O_{13}(H_2O)$ is isostructural to $Fe_2Mo_2Se_2O_{13}(H_2O)$ [66]. $In_2Mo_2Se_2O_{13}(H_2O)$ (*C*2/c, CS) can also be formulated as $In_2\{Mo_2O_7(H_2O)\}(SeO_3)_2$. Its structure features a pillared-layered structure in which the indium selenite layers are bridged by $Mo_2O_9(H_2O)$ dimers. Colorless prism-shaped crystals of $In_2MoTe_2O_{10}$ were obtained by heating a mixture of MoO_3 (0.3 mmol), In_2O_3 (0.25 mmol), TeO_2 (0.58 mmol), and H_2O (8 mL) at 230°C for 7 days. It should be note that the single phase powder sample of $In_2MoTe_2O_{10}$ was obtained by solid-state reaction of a mixture composed of MoO_3, In_2O_3, and TeO_2 in a molar ratio of 1:1:2. $In_2MoTe_2O_{10}$ ($P2_1/n$, CS) can also be formulated to be $In_2(MoO_4)(TeO_3)_2$ as in $Nd_2(MoO_4)(SeO_3)_2$. However, their structures are quite different. $In_2MoTe_2O_{10}$ features a 2D layered structure, which is built from indium oxide layers with MoO_4 and TeO_n ($n = 4, 5$) polyhedra hanging on both sides of the layer. The structure is composed of InO_7, InO_6, and MoO_6 octahedra as

well as TeO_3 groups. $In(1)O_7$ and $In(2)O_6$ polyhedra are interconnected via edge sharing into a dimer, such dimers are further interconnected via corner sharing into a indium(III) oxide layer. The MoO_4 and TeO_n ($n = 4, 5$) groups capped on both sides of the indium oxide layer. The lone pairs of the Te^{4+} cation are orientated toward the interlayer space. The interlayer distance is about 9.0 Å. There are also weak interlayer Te–O bonds (2.512(8) Å). It is interesting to note that the $Te(1)O_4$ group is "isolated," whereas $Te(2)O_5$ groups are interconnected via corner sharing into 1D tellurium(IV) oxide "zigzag chain" along *b*-axis.

These four compounds are also not SHG active since they are structurally centrosymmetric; hence, polarizations of asymmetric MoO_6 octahedra and selenite or tellurite groups have been completely cancelled out.

3.2 Metal Selenites or Tellurites Containing Halogen Anions

It is reported that the transition metal selenites or tellurites containing halogen anions can display many types of novel structures and interesting magnetic properties such as low dimensional magnets, etc. Transition metal Te(IV) or Se(IV) oxyhalides can be regarded as so-called "chemical scissors" [112, 113]. The later transition metal cations form bonds to both oxygen and halide, whereas lone-pair cations tend to form bonds only to oxygen anions. Such chemical difference can be utilized to prepare low dimensional transition metal materials with interesting magnetic properties [112, 113]. Furthermore, it is well known that the introduction of halogen anions can widen the transparency of NLO materials in the UV region as in $KBe_2BO_3F_2$ (KBBF) [114]. Recent studies also show that the introduction of the halogen anions into the lead(II) borates can significantly enhance the SHG efficiency of the inorganic compounds [115]. So far, a few of compounds in metal Te(IV) or Se(IV) oxyhalides have been reported, some of which exhibit NCS structures. For example, $Bi_4Te_2O_9Br_2$ crystallizes in the polar space group *P*mm2, and it also displays pyroelectric property. Its structure features a 2D layer of $[Bi_4Te_2O_9]^{2+}$ separated by bromine anions [116]. $BaCu_2Te_2O_6Cl_2$ crystallized in the polar space group $P2_1$, its structure is a 3D network composed of edge-shared $Cu(1)Cl_2O_3$ and $Cu(2)ClO_4$ square pyramidal dimers bridged by $Te(1)O_3$ and $Te(2)O_4$ groups with the Ba^{2+} cations being located at the cavities of the structure [117].

Based on above reasons, we have performed systematic explorations in the transition metal or lanthanide transition metal Te(IV) or Se(IV) oxyhalide systems, 12 new compounds were isolated by solid-state reactions at high temperatures, including $\{Cd_2(Te_6O_{13})\}\{Cd_2Cl_6\}$, $Cd_7Cl_8(Te_7O_{17})$ [118], $Ni_5(SeO_3)_4Cl_2$, $Ni_5(SeO_3)_4Br_2$, $Ni_7(TeO_3)_6Cl_2$, $Ni_{11}(TeO_3)_{10}Cl_2$, [119, 120], $DyCuTe_2O_6Cl$, $ErCuTe_2O_6Cl$, $ErCuTe_2O_6Br$, $Sm_2Mn(Te5O_{13})Cl_2$, $Dy_2Cu(Te_5O_{13})Br_2$, and $Nd_4Cu(TeO_3)_5Cl_3$ [121]. Among these compounds, $Cd_7Cl_8(Te_7O_{17})$ and $Nd_4Cu(TeO_3)_5Cl_3$ crystallized in polar space group.

$[Cd_2(Te_6O_{13})][Cd_2Cl_6]$ was obtained quantitatively by the reaction of a mixture of $CdO/CdCl_2/TeO_2$ in a molar ratio of 1: 3: 6 at 670°C for 6 days. The structure of $[Cd_2(Te_6O_{13})][Cd_2Cl_6]$ (*P*-1) features cationic cadmium(II) tellurium(IV) oxide layers parallel to *ab* plane and "isolated" anionic cadmium(II) chloride double chains along the *a*-axis. The $[Cd_2Cl_6]^{2-}$ double chain passing through the cell edge is formed by edge-shared $Cd(3)Cl_6$ and $Cd(4)Cl_6$ octahedra. The cadmium (II) tellurium(IV) oxide layer in $[Cd_2(Te_6O_{13})][Cd_2Cl_6]$ is formed by novel 1D slabs of $Te_6O_{13}^{2-}$ anions interconnected by Cd–O double chains. $Te(1)O_4$, $Te(2)O_4$, and $Te(3)O_4$ groups are interconnected via corner- and edge sharing into a trinuclear unit, and neighboring units are corner shared into a 1D chain along the *a*-axis. Two $Te(5)O_5$ and two $Te(6)O_3$ groups form a tetranuclear unit via corner- and edge sharing. The above 1D chains and tetranuclear units are bridged by $Te(4)O_4$ groups, through corner sharing, into a 1D $Te_6O_{13}^{2-}$ slab, forming six- and seven-member polyhedral rings (Scheme 1f). The width of the slab is about 14.6 Å. The lone-pair electrons of the Te(IV) atoms are oriented toward the open space between the cadmium chloride chains and cadmium tellurium(IV) oxide layers.

Colorless crystalline sample of $Cd_7Cl_8(Te_7O_{17})$ was then obtained quantitatively by the reaction of a mixture of $CdO/CdCl_2/TeO_2$ in a molar ratio of 3/4/7 at 720°C for 6 days. $Cd_7Cl_8(Te_7O_{17})$ crystallized in a polar space group $Pca2_1$, its structure features a 3D network composed of different tellurium(IV) oxide and cadmium chloride substructures with long narrow tunnels along the *b*-axis. The two structural building blocks are 1D $[Te_7O_{17}]^{6-}$ anions and unusual corrugated $[Cd_7Cl_8]^{6+}$ layers based on cyclohexane-type Cd_3Cl_3 rings. The $Te_7O_{17}^{6-}$ anion features a 1D architecture different from that of the $Te_6O_{13}^{2-}$ anion in $[Cd_2(Te_6O_{13})][Cd_2Cl_6]$. Only two types of tellurium(IV) oxide polyhedra are found: TeO_3 for Te(7) and TeO_4 for the remaining six tellurium atoms. TeO_3 and TeO_4 groups are interconnected via corner sharing into another type of 1D slab, forming two types of six-member polyhedral rings and one type of three-member polyhedral ring (Scheme 1g). The three-member ring is composed of three TeO_4 groups. One type of the six-member ring is formed by solely TeO_4 groups in a "pear" shape, whereas the other type is made of two TeO_3 and four TeO_4 groups. The width of this 1D slab is 12.1 Å, which is slightly narrower than that of the $Te_6O_{13}^{2-}$ anion in $[Cd_2(Te_6O_{13})][Cd_2Cl_6]$. In contrast to those in $[Cd_2(Te_6O_{13})][Cd_2Cl_6]$, the Cd and Cl atoms in $Cd_7Cl_8(Te_7O_{17})$ are interconnected to a novel corrugated 2D layer parallel to the *bc* plane. The layer is based on distorted cyclohexane-type Cd_3Cl_3 rings. These 2D layers can be viewed as the result of removing 1/8 of Cd(II) ions from a perfect "Cd_8Cl_8" 2D layer leaving vacant Cd_6Cl_6 rings. The above two types of building units are interconnected via Te–O–Cd bridges into a 3D network with long narrow tunnels along the *b*-axis. The stereoactive lone pairs of the Te(IV) atoms are oriented toward the narrow tunnels [118]. The polarization directions of tellurite groups are almost opposite, resulting in mostly cancellation of the local dipole moments, which is also confirmed by a very weak SHG response we measured recently.

When Ni(II) halide was used instead of Cd(II) halide, four different structures with a general formula of $Ni_{n+1}(QO_3)_nX_2$ (Q = Se, X = Cl, Br, $n = 4$; Q = Te, X = Cl, $n = 6$, 10) were isolated.

$Ni_5(SeO_3)_4Cl_2$ was prepared by solid-state reaction of 0.4 mmol of $NiCl_2$, 0.8 mmol of Ni_2O_3, and 1.6 mmol of SeO_2 at 700°C for 6 days. $Ni_5(SeO_3)_4Cl_2$ (*P*-1, CS) features a 3D network formed by the interconnection of nickel(II) octahedra via corner-, edge- and face sharing with Se^{4+} ions capping on its cavities. Such a structure is different from $Ni_5(TeO_3)_4Cl_2$ with a similar formula. $Ni_5(TeO_3)_4Cl_2$ exhibits a layered structure composed of corner-, edge- and face shared 2D Ni(II) octahedral layer capped by TeO_3 groups on the both sides [119].

Red brick-shaped single crystals of $Ni_5(SeO_3)_4Br_2$ were prepared by the solid-state reaction of a mixture containing Ni_2O_3 (1.2 mmol), $NiBr_2$ (0.6 mmol), and SeO_2 (2.4 mmol) at 670°C for 6 days. $Ni_5(SeO_3)_4Br_2$ (*P*-1, CS) features a 3D network different from that of $Ni_5(SeO_3)_4Cl_2$. Its 3D structure can be viewed as nickel(II) oxy-bromide layers that are bridged by Se(IV) and additional Ni(II) ions. $Ni(1)O_5Br$ and $Ni(3)O_5Br$ octahedra are interconnected via edge sharing into a 1D chain, and neighboring chains are further interconnected via corner sharing into a layered architecture. The above 2D nickel oxybromide layers are further interconnected by Ni(2) and Se(IV) atoms into a condensed 3D network. Such a 3D network can also be viewed as a pillared layered structure in which Ni(2) and selenite groups act as pillars [120].

Green brick single crystals of $Ni_7(TeO_3)_6Cl_2$ and orange plates of $Ni_{11}(TeO_3)_{10}Cl_2$ were obtained from a same solid-state reaction of a mixture of NiO (2.4 mmol), $NiCl_2$ (0.6 mmol), and TeO_2 (1.8 mmol) at 710°C for 6 days. The structure of $Ni_7(TeO_3)_6Cl_2$ (*R*-3, CS) features a novel 3D network based on Ni_4ClO_3 cubane-like clusters with Te atoms located at the cavities of the network. Three $Ni(1)O_5Cl$ moieties and one $Ni(2)O_6$ unit forms a Ni_4ClO_3 cubane-like cluster via O···O and O···Cl edge sharing. The four nickel(II) ions within the Ni_4ClO_3 cluster displays a slightly distorted tetrahedron. Each pair of cubanes are condensed into a dimeric unit by sharing a Ni(2) atom. Along the *ab* plane, the Ni_4ClO_3 cubanes are interconnected via edge sharing into a novel 2D cluster layer, forming 12-member polyhedral rings. Each ring is composed of six Ni_4ClO_3 cubanes; hence, such cubane cluster layers are to some extent similar to those of graphite. Neighboring 2D layers are interconnected by sharing Ni(2) atoms into a 3D network with small long-narrow-shaped tunnels along the *a*-axis. The Te atoms are located at the above tunnels and connected to the cubanes via Te–O–Ni bridges. It should be pointed out that such stacking of the cluster layers eliminates the large tunnels along *c*-axis created by 12-member rings.

The structure of $Ni_{11}(TeO_3)_{10}Cl_2$ (*P*-1, CS) features a very complicated 3D network. There are six unique nickel(II) ions, five tellurite groups, and one chloride anion in its asymmetric unit. The interconnection of NiO_5Cl, NiO_6, and NiO_5 polyhedra via corner- and edge sharing led to a complex 3D network of nickel oxychloride. The Te(IV) atoms are located at the voids of the network and also connect with the framework through Ni–O–Te bridges. The 3D nickel oxychloride network can also be considered as a pillared layered architecture based on the nickel oxide layers composed of Ni(2), Ni(3), Ni(4), and Ni(5). Each pair of $Ni(1)O_5Cl$ octahedra form a dimeric unit via edge sharing; these dimers act as pillars between two neighboring nickel oxide layers.

It is interesting to note that the four nickel(II) compounds can be generally formulated as $Ni_{n+1}(QO_3)_nX_2$, where Q and X represent Se(or Te) and halide anion, respectively. Also, the nickel sites may be partially occupied when *n* is large such as in $Ni_{11}(TeO_3)_{10}Cl_2$. It is also noted that change of halide anion or change of selenite anion by tellurite anion may lead to complete different structural types even though their compounds have similar chemical formulae.

When lanthanide(III) ion was introduced into transition metal Te(IV) or Se(IV) oxyhalides, six new lanthanide transition metal tellurium(IV) oxyhalides were obtained, namely, $DyCuTe_2O_6Cl$, $ErCuTe_2O_6Cl$, $ErCuTe_2O_6Br$, $Sm_2Mn(Te_5O_{13})Cl_2$, $Dy_2Cu(Te_5O_{13})Br_2$, and $Nd_4Cu(TeO_3)_5Cl_3$. They form three different structural types [121].

$DyCuTe_2O_6Cl$, $ErCuTe_2O_6Cl$, and $ErCuTe_2O_6Br$ ($P2_1/c$, CS) are isostructural. They were prepared by the solid-state reaction of a mixture of Dy_2O_3 (or Er_2O_3), CuO, $CuCl_2$ (or $CuBr_2$), and TeO_2 at 750 or 720°C. They feature a 3D network structure. LnO_8 polyhedra are interconnected via edge sharing into a 1D lanthanide (III) oxide chain along the *a*-axis. Each pair of CuO_4Cl polyhedra is bridged by a pair of tellurite groups to form a 1D chain along the *a*-axis. The interconnection of LnO_8 and CuO_4Cl polyhedra via bridging tellurite groups led to a 3D network with apertures running along the *a*-axis. These apertures are formed by ten polyhedral rings composed of 4 Dy, 4 Cu, and 2 tellurite anions. The halide anions and the lone pairs of the tellurium(IV) atoms are orientated toward the above apertures.

Single crystals of $Sm_2MnTe_5O_{13}Cl_2$ and $Dy_2CuTe_5O_{13}Br_2$ were obtained from the solid-state reactions of a mixture containing Sm_2O_3 (or Dy_2O_3), MnO_2 (or CuO), $MnCl_2$ (or $CuBr_2$), and TeO_2 at 750°C for 6 days. $Sm_2MnTe_5O_{13}Cl_2$ and $Dy_2CuTe_5O_{13}Br_2$ ($P2_1/n$, CS) are isostructural and their structures feature a 3D network of lanthanide transition metal tellurite with long, narrow-shaped tunnels occupied by the isolated halides. TeO_3 and TeO_4 polyhedra are interconnected via corner- and edge sharing to form two different tellurium(IV) oxide anions: $Te_3O_8^{4-}$ and $Te_4O_{10}^{4-}$. In $Te_4O_{10}^{4-}$, two TeO_4 form a dimeric unit by edge sharing, and the dimer further corner shares with two TeO_3 groups. $Te_3O_8^{4-}$ is composed of three corner-sharing TeO_3 groups. The interconnection of the Sm^{III} (or Dy^{III}) ions and Mn^{II} (or Cu^{II}) ions by $Te_3O_8^{4-}$ and $Te_4O_{10}^{4-}$ anions results in a 3D network with tunnels running along the *b*-axis. The halide anions remain isolated and are located at the above tunnels. The lone-pair electrons of the tellurium(IV) atoms are also oriented toward the tunnels.

$Nd_4Cu(TeO_3)_5Cl_3$ was obtained as a single phase by the following reactions at 650°C: $2NdOCl + Nd_2O_3 + CuCl + 5TeO_2 \rightarrow Nd_4CuTe_5O_{15}Cl_3$. $Nd_4Cu(TeO_3)_5Cl_3$ crystallizes in the polar space group *I*2, its structure features a 3D network of neodymium(III) tellurite with large tunnels in which 1D chains of copper(I) chloride are inserted. The interconnection of Nd(III) ions by bridging and chelating tellurite groups led to a 3D network with large tunnels along the *b*-axis. The tunnels are formed by 16-membered polyhedral rings composed of 8 TeO_3 and 8 Nd atoms. The lone-pair electrons of the tellurite groups are located at the above tunnels. Neighboring $CuCl_4$ tetrahedra are interconnected via corner sharing into a 1D two-unit repeating (zweier) chain along the *b*-axis. These copper(I) chloride chains are inserted in the centers of the above tunnels and form Cu–Cl–Nd bridges.

In this structure, the polarizations of $Te(2)O_3$, $Te(3)O_3$, $Te(4)O_3$, and $Te(5)O_3$ groups are mostly cancelled out but the polarizations of $Te(1)O_3$ groups are aligned in the same direction to produce a moderate net dipole moment along the *b*-axis [121]. Unfortunately, no SHG measurements for this compound have been made.

3.3 *Metal Tellurites and Selenites Containing Tetrahedral Groups of Main Group Elements*

Tetrahedral groups of main group elements, such as PO_4, BO_4, SiO_4, may also be SHG active and induce the formation of the NCS structures. Hence, metal tellurites and selenites containing additional tetrahedral groups may lead to the formation of new NCS structures with excellent SHG properties. So far such compounds are still rare and mainly focused on tellurite phosphates, namely, $Te_2O_3(HPO_4)$, $Te_8O_{10}(PO_4)_4$, $Te_3O_3(PO_4)_2$, $Te_2O(PO_4)_2$, $Ba_2TeO(PO_4)_2$, $BaTeMO_4(PO_4)$ ($M = Nb^{5+}$ or Ta^{5+}), and $A_2TeMo_2O_6(PO_4)_2$ ($A = K$, Rb, Cs, or Tl) [65, 122–127]. In these compounds, only $Te_2O_3(HPO_4)$ ($Pca2_1$, NCS) and $Te_2O(PO_4)_2$ (Cc, NCS) crystallized in polar space groups. The structure of $Te_2O_3(HPO_4)$ features a 3D framework composed of 2D $Te_2O_3^{2+}$ cationic layer bridged by PO_4 tetrahedra. In this structure, the polarizations of $Te(2)O_4$ groups are toward almost opposite directions, whereas the polarizations of $Te(1)O_4$ groups are align in the same direction; hence, a net dipole moment is produced [122]. $Te_2O(PO_4)_2$ shows a 3D framework structure composed of slightly distorted TeO_5 square pyramids and PO_4 tetrahedra. The polarization directions of $Te(1)O_5$ and $Te(2)O_5$ groups are almost opposite, resulting the cancellation of most of their local dipole moments. SHG measurements reveal that $Te_2O(PO_4)_2$ displays a weak SHG efficiency of approximately 50 × α-SiO_2 [65].

Our explorations in such systems by solid-state reactions and hydrothermal syntheses afford four new compounds with different structures, namely, two novel lanthanum(III) tellurites with additional SiO_4 or GeO_4 tetrahedra ($La_4(Si_{5.2}Ge_{2.8}O_{18})(TeO_3)_4$ and $La_2(Si_6O_{13})(TeO_3)_2$) [128], one selenite with BO_4 tetrahedra ($B_2Se_2O_7$) [14] and one tellurite with GaO_4 tetraheda ($Ga_2Te_3O_9$) [67]. Both $B_2Se_2O_7$ and $Ga_2Te_3O_9$ crystallized in NCS structure and are SHG active.

$La_4(Si_{5.2}Ge_{2.8}O_{18})(TeO_3)_4$ was initially obtained by solid-state reaction of La_2O_3 (0.4 mmol), GeO_2 (0.4 mmol), TeO_2 (1.2 mmol), with 0.4 mmol of CsCl as flux in an evacuated quartz tube at 800°C for 6 days. Si element came from the silica tube. The structure of $La_4(Si_{5.2}Ge_{2.8}O_{18})(TeO_3)_4$ (P-1, CS) features a 3D network composed of the $[(Ge_{2.82}Si_{5.18})O_{18}]^{4-}$ layers and the $[La_4(TeO_3)_4]^{4+}$ layers that alternating along *b*-axis. The germanate-silicate layer consists of corner-shared XO_4 ($X = Si/Ge$) tetrahedra, forming four- and six-member rings. The 2D $[La_4(TeO_3)_4]^{4+}$ layer is formed by lanthanide(III) ions bridged by TeO_3 groups.

$La_2(Si_6O_{13})(TeO_3)_2$ was prepared by solid-state reaction of La_2O_3 (0.4 mmol), SiO_2 (1.6 mmol), and TeO_2 (0.8 mmol) at 960°C for 6 days. The structure of $La_2(Si_6O_{13})(TeO_3)_2$ ($P2_1/c$, CS) is a 3D network composed of the $[Si_6O_{13}]^{2-}$ double layers and the $[La_2(TeO_3)_2]^{2+}$ layers that alternate along *a*-axis. The $[Si_6O_{13}]^{2-}$ double layer is built by corner sharing SiO_4 tetrahedra, forming four-, five-, and eight-member rings. The $[La_2(TeO_3)_2]^{2+}$ layer perpendicular to the *a*-axis is similar to that in $La_4(Si_{5.2}Ge_{2.8}O_{18})(TeO_3)_4$. The TeO_3^{2-} anions in both compounds are only involved in the coordination with the La^{3+} ions to form a lanthanum(III) tellurite layer [128].

Compounds containing both borate anion and selenium(IV) may also possess good SHG properties due to the presence of two types of SHG active groups. So far, $B_2Se_2O_7$, prepared by our group is the only such example. Single crystals of $Se_2B_2O_7$ were isolated quantitatively by the solid-state reaction of B_2O_3 (1.2 mmol) and SeO_2 (2.4 mmol) at 320°C in an evacuated quartz tube. The structure of $Se_2B_2O_7$ ($P2_12_12_1$, NCS) features a 3D network in which B_2O_7 dimers composed of two corner sharing BO_4 tetrahedra are bridged by SeO_3 groups (Fig. 27). The open framework of $Se_2B_2O_7$ can also be described as an interesting mixed (3,4)-connected net of the B and Se (linked by –O– bridges). Right-handed helical tunnels along *c*-axis are formed. These tunnels are based on B_6Se_4 10-member rings. The lone pairs of the Se^{IV} cations are orientated toward the above tunnels. $B_2Se_2O_7$ exhibits a moderate strong SHG efficiency of about 2.2 times of KDP [14].

Many efforts were tried to prepare $Te_2B_2O_7$, the analog of $Se_2B_2O_7$, but were unsuccessful. Probably it is due to too large difference between the distance of Te–O and B–O bonds. We therefore tried to prepare the gallium tellurites. Two isomeric gallium(III) tellurites, namely, α-$Ga_2(TeO_3)_3$ and β-$Ga_2(TeO_3)_3$ were isolated [67].

The two compounds were hydrothermally synthesized by reactions of a mixture of Ga_2O_3 (0.2 mmol), TeO_2 (0.6 mmol), and Li_2CO_3 (0.10 mmol for α-$Ga_2(TeO_3)_3$ or 0.25 mmol for β-$Ga_2(TeO_3)_3$) in 6 mL of distilled water at 230°C for 7 days. It is found

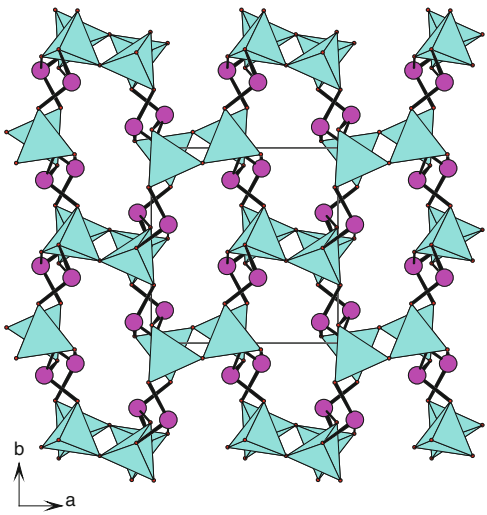

Fig. 27 View of the structure of $Se_2B_2O_7$ down the *b*-axis. BO_4 tetrahedra are shaded in *cyan*. Se, B and O atoms are drawn as *pink*, *cyan* and *red circles*, respectively

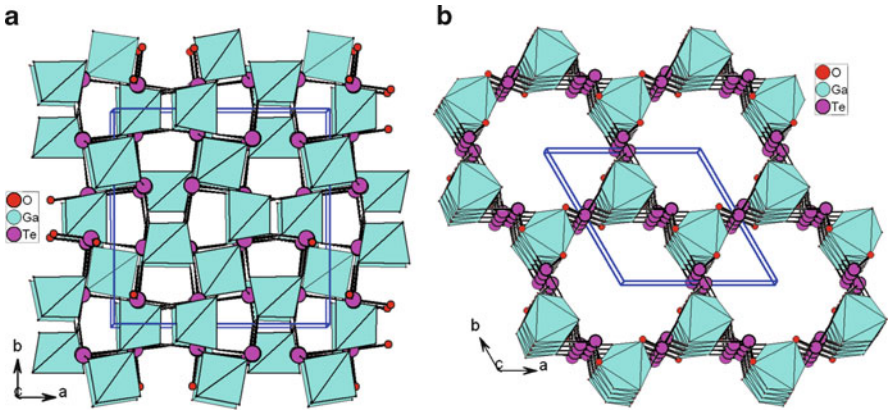

Fig. 28 View of the structure of α-$Ga_2(TeO_3)_3$ (**a**) and β-$Ga_2(TeO_3)_3$ (**b**) down the *c*-axis

that the amount of Li_2CO_3 added is very important to the chemical compositions and structures of the products formed. If 0.10 mmol Li_2CO_3 was used, the noncentrosymmetric α-$Ga_2(TeO_3)_3$ was isolated. When the amount of Li_2CO_3 used was increased to 0.25 mmol, centrosymmetric β-$Ga_2(TeO_3)_3$ was isolated in a very low yield. The structure of acentric α-$Ga_2(TeO_3)_3$ (*I*-43d) features a close packing 3D network with alternatively linkage of GaO_4 tetrahedra and TeO_3 trigonal pyramids via corner sharing (Fig. 28a). The structure of centrosymmetric β-$Ga_2(TeO_3)_3$ ($P6_3/m$) features a 3D open framework with 1D 12-MR tunnels along the *c*-axis. Different from the α phase, the gallium(III) ion in the β phase is octahedrally coordinated. Two GaO_6 octahedra are interconnected to a Ga_2O_9 dimer via face sharing, and such dimers are bridged by the TeO_3 groups into a 1D gallium tellurite chain along the *c*-axis. The above chains are further linked by additional TeO_3 groups into a 3D open framework with 1D 12-MR tunnels along the *c*-axis (Fig. 28b). The internal diameter of the channel is 7.983 Å (about 0.8 nm). SHG measurements on a Q-switched Nd:YAG laser with the sieved powder samples revealed that α-$Ga_2(TeO_3)_3$ displays a moderate-strong SHG response about that of KDP [67].

4 Conclusions and Outlook

In summary, the syntheses, structures, and SHG properties of metal iodates, selenites, and tellurites with lone-pair electrons containing d^0 TM cations, other lone pairs and tetrahedral groups were reviewed. Combination of two or more types of asymmetric units into a same compound not only can gives rise to a rich structural chemistry but also may afford many *NCS* compounds with excellent SHG properties. As for the direction of the out-of-center distortion, it was found that V^{5+} and Nb^{5+} usually displace toward an edge or corner, whereas Mo^{6+} and

W^{6+} are more likely distorted toward an edge or face. V^{5+} cation may adopt the square pyramidal geometry beside tetrahedron and octahedron, whereas Mo^{6+} and W^{6+} are usually tetrahedrally or octahedrally coordinated. Furthermore, V^{5+} cation is not as stable as other d^0 TM cations, and on some occasions it can be reduced to V^{4+} during the reaction. The bond polarization follows the following order of I (V) > Te(IV) > Se(IV), and $Mo^{6+} > V^{5+} > W^{6+} > Nb^{5+} > Ta^{5+}$. Furthermore, the counterions also have dramatic effects on the structural topologies and the SHG properties of the compounds formed. The slight change of the ionic radius of the cation such as A(I) or lanthanide(III) ion could lead to a completely different structure as exampled by $A_2W_3TeO_{12}$ ($A = K^+$, Rb^+, and Cs^+) and $Ln_2MoTe_3O_{12}$ (Ln = La, Nd). $A(VO)_2O_2(IO_3)_3$ ($A = K^+$, Rb^+, Cs^+, NH_4^+) are isostructural but their SHG responses follow a sequence as below, K > Rb > Cs > NH_4. The isostructural compounds of $Ln_3Pb_3(IO_3)_{13}(\mu^3\text{-}O)$ (Ln = La, Pr, Nd) display SHG signals that about 2.0, 1.0, and 0.8 times of KDP, respectively, whereas the SHG signal for the cerium compound is very weak. With respect to synthesis, molar ratios of the starting materials, synthetic methods, and reaction temperatures are also very important to the chemical compositions, structures, and physical properties of materials formed. For example, the amount of Li_2CO_3 controlled whether noncentrosymmetric cubic phase α-$Ga_2(TeO_3)_3$ or centrosymmetric hexagonal phase β-$Ga_2(TeO_3)_3$ is isolated.

As for the different anions, it is worthy to mention that I(V) mainly appears as IO_3 group, but polymeric anionic clusters such as $I_3O_8^-$ in NaI_3O_8 and layered $I_4O_{11}^{2-}$ anion in $Cs_2I_4O_{11}$ are also possible. The Se(IV) cation mainly exists as SeO_3 group (in some cases as the diselenite group), whereas Te(IV) can be 3-, 4-, or 5-coordinated, and the most amazing aspect is that these TeO_x (x = 3–5) polyhedra can be polymerized into many types of polynuclear clusters or extended skeletons (Scheme 1) besides ditellurite anion. Inorganic solids with various polymeric tellurium(IV) oxide anions include $Te_3O_8^{4-}$ trimer in $La_2MoTe_3O_{12}$, $Te_4O_{11}^{6-}$ tetramer in $Er_2Te_4O_{11}$,[29] $Te_5O_{13}^{6-}$ pentamer in $Ln_5MTe_7O_{23}Cl_3$ (Ln = Pr, Nd; M = Mo, W), 1D $Te_4O_{10}^{4-}$ in $Ln_2MoTe_4O_{14}$ (Ln = Pr, Nd), 1D $Te_6O_{13}^{2-}$ in $\{Cd_2(Te_6O_{13})\}\{Cd_2Cl_6\}$ and 1D $Te_7O_{17}^{6-}$ in $Cd_7Cl_8(Te_7O_{17})$, layered $Te_3O_7^{2-}$ in $La_2WTe_6O_{18}$, 1D $[Te_4O_9(OH)]^{3-}$ in $Ba_2(VO_3)Te_4O_9(OH)$, 1D TeO_3^{2-} in $Cs_3Nb_9O_{18}(TeO_3)_2(TeO_4)_2$, 2D $Te_4O_9^{2-}$ in $K_2Te_4O_9{\cdot}3.2H_2O$ and 2D $Te_2O_5^{2-}$ in $Ln(Te_2O_5)X$ (Ln = Nd, X = Cl, Br; Ln = Gd, X = Cl) [14], etc. Certainly more such examples will be discovered in the future and extensive theoretical studies are needed to understand its origin.

Based on this review, several opportunities and challenges are apparent. For d^0 TM–I(V)–O system, no metal iodates containing W(VI) or Ta(V) cation has been reported because of the synthetic difficulties, and only one Nb(V) iodate is reported. For the metal iodates containing other lone pairs, there is no metal iodates with lone pair-containing Sb(III), Sn(II), Se(IV), or Te(IV) reported, and little is known about the bismuth iodates except two centrosymmetric $Bi(IO_3)_3$ and $Bi(IO_3)_3(H_2O)_2$. With respect to metal selenites or tellurites, the combination of lone pair Te(IV) or Se(IV) with borate is quite promising in searching for new SHG materials. Very recently, a series of alkali metal boroselenites were synthesized by solid-state reactions in our group, some of which crystallized in NCS structures and display

excellent SHG properties due to the polarizations from both B–O polyhedra and SeO_3 groups. Furthermore, metal Te(IV) or Se(IV) oxyhalides are mainly focused on low dimensional magnets before, and their SHG properties have been somewhat overlooked. Some metal Te(IV) oxyhalides reported crystallized in polar structures but their NLO properties have not been studied.

Also the crystal growth for the compounds with excellent SHG properties is also very important for practical applications. Large single crystals of $BaMo_2TeO_9$, $Na_2W_2TeO_9$, and $Cs_2Mo_3TeO_{12}$ have been obtained and their physical properties studied in more details; however, large single crystals for other SHG compounds remain to be grown and their physical properties studied more deeply. To fully address these problems, strong interactions between synthetic and theoretical chemists as well as materials chemists are necessary.

Acknowledgments This work was supported by the National Natural Science Foundation of China (Grants Nos. 20731006, 20825104, 21001107, and 20821061), NSF of Fujian Province (Grant 2011J05037) and Key Laboratory of Optoelectronic Materials Chemistry and Physics, Chinese Academy of Sciences (Grant No 2008DP173016).

References

1. Chen CT, Liu G (1986) Annu Rev Mater Sci 16:203–243
2. Halasyamani PS, Poeppelmeier KR (1998) Chem Mater 10:2753–2769
3. Wickleder MS (2002) Chem Rev 102:2011–2087
4. Becker P (1998) Adv Mater 10:979–992
5. Chen CT, Wang YB, Wu BC, Wu KC, Zeng WL, Yu LH (1995) Nature 373:322–324
6. Chen CT, Wu BC, Jiang AD, You GM (1985) Sci Sin Ser B 28:235–243
7. Hagerman ME, Poeppelmeier KR (1995) Chem Mater 7:602–621
8. Bera TK, Jang JI, Song JH, Malliakas CD, Freeman AJ, Ketterson JB, Kanatzidis MG (2010) J Am Chem Soc 132:3484–3495
9. Dmitriev VG, Gurzadyan GG, Nikogosyan DN (1991) Handbook of nonlinear optical crystals. Springer, Berlin
10. Phanon D, Gautier-Luneau I (2007) Angew Chem Int Ed 46:8488–8491
11. Pan SL, Smit JP, Watkins B, Marvel MR, Stern CL, Poeppelmeier KR (2006) J Am Chem Soc 128:11631–11634
12. Zhang WL, Cheng WD, Zhang H, Geng L, Lin CS, He ZZ (2010) J Am Chem Soc 132:1508–1509
13. Kong F, Huang SP, Sun ZM, Mao JG, Cheng WD (2006) J Am Chem Soc 128:7750–7751
14. Mao JG, Jiang HL, Kong F (2008) Inorg Chem 47:8498–8510
15. Wang SC, Ye N, Li W, Zhao D (2010) J Am Chem Soc 132:8779–8786
16. Halasyamani PS (2004) Chem Mater 16:3586–3592
17. Sun CF, Yang BP, Mao JG (2011) Sci China Ser B Chem 54:911–922
18. Ok KM, Halasyamani PS (2006) Chem Mater 18:3176–3183
19. Ok KM, Halasyamani PS (2004) Angew Chem Int Ed 43:5489–5491
20. Phanon D, Gautier-Luneau I (2007) J Mater Chem 17:1123–1130
21. Kim SH, Yeon J, Halasyamani PS (2009) Chem Mater 21:5335–5342
22. Wu BC, Tang DY, Ye N, Chen CT (1996) Opt Mater 5:105–109
23. Sykora RE, Ok KM, Halasyamani PS (2002) J Am Chem Soc 124:1951–1957

24. Sykora RE, Ok KM, Halasyamani PS, Wells DM, Albrecht-Schmitt TE (2002) Chem Mater 14:2741–2749
25. Shehee TC, Sykora RE, Ok KM, Halasyamani PS, Albrecht-Schmitt TE (2003) Inorg Chem 42:457–462
26. Chang HY, Kim SH, Halasyamani PS, Ok KM (2009) J Am Chem Soc 131:2426–2427
27. Chang HY, Kim SH, Ok KM, Halasyamani PS (2009) J Am Chem Soc 131:6865–6873
28. Sun CF, Hu CL, Xu X, Ling JB, Hu T, Kong F, Long XF, Mao JG (2009) J Am Chem Soc 131:9486–9487
29. Yang BP, Hu CL, Xu X, Sun CF, Zhang JH, Mao JG (2010) Chem Mater 22:1545–1550
30. Sun CF, Hu CL, Xu X, Yang BP, Mao JG (2011) J Am Chem Soc 133:5561–5572
31. Porter Y, Bhuvanesh NSP, Halasyamani PS (2001) Inorg Chem 40:1172–1175
32. Porter Y, Ok KM, Bhuvanesh NSP, Halasyamani PS (2001) Chem Mater 13:1910–1915
33. Ok KM, Bhuvanesh NSP, Halasyamani PS (2001) Inorg Chem 40:1978–1980
34. Ra HS, Ok KM, Halasyamani PS (2003) J Am Chem Soc 125:7764–7765
35. Zhang WG, Tao XT, Zhang CQ, Gao ZL, Yu WT, Cheng XF, Liu XS, Jiang MH (2008) Cryst Growth Des 8:304–307
36. Zhang WG, Tao XT, Zhang CQ, Zhang HJ, Jiang MH (2009) Cryst Growth Des 9:2633–2636
37. Ok KM, Halasyamani PS (2004) Inorg Chem 43:4248–4253
38. Hart RT, Ok KM, Halasyamani PS, Zwanziger JW (2004) Appl Phys Lett 85:938–939
39. Goodey J, Broussard J, Halasyamani PS (2002) Chem Mater 14:3174–3180
40. Johnston MG, Harrison WTA (2001) Inorg Chem 40:6518–6520
41. Balraj V, Vidyasagar K (1999) Inorg Chem 38:5809–5813
42. Ok KM, Halasyamani PS (2005) Inorg Chem 44:9353–9359
43. Li PX, Hu CL, Xu X, Wang RY, Sun CF, Mao JG (2010) Inorg Chem 49:4599–4605
44. Liu XM, Li GH, Hu YW, Yang M, Kong XG, Shi Z, Feng SH (2008) Cryst Growth Des 8:2453–2457
45. Sun CF, Hu CL, Xu X, Mao JG (2010) Inorg Chem 49:9581–9589
46. Hu T, Qin L, Kong F, Zhou Y, Mao JG (2009) Inorg Chem 48:2193–2199
47. Sun CF, Hu T, Xu X, Mao JG (2010) Dalton Trans 39:7960–7967
48. Sullens TA, Almond PM, Byrd JA, Beitz JV, Bray TH, Albrecht-Schmitt TE (2006) J Solid State Chem 179:1192–1201
49. Chen XA, Zhang L, Chang X, Xue HP, Zang HG, Xiao WQ, Song XM, Yan H (2007) J Alloy Compd 428:54–58
50. Chang HY, Kim SW, Halasyamani PS (2010) Chem Mater 22:3241–3250
51. Chang HY, Kim SH, Ok KM, Halasyamani PS (2009) Chem Mater 21:1654–1662
52. Harrison WTA, Buttery JHN (2000) Z Anorg Allg Chem 626:867–870
53. Harrison WTA, Dussack LL, Jacobson AJ (1994) Inorg Chem 33:6043–6049
54. Balraj V, Vidyasagar K (1998) Inorg Chem 37:4764–4774
55. Harrison WTA, Dussack LL, Vogt T, Jacobson AJ (1995) J Solid State Chem 120:112–120
56. Goodey J, Ok KM, Broussard J, Hofmann C, Escobedo FV, Halasyamani PS (2003) J Solid State Chem 175:3–12
57. Chi EO, Ok KM, Porter Y, Halasyamani PS (2006) Chem Mater 18:2070–2074
58. Zhou Y, Hu CL, Hu T, Kong F, Mao JG (2009) Dalton Trans 38:5747–5754
59. Kim JH, Baek J, Halasyamani PS (2007) Chem Mater 19:5637–5641
60. Porter Y, Halasyamani PS (2003) J Solid State Chem 174:441–449
61. Jiang HL, Huang SP, Fan Y, Mao JG (2008) Chem Eur J 14:1972–1981
62. Nguyen SD, Kim SH, Halasyamani PS (2011) Inorg Chem 50:5215–5222
63. Sivakumar T, Chang HY, Baek J, Halasyamani PS (2007) Chem Mater 19:4710–4715
64. Lee DW, Oh SJ, Halasyamani PS, Ok KM (2011) Inorg Chem 50:4473–4480
65. Kim MK, Kim SH, Chang HY, Halasyamani PS, Ok KM (2010) Inorg Chem 49:7028–7034
66. Zhang SY, Jiang HL, Sun CF, Mao JG (2009) Inorg Chem 48:11809–11820
67. Kong F, Xu X, Mao JG (2010) Inorg Chem 49:11573–11580
68. Sun CF, Hu CL, Kong F, Yang BP, Mao JG (2010) Dalton Trans 39:1473–1479

69. Sykora RE, Wells DM, Albrecht-Schmitt TE (2002) J Solid State Chem 166:442–448
70. Shehee TC, Pehler SF, Albrecht-Schmitt TE (2005) J Alloy Compd 388:225–229
71. Ok KM, Halasyamani PS (2005) Inorg Chem 44:2263–2271
72. Sykora RE, Wells DM, Albrecht-Schmitt TE (2002) Inorg Chem 41:2697–2703
73. Chen XA, Chang X, Zang HG, Wang Q, Xiao WQ (2005) J Alloy Compd 396:255–259
74. Chen XA, Zhang L, Chang X, Zang HG, Xiao WQ (2006) Acta Crystallogr Sect C 62:i76–i78
75. Loefgren P (1967) Acta Chem Scand 21:2781–2791
76. Bergman JG, Wood JS (1987) Acta Crystallogr C 43:1831–1832
77. Yeon J, Kim SH, Halasyamani PS (2009) J Solid State Chem 182:3269–3274
78. Bentria B, Benbertal D, Bagieu-Beucher M, Masse R, Mosset A (2003) J Chem Crystallogr 33:867–873
79. Phanon D, Gautier-Luneau I (2006) Z Kristallogr 221:243–244
80. Kellersohn T, Alici E, Esser D, Lutz HD (1993) Z Kristallogr 203:225–233
81. Belokoneva EL, Dimitrova OV (2010) Kristallografiya 55:24–27
82. Bindi L, Welch MD, Bonazzi P, Pratesi G, Menchetti S (2008) Mineral Mag 72:771–783
83. Yang BP, Sun CF, Hu CL, Mao JG (2011) Dalton Trans 40:1055–1060
84. Ling J, Albrecht-Schmitt TE (2007) Eur J Inorg Chem 5:652–655
85. Zhang JJ, Tao XT, Sun YX, Zhang ZH, Zhang CQ, Gao ZL, Xia HB, Xia SQ (2011) Cryst Growth Des 11:1863–1868
86. Zhang WG, Li F, Kim SH, Halasyamani PS (2010) Cryst Growth Des 10:4091–4095
87. Kortz U, Savelieff MG, Ghali FYA, Khalil LM, Maalouf SA, Sinno DI (2002) Angew Chem Int Ed 41:4070–4073
88. Harrison WTA, Dussack LL, Jacobson AJ (1996) J Solid State Chem 125:234–242
89. Vaughey JT, Harrison WTA, Dussack LL, Jacobson AJ (1994) Inorg Chem 33:4370–4375
90. Kwon YU, Lee KS, Kim YH (1996) Inorg Chem 35:1161–1167
91. Lee KS, Kwon YU, Namgung H, Kim SW (1995) Inorg Chem 34:4178–4181
92. Hou JY, Huang CC, Zhang HH, Yang QY, Chen YP, Xu JF (2005) Acta Crystallogr Sect C 61:i59–i60
93. Sivakumar T, Ok KM, Halasyamani PS (2006) Inorg Chem 45:3602–3605
94. Harrison WTA, Vaughey JT, Goshorn JW (1995) J Solid State Chem 116:77–86
95. Zhang SY, Hu CL, Sun CF, Mao JG (2010) Inorg Chem 49:11627–11636
96. Ok KM, Halasyamani PS (2005) Inorg Chem 44:3919–3925
97. Muller-Buschbaum H, Wedel B (1996) Z Naturforsch B51:1411–1414
98. Ok KM, Orzechowski J, Halasyamani PS (2004) Inorg Chem 43:964–968
99. Gu QH, Hu CL, Zhang JH, Mao JG (2011) Dalton Trans 40:2562–2569
100. Ok KM, Zhang L, Halasyamani PS (2003) J Solid State Chem 175:264–271
101. Shen YL, Jiang HL, Xu J, Mao JG, Cheah KW (2005) Inorg Chem 44:9314–9321
102. Jiang HL, Ma E, Mao JG (2007) Inorg Chem 46:7012–7023
103. Zhang SY, Mao JG (2011) Inorg Chem 50:4934–4943
104. Li PX, Zhang SY, Mao JG (2010) Dalton Trans 39:11560–11567
105. Jiang HL, Kong F, Fan Y, Mao JG (2008) Inorg Chem 47:7430–7437
106. Jiang HL, Xie Z, Mao JG (2007) Inorg Chem 46:6495–6501
107. Champarnaud-Mesjard JC, Frit B, Chagraoui A, Tairi A (1996) Z Anorg Allg Chem 622:1907–1912
108. Champarnaud-Mesjard JC, Frit B, Chagraoui A, Tairi A (1996) J Solid State Chem 127:248–255
109. Blanchandin S, Champarnaud-Mesjard JC, Thomas P, Frit B (2000) Solid State Sci 2:223–228
110. Li PX, Kong F, Hu CL, Zhao Na, Mao JG (2010) Inorg Chem 49:5943–5952
111. Kong F, Hu CL, Hu T, Zhou Y, Mao JG (2009) Dalton Trans 38:4962–4970
112. Johnsson M, Törnroos KW, Mila F, Millet P (2000) Chem Mater 12:2853–2857
113. Johnsson M, Lidin S, Törnroos KW, Bürgi HB, Millet P (2004) Angew Chem Int Ed 43:4292–4295

114. Wu HQ, Pan SL, Poeppelmeier KR, Li HY, Jia DZ, Chen ZH, Fan XY, Yang Y, Rondinelli JM, Luo HS (2011) J Am Chem Soc 133:7786–7790
115. Huang YZ, Wu LM, Wu XT, Li LH, Chen L, Zhang YF (2010) J Am Chem Soc 132:12788–12789
116. Kholodkovskaya LN, Dolgikh VA, Popovkin BA (1995) J Solid State Chem 116:406–408
117. Feger CR, Kolis JW (1998) Inorg Chem 37:4046–4051
118. Jiang HL, Mao JG (2006) Inorg Chem 45:717–721
119. Shen YL, Mao JG, Jiang HL (2005) J Solid State Chem 178:2949–2953
120. Jiang HL, Mao JG (2006) Inorg Chem 45:7593–7599
121. Shen YL, Mao JG (2005) Inorg Chem 44:5328–5335
122. Mayer H (1975) Z Kristallogr 141:354–362
123. Mayer H, Weil M (2003) Z Anorg Allg Chem 629:1068–1072
124. Alcock NW, Harrison WD (1982) Acta Crystallogr B38:1809–1811
125. Mayer H, Pupp G (1977) Z Kristallogr 145:321–333
126. Ok KM, Halasyamani PS (2006) J Solid State Chem 179:1345–1350
127. Guesdon A, Raveau B (2000) Chem Mater 12:2239–2243
128. Kong F, Jiang HL, Mao JG (2008) J Solid State Chem 181:263–268

Struct Bond (2012) 144: 105–120
DOI: 10.1007/430_2011_67
© Springer-Verlag Berlin Heidelberg 2012
Published online: 3 March 2012

Structure, Growth, Nonlinear Optics, and Laser Properties of $RX_3(BO_3)_4$ (R = Y, Gd, La; X = Al, Sc)

Guo-Fu Wang

Abstract As well known, the borate crystals are an important laser host material and nonlinear optical crystal. After an examination on the crystal structure and growth technology of $RX_3(BO_3)_4$ (R = Y, Gd, La; X = Al, Sc), this chapter reviews research progress of Nd^{3+}-, Cr^{3+}- and Ti^{3+}-doped $RX_3(BO_3)_4$ (R = Y, Gd, La; X = Al, Sc) including the nonlinear optical crystal materials.

Keywords Borate crystals · Nonlinear optical crystal

Contents

1 Introduction 105
2 Structural Characteristic of $RX_3(BO_3)_4$ Crystals 106
3 Crystal Growth of $REX_3(BO_3)_4$ Crystals 107
4 Nonlinear Optical and Self-Frequency Doubling Laser Properties 110
5 Spectral Properties of Cr^{3+} and Ti^{3+}-Doped $RX_3(BO_3)_4$ Crystals 112
6 Summary 117
References 117

1 Introduction

It is well known that the borate crystals are an important laser material and nonlinear optical crystal. A family double borate with general formula $RAl_3(BO_3)_4$ (where R = Y, La, Nd, Gd, Lu, Tb, Dy, Ho, Er, Yb; X = Al, Cr, Sc) received much attention since they have an excellent physical and spectral properties. For example, the crystals of Nd^{3+}:$YAl_3(BO_3)_4$ [1] and Nd^{3+}: $GdAl_3(BO_3)_4$ [2] can be used as a

G.-F.Wang (✉)
Fujian Institute of Research on the Structure of Matter, Chinese Academy of Sciences, Fuzhou, Fujian 350002, China
e-mail: wgf@fjirsm.ac.cn

self-frequency doubling (SFD) laser crystal. After examination on the structure and crystal growth, this chapter reviews research progress of rare-earth and Cr^{3+}-doped $RX_3(BO_3)_4$ laser properties and self-doubling frequency laser properties, as well as the nonlinear optical property.

2 Structural Characteristic of $RX_3(BO_3)_4$ Crystals

The double borate with general formula $RAl_3(BO_3)_4$ (where R = Y, La, Nd, Gd, Lu, Tb, Dy, Ho, Er, Yb) were firstly reported by Ballman [3], which were synthesized by a flux method from K_2SO_4-$3MoO_3$ and PbF_2-$3B_2O_3$ fluxes. These compounds with space group R32 are isostructural with the mineral huntite $CaMg_3(CO_3)_4$ [4]. Hong et al. firstly reported the structural details of $NdAl_3(BO_3)_4$ crystal. $NdAl_3(BO_3)_4$ crystal belongs to hexagonal with space group R32 and the unit cell dimensions of $a = 9.341$ Å, $c = 7.3066$ Å, $Z = 3$ [5]. The structure of $NdAl_3(BO_3)_4$ crystal consists of NdO_6 distorted octahedra, AlO_6 distorted octahedra, and BO_3 planar triangle. The structure of $NdAl_3(BO_3)_4$ crystal is illustrated in Fig. 1 [5]. However, in 1979, Jarchow reported that the $NdAl_3(BO_3)_4$ crystal was monoclinic with two space groups C2/c and C2 [7]. In 1981 and 1983, Lutz and Zwiter also reported that $NdAl_3(BO_3)_4$ crystal is monoclinic with two space group C2/c and C2 [8, 9]. In 1983, Belokoneva reported that $NdAl_3(BO_3)_4$ crystal was monoclinic with space group C2/c [10]. Therefore, the reported structure of $NdAl_3(BO_3)_4$ crystal was confused. Finally, author discovered that $NdAl_3(BO_3)_4$ crystal is a polymorphous compound and has two-phase transition

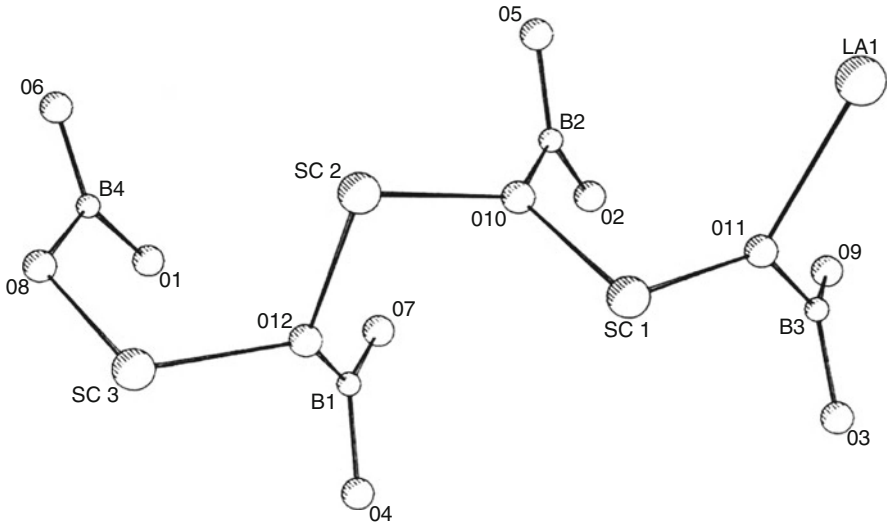

Fig. 1 Joint of atoms in $LaSc_3(BO_3)_4$ crystal [6]

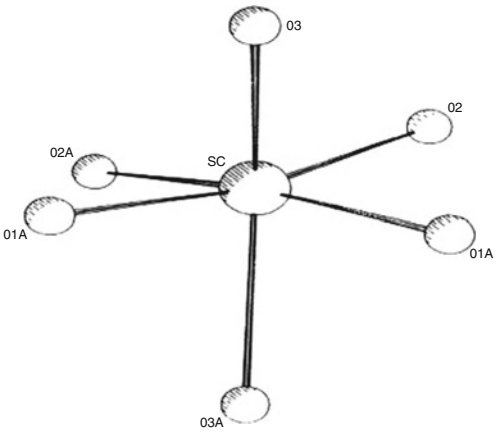

Fig. 2 ScO_6 polyhedra in β-$LaSc_3(BO_3)_4$ crystal [13]

points and three-phase structure, i.e., R32, C2/c, and C2 space groups [11]. In fact, the other $RX_3(BO_3)_4$ crystals also exist in the polymorphous phenomena. For example, $GdAl_3(BO_3)_4$ crystal has a space group C2 except the space group R32 [12]. $LaSc_3(BO_3)_4$ crystal also exists in three-phase structures of R32, C2/c, and Cc [6, 13, 14]. It is interesting that $RX_3(BO_3)_4$ crystals always consist of the RO_6 distorted octahedra, XO_6 distorted octahedra, and BO_3 planar triangle. The RO_6 polyhedra are isolated with R ion, and R ion is joined by means of R–O–X–O–R, as shown in Fig. 1. The distance between R–R is from 5.596 to 6.623 Å. In $RX_3(BO_3)_4$ crystals, RO_6 polyhedra can provide substitution sites for the laser active ions Nd^{3+}. When the active ions Nd^{3+} is substituted with the R ion, such crystal structure will result in a weak ion–ion interactions of laser upper levels, which reduces luminescence quenching and enables high concentrations of laser active ion [5, 6, 11, 13]. The X ion in XO_6 distorted octahedra which the symmetry is approximately octahedral can also be replaced by the transition metal active Cr^{3+} and Ti^{3+} ions (Fig. 2). Therefore, $RX_3(BO_3)_4$ crystals are an excellent laser host material. In addition, since the BO_3 planar triangle in $RX_3(BO_3)_4$ crystals plays an important role for second harmonic generation (SHG) effect, $RX_3(BO_3)_4$ crystals with space group R32 and Cc have SHG effect. Therefore, they can be used as nonlinear optical crystal materials and self-doubling frequency laser crystal materials.

3 Crystal Growth of $REX_3(BO_3)_4$ Crystals

Since $RX_3(BO_3)_4$ crystals melt incongruently at high temperature and decompose into their constituent phase of RBO_3 and $AlBO_3$ [15], the $RX_3(BO_3)_4$ crystals are only grown from the high-temperature solutions except $LaSc_3(BO_3)_4$ crystal. Previously, a number fluxes were reported for the growth of $RAl_3(BO_3)_4$ crystals, such as PbF_2-B_2O_3, $Li_2B_4O_7$, $Na_2B_4O_7$, BaO-B_2O_3, $K_2Mo_3O_{10}$, and $K_2Mo_3O_{10}$–KF (K_2SO_4 or PbF_2) [16–35]. In these fluxes, the $K_2Mo_3O_{10}$ is available to grow the

$RX_3(BO_3)_4$ crystals. In 1995, the author and Jung developed a $K_2Mo_3O_{10}$–B_2O_3 mixed flux [36, 37]. In comparison with $K_2Mo_3O_{10}$ flux, the $K_2Mo_3O_{10}$–B_2O_3 mixed flux has some advantages as follows: The addition of B_2O_3 to the $K_2Mo_3O_{10}$–B_2O_3 mixed flux can increase the solubility of $RX_3(BO_3)_4$ crystals and reduced the saturation temperature, the volatility of flux can be reduced, enhancing the crystallization conditions for grow $RX_3(BO_3)_4$ crystals. Therefore, among theses fluxes, the $K_2Mo_3O_{10}$–B_2O_3 mixed flux is more available to grow the $RX_3(BO_3)_4$ crystals [2, 36–39]. However, the Mo ions easily incorporate into the crystal, which leads to a near ultraviolet (UV) absorption band that limits the potential applications at short wavelength for nonlinear optical crystal [18, 38–41]. Recently, Ye et al. developed a new flux of Li_2WO_4-B_2O_3 to grow $YAl_3(BO_3)_4$ crystal [42].

The $RX_3(BO_3)_4$ crystals with large size and good quality were grown by the top-seeded solution growth (TSSG) method. The crystal growth was carried out in a vertical tubular furnace with temperature controller to control the furnace temperature and the cooling rate, as shown in Fig. 3.

Before the growing, in order to select the suitable composition of the solution, the solubility curve of $RX_3(BO_3)_4$ crystal in the solution of $RX_3(BO_3)_4$ crystal flux was generally determined by the trial seeding method. The saturation temperatures were determined for various compositions by adjusting the temperature of the solution until a trial seeding showed no change in weight or surface microtopography after 3–4-h immersion. The growing procedure is as follows: Firstly, the starting materials of $RX_3(BO_3)_4$ crystal and flux were weighed. The weighed materials were mixed and put into the platinum crucible. The fully charged crucible was placed into the furnace and kept at high temperature to make the solution melt completely and homogeneously. Secondly, a platinum wire was a seed crystal that was soaked into the solution, and the temperature was cooled down from high temperature to lower temperature at a cooling rate of 1–3°C/d. Then, the crystals grown on the platinum wire were drawn out of the solution surface and cooled down to room temperature at a cooling rate of 20–30°C/h. Finally, after obtaining the small crystals, a seed cut from the as-obtained crystal was used to grow large-size crystals. The saturation temperature of the solution was exactly determined by repeated seeding. Then, the seed was dipped into the solution at a temperature 20°C above saturation temperature and was kept at this temperature for 20 min to dissolve the surface of the seed.

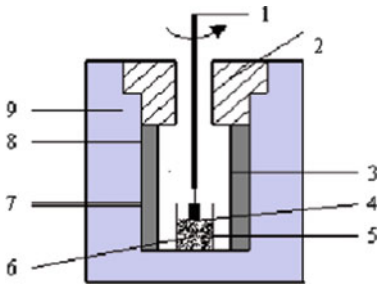

Fig. 3 Schematic diagram of crystal growth apparatuses: (*1*) seed holder, (*2*) furnace cover, (*3*) heating element, (*4*) seed, (*5*) crucible, (*6*) solution, (*7*) thermocouple, (*8*) Al_2O_3 tube, and (*9*) thermal insulation material

Fig. 4 Ti^{3+}:$YAl_3(BO_3)_4$ crystal with dimension 42 × 36 × 24 mm^3 grown by TSSG method from flux of $K_2Mo_3O_{10}$–B_2O_3 [43]

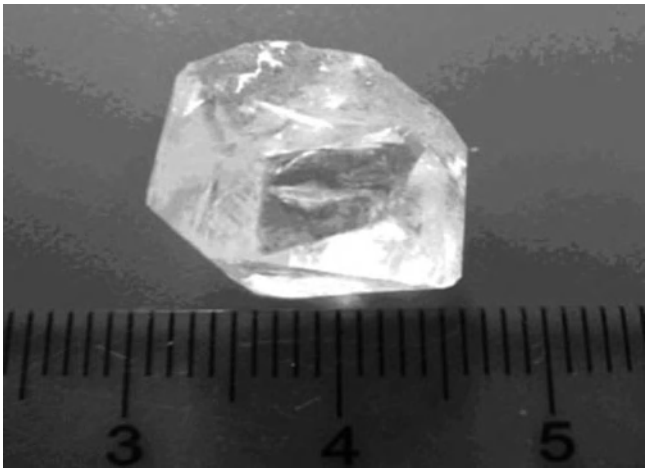

Fig. 5 $YAl_3(BO_3)_4$ crystal with dimension 45 × 27 × 20 mm^3 grown by TSSG method from flux of Li_2WO_4-B_2O_3 [42]

The crystals were grown at a cooling rate of 1–3°C/d and rotated at a rotating rate of ~15 rpm. When the growth process ended, the crystals were pulled out of the solution and cooled to room temperature at a cooling rate of 20–30°C/h. Figures 4–6 show some $RAl_3(BO_3)_4$ crystal grown by the TSSG method from different flux. $LaSc_3(BO_3)_4$ and $NdSc_3(BO_3)_4$ can be only grown by the Czochralski method in $RX_3(BO_3)_4$ borate family. Nd^{3+}:$LaSc_3(BO_3)_4$ crystals with dimension ϕ20 × 50 mm^3 were successfully grown by the Czochralski method [45]. Recently, Cr^{3+}-doped $LaSc_3(BO_3)_4$ with dimension ϕ25 × 35 mm^3 has also been grown at a pulling rate of 1.5 mm/h and a rotating rate of 15 rpm by the Czochralski method, as shown in Fig. 7 [44].

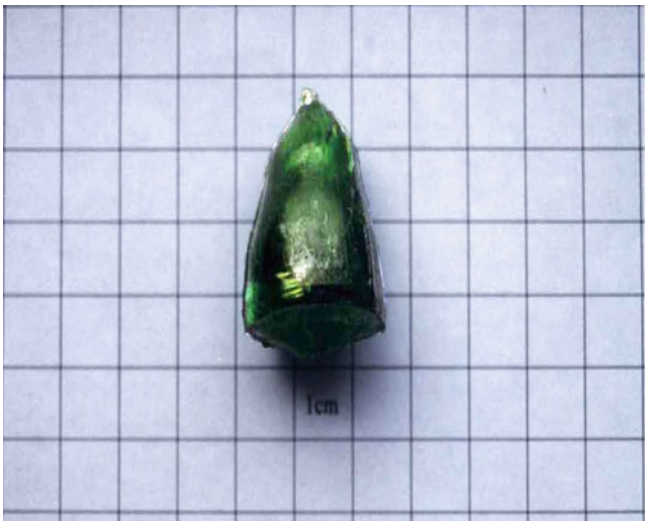

Fig. 6 Cr^{3+}:$LaSc_3(BO_3)_4$ crystal grown by the Czochralski method [44]

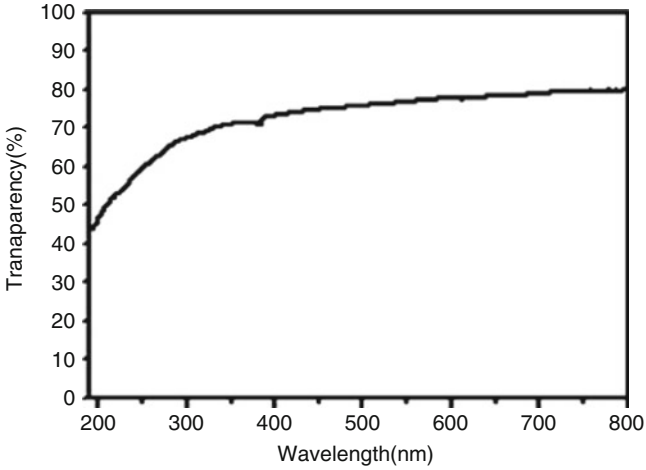

Fig. 7 Ultraviolet transparency curve of YAB crystal [46]

4 Nonlinear Optical and Self-Frequency Doubling Laser Properties

$YAl_3(BO_3)_4$ (YAB) crystal was first discovered in 1962. $YAl_3(BO_3)_4$ crystal belongs to trigonal system with R32 space group, and the cell unite parameters are $a = b = 9.293$ Å and $c = 7.245$ Å [47]. Leonyuk and Flimonov firstly found that the $YAl_3(BO_3)_4$ crystal has nonlinear optical (NLO) coefficient in 1974 [48].

The conjugate bonds inside BO_3 groups take an important part in the NLO effect in this crystal. $YAl_3(BO_3)_4$ crystal has a high NLO coefficient d_{11} of $3.9d_{36}$ (KDP) [47]. In the past three decades, the Nd^{3+}-doped $YAl_3(BO_3)_4$ (NYAB) crystal has been extensively studied as an excellent SFD laser crystal [1, 49–54]. In 1981, Dorozhkin et al. firstly realized the SFD laser output of NYAB crystal is from 1.32 μm to 0.66 μm [49]. Then Lu et al. and Luo et al. further realized the SFD green laser output of NYAB crystal is from 1.064 μm to 0.532 μm by means of the xenon flash lamp, respectively [1, 50]. In 1999, Jaque et al. realized the output of continuous wave red, green, and blue laser lights using a Ti:sapphire laser as pumping source [55]. The red (669 nm) and green (532 nm) radiations are obtained by SFD of the fundamental laser lines at 1,338 nm ($^4F_{3/2} \rightarrow {}^4I_{13/2}$ channel) and 1,062 nm ($^4F_{3/2} \rightarrow {}^4I_{11/2}$ channel), respectively. Blue laser radiation (458 nm) is achieved by self-sum-frequency mixing of the main laser line at 1,062 nm and the pumping radiation at 807 nm. In 1996, Chen et al. obtained the 67 mW green laser from a fiber-coupled diode end-pumped NYAB crystal [56]. When pumped by a 650 mW fiber-coupled laser diode, the green laser output was 67 mW, the conversion efficiency achieved to 10.3% [56]. The basic properties of NYAB crystal are listed in Table 1.

Recently, it was found that $YAl_3(BO_3)_4$ crystal can be used as a UV nonlinear optical crystal, wherein the YAB crystal was grown from flux of Li_2WO_4-B_2O_3 [42]. Figure 7 shows the UV transparency curve of YAB crystal, the UV-visible region, and the near-infrared wavelength. The YAB crystal exhibits high transparency, and the UV cutoff wavelength of the YAB crystal was shorter than 190 nm [46]. Figure 8 shows the phase-matching curve of the YAB crystal for SHG at 473 nm as a function of temperature. The coefficient of frequency doubling d_{11} of the YAB crystal is 1.30 pm/V [46]. These data indicate that the YAB crystal can be used as a potential near UV nonlinear optical crystal.

Table 1 Basic properties of NYAB crystal

Structure	Trigonal system, R32 space group	
Cell unit parameters	$a = 9.293$ Å, $b = 9.293$ Å, $c = 7.245$ Å	
Mobs hardness	8	
Refractive	1.064 μm	$n_o = 1.7553$
		$n_e = 1.6869$
	0.532 μm	$n_o = 1.7808$
		$n_e = 1.7075$
Phase-matching angle	Type I: $32^0 9$	
	Type II: 51^0	
d_{ij} Coefficient	$d_{11} = 1.7$(pm/V) $= 3.9 \times d_{36}$ (KDP)	
Effective SHG coefficient	Type I: $d_{eff} = 1.43$ pm/V	
	Type II: $d_{eff} = 0.67$ pm/V	
Fluorescence lifetime of $^4F_{3/2}$	50 μs	
Emission cross-section of 1.064 μm	10.0×10^{-19} cm^2	

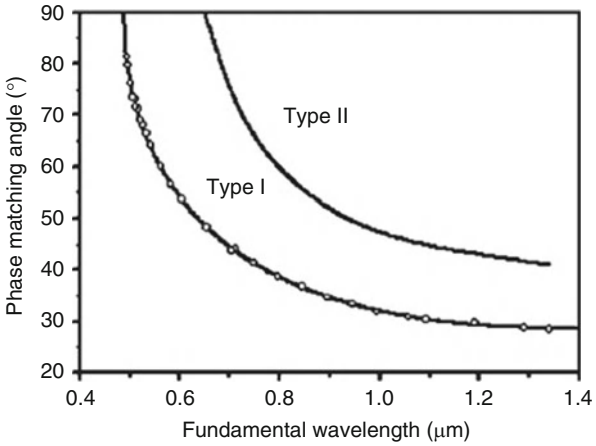

Fig. 8 Phase-matching curves of YAB crystal [46]

5 Spectral Properties of Cr^{3+} and Ti^{3+}-Doped $RX_3(BO_3)_4$ Crystals

Tunable solid-state lasers have a wide field of applications in medicine, military, ultrashort pulse generation, and communication [57, 58]. Since 1960, many Cr^{3+}-doped tunable laser crystals have been investigated, such as $BeAl_2O_4$, $LiCaAlF_6$, $Be_3Al_2(SiO_3)_6$, GdScGa-Garnet, and $LaSc(BO_3)_4$ [59–65]. In $RX_3(BO_3)_4$ crystals, the X ion can be replaced by the transition metal active Cr^{3+} and Ti^{3+} ions, $RX_3(BO_3)_4$ crystals can be considered as a potential tunable solid-state laser host materials.

Figures 9–12 show the absorption and fluorescence spectra of Cr^{3+}:$YAl_3(BO_3)_4$ (Cr:YAB), Cr^{3+}:$GdAl_3(BO_3)_4$ (Cr:GAB), Cr^{3+}:$YSc_3(BO_3)_4$ (Cr:YSB), Cr^{3+}:$GdSc_3(BO_3)_4$ (Cr:GSB), and Cr^{3+}:$LaSc_3(BO_3)_4$ crystals at room temperature. They demonstrated the different spectral features. As well known, the spectrum of Cr^{3+}-doped tunable solid-state laser is dependent on the crystal field strength Dq and Racah parameters B and C. When the active ion Cr^{3+} occupies in the different crystal field sites which depend on the value of Dq/B, they exhibit the different spectral feature. When in the strong crystal field, the fluorescence spectrum exhibits only sharp line (R-line); when in medium crystal field, the fluorescence spectrum consists of R-line and broad band such as Cr:YAB and Cr:GAB (Fig. 11); and when in the weak crystal field, the fluorescence spectrum is only a broad band such as Cr:YSB and Cr:GSB (Fig. 11) and Cr^{3+}:$LaSc_3(BO_3)_4$ (Fig. 12). We believe that these spectral features are closely related to chemical composition of $RX_3(BO_3)_4$ double borate crystals. In $RX_3(BO_3)_4$ double borate crystals, there are two trivalent cation positions: R = Y^{3+} and rare-earth element occupy the distorted oxygen trigonal prisms; X = Al^{3+}, Sc^{3+}, Ga^{3+}, or Cr^{3+} occupy the center of distorted oxygen octahedra. The ionic radii of R^{3+} and X^{3+} ions cover a wide range: La^{3+}(1.15 Å) > Gd^{3+}(1.11 Å) > Y^{3+}(0.95 Å) > Lu^{3+}(0.86 Å); Sc^{3+}(0.83 Å) >

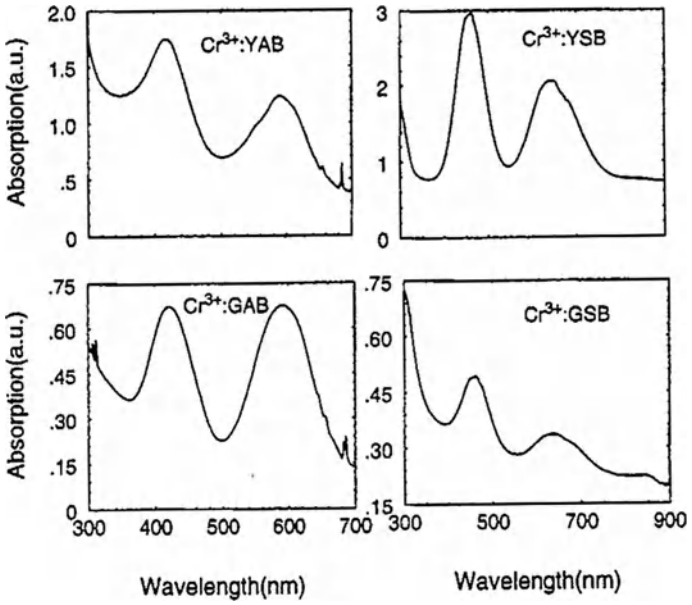

Fig. 9 Absorption spectra of Cr^{3+}:$RX_3(BO_3)_4$ (R = Y, Gd; X = Al, Sc) at room temperature [66]

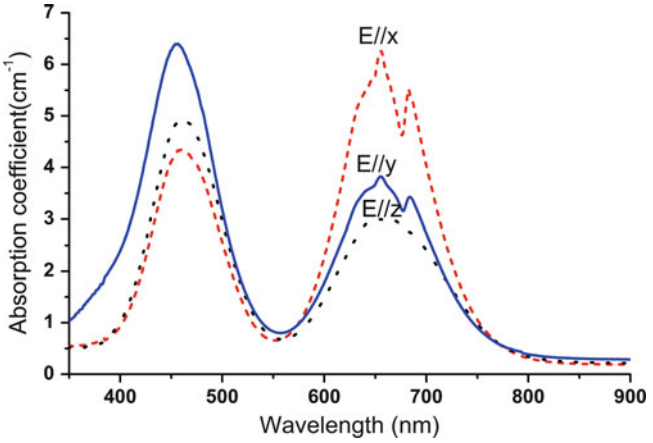

Fig. 10 Polarized absorption spectra of Cr^{3+}:$LaSc_3(BO_3)_4$ at room temperature [52]

Cr^{3+}(0.65 Å) > Ga^{3+}(0.62 Å) > Al^{3+}(0.55 Å). Table 1 shows the relationship between the crystal field strength Dq/B and the ionic radii of R^{3+} and X^{3+} ions of Cr^{3+}:$RX_3(BO_3)_4$ crystals. It is found that the crystal field strength Dq/B is decreased with the increasing of R^{3+} and X^{3+} radium. The larger the size of R^{3+} and X^{3+} is, the weaker the crystal field strength in Cr^{3+}:$RX_3(BO_3)_4$ crystals is. In other words, the "size effect" of R^{3+} and X^{3+} strongly affects on crystal field strength of tunable laser

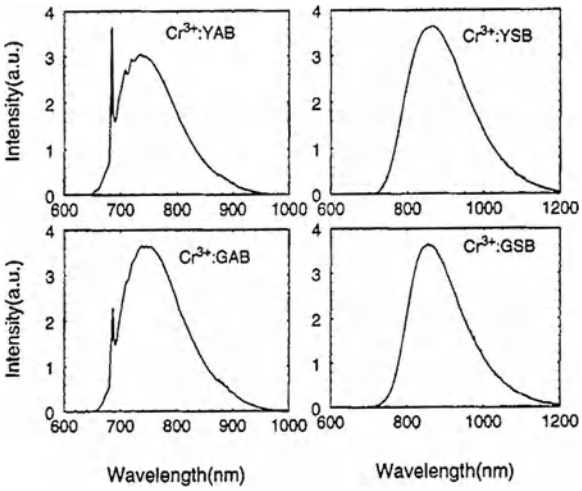

Fig. 11 Photoluminescence spectra of Cr^{3+}:$RX_3(BO_3)_4$ (R = Y, Gd; X = Al, Sc) at room temperature [66]

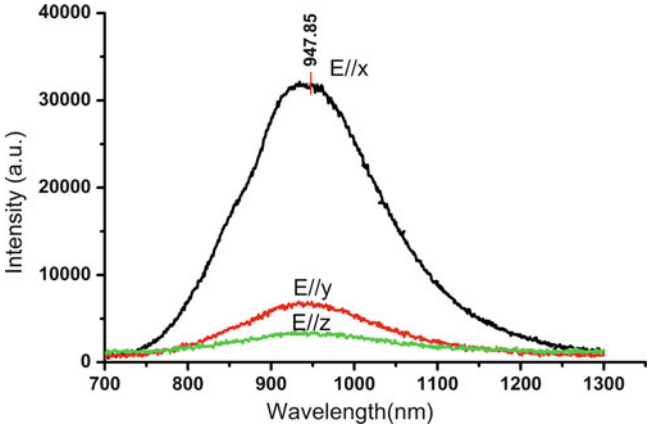

Fig. 12 Polarized photoluminescence spectra of Cr^{3+}:$LaSc_3(BO_3)_4$ at room temperature [56]

crystals. According to the "size effect," we guessed that the Cr^{3+}:$LaSc_3(BO_3)_4$ crystal should have a weak crystal field since it has the largest ionic radii of R^{3+} and X^{3+} ions in $RX_3(BO_3)_4$ borate family. The spectroscopic characterizations of Cr^{3+}:$LaSc_3(BO_3)_4$ crystals have been investigated [55, 56]. Figure 12 shows the fluorescence spectrum of Cr^{3+}:$LaSc_3(BO_3)_4$ crystal. The Cr^{3+}:$LaSc_3(BO_3)_4$ crystal has a weak crystal field strength (Dq/B = 2.27) and broad emission band extending from 740 to 1,280 nm with a peak at 960 nm and a full width at half maximum (FWHM) of 194 nm [55, 56]. In comparison with the other Cr^{3+}-doped materials (Table 2), the Cr^{3+}:$LaSc_3(BO_3)_4$ crystal can be regarded as a tunable solid-state laser crystal.

Table 2 Comparison of spectroscopy properties of Cr^{3+}:$LaSc_3(BO_3)_4$ crystal with other Cr^{3+}-doped materials

Materials	$LaSc_3(BO_3)_4$	$BeAl_2O_4$	$LaCaAlF_6$	$LiSrAlF_6$	GSGG	$ScBO_3$	$SrAlF_5$
Lifetime (μs)	17	260	175	67	114	115	93
Emission cross-section (10^{-20} cm^2)	6.65	0.7	1.23	5	0.8	1.2	2.3
	740–1,280	700–820	720–840	780–1,010	742–842	785–865	852–947
Emission peak (nm)	953	752	780	825	785	843	932
Reference	[44]	[67]	[68]	[69]	[63]	[70]	[71]

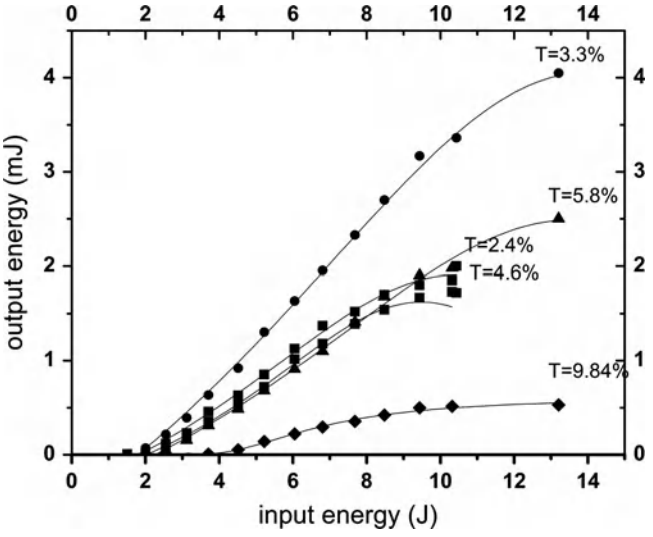

Fig. 13 Laser output energy vs. input energy as pumped by a flash lamp

Recently, the laser characterization of Cr^{3+}:$LaSc_3(BO_3)_4$ crystal has been investigated in our laboratory. The lasing output has been firstly achieved in Cr^{3+}:$LaSc_3(BO_3)_4$ crystal. The laser rod of 0.6% at Cr^{3+}:$LaSc_3(BO_3)_4$ with dimensions of $\phi 3.3 \times 11$ mm^2 was cut from the as-grown crystal. Laser rod was pumped by a single xenon flash lamp with different transmittances of the output mirrors at 963 nm, which were 9.8%, 5.8%, 4.6%, 3.3%, and 2.4%, respectively. Figure 13 shows the pulse output energy versus the total input energy to the flash lamp with $T = 3.3\%$, 5.8%, and 9.84%. The results show that the pulsed laser output energy of 4.05 mJ at 963 nm for Cr^{3+}:$LaSc_3(BO_3)_4$ crystal with the size of $\phi 3.3 \times 11$ mm^3 has been obtained, when pumped by a xenon flash lamp, of which input energy is 13.2 J and the transmittance of the output mirror $T = 3.3\%$ at 963 nm. The over and slope efficiencies are $\eta_o = 0.036\%$ and $\eta_s = 0.04\%$, respectively.

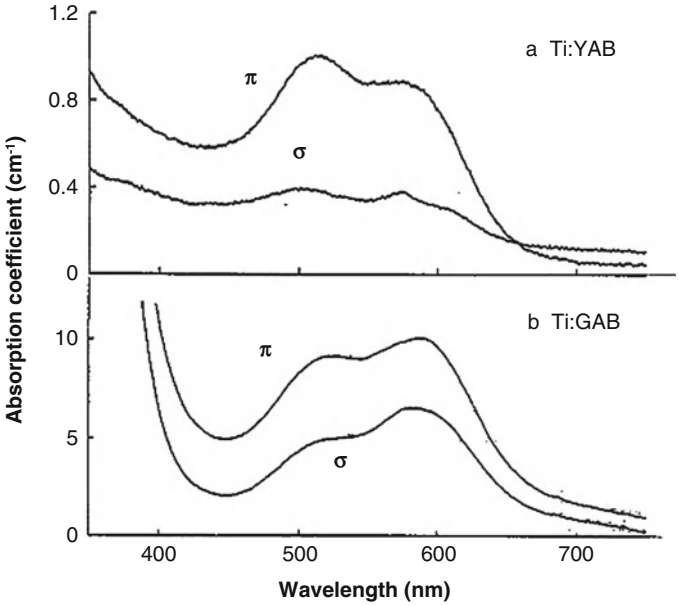

Fig. 14 Absorption spectra of Ti^{3+}:$RAl_3(BO_3)_4$ (R = Y, Gd) at room temperature [43]

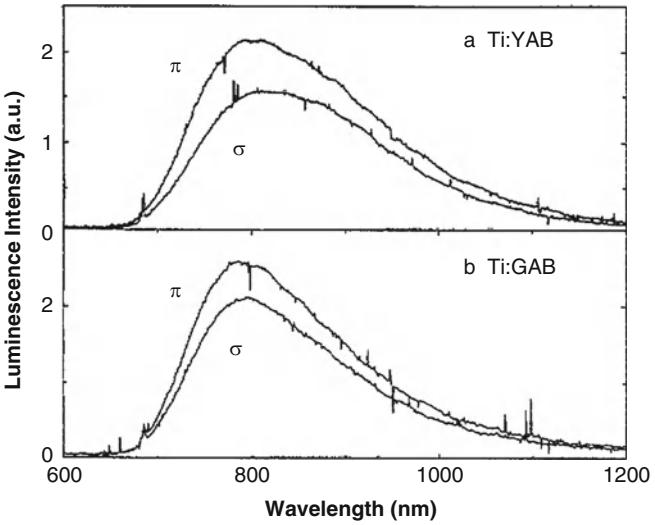

Fig. 15 Photoluminescence spectra of Ti^{3+}:$RAl_3(BO_3)_4$ (R = Y, Gd) at room temperature [43]

Ti^{3+}-doped materials is another much interesting tunable solid-state laser crystal. For example, Ti^{3+}-sapphire laser, which is tunable over the wavelength range 660–1,100 nm at room temperature [72–74], has become the most commercially

successful solid-state laser. Figure 14 shows the absorption spectra of Ti^{3+}:$RAl_3(BO_3)_4$ (R = Y, Gd) at room temperature. Two overlapping broad bands are observed at 514 nm for Ti^{3+}: $RAl_3(BO_3)_4$ (Ti^{3+}:YAB) and at 576 nm Ti^{3+}:$RAl_3(BO_3)_4$ (Ti^{3+}:GAB). These bands correspond to transition from the ground $^2T_2$ state to the excited ^2E state split by a static Jahn–Teller effect. The photoluminescence spectra of Ti^{3+}:$RAl_3(BO_3)_4$ (R = Y, Gd) at room temperature are shown in Fig. 15. The absorption cross-sections are 1.2×10^{-20} cm^2 and 1.0×10^{-20} cm^2 for Ti^{3+}:YAB and Ti^{3+}:GAB crystals, respectively. The strong broad-band emission bands observed for Ti^{3+}:YAB and Ti^{3+}:GAB crystal are due to the $^2E \rightarrow {}^2T_2$ transition of Ti^{3+} ion. The broad-band luminescence covers the wavelength range 650–1,200 nm with peaks at 760 nm (π-polarization) and 775 nm (σ-polarization) for Ti^{3+}:YAB and 765 nm (π-polarization) and 775 nm (σ-polarization) for Ti^{3+}:GAB. The fluorescence lifetime is 1.0 μs for both crystals. The emission cross-sections are 2.2×10^{-19} cm^2 for Ti^{3+}:YAB and 2.4×10^{-19} cm^2 for Ti^{3+}:GAB. These spectroscopic characterizations of both crystals suggest that Ti^{3+}:YAB and Ti^{3+}:GAB crystals have significant potential as gain media in tunable near-infrared lasers [43].

6 Summary

For many years, the $RX_3(BO_3)_4$ crystals have attracted much attention due to their structure characterization and excellent physical properties. In past three decades, there are publications on Nd^{3+}-, Cr^{3+}-, and Ti^{3+}-doped $RX_3(BO_3)_4$ crystals. With the improvement of the growth technology of these crystals, some of $RX_3(BO_3)_4$ crystals have been becoming excellent laser crystal materials and nonlinear optical crystal materials. For example, Nd^{3+}:$YAl_3(BO_3)_4$ crystal has been becoming an excellent SFD laser crystal, Cr^{3+}:$LaSc_3(BO_3)_4$ crystal can be regarded as a tunable solid-state laser crystal, and the YAB crystal can be used as a potential near UV nonlinear optical crystal.

References

1. Luo ZD, Jiang AD, Huang YC, Qiu MW (1989) Chinese Phys Lett 6:440
2. Wang GF, Lin ZB, Hu ZS, Han TPJ, Gallagher HG, Welld J-PR (2001) J Cryst Growth 233:755
3. Ballman AA (1962) Am Mineral 47:1380–1383
4. Mills AD (1962) Inorg Chem 1:960
5. Hong HH-P, Dwight K (1974) Mat Res Bull 9:1661
6. Wang GF, He MY, Chen WZ, Lin ZB, Lu SF, Wu QJ (1999) Mater Res Innovat 2:341
7. Jarchow O, Lutz F, Klaska KH (1981) Z Krist 149:162
8. Lutz F, Huber G (1981) J Cryst Growth 52:646
9. Zwiker W, Colak S (1983) AD-A119457(US)

10. Belokoneva EL, Timchenko TI (1983) Kristall 28:1118
11. Wang GF, He MY, Luo ZD (1991) Mater Res Bull 26:1085
12. Belokoneva EL, Timchenko TI (1983) Spv Phys Crystallogr 28:658
13. He MY, Wang GF, Lin ZB, Chen WZ, Lu SF, Wu QJ (1999) Mater Res Innovat 2:345
14. Goryunov AV, Kuzmicheva GM, Mukhin BV, Zharikov EV, Ageev AYu (1996) Zhurnal Neorgan Khimii 41:1605
15. Akhmetov SF, Akhmetova GL, Kovalenko VS, Leonyuk NI, Pashkova AV (1978) Sov Phys Dokl 23:107
16. Leonyuk NI (1976) Izv Akad Nauk SSSR, Neorg Mater 12:554
17. Akhmetov SF, Akhmetova GL, Kovalenko LVS, Leoyuk NI, Pashkova AV (1978) Kristallografiya 23:230
18. Azizov AV, Leonyuk NI, Timchenko STI, Belov ANV (1979) Sov Phys Dokl 24:313
19. Leonyuk NI, Pashkova AV, Timchenko TI (1979) Sov Phys Dokl 24:233
20. Azizov AV, Leonyuk NI, Rezvyi VR, Timchenko TI, Belov ANV (1982) Sov Phys Dokl 27:95
21. Wang J, Lu BS, Pan HF, Jiang MH (1986) J Shandong University (Chinese) 21:14
22. Kolov VN, Peshev P (1994) J Cryst Growth 144:187
23. Lu BS, Pan HF (1986) J Shandong University (Chinese) 21:31
24. Leonyuk NI, Azizov AV, Belov ANV (1978) Sov Phys Dokl 27:374
25. Kellendonk F, Blasse G (1981) J Chem Phys 75:511
26. Dianov EM, Dmitruk MV, Karasik AY, Kirpichenkova EO, Osiko VV, Ostroumov VG, Timosheckkin MI, Shcherbakov IA (1980) Sov Quantum Electron 10:1222
27. Chani VI, Shimamura K, Inoue K, Fukuda T, Sugiyama K (1993) J Cryst Growth 132:173
28. Jung ST, Choi DY, Kaug JK, Chung ST (1995) J Cryst Growth 148:207
29. Jung ST, Kang JK, Chung SJ (1995) J Cryst Growth 149:207
30. Chinn SR, Hong HY-P (1975) Opt Commun 15:345
31. Chen C (1988) J Cryst Growth 89:295
32. Timchenko TI, Leonyuk NI, Butzuova GS (1980) Sov Phys Cryst 25:515
33. Lutz F, Ieiss M, Muller J (1979) J Cryst Growth 47:130
34. Lutz F, Ruppel D, Leiss M (1980) J Cryst Growth 48:41
35. Leonyuk NI, Pashkova AV, Semenova TDL (1975) Izv Akad Nauk SSSR, Neorg Mater 11:181
36. Wang GF, Gallagher HG, Han TPJ, Henderson B (1995) J Cryst Growth 153:169
37. Jung ST, Choi DY, Kang JK, Chung SJ (1995) J Cryst Growth 148:207
38. Leonyuk NI, Leonyuk LI (1995) Prog Cryst Growth Charact 31:179
39. Leonyuk NI (1995) Prog Cryst Growth Charact 31:279
40. Ye N, Stone-Sundberg JL, Hruschka MA, Aka G, Kong W, Keszler DA (2005) Chem Mater 17:2687
41. Dhanaraj G, Srinivassn MR, Bhat HL, Jayanna HS, Subramanyam SV (2003) J Appl Phys 76B:289
42. Liu H, Li J, Fang SH, Wang JY, Ye N (2011) Mater Res Innovat 15:102
43. Wang GF, Han TPJ, Gallagher HG, Henderson B (1997) J Cryst Growth 181:48
44. Long XF, Wang GF, Han TPJ (2003) J Cryst Growth 249:191
45. Meyn J-P, Jensen T, Huber G (1994) IEEE J Quantum Electron 30:913
46. Liu H, Chen X, Huang LX, Xu X, Zhang G, Ye N (2011) Mater Res Innovat 15:140
47. Leonyuk NI, Leonyuk LI (1995) Prog Cryst Growth Charact 31:179
48. Leonyuk NI, Flimonov AA (1974) Kristall Tech 9:63
49. Dorozhkin LM et al (1981) Sov Tech Phys Lett 7:555
50. Lu BS et al (1986) Chin Phys Lett 3:411
51. Brenier A (1997) Opt Commun 141:221
52. Jaque D, Capmany J, Qarcia S (1999) Appl Phys Lett 75:325
53. Bbartschke J, Knappe R, Roller KJ (1997) IEEE J Quantum Electron 33:2295
54. Koporulina EV, Leonyuk NI, Hansen D (1998) J Cryst Growth 191:767
55. Jaque D, Capmany J, Sole JG (1999) Opt Eng 38:1794

56. Chen YF, Wang SC, Kao CF, Huang TM (1996) IEEE Photon Technol Lett 8:1313
57. Kück S (2001) Appl Phys B 72:515
58. Samtleben TA, Hulliger J (2005) Opt Laser Eng 43:251
59. Kenyon PT, Andrews L, McCollum B, Lempicki A (1982) IEEE J Quantum Electron QE-18:1189
60. Payne SA, Chase LL, Newkirk HW, Smith LK, Krupke WF (1988) IEEE J Quantum Electron 24:2243
61. Payne SA, Chase LL, Smith LK, Kway WL, Newkirk HW (1989) J Appl Phys 66:1051
62. Kisliuk P, Moore CA (1967) Phys Rev 160:307
63. Struve B, Huber G, Laptev VV, Shcherbakov IA, Zharikov EV (1983) Appl Phys B 30:117
64. Long XF, Lin ZB, Hu ZS, Wang GF (2004) Chem Phys Lett 392:192
65. Lai ST, Chai BT, Long M, Morris RC (1986) IEEE J Quantum Electron 22:1931
66. Wang GF, Gallagher HG, Han TPJ, Henderson B (1996) J Cryst Growth 163:272
67. Walling JC, Peterson OG, Jenssen HP, Morris RC, O'Dell EW (1980) IEEE J Quantum Electron QE-16:1302
68. Lai ST, Shand ML (1983) J Appl Phys 54:5642
69. Walling JC, Heller DF, Samuelson H, Harter DJ, Pete JA, Morris RC (1985) IEEE J Quantum Electron QE-21:1568
70. Meter JV, Barnes NP, Remelius DK, Kokta MR (1986) IEEE J Quantum Electron 22:2058
71. Krupke WF, Shinn MD, Marion JE, Caird JA, Stokowski SE (1986) J Opt Soc Am B 3:102
72. Moulton P (1982) Opt News 8:9
73. Moultion P (1986) J Opt Soc Am B 3:125
74. Moulton PF, Lacovara P, Esterowitz L, Allen R (1985) In: Hammerling P, Budgor A, Pinto A (eds) Tunable solid state lasers. Springer, Berlin

Struct Bond (2012) 144: 121–180
DOI: 10.1007/430_2011_66
© Springer-Verlag Berlin Heidelberg 2012
Published online: 29 February 2012

The Recent Development of Borate SF-Conversion Laser Crystal

Chaoyang Tu, Zhaojie Zhu, Zhenyu You, Jianfu Li, Yan Wang, and Alain Brenier

Abstract As a laser host, Borates possess favorable chemical and physical characteristics as well as higher damnification threshold. Especially, Borates usually have higher nonlinear optical efficiency resulted from its B–O structure. When doped with active ions, Borates can serve as a self-frequency conversion multifunction laser medium. For example, rare-earth ions and Cr^{3+}-doped $RX_3(BO_3)_4$, especially $GdAl_3(BO_3)_4$ and $TmAl_3(BO_3)_4$, are typical self-frequency conversion multifunction laser crystals. After wide surveys of known research on the growth, crystal structure, and properties including thermal, optical, and spectral characteristics and laser property, this chapter reviews the recent advances in the development of these crystals. Self-frequency conversion laser technology including the self-frequency doubling, self-difference-frequency mixing and self-sum-frequency mixing methods were dealt with. As a result, the laser outputs with high efficiency at various wavelengths ranged from UV to IR have been achieved.

Keywords Crystal growth · $GdAl_3(BO_3)_4$ crystal · Optical properties · Self-frequency conversion laser properties · $TmAl_3(BO_3)_4$ crystal

Contents

1 Introduction 122
2 Rare Earth/Cr^{3+}-Doped $GdAl_3(BO_3)_4$ Self-Frequency-Conversion Laser Crystals 124
2.1 The Structure Characteristic of $RX_3(BO_3)_4$ Crystals 124
2.2 The Growth of Pure $GdAl_3(BO_3)_4$ and Rare Earth/Cr^{3+}-Doped Crystals 127

C. Tu (✉), Z. Zhu, Z. You, J. Li, and Y. Wang
Key Laboratory of Photoelectric Materials Chemistry and Physics of CAS, Fujian Institute of Research on the structure of Matter, Chinese Academy of Sciences, Fuzhou, Fujian 350002, China
e-mail: tcy@fjirsm.ac.cn

A. Brenier
Laboratoire de Physico-Chimie des Matériaux Luminescents, UMR CNRS 5620, Université Claude Bernard-Lyon1, F-69622 Villeurbanne, France

2.3 The Thermal Characteristics of $GdAl_3(BO_3)_4$ and $TmAl_3(BO_3)_4$ Crystals 135
2.4 The Refractive Index of Nd^{3+}:$GdAl_3(BO_3)_4$ Crystals 138
2.5 The Spectra Characteristics of Rare Earth /Cr^{3+}-Doped $GdAl_3(BO_3)_4$ Crystals ... 139
2.6 The Laser Characteristics of Pure $GdAl_3(BO_3)_4$ and Nd^{3+}-Doped Crystals 157
3 Summary 177
References 177

1 Introduction

Owing to their advantages including the compactness of the devices, efficiency, low maintenance, and low cost, all-solid-state laser sources are of special importance for a variety of applications: color projection, high-density optical data storage, laser printing, medicine, photodynamic therapy, military devices, biotechnology, submarine communications. Moreover, many of these laser plus-materials can be pumped by commercially available laser diodes, such as around 800 or 900 nm.

Many rare earth ions or transition ions doped in the laser host materials can serve as the emission centers to produce laser with the different specific wavelengths directly. For examples, some specific wavelengths can be achieved by direct laser operation of the most well-known luminescent ions: Nd^{3+}(1.06 μm, 1.3 μm), Yb^{3+}(1.03 μm), Er^{3+}(1.5 μm), Tm^{3+}(1.8–2.0 μm), Ho^{3+}(2.0 μm), Cr^{3+}(0.7–1.0 μm) incorporated into a suitable laser plus crystal or glass host. Furthermore, more new specific wavelengths can be obtained from a second-order nonlinear optical interaction in noncentrosymmetric crystals, such as β-BaB_2O_4, $LiBO_3$, $KTiOPO_4$, BiB_3O_6, $GdAl_3(BO_3)_4$, $YAl_3(BO_3)_4$, $KNbO_3$, $LiNbO_3$, KDP, $KBe_2BO_3F_2$, $Ca_4RO(BO_3)_3$, $K_2Al_2B_2O_7$, BPO_4. Only if the following phase-matching condition is satisfied (here restricted to collinear type I phase matching), the second-order nonlinearity, mixing three waves and responsible for the frequency conversion is efficiency:

$$\varpi_1 n_1{}^{\uparrow}(\theta,\varphi) + \varpi_2 n_2{}^{\uparrow}(\theta,\varphi) = \varpi_3 n_3{}^{\downarrow}(\theta,\varphi),$$

where the ϖ_i is the angular frequency of the wave i, which is proportional to $\frac{1}{\lambda i}$, $n_i{}^{\uparrow}(\theta,\phi), n_i{\downarrow}(\theta,\phi)$are the larger and weaker refractive index in the direction of propagation, corresponding to the slow and fast waves, respectively.

If the laser effect and the nonlinear optical phenomena occur simultaneously inside the same crystal, simplifying the devices, a simplified and attractive scheme namely the self-frequency conversion process is obtained. Only if the following two conditions are satisfied (here restricted to collinear type I phase matching), an optical nonlinear crystal can serve as the self-frequency conversion crystal: (1) the crystal must provide the localities for luminescent ions; (2) the crystal must be phase matchable for its laser emission. Based on the phase-matching condition and depending upon which wave is the laser wave, three devices shown in Table 1 can be designed: (1) the self-frequency doubling (SFD) laser, (2) the self-sum-frequency mixing (SSFM) laser, and (3) the self-difference-frequency mixing (SDFM) laser.

Table 1 Self-frequency conversion technology

Pump	ω_θ	ω_3	ω_1
Self-frequency conversion technology	SFD method (self-frequency doubling)	SDFM method (self-difference-frequency mixing)	SSFM method (self-sum-frequency mixing)
Laser	Laser $\omega_1 = \omega_2$;$\omega_3 = 2\omega_2$	Laser ω_2, $\omega_1 = \omega_3 - \omega_2$	Laser ω_2, $\omega_3 = \omega_1 + \omega_2$

Table 2 Main optical and spectroscopic properties of Nd-doped and Yb-doped LNB,YAB,BNN and GdCOB crystals

	τ (μs)	σ_p (10^{-20} cm^2)	σ_L (10^{-20} cm^2)	σ_2 (10^{-20} cm^2)	d_{eff} (pm/v)	n	λ_L (nm)	λ_p (nm)
NYAB	60	3.8	20/100.3	0.47	1.4	1.78	1,062	808
LNB:Mg:Nd	120	5.4	5.1	0.3	5.9	2.23	1,094	810
GdCOB:Nd	68	2.23	1.9	0.22	0.53	1.7	1,060	810
BNN:Nd	180	2.8	2	0.49	13.2	2.25	1,071	800
YAB:Yb	680	3.4	0.8	0	1.4	1.78	1,040	975
GdCOB:Yb	2,500	1.1	0.5	0	0.53	1.7	1035.3	975
LNB:Yb	540	1.55	0.15	0	5.9	2.23	1,060	980

There are only a few crystals, which satisfy these requirements and have been tried with success. These crystals are $LiNbO_3$ (LNB), $LaBGeO_5$ (LBG), $Ba_2NaNb_5O_{15}$ (BNN), $YAl_3(BO_3)_4$ (YAB), $GdAl_3(BO_3)_4$ (GAB),$Ca_4YO(BO_3)_3$ (YCOB), $Ca_4GdO(BO_3)_3$ (GCOB). Table 2 shows the main optical and spectroscopic properties of Nd-doped and Yb-doped LNB, YAB, BNN, and GdCOB crystals. Table 3 shows the main result of SFD lasers of Nd-doped crystals.

Due to the three and fourfold coordination of B, Borates have many complicated structure groups, which includes: $(BO_3)^{3-}$, $(BO_4)^{5-}$, $(B_2O_5)^{4-}$, $(B_2O_7)^{8-}$, $(B_3O_6)^{3-}$, $(B_3O_7)^{5-}$, $(B_3O_8)^{7-}$, $(B_3O_9)^{9-}$, $(B_4O_9)^{6-}$, and $(B_5O_{10})^{5-}$. The planar borate rings containing π-orbital systems are more favorable for the large second-order susceptibilities but go against the shorter absorption edge, compared with the nonplanar groups containing no π-conjugation. For instance, the absorption edges of the planar groups lie within the wavelength of 190–200 nm, while those of nonplanar groups can move to 160 nm.

$GdAl_3(BO_3)_4$ (GAB) crystal belongs to the $RX_3(BO_3)_4$ [R = Y,Gd,Nd,La,Lu, Ytb,Dy,Er,Yb; X = Al, Sc,Ga] family crystals. One type of BO_3 groups in GAB crystal structure parallel to each other and form the planar borate rings, which is favorable for a larger second-order susceptibilities. Because the radius of Gd^{3+} ion is something larger than those of luminescent ions Nd^{3+}, Yb^{3+}, Tm^{3+} ions, it is easier to be replaced by latter. Incorporated with these luminescent ions, $GdAl_3(BO_3)_4$ (GAB) crystal will become a self-frequency conversion crystals. In this chapter, the study on the rare earth-doped $Al_3Gd(BO_3)_4$ self-frequency conversion laser crystals is covered. The growth, crystal structure and thermal, optical, and spectral characteristics of these crystals are presented. The series self-frequency conversion laser characteristics are also presented.

Table 3 Main result of SFD lasers of Nd-doped crystals

Crystal	Input power (mW)	Out power (mW)	Pumping	Reference
LNB:MgO	100	0.2	D/QCW	[1]
LNB:Sc_2O_3	65	0.14	TS/QCW	[2]
LNB:MgO	215	1	Dye	[3]
NYAB	1,380	51	D/CW	[4]
NYAB	369	35	D/CW	[5]
NYAB	400	69	D/CW	[6]
NYAB	870	10	D/CW	[7]
NYAB	280	3	D/CW	[8]
NYAB	1,600	225	D/CW	[9]
NYAB	2,200	450	TS/CW	[9]
GdCOB	1,600	192	TS/CW	[10]
GdCOB	1,250	115	D/CW	[11]
YCOB	900	62	D/CW	[12]
LBG	600	0.09	TS/CW	[13]
BNN	270	46	TS/CW	[14]
LNB:Zn	430	0.65	TS/CW	[15]
LNB:MgO	850	18	Dye	[16]
Nd,Lu:YAB	880	24	D/CW	[17]

2 Rare Earth/Cr^{3+}-Doped $GdAl_3(BO_3)_4$ Self-Frequency-Conversion Laser Crystals

2.1 The Structure Characteristic of $RX_3(BO_3)_4$ Crystals

$RX_3(BO_3)_4$ [R = Y,Gd,Nd,La,Lu,Tb,Dy,Er,Yb; X = Al, Sc,Ga] and $RCr_3(BO_3)_4$[R = Sm,Gd] were first reported by Ballman [18], which were synthesized by a flux method from K_2SO_4-3MoO_3 and PbF_2-3B_2O_3 flues. These compounds were confirmed to be isostructural with the mineral huntite $CaMg_3(CO_3)_4$ with space group R32 [19]. For example, Hong et al. first reported that the structure of $NdAl_3(BO_3)_4$ crystal belongs to hexagonal with space group R32 and the unit cell dimensions of $a = 9.341$ Å, $c = 7.3066$ Å, $Z = 3$ [20]. However, some other structures were detected from these compounds subsequently. For example, the structures of monoclinic with two space groups C2/c and C2 were discovered in $NdAl_3(BO_3)_4$ crystal by Jarchow in 1979. The above three crystal phase structures were also determined in $NdAl_3(BO_3)_4$ crystal by Lutz and Zwiter in 1981 and 1983 [21]. Two space groups R32 and C2 were also determined in $GdAl_3(BO_3)_4$ crystal structure [22]. And $LaSc_3(BO_3)_4$ crystal also exists the above three phase structures [23, 24]. The concomitant structures lead to the presence of twinned crystal, which results in the wrapper and crack of crystal and thus reduces the crystal quality.

Although $RX_3(BO_3)_4$ crystals exist three phase structures, they always consist of the distorted RO_6 trigonal prisms, XO_6 distorted octahedra and planar triangular BO_3 groups. The distorted RO_6 trigonal prisms are isolated from each other by X^{3+} ions and couple each other by O–X–O. Therefore, distance between R–R ranges

from 5.596 Å to 6.623 Å, which results in a weaker interaction between laser upper-levels of doped active ions, such as Nd^{3+},Yb^{3+}. As a result, the rare earth active ions-doped $RX_3(BO_3)_4$ crystals display an advantage of lower fluorescence concentration quenching effect [20, 23–25]. Among the two types of isolated BO_3 groups in the structure, one type of BO_3 groups parallels to each other, which is in favor of the higher SHG coefficient of $RX_3(BO_3)_4$ crystals. Therefore, the SHG coefficient of $RX_3(BO_3)_4$ crystals is about four times as large as that of KDP. As a result, the rare earth active ions-doped $RX_3(BO_3)_4$ crystals become an attractive multifunction optical materials, namely self-frequency-conversion laser crystals, in which the laser effect and the nonlinear optical phenomena occur simultaneously inside the same crystal, simplifying the device.

As an example, the structure of $TmAl_3(BO_3)_4$ – a new crystal of $RX_3(BO_3)_4$ family grown by Guohua Jia recently – is presented here. Its crystal structure was also determined and resolved by Dr. Jia [26]. $TmAl_3(BO_3)_4$ crystallizes in the trigonal system R32 (No. 155) and the cell parameters determined are $a = 9.2741$ (13), $c = 7.218(3)$, $\gamma = 120^{o}$, $v = 537.7(2)$ $Å^3$, Dc = 4.494 g/cm^3, and $Z = 3$.

Similar to the other known crystal of $RX_3(BO_3)_4$ family, in this compound there are three kinds of coordinations with oxygen: distorted TmO_6 trigonal prisms, AlO_6 octahedra, and two types of triangular BO_3 groups (shown in Fig. 1). Among the two types of isolated BO_3 groups, one set of B(2) is perpendicular, which are isosceles triangles with their double-fold rotation axis parallel to the ab crystal plane, the other set of B(1) nearly so, to the *c*-axis. The Al^{3+} and Tm^{3+} ions occupy oxygen octahedral and trigonal prisms, respectively. Edge-shared Al^{3+} octahedral form helices along the *c*-axis, the average distance of Al–O range from 1.860(2) to 1.928(2) Å. The Tm^{3+} cations, which are located between adjacent layers of anions, are coordinated to six O(3) atoms, three of them are common to the B(2) borate anions of the layer above and the other three anions with B(2) borates of the layer below. The Tm–O bands are equally 2.305(2) Å.

The huntite structure of $TmAl_3(BO_3)_4$ can be viewed as formed by layers normal to the *c*-axis (shown in Fig. 2) in which there are TmO_6 prisms and smaller AlO_6 octahedra. The three AlO_6 octahedra repeat edge-sharing forms the infinite

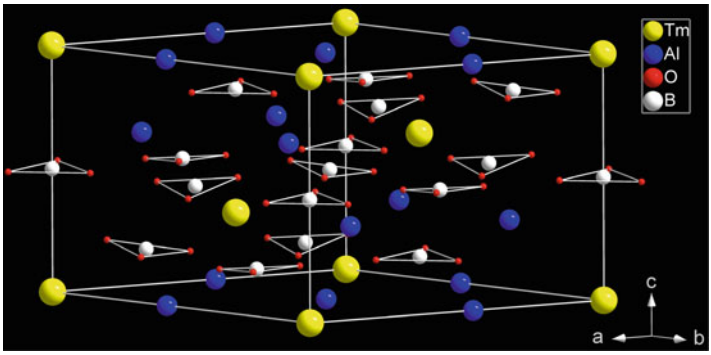

Fig. 1 View of the TmO_6 trigonal prism and AlO_6 octahedra, BO_3 triangle in the structure of $TmAl_3(BO_3)_4$

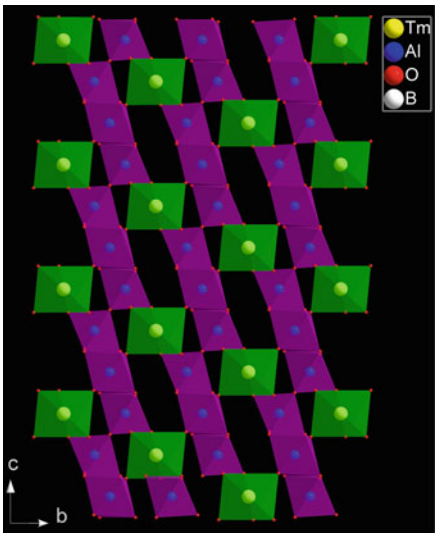

Fig. 2 View of the helicoidal chains of TmO_6 trigonal prism and AlO_6 octahedra parallel to the *c*-axis in $TmAl_3(BO_3)_4$

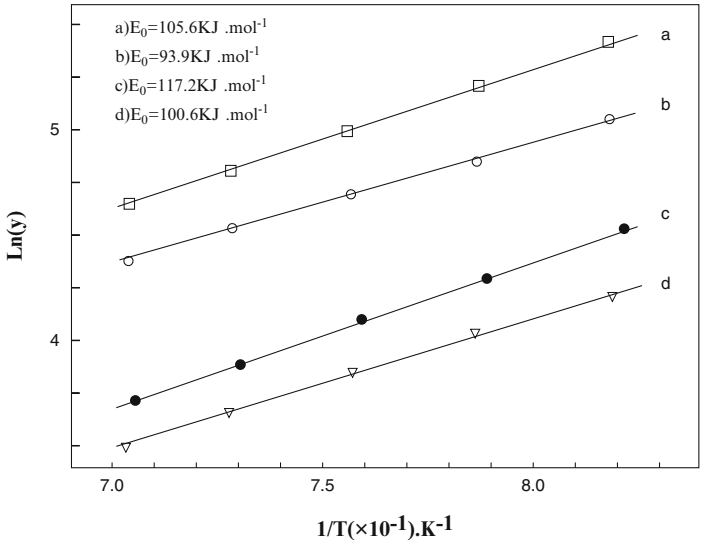

Fig. 3 Arrhenius plot of evaporation rate versus temperature for solutions of (a) $YAl_3(BO_3)_4$ in $K_2Mo_3O_{10}$-B_2O_3; (b) $YAl_3(BO_3)_4$ in $K_2Mo_3O_{10}$; (c) $GdAl_3(BO_3)_4$ in $K_2Mo_3O_{10}$-B_2O_3 and (d) $GdAl_3(BO_3)_4$ in $K_2Mo_3O_{10}$

helicoidal chains along the *c*-axis (shown in Fig. 3). TmO_6 polyhedra are interconnected within the layers by corner sharing with two types of BO_3 trigonal groups and AlO_6 octahedra and the nearest distance between Tm^{3+} ions is as far as 5.870 Å. This unique structure of isolated Tm trigonal prisms will result in a weak interaction and a lower fluorescence concentration quenching effect [20, 27].

2.2 The Growth of Pure $GdAl_3(BO_3)_4$ and Rare Earth/Cr^{3+}-Doped Crystals

2.2.1 Selection of Fluxes

$RAl_3(BO_3)_4$ crystals can only be grown from the high temperature flux solutions except $RSc_3(BO_3)_4$ crystal because $RAl_3(BO_3)_4$ crystals decompose at 1,040–1,050°C and melt incongruently at high temperature [28, 29]. The choice of the appropriate flux certainly is one of the sticking points to obtain the $RAl_3(BO_3)_4$ crystals with the large size and high quality. It is well known that an appropriate flux should meet some essential requirements, such as: (1) The desired crystal should possess high solubility in the flux solutions; (2) without any other stable compound come into being; (3) it has a low volatility at high temperature; (4) it also has a low viscosity; (5) it is innocuity. As usual, the compositions of the mixed fluxs may be varied so as to achieve a compromise among these essential requirements and hence optimize the properties of the flux. Therefore, scientists had made great efforts to explore the appropriate flux. A number fluxes hence were discovered for growing $RAl_3(BO_3)_4$ crystals, such as PbF_2-B_2O_3, $Li_2B_4O_7$, $Na_2B_4O_7$, BaO-B_2O_3, $K_2Mo_3O_{10}$-KF (K_2SO_4, PbF_2),PbF_2-B_2O_3 [30–48]. However, little success was achieved to grow the $RAl_3(BO_3)_4$ crystals with the large size and high quality until $K_2Mo_3O_{10}$-B_2O_3 was used as a flux [48]. Obviously, the higher ionization of F^- ion can not only enhance the solvency of solute but also increase the volatility. The BO_3 triangle units from the composition B_2O_3 of flux form the planar networks by coupling oxygen atoms, which can not only enhance the solubility and depresses the volatility but also increase the viscosity. The high volatility of molybdenum oxide can enhance the volatility of solution greatly.

Although $K_2Mo_3O_{10}$ had been used successfully as a flux for growing $RAl_3(BO_3)_4$ crystals early, there were some serious limitations. The primary two disadvantages are the quite low solubility of desired crystals and the quite high volatility of flux, which result in incomplete dissolution of the solute and the substantive loss of $K_2Mo_3O_{10}$ [37]. The rapid and uncontrolled fluctuations in the growth rate resulted from the substantive loss of $K_2Mo_3O_{10}$ only promised the poor quality crystals with the significant solution inclusions [49]. Fortunately, Cr^{3+} or Nd^{3+}-doped $YAl_3(BO_3)_4$, $GdAl_3(BO_3)_4$, and $Gd_{0.2}Y_{0.766}Al_3(BO_3)_4$ crystals with the large size and high quality were then successfully obtained from the $K_2Mo_3O_{10}$-B_2O_3 flux by author and Prof. Wang et al. [41, 50, 51]. A further investigation demonstrated that the solubility of desired crystals was increased and the volatility of flux was decreased by the addition of B_2O_3 composition, which are shown in Figs. 3 and 4 [52]. The composition region in the $YAl_3(BO_3)_4$-$K_2Mo_3O_{10}$-B_2O_3 ternary system from which Cr^{3+}:$YAl_3(BO_3)_4$ crystal was grown is presented in Fig. 5 [53]. Although it has higher viscosity, $Li_6B_4O_9$ was also used as the flux successfully to grow the new UV nonlinear optical crystals $Lu_{0.66}La_{0.73}Sc_{2.39}(BO_3)_4$ and $Y_{0.57}La_{0.73}Sc_{2.71}(BO_3)_4$ recently so as to abstain the introduction of Mo^{6+}ions into the crystals from $K_2Mo_3O_{10}$-B_2O_3 flux, which can

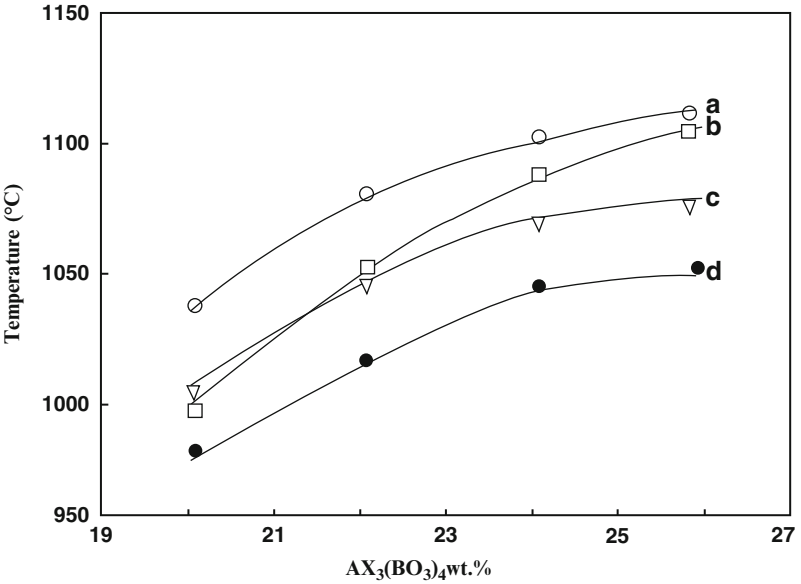

Fig. 4 Solubility curves of (a) $YAl_3(BO_3)_4$ in $K_2Mo_3O_{10}$; (b) $GdAl_3(BO_3)_4$ in $K_2Mo_3O_{10}$ and (c) $GdAl_3(BO_3)_4$ in $K_2Mo_3O_{10}$-B_2O_3

result in the strong UV absorption of the crystals [52, 54]. Recently, $YAl_3(BO_3)_4$ crystal with large size was first grown from Li_2WO_4 –B_2O_3 system by Prof. Ye [55].

2.2.2 Crystal Growth

$LaSc_3(BO_3)_4$ and $NdSc_3(BO_3)_4$ crystals can be grown by the Czochralski method in $RX_3(BO_3)_4$ borate family. Nd^{3+}: $LaSc_3(BO_3)_4$ crystal with dimension $\Phi 20 \times 50$ mm^3 and Nd^{3+}: $LaSc_3(BO_3)_4$ crystal with dimension $\Phi 25 \times 35$ mm^3 have been grown by the Czochralski method [56, 57]. All the rest crystals of $RX_3(BO_3)_4$ borate family can only be grown by top-seeded solution growth (TSSG) method. For example, Nd^{3+}:$YAl_3(BO_3)_4$, Cr^{3+}:$YAl_3(BO_3)_4$, and Ti^{3+}:$YAl_3(BO_3)_4$ crystals have been grown by top-seeded solution growth (TSSG) method early [50, 58, 59].

Recently, the pure $GdAl_3(BO_3)_4$, Nd^{3+}:$GdAl_3(BO_3)_4$, Cr^{3+}: $GdAl_3(BO_3)_4$, Tm^{3+}: $GdAl_3(BO_3)_4$, Yb^{3+}:$GdAl_3(BO_3)_4$, $TmAl_3(BO_3)_4$, and $Gd_{0.2}Y_{0.766}Al_3(BO_3)_4$ crystals were grown from the $K_2Mo_3O_{10}$-B_2O_3 [50, 51, 53, 60–66] using a seed with <001> direction. Figures 6–13 show these as-grown pure $GdAl_3(BO_3)_4$, $TmAl_3(BO_3)_4$, and rare-earth or Cr^{3+}-doped $RAl_3(BO_3)_4$ crystals. The growth of these crystals was carried out in a vertical tubular muffle furnace controlled by an AI-808P artificial intelligence industrial controller to ensure the maintenance of temperature with an accuracy of ±0.2°C and a programmed cooling rate. A Pt crucible with the diameter

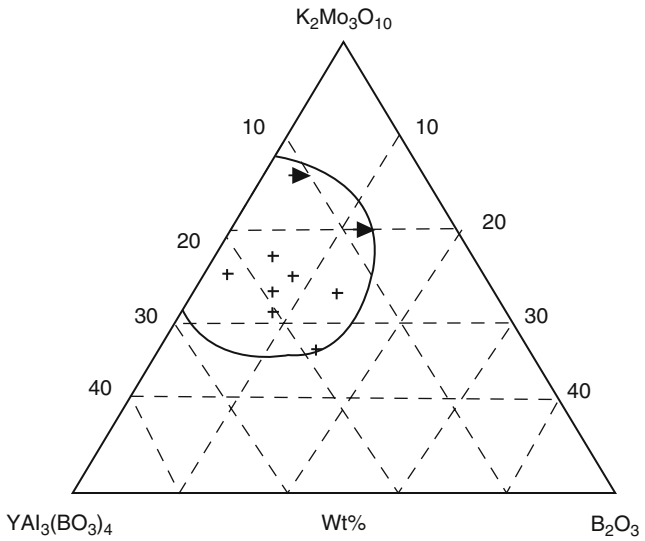

Fig. 5 The region in the $YAl_3(BO_3)_4 - K_2Mo_3O_{10}$-$B_2O_3$ ternary system from which crystals Cr^{3+}: YAB were grown. Specific compositions are indicated by the symbol (*plus*) in the diagram

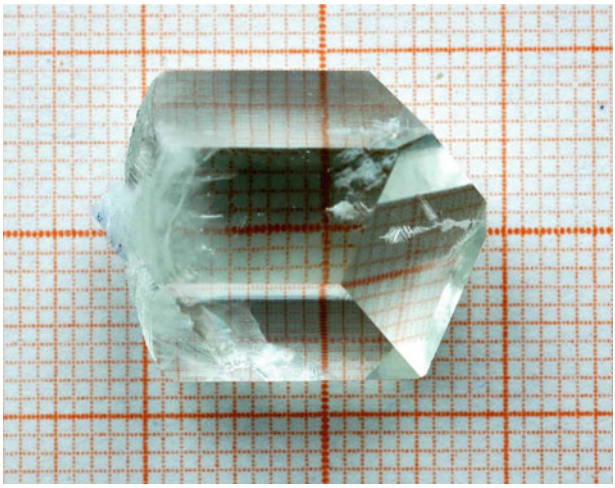

Fig. 6 As-grown pure $GdAl_3(BO_3)_4$ crystal

of 60 mm was used. The crystal was grown using 87 mol%$K_2Mo_3O_{10}$-13 mol%B_2O_3 as the flux. The mixtures were synthesized according to the following reactions:

$$3Al_2O_3 + xR_2O_3 + (1 - x)Gd_2O_3 + 8H_3BO_3 \rightarrow 2Gd_{(1-x)}R_xAl_3(BO_3)_4 + 12H_2O\uparrow$$
$$3MoO_3 + K_2CO_3 \rightarrow K_2Mo_3O_{10} + CO_2\uparrow$$
$$2H_3BO_3 \rightarrow B_2O_3 + 3H_2O\uparrow$$

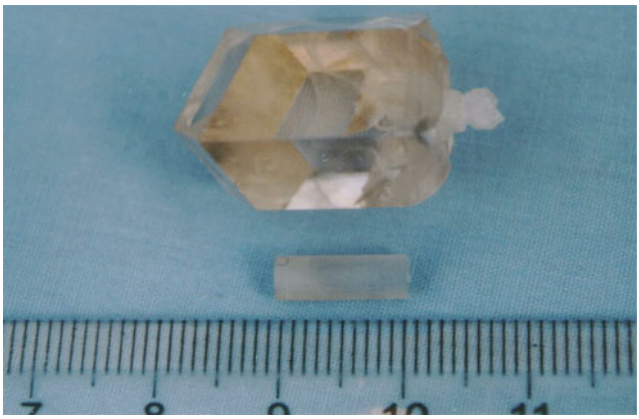

Fig. 7 As-grown Nd^{3+}:$GdAl_3(BO_3)_4$ crystal

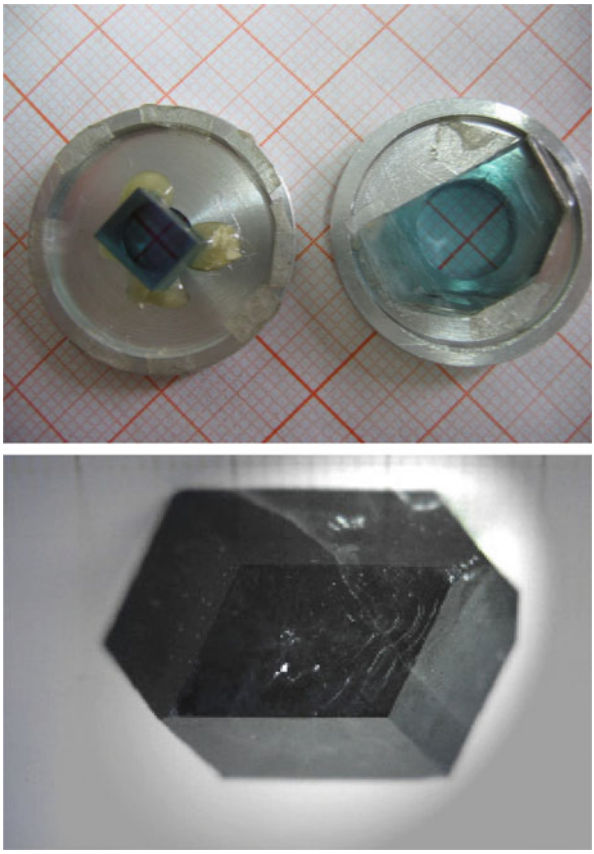

Fig. 8 As-grown Cr^{3+}: $GdAl_3(BO_3)_4$ crystal

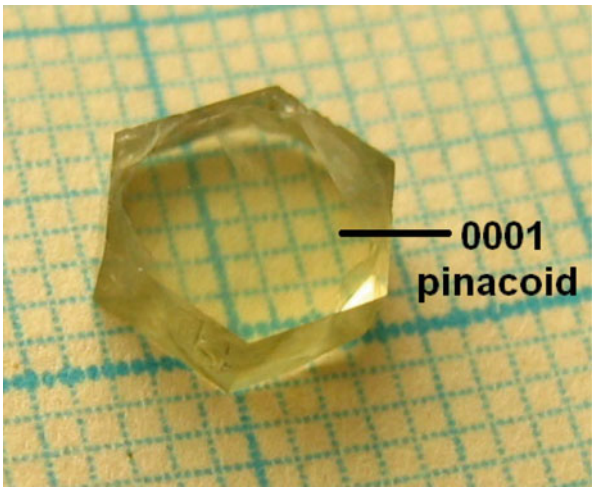

Fig. 9 As-grown $TmAl_3(BO_3)_4$ crystal

Fig. 10 As-grown $Gd_{0.2}Y_{0.766}Al_3(BO_3)_4$ crystal

The temperature gradient of the stove was shown in Fig. 14, which contributed to the improvement of the crystal quality. The growing crystal was rotated at a rate of 10–20 rpm, and the cooling rate was 1–3°C/day. After about 40 days, the process was over and the crystal was drawn out of the melt. Then it was cooled down to room temperature at the rate of 50°C/h.

Table 4 lists the grown crystals of $RX_3(BO_3)_4$ borate family. Some crystals generally contained more or less inclusion and crack. Some grown crystals demonstrated the excellent quality, such as Nd^{3+}:$GdAl_3(BO_3)_4$ and Tm^{3+}:$GdAl_3(BO_3)_4$ crystals shown in Figs. 7 and 11.

From the figures of as-grown crystals, the grown $RAl_3(BO_3)_4$ single crystal presents hexagonal prisms elongated along the *c*-axis. RAB crystals, like huntite, tend to grow with well-developed faces as a result of similarity of their structures

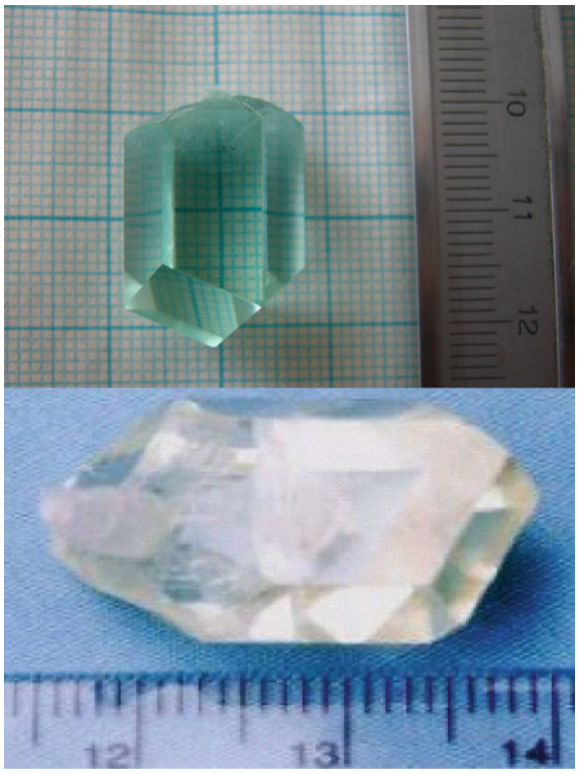

Fig. 11 As-grown Tm^{3+}: $GdAl_3(BO_3)_4$ crystal

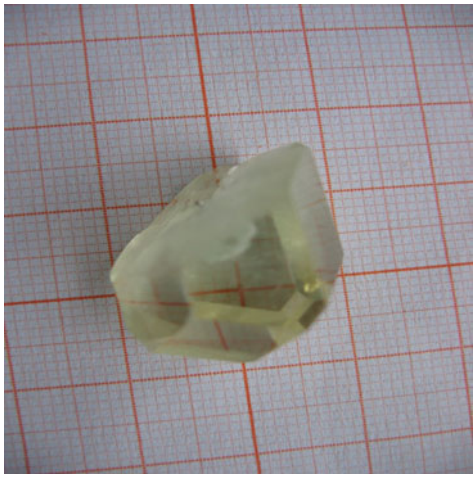

Fig. 12 As-grown Yb^{3+} (5at%):$GdAl_3(BO_3)_4$ crystal

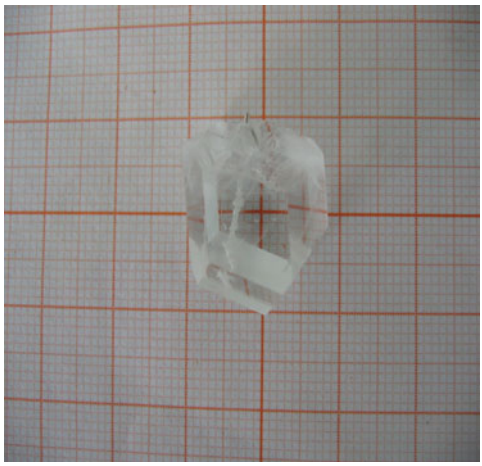

Fig. 13 As-grown Yb^{3+} (10at%):$GdAl_3(BO_3)_4$ crystal

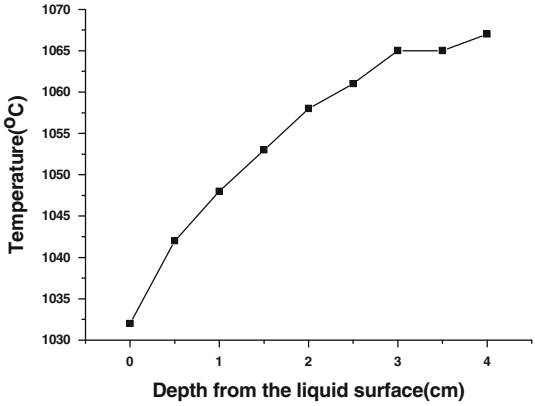

Fig. 14 Temperature gradient of the stove

Table 4 The crystals of $RX_3(BO_3)_4$ borate family grown by TSSG method

Crystals	Flux	Crystal size	Ref.
Nd^{3+}:$YAl_3(BO_3)_4$	Unknown	Up to 45 mm	[59]
Nd^{3+}:$GdAl_3(BO_3)_4$	$K_2Mo_3O_{10}$-LiF	20 × 18 × 15 mm^3	[67]
Cr^{3+} :$YAl_3(BO_3)_4$	$K_2Mo_3O_{10}$-B_2O_3	22 × 16 × 12 mm^3	[50, 53]
Yb^{3+}:$YAl_3(BO_3)_4$	$K_2Mo_3O_{10}$-B_2O_3	15 × 10 × 10 mm^3	[68]
Yb^{3+}:$YAl_3(BO_3)_4$	$K_2Mo_3O_{10}$-PbF-PbO	15 × 15 × 30 mm^3	[69]
Yb^{3+}:$GdAl_3(BO_3)_4$	K_2O-MoO_3-B_2O_3	5 × 10 × 10 mm^3	[70]
$Lu_{0.66}La_{0.95}Sc_{2.39}(BO_3)_4$	$Li_6B_4O_9$	30 × 28 × 6 mm^3	[54]
$YAl_3(BO_3)_4$	Li_2O-WO_3	20 × 15 × 10 mm^3	[55]
$Y_{0.57}La_{0.72}Sc_{2.71}(BO_3)_4$	$Li_6B_4O_9$	30 × 30 × 30 mm^3	[52]

and crystallochemical peculiarities of $[BO_3]^{3-}$ triangles and $[RO_6]^{3-}$ trigonal prisms. The RAB crystals can visually be divided into two habit types:

1. Crystals having approximately equal rhombohedral faces $(10\bar{1}1)$, $(0\bar{1}11)$, and $(\bar{1}101)$ along the threefold axis;
2. Crystals with strongly developed rhombohedron indexed as $(1\bar{2}10)$, $(2\bar{1}\bar{1}0)$, and $(1\bar{1}20)$.

Goniometric measurements allowed one to determine the following simple forms: trigonal prisms $(11\bar{2}0)$ and $(2\bar{1}\bar{1}0)$, and rhombohedron $(10\bar{1}1)$. Also, it is found that $(0\bar{1}11)$ and $(\bar{1}\,101)$ rhombohedra are stable growth faces for all the huntite crystals. Figure 15 shows the grown RAB single crystal with nine well developed faces indexed as $(10\bar{1}1)$, $(0\bar{1}11)$, $(\bar{1}101)$, $(1\bar{2}10)$, $(\bar{1}2\bar{1}0)$, $(2\bar{1}\bar{1}0)$, $(\bar{2}110)$, $(\bar{1}\bar{1}20)$ and $(11\bar{2}0)$. Among the above faces, the corresponding faces parallel to $(1\bar{2}10)$, $(2\bar{1}\bar{1}0)$ and $(\bar{1}\bar{1}20)$ are $(\bar{1}2\bar{1}0)$, $(\bar{2}110)$, $(11\bar{2}0)$, respectively. Figure 13 presents the as-grown single crystal and the growth morphology. The dominance of the $(1\bar{2}10)$ faces is thought to be attribute to adsorption of a layer of molybdate ions on these faces, which is the most favorable for epitaxial adsorption of MoO_3 [71]. This is the most prominent face, which dominates the crystal morphology. Figure 9 shows a sample cut from the grown $TmAl_3(BO_3)_4$ crystal with two parallel transverse sections perpendicular to the *c*-axis. The sample with two polished faces indexed as (0001) was good, transparent, straw yellow. The basal pinacoids are benzene-ring alike, which are perpendicular to the other three pair of parallel faces indexed as $(1\bar{2}10)$, $(2\bar{1}\bar{1}0)$, $(\bar{1}\bar{1}20)$, $(\bar{1}2\bar{1}0)$, $(\bar{2}110)$ and $(11\bar{2}0)$. The $TmAl_3(BO_3)_4$ crystal is chemically stable and its hardness is similar to that of YAG crystals.

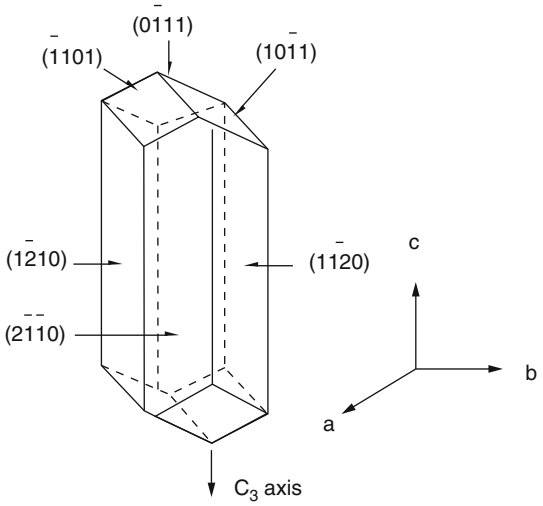

Fig. 15 Growth morphology of the crystal

2.3 The Thermal Characteristics of $GdAl_3(BO_3)_4$ and $TmAl_3(BO_3)_4$ Crystals

Measurements of thermal expansion have greatly increased our knowledge of material properties such as lattice dynamics, electronic and magnetic interactions, thermal defects, and phase transitions [72]. As a significant part of the power pump is converted into heat inside the material during laser operation, it is important to know its linear thermal expansion coefficients to predict how the material behaves when the temperature increases [73]. As regards hexagonal with space group R32, thermal expansion coefficients can be expressed as the following tensor,

$$\alpha_{ij(\mathrm{TAB})} = \begin{vmatrix} \alpha_1 & 0 & 0 \\ 0 & \alpha_1 & 0 \\ 0 & 0 & \alpha_3 \end{vmatrix}.$$

There are only two independence expansion factors: α_1 and α_3, which are along crystallographic *a*- and *c*-axes, respectively.

The sample lengths of the three crystallographic *a*- and *c*-axes were 3.68 mm and 4.06 mm for $TmAl_3(BO_3)_4$ Crystal, 4.28 mm and 4.32 mm for $GdAl_3(BO_3)_4$ Crystal, respectively. The figure of linear expansions versus temperature was shown in Figs. 16 and 17. The linear thermal expansion coefficient is defined as:

$$\alpha = \frac{1}{T}\frac{\Delta L}{\Delta T},$$

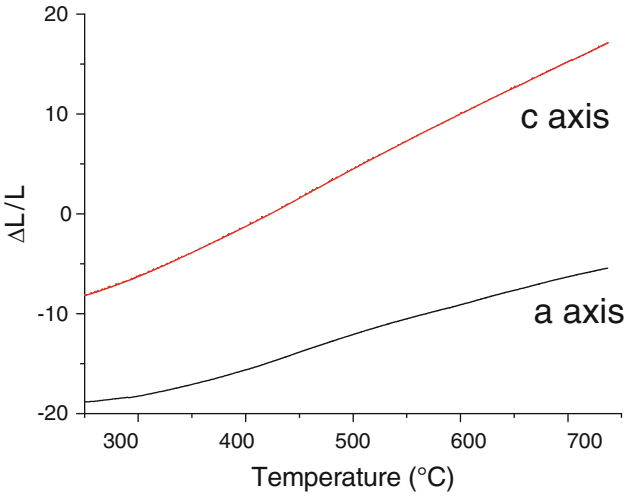

Fig. 16 Linear thermal expansion in a function of temperature along the crystallographic (001), (100) directions of $GdAl_3(BO_3)_4$ crystal

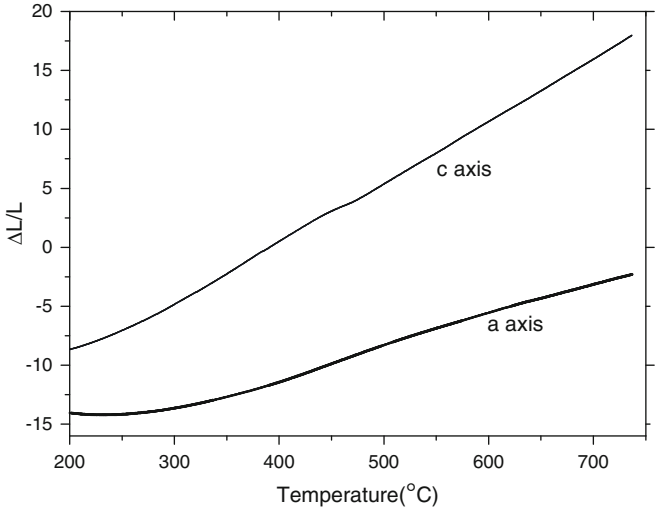

Fig. 17 Linear thermal expansion in a function of temperature along the crystallographic (001), (100) directions of $TmAl_3(BO_3)_4$ crystal

where L is the initial length of the sample at room temperature and ΔL is the change in length when the temperature changes ΔT. We can calculate the thermal expansion coefficient from the slope of the linear fitting of the linear relationship between $\Delta T/T$ and the temperature. In this case, the linear thermal expansion coefficients for different crystallographic direction c-, and a-axes of $TmAl_3(BO_3)_4$ Crystal are $2.46 \times 10^{-6}\,^{\circ}C^{-1}$, $5.33 \times 10^{-6}\,^{\circ}C^{-1}$, respectively.

$$\alpha_{ij(\mathrm{TAB})} = \begin{vmatrix} 2.46 & 0 & 0 \\ 0 & 2.46 & 0 \\ 0 & 0 & 5.33 \end{vmatrix} \times 10^{-6}\,^{\circ}\mathrm{C}.$$

The linear thermal expansion coefficients for different crystallographic direction c- and a-axes of $GdAl_3(BO_3)_4$ crystal are $5.33 \times 10^{-6\circ}C^{-1}$, $1.88 \times 10^{-5\circ}C^{-1}$, respectively. Table 5 shows the comparison of thermal expansion coefficiencies between $GdAl_3(BO_3)_4$ and $TmAl_3(BO_3)_4$crystals.

$$\alpha_{ij(\mathrm{GAB})} = \begin{vmatrix} 5.33 & 0 & 0 \\ 0 & 5.33 & 0 \\ 0 & 0 & 18.8 \end{vmatrix} \times 10^{-6\circ}\mathrm{C}.$$

It shows that the thermal expansion coefficients are positive as no thermal contraction occurs when the crystal is heated. In the uniaxial $TmAl_3(BO_3)_4$ and $GdAl_3(BO_3)_4$ crystals, the thermal properties perpendicular to the crystallographic c-axis are theoretically equivalent. The value of thermal expansion along the c-axis is about two times larger than that of the a-axis. Thus, crystal growth along the c-axis can largely avoid internal pressure and fracture of these crystals.

Table 5 Comparison of thermal expansion coefficiencies between $GdAl_3(BO_3)_4$ and $TmAl_3(BO_3)_4$crystals

Crystals	Average thermal expansion coefficient ($°C^{-1}$)	
	(001)	(100)
$GdAl_3(BO_3)_4$	5.35×10^{-6}	2.98×10^{-6}
$TmAl_3(BO_3)_4$	5.33×10^{-5}	2.46×10^{-6}

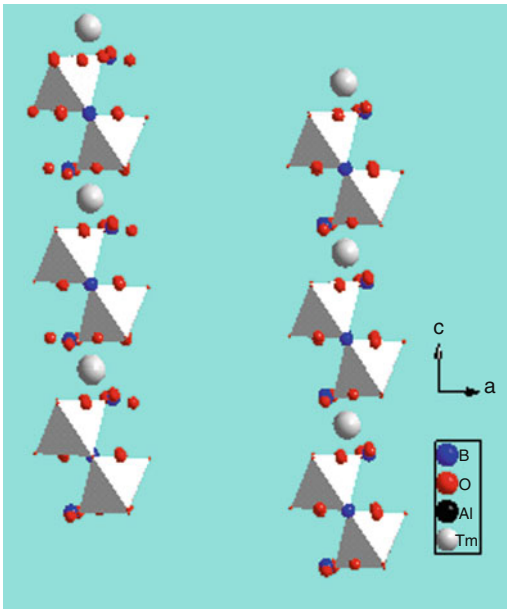

Fig. 18 View of the helicoidal chains of AlO_6 octahedra parallel to the *c*-axis in $TmAl_3(BO_3)_4$

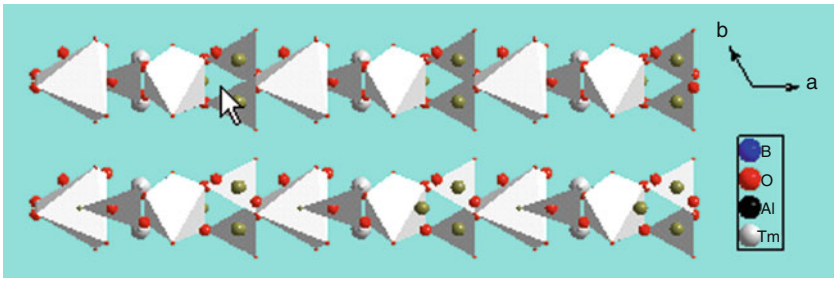

Fig. 19 Chains of projection on the ab plane of the $TmAl_3(BO_3)_4$

The large differences of thermal expansion coefficients between the *c*- and *a*-crystallographic axes can be explained based on the structure of this crystal. The structure of the $TmAl_3(BO_3)_4$ can be viewed as formed by layers normal to the *c*-axis (Fig. 18) in which there are TmO_6 and AlO_6 octahedra. TmO_6 polyhedra are interconnected within the layers. Figure 19 shows the projection on the *ac*-plane of $TmAl_3(BO_3)_4$. AlO_6 octahedra form helicoidal chains, which run parallel to the *c*-axis. TmO_6 trigonal prisms are isolated polyhedra, and each of them connects three

helicoidal chains of AlO_6 octahedra through common O oxygen atoms. This unique helical structure contributes to more internal extension along the *c*-axis when the crystal is heated. Consequentially, the relative expansion value in the *c*-axis direction is larger than that in the *a*-axis, which leads to a larger thermal expansion coefficient in the *c*-axis direction. This explanation is also propitious to $GdAl_3(BO_3)_4$ crystal.

In the uniaxial $GdAl_3(BO_3)_4$ and $TmAl_3(BO_3)_4$ crystals, the thermal properties perpendicular to the crystallographic *c*-axis are theoretically equivalent. The value of thermal expansion along the *c*-axis is about two times larger than that of the *a*-axis. Thus, crystal growth along the *c*-axis can largely avoid internal pressure and fracture of these crystals.

2.4 The Refractive Index of Nd^{3+}:$GdAl_3(BO_3)_4$ Crystals

The minimum deviation technique with a prism sample is a popular method used in the refractive index measurements [74]. To full characterize Nd^{3+}:$GdAl_3(BO_3)_4$ in terms of refractive indices as a function of wavelength, we have measured them with a precision of 1×10^{-4} at several different wavelength from the visible to the near infrared. These data listed in Table 6 were fitted by the least-square method according to the Sellmeir equation [75]

$$n^2(\lambda) = A + B_1/(\lambda^2 + B_2),$$

where λ is the wavelength, and A, B_1, and B_2 are the Sellmeir parameters. By fitting the data reported in Table 6, the following equations (λ is in the unit of μm) were obtained:

$$n_o^2 = 3.07389 + \frac{0.03079}{\lambda^2 + 0.03265}$$

$$n_e^2 = 2.82998 + \frac{0.0242}{\lambda^2 + 0.03127}.$$

Changes in the temperature of the polarization crystal will cause changes in refractive index and the phase-matching angle varies with changes of the refractive

Table 6 The refractive indices measured from the visible to the near infrared

λ(Å)	n_o	n_e	Δn
4,368	1.7921	1.7144	0.0777
4,861	1.7851	1.7089	0.0762
5,321	1.7801	1.7050	0.0751
5,461	1.7792	1.7036	0.0756
5,893	1.7760	1.7012	0.0748
6,328	1.7733	1.6991	0.0742
6,563	1.7723	1.6980	0.0743
7,065	1.7694	1.6955	0.0739
10,642	1.7603	1.6884	0.0719

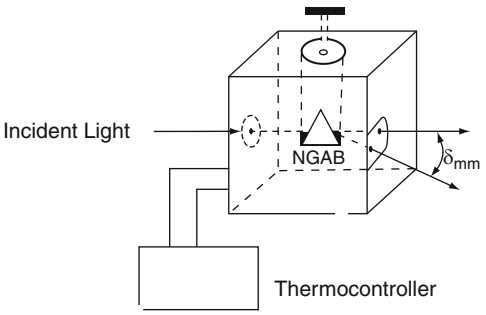

Fig. 20 The experimental furnace

Table 7 Relationship between refractive indices n_o, n_e, and temperature (T)

T (°C)	17	20	30	48	65.5	82	103
n_o	1.7760	1.7761	1.7761	1.7762	1.7764	1.7766	1.7768
n_e	1.7011	1.7012	1.7013	1.7014	1.7016	1.7018	1.7020

index. Therefore, the phase-matching angles vary with the changes in the temperature of the polarization crystal. It is very important to measure the temperature coefficients of refractive indices for the application of the crystal. The refractive indices at different temperatures are also measured by the method of the angle of minimum deviation. Figure 20 shows the experimental furnace used for measuring the temperature coefficient of refractive indices. The furnace has two windows through which the light can pass. It was placed on the work platform of angle indicator with the power of 32 J and the level of 0.5 S. The triangular prism of NGAB crystal was placed inside the furnace and the light of sodium lamp used as the source. A DWT-702 controller was used to control the temperature. Dates of refractive indices in different temperatures are listed in Table 7 Meanwhile, the temperature coefficients of refractive indices have been calculated as follows:

$$\frac{\Delta n_o}{\Delta T} = 9.30 \times 10^{-6}/^{\circ}\mathrm{C} \qquad \frac{\Delta n_o}{\Delta T} = 1.05 \times 10^{-5}/^{\circ}\mathrm{C}.$$

Obviously, the temperature coefficients of refractive indices n_o and n_e are small, which means that NGAB crystal has a good thermal stability.

2.5 The Spectra Characteristics of Rare Earth /Cr^{3+}-Doped $GdAl_3(BO_3)_4$ Crystals

2.5.1 The Spectra Characteristics of Nd^{3+}:$GdAl_3(BO_3)_4$ Crystal

Nd^{3+}:$YAl_3(BO_3)_4$ and Nd^{3+}:$GdAl_3(BO_3)_4$ crystals are the important self-frequency-conversion laser crystals of Nd^{3+}:$RX_3(BO_3)_4$ borate crystals [61, 63, 76].

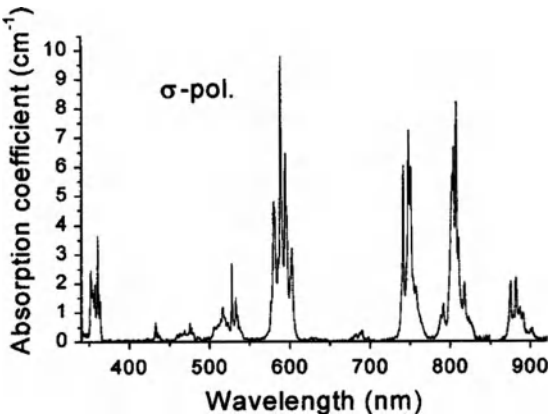

Fig. 21 σ Polarized absorption spectra of NGAB

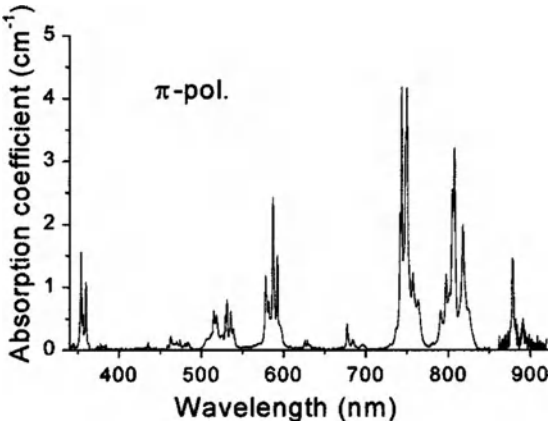

Fig. 22 π Polarized absorption spectra of NGAB

The absorption and emission spectra of Nd^{3+}:$GdAl_3(BO_3)_4$ crystal as functions of σ and π polarizations are presented in Figs. 21–24 [71]. Three main peaks at 802.4, 804.2, and 807.4 nm corresponding to the ${}^4I_{9/2} \rightarrow {}^4F_{5/2},{}^2H_{9/2}$ transition in the absorption spectra are very important for GaAlAs laser diode pumping near 800 nm. The absorption cross section of σ and π polarizations at 800 nm are 5.3×10^{-19} $cm^2$and 5.3×10^{-19} cm^2 , respectively. Table 8 shows the experimental (P_{exp}) and theoretical (P_{th}) oscillator strengths (10^6) of the transitions from the ${}^4I_{9/2}$ ground state for σ and π polarization. The σ-polarized stimulated emission cross section at 1061.9 nm corresponding to ${}^4F_{3/2} \rightarrow {}^4I_{11/2}$ transition is 3.0×10^{-19} cm^2. The σ-polarized stimulated emission cross section at 1061.9 nm corresponding to ${}^4F_{3/2} \rightarrow {}^4I_{13/2}$ is 5.5×10^{-20} cm^2. The radiative lifetime of ${}^4F_{3/2}$ level is 293 μs. Table 9 presents the comparison of optical parameters of NGAB and NYAB crystals.

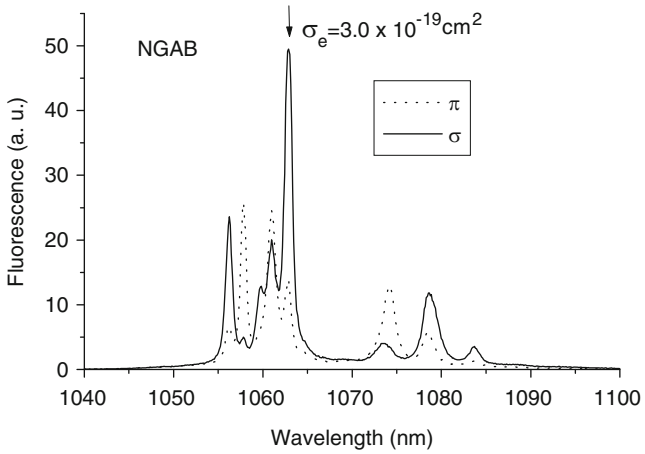

Fig. 23 Polarized emission spectra corresponding to the ${}^4F_{3/2} \rightarrow {}^4I_{11/2}$ transition

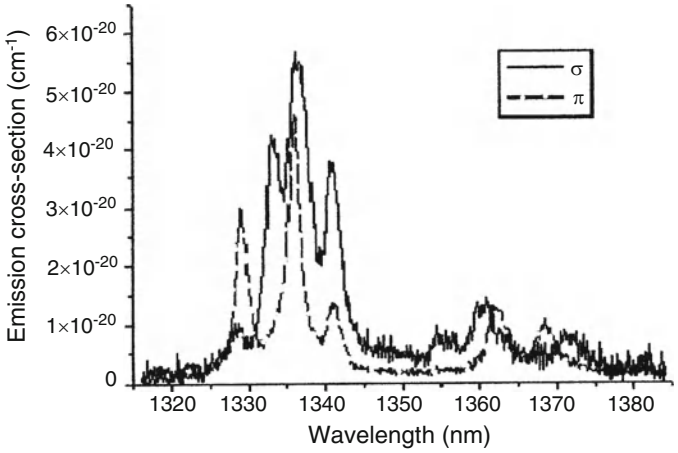

Fig. 24 Polarized emission spectra corresponding to the ${}^4F_{3/2} \rightarrow {}^4I_{13/2}$ transition

2.5.2 The Spectra Characteristics of Yb^{3+}:$GdAl_3(BO_3)_4$ Crystal

The absorption and emission spectra of Yb^{3+}:$GdAl_3(BO_3)_4$ crystal as functions of σ and π polarizations are presented in Figs. 25 and 26 [77]. For the σ-polarization, the intensities of both absorption and emission spectra are stronger than those for the π polarization. The absorption cross section of σ- and π-polarizations at 977 nm are 3.43×10^{-20} cm^2. The σ-polarized stimulated emission cross section at 1,045 nm corresponding to ${}^2F_{5/2} \rightarrow {}^2F_{7/2}$ transition is 0.98×10^{-20} cm^2. The radiative lifetime of ${}^2F_{5/2}$ level is 800 μs. The spectroscopic and laser parameters of Yb:GAB and some Yb-doped crystals are shown in Table 10. Figure 27 shows

Table 8 The experimental (P_{exp}) and theoretical (P_{th}) oscillator strengths (10^6) of the transitions from the $^4I_{9/2}$ ground state for σ- and π-polarizations

Level	Wavelength (nm)	σ Polarization		π Polarization	
		P_{th}	P_{exp}	P_{th}	P_{exp}
$^4F_{3/2}$	880	2.338	2.541	0.835	0.934
$^4F_{5/2} + {}^2H_{9/2}$	808	9.009	9.856	4.593	4.555
$^4F_{7/2} + {}^4S_{3/2}$	750	10.072	9.24	5.734	5.537
$^4F_{9/2}$	681	0.758	0.706	0.409	0.468
$^2H_{11/2}$	628	0.207	0.378	0.112	0.28
$^4G_{5/2} + {}^2G_{7/2}$	587	20.369	20.309	4.071	4.005
$^4G_{9/2} + {}^4G_{7/2} + {}^3K_{13/2}$	525	6.51	7.175	2.426	3.246
$^2G_{9/2} + {}^3D_{3/2} + {}^4G_{11/2} + {}^3K_{15/2}$	470	1.139	2.457	0.472	0.892
$^2P_{1/2} + {}^2D_{5/2}$	431	0.097	1.409	0.318	0.40
$^2P_{3/2}$	385	0.035	0	0.015	0.365
$^4D_{5/2}$	357	11.356	10.926	3.449	3.224

Table 9 Comparison of optical parameters of NGAB and NYAB crystals

Crystal (Ref.)	$\Omega_{2\ eff}$ (10^{-20} cm^2)	$\Omega_{4\ eff}$ (10^{-20} cm^2)	$\Omega_{6\ eff}$ (10^{-20} cm^2)	τ_{rad} (μs)	$\beta_{1.00}$	σ_e (laser) (10^{-19} cm^2)
NGAB (this work)	3.118	2.6876	5.343	293	0.55	3.0
NGAB 11	1.807	1.815	3.793	377	0.523	
NYAB 13	3.09	5.04	3.11	302	0.431	1.0
NYAB 16	1.79	2.44	3.25	409	0.499	
NYAB 17	3.83	2.58	6.0	267	0.522	2.2

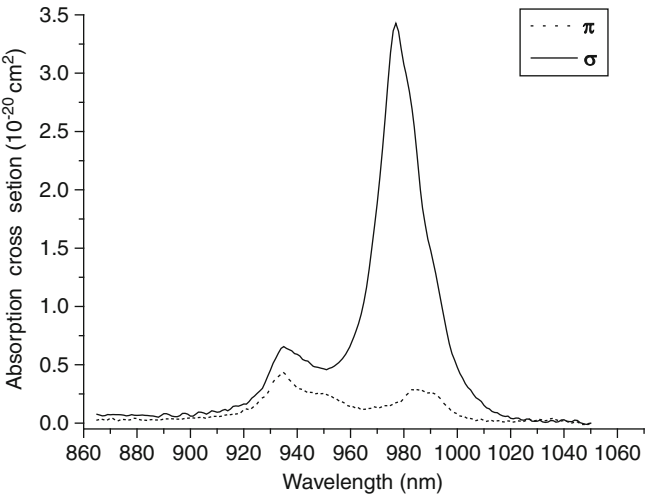

Fig. 25 The polarized absorption spectra of YbGAB

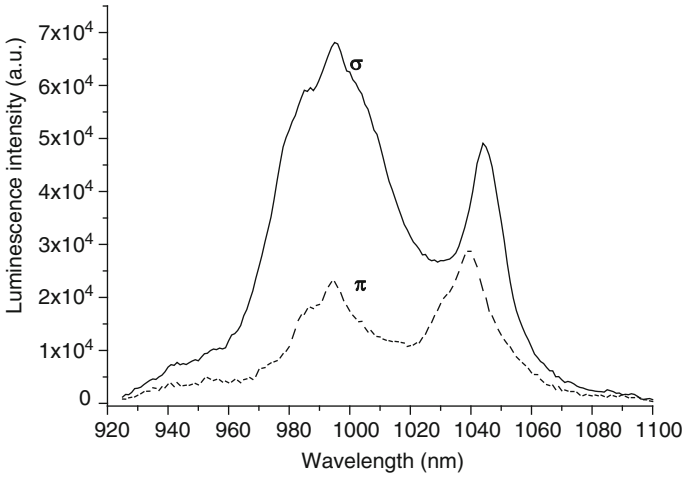

Fig. 26 The polarized emission spectra of YbGAB

Table 10 The spectroscopic and laser parameters of Yb:GAB and some Yb-doped crystals

Crystal	GAB	GAB*	YAB	YAG	FAP	YCOB	GCOB
λ_{pump} (nm)	977	978	975	942	905	976	902
FWHM (nm)	20	22	20	18	2.4	–	15
σ_{abs} (λ_{pump})(10^{-20} cm^2)	3.43	2.5	3.4	0.8	10	0.94	0.41
λ_{ext} (nm)	1,045	1,040	1,040	1,031	1,043	1,030	1,032
σ_{ext}(λ_{ext})(10^{-20} cm^2)	0.98	0.7	0.8	2.0	5.9	0.55	0.55
τ (ms)	0.569	0.298	0.68	1.08	1.08	2.65	2.6
β_{min}	0.022	–	0.043	0.055	0.046	0.058	0.06
I(kW/cm^2)	10.4	–	8.8	28	2.6	8.2	25.5
I_{min}(kW/cm^2)	0.23	–	0.38	1.54	0.132	0.48	1.54
Ref.	[77]	[78]	[79]	[80]	[81]	[82]	[83]

the gain cross section in σ-polarization calculated of different values of P for the $^2F_{5/2} \rightarrow {}^2F_{7/2}$ transition in the Yb:GAB crystal. Figure 28 presents the room-temperature fluorescence decay curves of Yb:GAB crystal excited at 980 nm.

2.5.3 The Spectra Characteristics of Nd^{3+}:$Gd_{0.2}Y_{0.766}Al_3(BO_3)_4$ Crystal

Figure 29 presents the relative intensities of SH signal for $Gd_xY_{1-x}Al_3(BO_3)_4$ system samples and compared with that of BBO crystal [84]. The result shows the relative intensities of SH signal for $Gd_xY_{1-x}Al_3(BO_3)_4$ ($x = 0.1$–0.5) crystals enhance with the increase of x value and comparable to that of BBO crystal, which resulted from the decrease of local symmetry in crystal because of the Gd^{3+} doping. Figure 30 shows the absorption spectrum of Nd^{3+}:$Gd_{0.2}Y_{0.766}Al_3(BO_3)_4$ crystal [51]. Three main peaks at 805 nm corresponding to the $^4I_{9/2} \rightarrow {}^4F_{5/2}, {}^2H_{9/2}$ transition in the absorption spectra

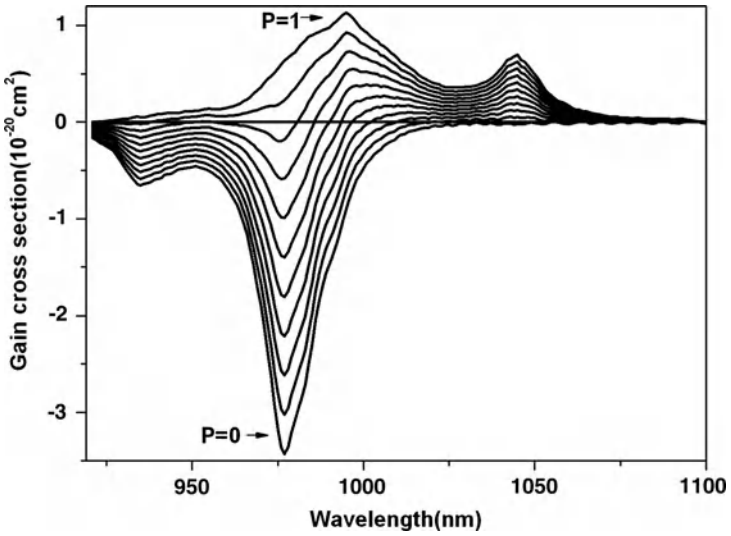

Fig. 27 Gain cross section calculated for different values of P for the ${}^2F_{5/2} \rightarrow {}^2H_{7/2}$ transition of Yb^{3+} in $GdAl_3(BO_3)_4$ crystal for σ-polarization

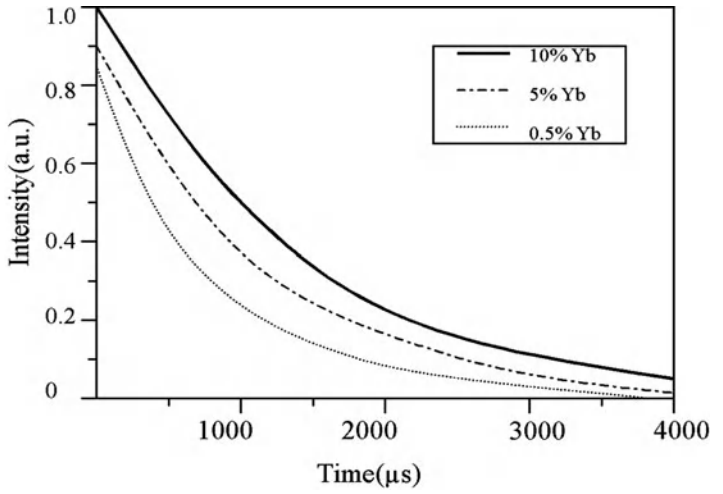

Fig. 28 The room-temperature fluorescence decay curves of Yb^{3+} in $GdAl_3(BO_3)_4$ crystal excited at 980 nm

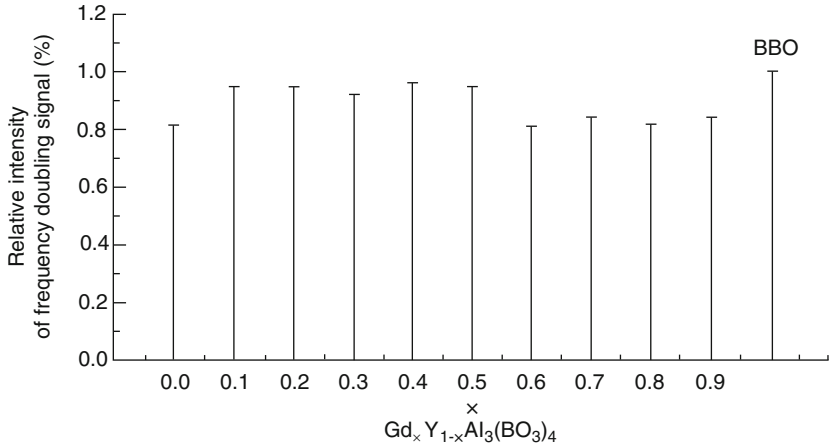

Fig. 29 Presents the relative intensities of SH signal for $Gd_xY_{1-x}Al_3(BO_3)_4$ system samples and BBO crystal

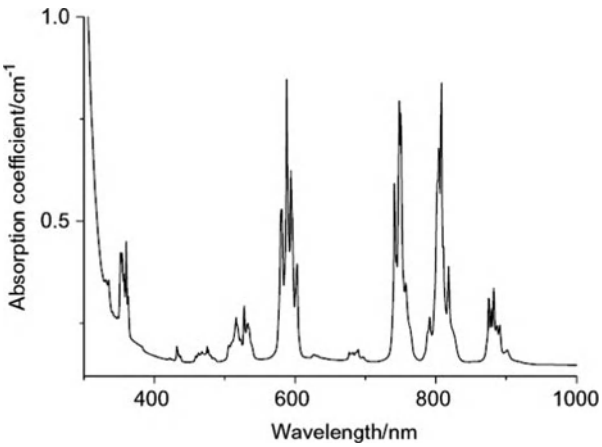

Fig. 30 The absorption spectrum of Nd^{3+}:$Gd_{0.2}Y_{0.766}Al_3(BO_3)_4$ crystal

are very important for GaAlAs laser diode pumping near 800 nm. Figure 31 presents the fluorescence spectrum of Nd^{3+}:$Gd_{0.2}Y_{0.766}Al_3(BO_3)_4$ crystal. The stimulated emission cross section at 1,062 nm corresponding to ${}^4F_{3/2} \rightarrow {}^4I_{11/2}$ transition is 2.03×10^{-19} cm$^{2\cdot}$ The stimulated emission cross section at 1,338 nm corresponding to ${}^4F_{3/2} \rightarrow {}^4I_{13/2}$ is 3.98×10^{-20} cm^2. Figure 32 shows the fluorescence decay curve of Nd^{3+}:$Gd_{0.2}Y_{0.766}Al_3(BO_3)_4$ crystal. The radiative lifetime of ${}^4F_{3/2}$ level is 166.7 μs. Table 11 shows the experimental oscillation strength $Pi^{(exp)}$ and calculated oscillation strength $Pi^{(cal)}$. Table 12 shows the J–O parameters of Nd^{3+}:$Gd_{0.2}Y_{0.766}Al_3(BO_3)_4$ crystal and of some other crystals.

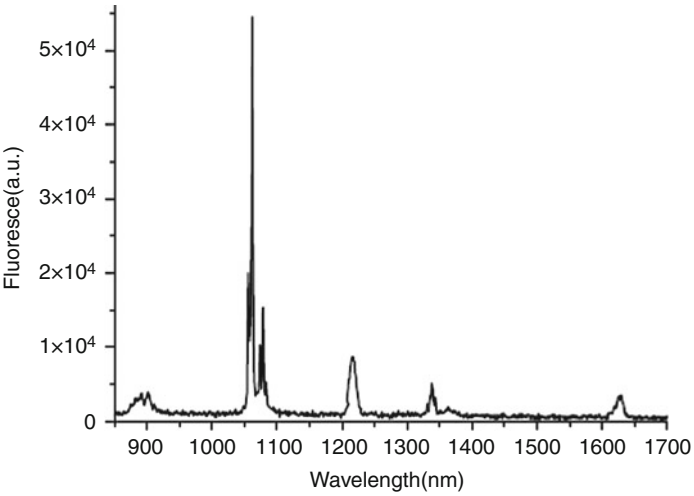

Fig. 31 The fluorescence spectrum of Nd^{3+}:$Gd_{0.2}Y_{0.766}Al_3(BO_3)_4$ crystal

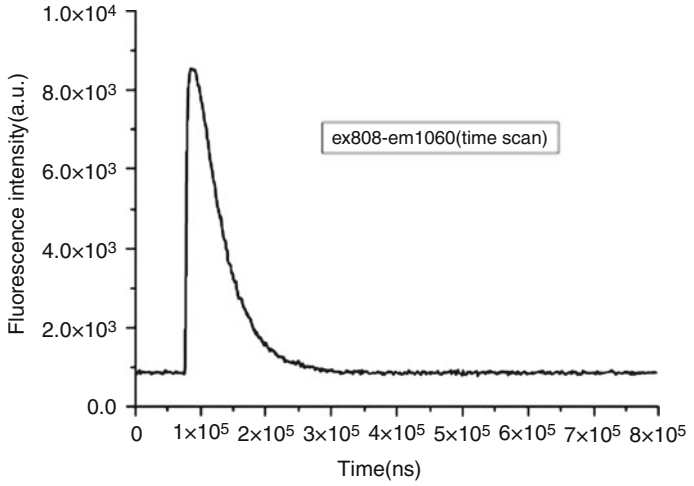

Fig. 32 The fluorescence decay curve of Nd^{3+}:$Gd_{0.2}Y_{0.766}Al_3(BO_3)_4$ crystal

2.5.4 The Spectra Characteristics of Cr^{3+}:$GdAl_3(BO_3)_4$ Crystal

The absorption and emission spectra of Cr^{3+}:$GdAl_3(BO_3)_4$ crystal as functions of σ-and π-polarizations are presented in Figs. 33–36 [65]. For the σ-polarization, the intensity of both absorption spectra is stronger than that for the π polarization. For the σ-polarization, the intensity of both absorption spectra is weaker than that for the π polarization. The dominant features of absorption spectra are two broad bands with peaks at 426 nm and 590 nm, which are identified to the parity-forbidden transitions $^4A_2 \rightarrow {}^4T_1$ and $^4A_2 \rightarrow {}^4T_2$ of the $3d^3$ configuration of Cr^{3+} ions in octahedral crystal

Table 11 The experimental oscillation strength P_i(exp) and calculated ones P_i(cal)

Wavelength (nm)	$P_i^{(cal)} \times 10^6$	$P_i^{(exp)} \times 10^6$
882	4.37	4.37
805	12.44	12.0
748	11.45	11.3
686	5.56	5.36
591	21.5	20.7
525	16.55	16.5
475	2.76	2.77
432	5.23	5.05
357	26.8	25.9
335	7.38	7.1

Table 12 The J–O parameters of Nd^{3+}: $Gd_{0.2}Yb_{0.8}Al_3(BO_3)_4$ crystal and of some other crystals

Crystal	Ω_2	Ω_4	Ω_6	Reference
$Gd_{0.2}Yb_{0.8}Al_3(BO_3)_4$	1.07	9.70	6.90	[51]
YAG	0.2	2.7	5.0	[85]
	0.37	2.29	5.97	[86]
YAP	1.24	4.68	5.85	[87]
$GdAl_3(BO_3)_4$	3.12	2.68	5.34	[55]
Y $Al_3(BO_3)_4$	1.79	2.44	3.25	[84]

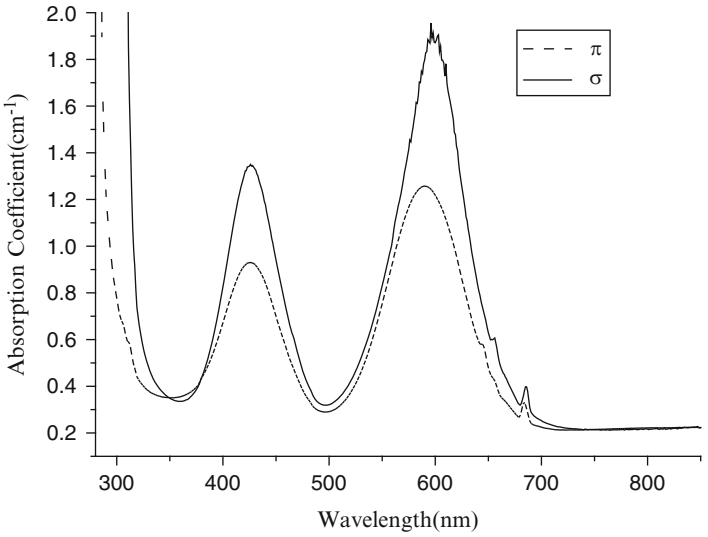

Fig. 33 The polarization absorption spectra of CGAB crystal

fields, respectively. Two weak sharp absorption bands with peaks at 656 and 685 nm, which correspond to spin- and parity-forbidden transitions $^4A_2 \rightarrow {}^2T_1$ and $^4A_2 \rightarrow {}^2E$, respectively, are superimposed on the long-wavelength edge of the $^4A_2 \rightarrow {}^4T_2$ band. The absorption cross section of $^4A_2 \rightarrow {}^4T_1$ and $^4A_2 \rightarrow {}^4T_2$ transitions were determined to be 4.07×10^{-20} cm^2 at 426 nm and 5.91×10^{-20} cm^2 at 590 nm for σ-polarized absorption spectra. While for the π-polarized absorption spectra, the

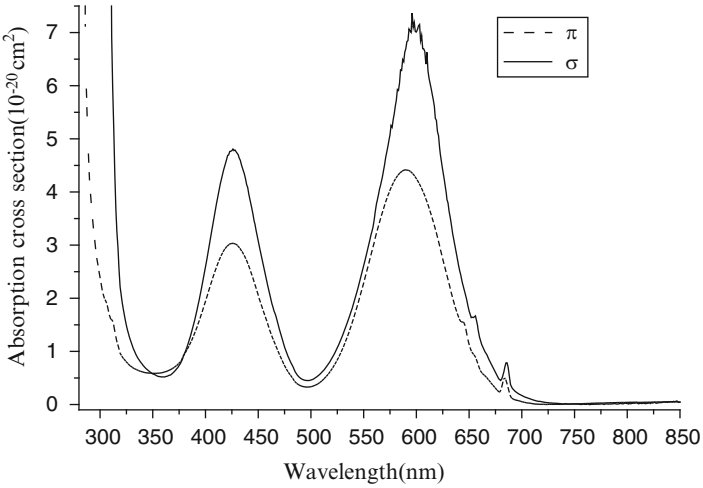

Fig. 34 The polarization absorption cross section of CGAB crystal

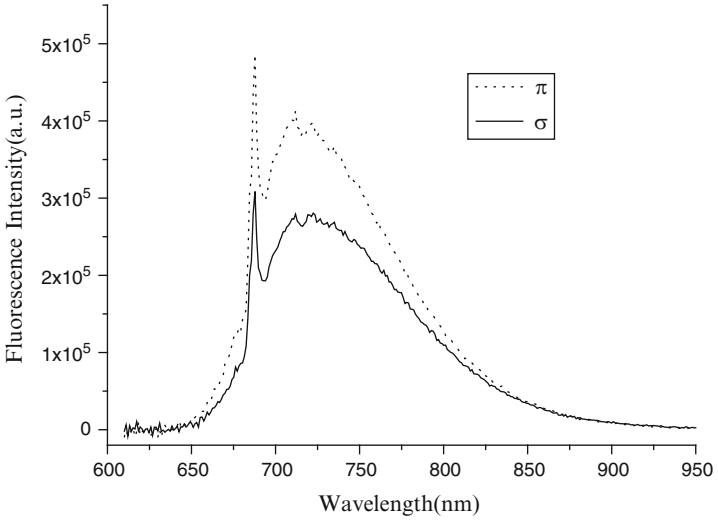

Fig. 35 The polarization fluorescence spectra of CGAB crystal excited at 590 nm

absorption cross section are 2.68×10^{-20} cm^2 at 426 nm and 3.67×10^{-20} cm^2 at 590 nm, respectively, corresponding to the $^4A_2 \rightarrow {}^4T_1$ and $^4A_2 \rightarrow {}^4T_2$ transition.

A broad band was observed extending from 650 nm to 850 nm with a peak at 721 nm and a full width at half maximum (FWHM) 100 nm. This emission is associated with the $^4A_2 \rightarrow {}^4T_2$ transition. The strong narrow line at 687 nm is responsible for the $^4A_2 \rightarrow {}^2E$ zero-phonon transition (R line). The emission cross sections of $^4A_2 \rightarrow {}^4T_2$ transition is 3.07×10^{-20} cm^2 at 721 nm wavelength for the σ spectra, while 2.62×10^{-20} cm^2 for the π spectra. The fluorescence decay curve of $^4A_2 \rightarrow {}^4T_2$ transition was measured shown in Fig. 37, from which the fluorescence lifetime, 135 μs, was derived.

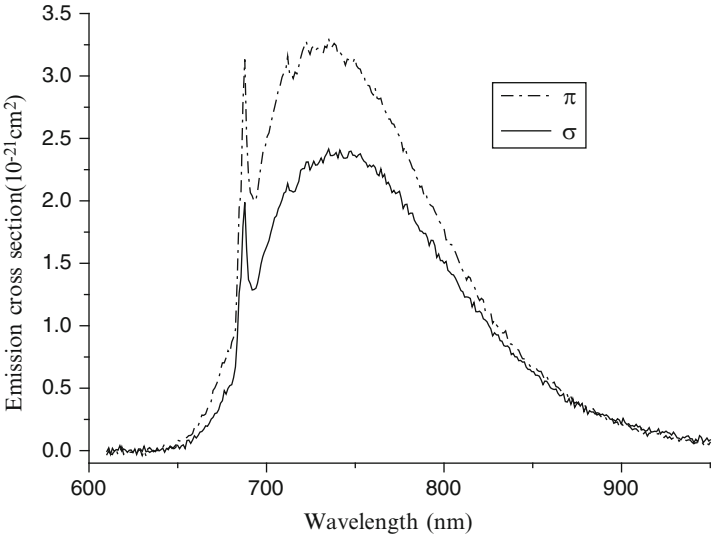

Fig. 36 The polarization fluorescence emission cross section of CGAB crystal excited at 590 nm

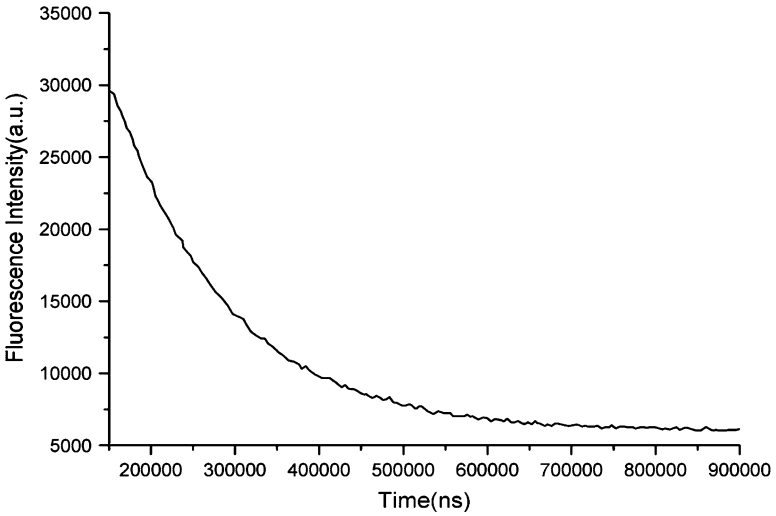

Fig. 37 The fluorescence decay curve of $^4A_2 \rightarrow {}^4T_2$ transition

Table 13 presents the comparison of ligand field parameters for Cr^{3+}:GAB with other Cr^{3+}-doped crystals. Table 14 shows the comparison of peaks wavelength and half-widths of Cr^{3+} emission transition in GAB with other crystals. The energy levels of Cr^{3+}in GAB crystal is presented in Table 15. Table 16 shows the Huang-Rhys parameter S of Cr^{3+}-doped GAB and other crystals.

Table 13 Comparison of ligand field parameters for Cr^{3+}:GAB with other Cr^{3+}-doped crystals

Material	Dq (cm^{-1})	B (cm^{-1})	Dq/B	C (cm^{-1})	C/B
LSB [88]	1,529	675	2.27	3,448	5.1
Al_2O_3 [89]	1,664	640	2.60	3,300	5.2
$BeAl_2O_4$ [90]	1,709	675	2.53	3,245	4.8
YAB [91]	1,680	672	2.50	3,225	4.8
GAB [91]	1,695	673	2.52	3,380	5.0
GAB [65]	1,678	669	2.51	3,441	5.1
YSB [91]	1,539	644	2.39	–	–
GSB [91]	1,563	638	2.45	–	–

Table 14 Comparison of peak wavelength and half-widths of Cr^{3+} transition in GAB with other Cr^{3+}-doped borate materials

Material	LSB [88]	YSB [91]	GSB [91]	YAB [91]	GAB [91]
$^4A_2 \rightarrow {}^2E$ peak (nm)	684	/	/	684	686
$^4A_2 \rightarrow {}^4T_2$ peak (nm)	654	650	645	595	590
FWHM (cm^{-1})	2,910	2,810	2,830	2,730	2,530
$^4A_2 \rightarrow {}^4T_1$ peak (nm)	457	460	458	425	422
FWHM (cm^{-1})	4,277	3,380	3,100	3,580	3,400
$^4T_2 \rightarrow {}^4A_2$ peak (nm)	963	875	860	750	760
FWHM (cm^{-1})	1,817	2,590	2,750	2,310	2,240

Table 15 Energy levels of Cr^{3+} in GAB crystal

O_h group show $^{2s+1}\Gamma_i$ state	Level	Energy (cm^{-1})	Energy of relative ground (cm^{-1})
$^2T_2(a^2D,b^2D,^2F,^2G,^2H)$	t_2^3	−7,349	22,822
	$t_2^2(^3T_1)e$	1,737	31,908
	$t_2^2(^1T_2)e$	11,593	41,764
	$t_2e^2(^1A_1)$	20,229	50,400
	$t_2e^2(^1E)$	40,507	70,678
$^2T_1(^2P,^2F,^2G,^2H)$	t_2^3	−14,317	15,854
	$t_2^2(^3T_1)e$	2,125	32,296
	$t_2^2(^1T_2)e$	6,815	36,986
	$t_2e^2(^3A_1)$	18,512	55,270
	$t_2e^2(^1E)$	25,099	69,208
$^2E(a^2D,b^2D,^2G,^2H)$	t_2^3	−14,890	15,281
	$t_2^2(^1A_1)e$	21,780	51,951
	$t_2^2(^1E)e$	3,930	34,101
	e^3	42,910	73,081
$^4T_1(^4P,^4F)$	$t_2^2(^3T_1)e$	−6,696	23,475
	$t_2e^2(^3A_2)$	6,729	36,900
$^4T_2(^4F)$	$t_2^2(^3T_1)e$	−13,391	16,780
$^2A_1(^2G)$	$t_2^2(^1E)e$	−392	29,779
$^2A_2(^2F)$	$t_2^2(^1E)e$	12,988	43,159
$^4A_2(^4F)$	t_2^3	−30,171	0

Table 16 Huang–Rhys parameter S of Cr^{3+}-doped GAB and other crystals

Crystal	T (K)	E_a (cm^{-1})	E_e (cm^{-1})	S	$\hbar\varpi$ (cm^{-1})	Ref.
CGAB	295	16,779	13,850	3.57	410	[65]
K_2NaScF_6	295	15,600	13,100	3.30	379	[92]
K_2NaGaF_6	295	16,000	13,600	3.03	396	[92]
$NaGa_2Li_3F_{12}$	18	16,069	13,313	3.7	372	[93]
ScF_3	14	14,280	12,028	3.0	367	[94]

It is well known that the ionic radii of R^{3+} and X^{3+} ions covered a wide range: La^{3+}(1.15 Å) > Gd^{3+}(1.11 Å) > Y^{3+}(0.95 Å) > Lu^{3+}(0.86 Å); Sc^{3+}(0.83 Å) > Cr^{3+} (0.65 Å) > Ga^{3+}(0.62 Å) > Al^{3+}(0.55 Å). It is easy to deduce the "size effect" that the field strength D_q/B decreases with the increase of R^{3+} and X^{3+} radium. The "size effect" also manifests that both the peak wavelength and the half-widths of Cr^{3+} emission transition increase with the increase of R^{3+} and X^{3+} radium.

Since there are a transparent window at 350–360 nm and the contented phase match condition, it is expected that an SHG at 350–360 nm can be obtained from Cr:GAB crystal by self-frequency-doubling technology.

2.5.5 The Spectra Characteristics of Tm:$GdAl_3(BO_3)_4$ Crystal

As shown in Fig. 38 the intensity of absorption bands depends significantly on the polarization of light [95–97]. The peak absorption cross section occurs at 797 nm with a 15 nm full width at half maximum (FWHM) for the σ polarization and 810 nm with a 13 nm FWHM for the π polarization; the corresponding absorption cross sections are

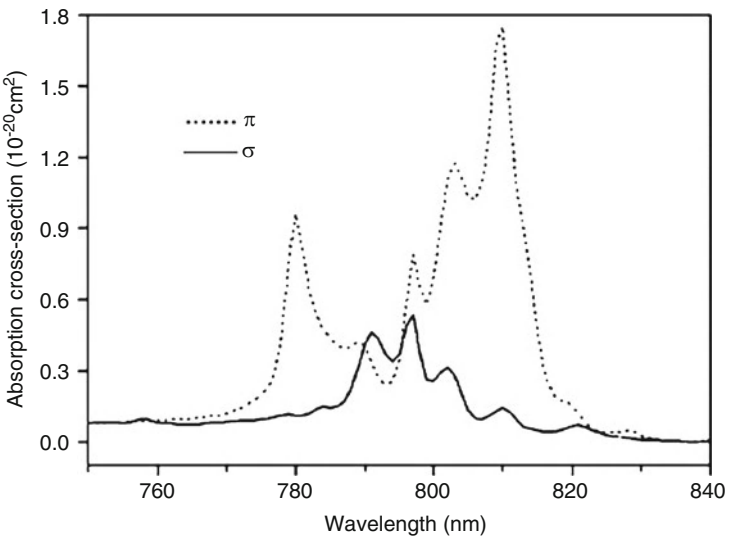

Fig. 38 Polarized absorption cross section for the $^3H_6 \rightarrow {}^3H_4$ transition of Tm^{3+}:$GdAl_3(BO_3)_4$ at room temperature

0.54×10^{-20} and 1.75×10^{-20} cm^2, respectively. This high absorption cross section is ideal as a microchip laser material, as the value is comparable with those of Tm^{3+}:YVO_4:2.5×10^{-20} cm^2 [98], of Tm^{3+}:YAG (yttrium aluminum garnet): 0.75×10^{-20} cm^2 [99]. A relative broad absorption band and a high cross section are very promising features for the efficient optical pumping of this system with laser diodes.

Figure 39 shows the polarized absorption cross section due to the $^3H_6 \rightarrow {}^3F_4$ transition (solid lines) and the derived emission cross section curves (dotted lines) for the $^3F_4 \rightarrow {}^3H_6$ transition. The maximum emission cross section centered at 1.85 μm are 1.29×10^{-20} cm^2 for the σ-polarization and 6.60×10^{-20} cm^2 for the π-polarization. These spectra exhibit the characteristic optical anisotropy of the host $GdAl_3(BO_3)_4$, where the spectrum for the π polarization is the most intense resulting in the highest possibility to obtain polarized stimulated emission. The radiative lifetime for the $^3F_4$ state was estimated to be 13,158 μs [100]. These values of the emission cross section are of the order of or higher than those reported for other Tm^{3+}-based laser crystals, as shown in Table 17.

The wavelength dependencies of the gain cross section for both π- and σ-polarizations were calculated in terms of population inversion P ($P = 0, 0.1, 0.2, \ldots, 1$) and are shown in Fig. 40. The population inversion rate needed to achieve application is expected to be higher than 0.1. For a population inversion level of 0.3, the gain is produced in the 1.815–2.0 μm spectral region. This wavelength range corresponds to the absorption bands of liquid water and water vapor [108]. High P

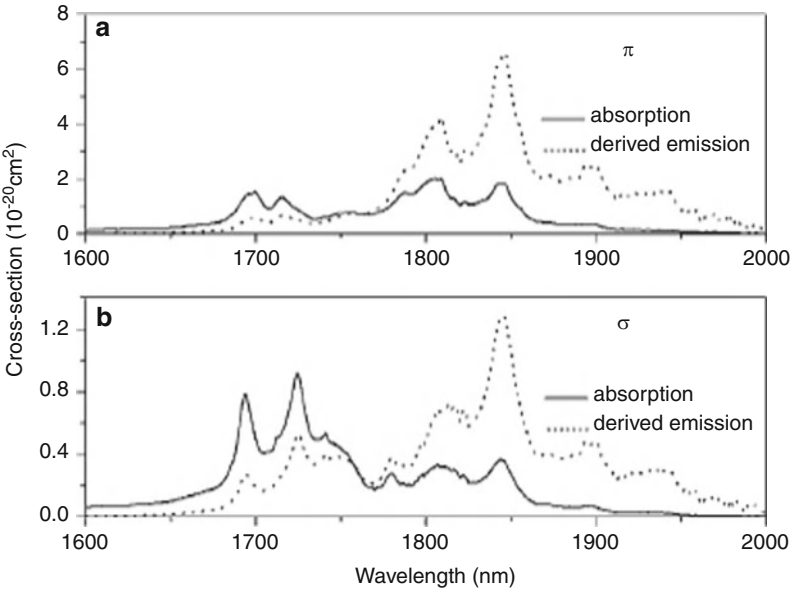

Fig. 39 Polarized absorption cross section due to the $^3H_6 \rightarrow {}^3F_4$ transition (*solid lines*) and the derived emission cross section curves (*dotted lines*) for the $^3F_4 \rightarrow {}^3H_6$ transition for (**a**) σ polarization and (**b**) π polarization

Table 17 The values of the emission cross section are of the order of or higher than those reported for other Tm^{3+}-based laser crystals

Crysrals	σ_{em} ($\times 10^{-20}$ cm^2)	$\tau[^3F_4(\mu s)]$	References
3.23%Tm:$GdAl_3(BO_3)_4$	6.60	13,158	[95]
5%Tm:YVO_4	1.60	800	[98]
3%Tm:$SrGdGa_3O_7$	0.39	4,700	[101]
1%Tm:$LiYF_4$	0.33	13,000	[102]
0.1%Tm:LaF_3	0.25	11,000	[102]
1%Tm:$Y_3Al_5O_{12}$	0.22	8,500	[102]
3%Tm:$KGd(WO_4)_2$	3.0	1,760	[103]
15%Tm:$KY(WO_4)_2$	1.90	1,470	[104]
1%Tm:KY_3F_{10}	0.40	15,400	[105]
6%Tm:$YAlO_3$	0.50	12,000	[106]
0.5%Tm:$LiTaO_3$	2.3	2,400	[107]

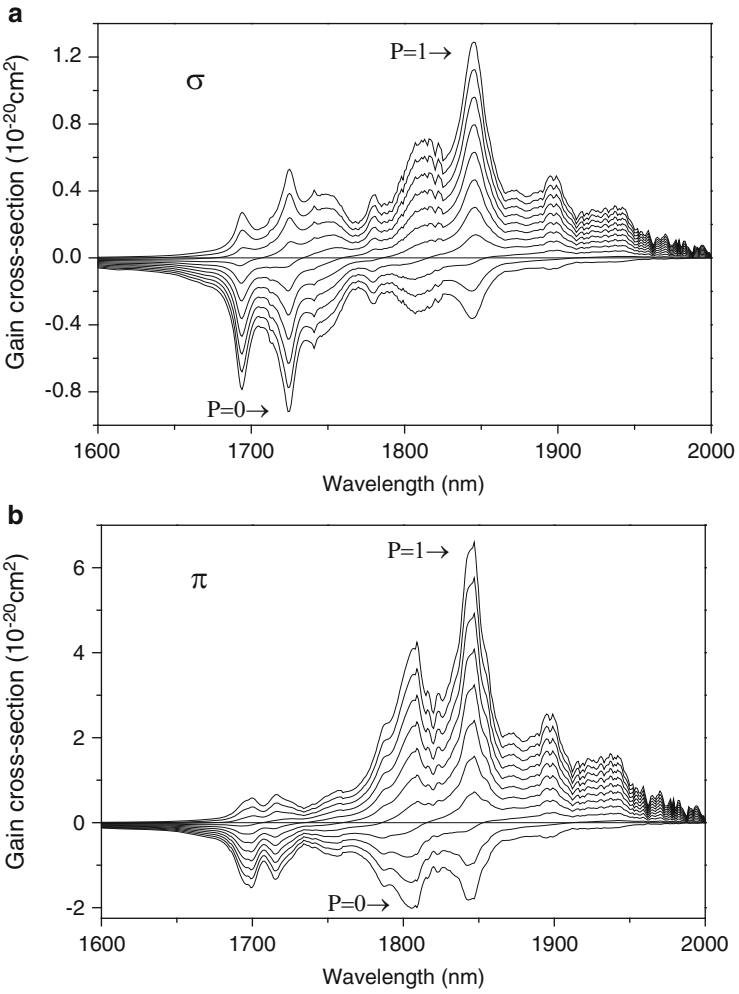

Fig. 40 Gain cross section calculated for different values of P for the $^3F_4 \rightarrow {}^3H_6$ transition of Tm^{3+}:$GdAl_3(BO_3)_4$ crystal for (**a**) σ polarization and (**b**) π polarization

can be achieved by high-power pulse pumping with the ground state depleted operation [109]. The higher energy limit of this interval increased when the population inversion level was increased, reaching up to 1.73 μm for a population inversion level of 0.5. For this level, the maximum gain cross section value centered at 1.85 μm for σ- and π-polarizations are 0.47×10^{-20} and 2.40×10^{-20} cm^2, respectively. The analysis of the gain coefficient implies the possible laser tunability in the range from 1.73 to 2.0 μm for the ${}^3F_4 \rightarrow {}^3H_6$ transition. Laser experiments for this emission are expected to find light amplification in future at this point.

2.5.6 The Spectra Characteristics of $TmAl_3(BO_3)_4$ Crystal

Figure 41 presents room temperature absorption spectrum of $TmAl_3(BO_3)_4$ crystal [26, 110, 111]. It consists of five groups of bands associated with the transitions from the ${}^3H_6$ ground state to the ${}^3F_4$, ${}^3H_5$, ${}^3H_4$, ${}^3F_3$ + ${}^3F_2$, and ${}^1G_4$ excited states. The absorption peak at 807 nm has a 8 nm full width at half maximum (FWHM) and the corresponding absorption cross section is 0.48×10^{-20} cm^2. This moderate absorption cross section is ideal as a microchip laser material, as the value is comparable with that of Tm^{3+}:YAG: 0.75×10^{-20} cm^2 [99]. A relative broad absorption band and a high cross section are very promising features for the efficient optical pumping of this system with laser diodes. The emission cross sections calculated by the reciprocity method (RM) [102, 112] together with the absorption cross sections (solid line) were shown in Fig. 42. The maximum emission cross section centered at 1.85 μm is 0.83×10^{-20} cm^2. The values of the emission cross section and the radiative lifetime for the ${}^3F_4$ state are of the order

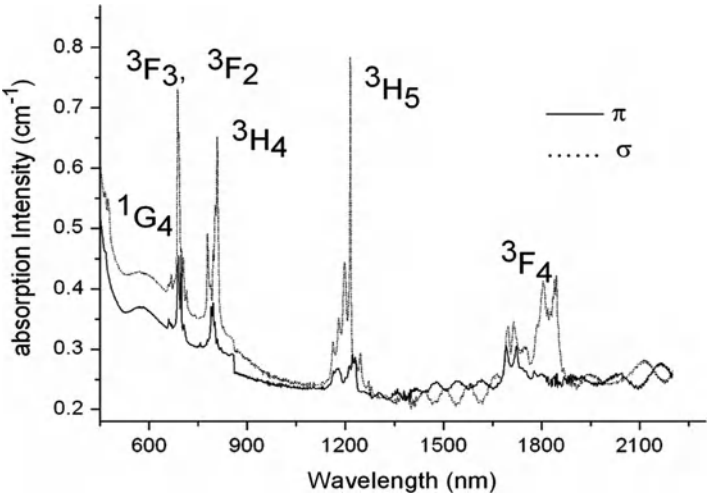

Fig. 41 Room temperature polarized emission spectra of $TmAl_3(BO_3)_4$ crystal

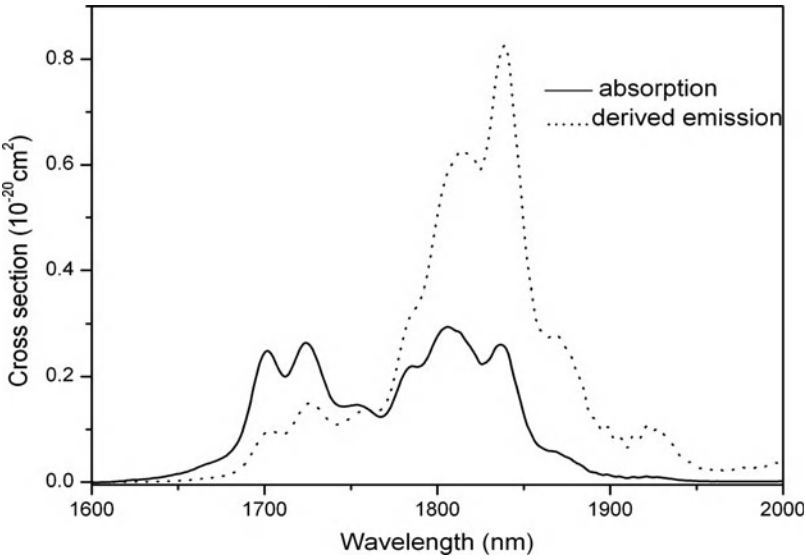

Fig. 42 Absorption cross section due to the $^3H_6 \rightarrow {}^3F_4$ transition (*solid lines*) and the derived emission cross section curves (*dotted lines*) for the $^3F_4 \rightarrow {}^3H_6$ transition

of or higher than those reported for other Tm^{3+}-based laser crystals, as shown in Table 17. If one compares with other reference material such as Tm^{3+}:YAG, with a peak emission cross section of about 0.22×10^{-20} cm^2, or Tm^{3+}:$SrGdGa_3O_7$, with a peak emission cross section of about 0.39×10^{-20} cm^2, the emission cross section of Tm^{3+} found in the case of $TmAl_3(BO_3)_4$ is much larger than these values.

Table 18 shows the calculated radiative transition rate, the branching ratios and the radiative lifetime for different transition levels. Table 19 shows fluorescence lifetimes of different levels in $TmAl_3(BO_3)_4$ crystal obtained by two-exponential decay functions. The wavelength dependencies of the gain cross section for both π and σ polarization were calculated in terms of population inversion P ($P = 0, 0.1, 0.2, \ldots, 1$) and are shown in Fig. 43. The population inversion rate needed to achieve application is expected to be higher than 0.1. For a population inversion level of 0.3, the gain is produced in the 1.82–2.0 μm spectral region. The analysis of the gain coefficient implies the possible laser tunability in the range from 1.82 μm to 2.0 μm for the $^3F_4 \rightarrow {}^3H_6$ transition. Large emission cross section and broad possible laser oscillation (nearly 200 nm) suggest that $TmAl_3(BO_3)_4$ crystal maybe regarded as a potential diode pumped solid state 1.8–1.9 μm laser media. It is also expected that an SHG at 0.9–0.95 nm can be obtained from TAB crystal by self-frequency-doubling technology.

Table 18 The calculated radiative transition rate, the branching ratios and the radiative lifetime for different transition levels

Start levels	Terminal levels	Wavelength/nm	A (s^{-1})	β A	τ/μs
$^1D_2$	$^3H_6$	359	10,005	0.575	57
	$^3F_4$	450	5,691	0.325	
	$^3H_5$	508	134	0.008	
	$^3H_4$	652	1,100	0.063	
	$^3F_3$,$^3F_2$	758	422	0.024	
	$^1G_4$	1,491	91	0.005	
$^1G_4$	$^3H_6$	472	641	0.373	518.403
	$^3F_4$	644	224	0.131	
	$^3H_5$	770	644	0.375	
	$^3H_4$	1,158	158	0.092	
	$^3F_3$,$^3F_4$	1,543	52	0.030	
$^3H_4$	$^3H_6$	798	6,380	0.92	144
	$^3F_4$	1,452	511	0.074	
	$^3H_5$	2,300	40	0.006	
$^3F_4$	$^3H_6$	1,771	76	1	13,158

Table 19 Fluorescence lifetimes of different levels in $TmAl_3(BO_3)_4$ crystal obtained by two-exponential decay functions

Levels	α_1	τ_1 (μs)	α_2	τ_1 (μs)	τ (μs)
$^3H_4$	1.27×10^3	39.51	9.50×10^2	71.68	53.28
$^1D_2$	2.92×10^3	43.53	1.44×10^3	76.26	54.34

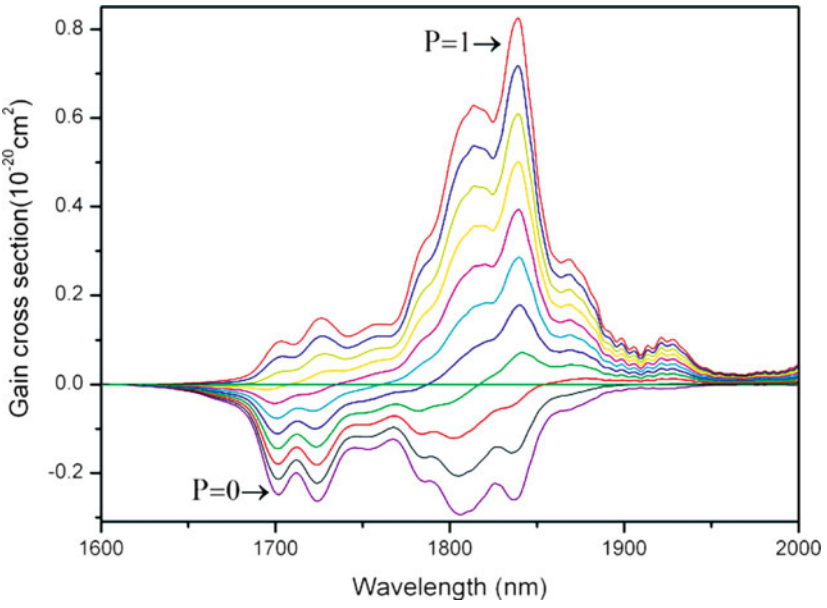

Fig. 43 Gain cross section calculated for different values of P for the $^3F_4 \rightarrow {}^3H_6$ transition

2.6 The Laser Characteristics of Pure $GdAl_3(BO_3)_4$ and Nd^{3+}-Doped Crystals

2.6.1 The Optical and Laser Characteristics of Pure $GdAl_3(BO_3)_4$ Crystal

UV–vis-NIR transparent spectrum of $GdAl_3(BO_3)_4$ crystal is shown in Fig. 44. Infrared transparent spectrum of $GdAl_3(BO_3)_4$ crystal is shown in Fig. 45. A short absorption edge of 310 nm is observed in Fig. 44 and a long one of 3,450 nm in Fig. 45 [112, 113]. Also, there are three absorption peaks centered at 2,765, 2,936, and 3,164 nm in Figs. 45 and 46, which belong to the hydroxy vibration absorption.

For SHG nonlinear optical crystal, the phase-matching angle and the effective frequency-doubling coefficient are very important to the optical conversion efficiency. $GdAl_3(BO_3)_4$ crystal belongs to hexagonal with space group R32, which is the negative uniaxial crystal. Therefore, the phase-matching conditions of $GdAl_3(BO_3)_4$ crystal are as follows:

$$\text{Type I phase matching} \qquad (\text{eoo}) - n_2^{\text{e}}(\theta_{\text{m}}) = n_1^{\text{o}}$$

$$\text{Type II phase matching} \qquad (\text{eeo}) - n_2^{\text{e}}(\theta_{\text{m}}) = \frac{1}{2}[n_1^{\text{e}}(\theta_{\text{m}}) + n_1^{\text{o}}].$$

The mark e and o denote the ordinary and extraordinary light, and

$$n_{\text{e}}(\theta) = \frac{n_{\text{o}} n_{\text{e}}}{(n_{\text{o}}^2 \sin^2\theta + n_{\text{e}}^2 \cos^2\theta)^{1/2}}.$$

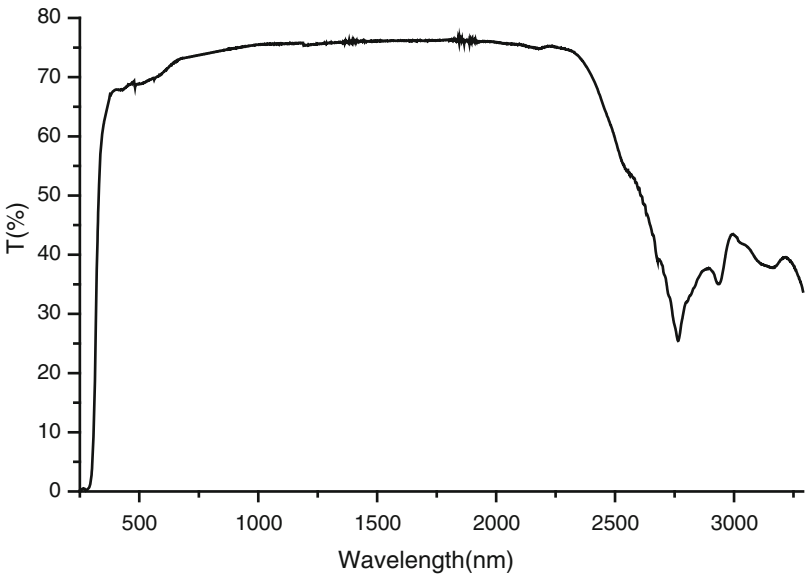

Fig. 44 The UV–vis-NIR transparent spectrum of $GdAl_3(BO_3)_4$ crystal

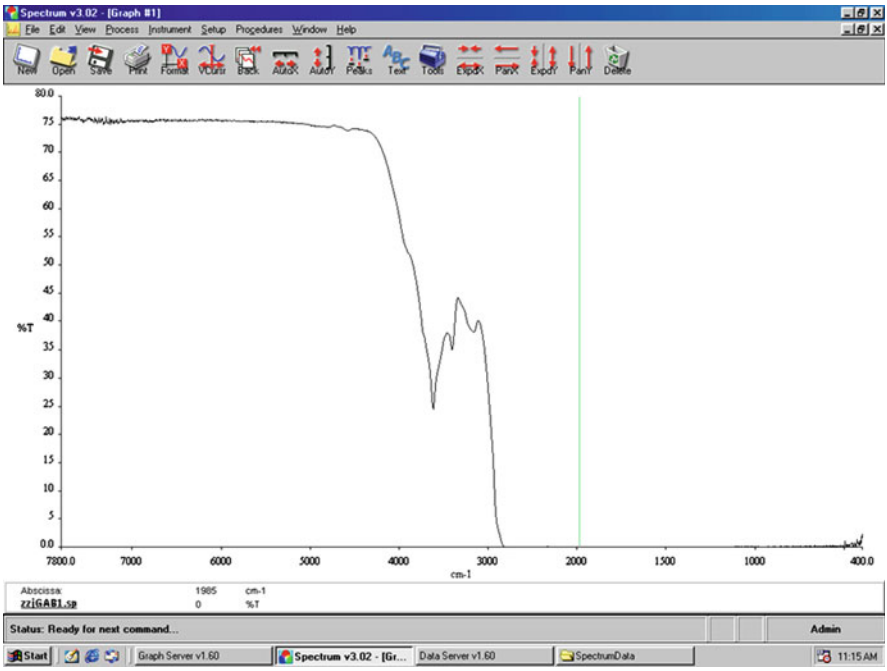

Fig. 45 The infrared transparent spectrum of $GdAl_3(BO_3)_4$ crystal

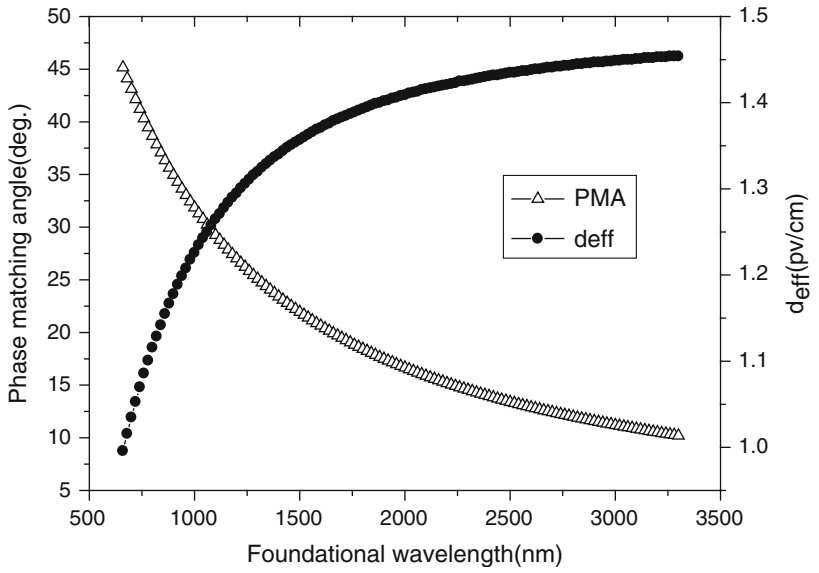

Fig. 46 The relationships among the second-harmonic coefficients, the phase matching angles and wavelengths

n_o and n_e are two primary refractive indices of refractive index ellipsoid. And for the hexagonal with space group R32, there is only one independent SHG nonlinear optical coefficient d_{11}, which is measured to be 1.45 pm/V for $GdAl_3(BO_3)_4$ crystal. Thereby, the effective SHG nonlinear optical coefficients are as follows:

$$\text{Type I phase matching} \qquad (\text{eoo}) - d_{\text{eff}} = d_{11}\cos\theta\cos 3\phi$$

$$\text{Type II phase matching} \qquad (\text{eeo}) - d_{\text{eff}} = d_{11}\cos^2\theta\sin 3\phi.$$

According to the index of refraction, the chromatic dispersion equations of $GdAl_3(BO_3)_4$ crystal

$$n_o^2(\lambda) = 3.07389 + 0.03079/(\lambda^2 + 0.03265) + 3.261 \times 10^{-5} \times (T - T_0)$$

$$n_e^2(\lambda) = 2.82998 + 0.0242/(\lambda^2 + 0.03127) + 3.533 \times 10^{-5} \times (T - T_0).$$

The SHG phase-matching properties and the effective nonlinear optical coefficients $d_{\text{eff.}}$ were investigated. Figure 46 indicated the relationships among the second-harmonic coefficients, the phase matching and wavelengths. From the results, it is found that the phase-matching angle decreased with the increasing of the wavelength. But the second-harmonic coefficients increased with the increasing of the wavelength. More important, the phase matching could be realized in the whole transmittance waveband.

A cross-superimposed laser crystal multiplier was designed to measure the frequency doubling of GAB. The laser configuration was shown in Fig. 47. The used pumping resource was 915 nm LD and the sample was cut to $5 \times 4 \times 2$ mm^3. According to the type I phase matching, the critical phase-matching parameters were calculated in Table 20. When the phase matching was suited, the blue laser at

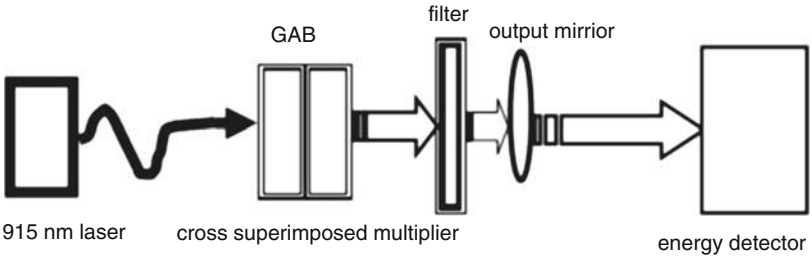

Fig. 47 The cross-superimposed laser crystal multiplier configuration

Table 20 The critical phase-matching parameters versus 915 nm frequency doubling

Crystal	θ, φ (degree)	d_{eff} (pm/V)	ρ (degree)	$\delta\theta$ (mrad-cm)	$\delta\lambda$ (nm-cm)
GAB	34.45, 0	1.186	2.396	1.093	0.5436

Fig. 48 The facular differences versus one, two and four GAB samples

Table 21 The comparison between GAB and other nonlinear optical crystals

Crystal	θ, φ (degree)	d_{eff} (pm/V)	Dispersion angle (ρ) (degree)	Angular width ($\delta\theta$) (mrad-cm)	Bandwidth ($\delta\lambda$) (nm-cm)	Q (FOM)
GAB	34.45, 0	1.186	2.396	1.093	0.5436	8.487
BBO	25.69, 0	1.413	3.524	0.743	0.521	14.5
LBO	90, 21.69	0.945	0.717	3.612(φ)	0.7924	7.102
YAB	34.63, 0	1.183	2.39	1.097	0.5775	8.438
$LiIO_3$	35.72, 0	3.722	4.688	0.558	0.1808	70.999
HIO_3	90, 56.33	3.146	3.605	1.259(φ)	0.1244	46.49

wavelength 457.5 nm was observed. In the process of experiment, the facular appearances of output blue laser were different with the different crystal sample numbers. Figure 48 presented the facular differences versus one, two, and four $GdAl_3(BO_3)_4$ samples. The facular appearances could demonstrate the output laser quality and intensity. Obviously, the facular properties of four $GdAl_3(BO_3)_4$ samples were better than those of one and two $GdAl_3(BO_3)_4$ samples. From the differences, it is found that the designed cross-superimposed laser crystal multiplier contributed to the frequency doubling conversion efficiency, which could take advantage of the pumping laser energy efficiently and improved the output laser quality. The output blue laser was measured to be 7.2, 12.6, and 18.2 mW corresponding to the one, two, and four $GdAl_3(BO_3)_4$ samples, respectively. Moreover, compared with other nonlinear optical crystals, shown in Table 21, it is found that the dispersion angle ρ, the angular width $\delta\theta$, the bandwidth $\delta\lambda$, and the moisture resistance were better than those of BBO crystal, the generally used frequency doubling crystal, which indicated that the $GdAl_3(BO_3)_4$ crystal was a promising host for the self-frequency doubling blue–red laser.

2.6.2 The Self-Frequency-Conversion Laser Characteristics of Nd^{3+}-Doped $GdAl_3(BO_3)_4$ Crystal

Self-Frequency-Doubling Laser Characteristics

Self-Frequency-Doubling for Green Generation

The Nd^{3+}:$GdAl_3(BO_3)_4$ crystal used with 4.6 mm in length was oriented with a polar angle of $\theta = 30^\circ\ 5'$ in respect to the optical axis to phase match the SHG (type I) of the fundamental laser wavelength at 1061.9 nm. This crystal was located inside a 4-cm-length laser cavity consists of a flat input mirror HM1037, which was highly reflective at 1061.9 nm and 531 nm and transparent at the pump wavelength of 748 nm (in the $^4F_{7/2}$ + $^4S_{3/2}$), and of a concave output mirror (18 cm radius of curvature), which was highly reflective at 1061.9 nm and transparent in the visible range. This crystal was longitudinally pumped with a tunable pulse dye laser (bandwidth:0.04 cm^{-1}; dye, LDS750) equipped with a computer-driven motor from Laser Analytical Systems, pumped with a frequency doubled Nd:YAG laser from BM Industries. The duration of the pulse was 8 ns and its waist was 170 μs. The pump was σ-polarization inside the crystal and the laser radiation at 1061.9 nm with 86% σ-polarization was observed, which is favorable for self-frequency-doubling. A green Second-Harmonic Generation of 119.5 μJ/pulse with a 4.3% yield was obtained. Figure 49 shows the SHG power versus the pump power incident on the crystal [114].

Self-Frequency-Doubling for Red Generation

Self-frequency conversion of the 1,338 nm laser emission corresponding to the $^4F_{3/2} \rightarrow {}^4I_{13/2}$ channel requires a cavity constituted of mirrors highly reflective at this wavelength and highly transparent at 1,062 nm to prevent oscillation of the $^4F_{3/2} \rightarrow {}^4I_{11/2}$ channel. The NGAB crystal used was 4.6 mm length and oriented with a polar angle $\theta = 30^\circ\ 5'$ with respect to the optical axis to phase-match the

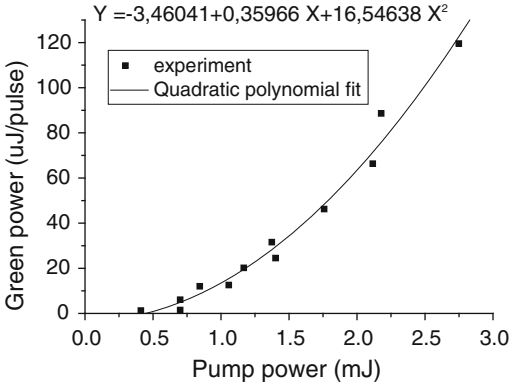

Fig. 49 The SHG power versus the pump power incident on the crystal

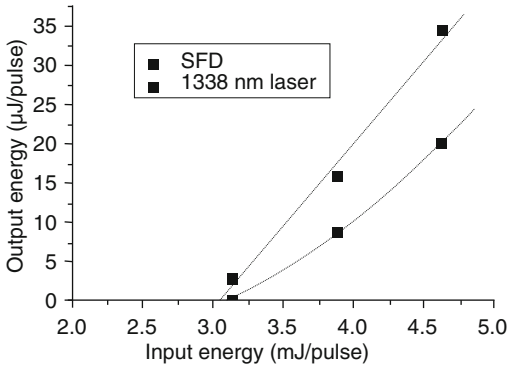

Fig. 50 The SHG power versus the pump power incident on the crystal

second-harmonic generation (type I) of the fundamental wavelength at 1061.9 nm. This orientation was much closer to the one required to achieve perfect self-frequency doubling of the 1,338 nm radiation: the exact phase matching would require a 24.4° polar angle (by comparison, in NYAB the phase-matching angle is 27°). The crystal was located inside a 2.5 cm length laser cavity and pumped longitudinally. The two mirrors have a weak 4% reflectivity at 1,062 nm. The laser waist was calculated to be 160 μm. The pump was σ-polarized inside the crystal. The laser radiation at 1,338 nm was σ-polarized, which is favorable for self-frequency doubling. A laser output of ~35 μJ/pulse at 1,338 nm and a red Second-Harmonic Generation of 19 μJ/pulse for 4.6 mJ/pulse pump was obtained. Their power is represented in Fig. 50 versus pump power *incident on the crystal* [115].

Self-Sum-Frequency Mixing Laser Characteristics

Self-Sum-Frequency Mixing for Blue Generation

When a laser wave at 1061.9 nm emitted from a Nd^{3+}:$GdAl_3(BO_3)_4$ crystal mixes with the pump wave whose wavelengths varies from 740 nm to 760 nm, a blue generation in the 436 to 443 nm range will be resulted [116]. Only if the conservation of the photon momentum, namely a phase-matching condition, is satisfied, the efficiency of the sum-frequency mixing $1/\lambda_1 + 1/\lambda_2 \rightarrow 1/\lambda_3$ is significant. In the case of mixing two ordinary waves to get an extraordinary wave, namely type I, oo–e interaction), the conservation condition can be written as:

$$\frac{n_{o1}}{\lambda_1} + \frac{n_{o2}}{\lambda_2} = \frac{n_3}{\lambda_3}.$$

Taking into account the θ dependence (the angle between wave propagation and c-axis) of the index of refraction n_3, the value of θ for any λ_1 can be calculated. When λ_2 is fixed to the laser wave at 1061.9 nm of Nd^{3+}:$GdAl_3(BO_3)_4$ crystal and the Sellmeier formula of Nd^{3+}:$GdAl_3(BO_3)_4$ crystal given in [50] was used, the

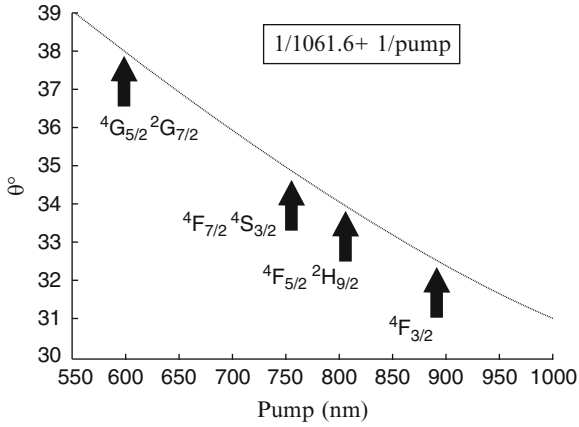

Fig. 51 The phase-matching angles in NGAB for SSFM

calculated result is presented in Fig. 48, where the values of λ_1 are in coincidence with the absorption lines of Nd^{3+}. The main lines and the corresponding Nd^{3+} energy levels are presented by arrows in Fig. 51. The pump and the laser emission have to be an ordinary for type I, oo–e interaction. When a pump of 748.2 nm was chosen to fit an absorption peak in the ${}^4F_{7/2} \rightarrow {}^4S_{3/2}$ levels, Nd^{3+}:$GdAl_3(BO_3)_4$ crystal was cut at an angle of 35.0^0 with respect to the c-axis, corresponding to the phase matching of $\frac{1}{1061.9} + \frac{1}{748.2} = \frac{1}{438.9}$.

The crystal with 4 mm in length was located inside a 4 cm length laser cavity consists of a flat input mirror 16MLB183, which was highly reflective at 1061.9 nm and transparent at the pump wavelength of 748.2 nm (in the ${}^4F_{7/2}$ + ${}^4S_{3/2}$), and of a flat output mirror, which was 90% reflective at 1061.9 nm and transparent in the visible range. This crystal was longitudinally pumped with a tunable pulse dye laser (bandwidth:0.04 cm^{-1}; dye,LDS750) equipped with a computer-driven motor from Laser Analytical Systems, pumped with a frequency doubled Nd:YAG laser from BM Industries. The duration of the pulse was 8 ns and its waist was 170 μs. A blue generation of 445 μJ/pulse with a 7.3% yield was obtained. Figure 52 shows the blue generation power versus the pump power incident on the crystal. This yield is the highest one ever obtained in this kind of device: 0.2% in GdCOB [116], 0.83% in NYAB [117], and 0.3% in NYAB [118] were obtained up to now. Figure 53 shows the time evolutions of the pump, near infrared laser and blue radiation pulses. It can be seen that the blue pulse coincides with the temporal overlap of the pump and laser pulses. The 7-ns delay between the laser pulse and pump one is interpreted as the de-excitation time from the ${}^4F_{7/2}$ + ${}^4S_{3/2}$ levels toward the ${}^4F_{3/2}$ initial laser level. Figure 54 shows the laser excitation spectra of the 1061.9 nm fluorescence and of the blue radiation. The full width at half maximum(FWHM) of blue radiation is much lower than that of 1061.9 nm fluorescence one, which is due to the phase-matching condition as the orientation of the crystal is fixed.

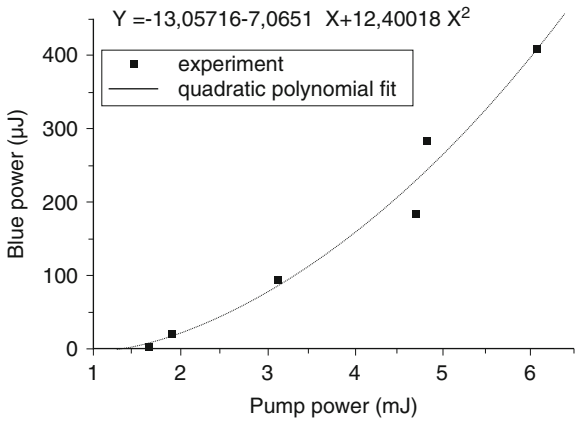

Fig. 52 The blue generation power versus the pump power incident on the crystal

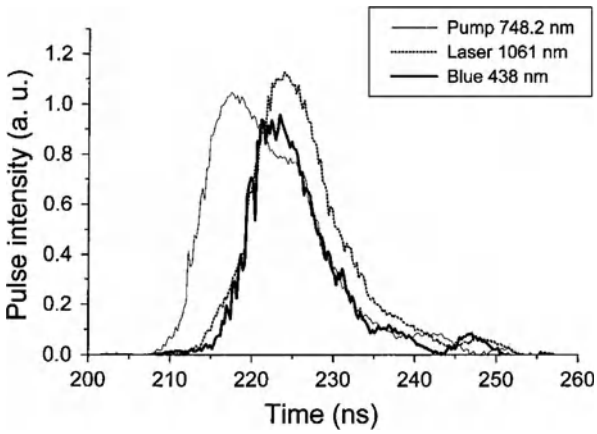

Fig. 53 The time evolutions of the pump, near infrared laser and *blue radiation pulses*

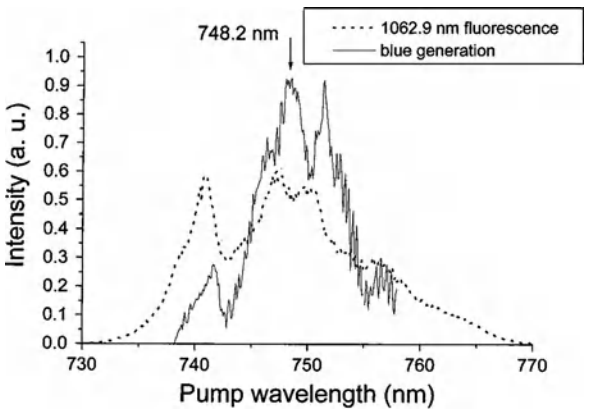

Fig. 54 The laser excitation spectra of the 1061.9 nm fluorescence and of the *blue radiation*

Self-Sum-Frequency Mixing for UV Generation

In this case, a new self-frequency-conversion for UV generation is explored [119]. First, the Nd^{3+}:$GdAl_3(BO_3)_4$ crystal was pumped at 588 nm into Nd^{3+} $^4G_{5/2} \rightarrow {}^2G_{7/2}$ levels and a laser emission at 1061.9 nm corresponding to the $^4F_{3/2} \rightarrow {}^4I_{11/2}$ was obtained. Then the SSFM process leads to UV generation near 379 nm:

$$\frac{1}{\text{pump}} + \frac{1}{588} = \frac{1}{\text{UV}}.$$

The SSFM process should satisfy the phase-matching condition:

$$\varpi_1 n_1(\theta, \varphi) + \varpi_2 n_2(\theta, \varphi) = \varpi_3 n_3(\theta, \varphi).$$

The phase-matching condition calculated from the Sellmeier [50] is shown in Fig. 55 and the absorption cross section of Nd^{3+} for σ-polarization is shown in Fig. 56.

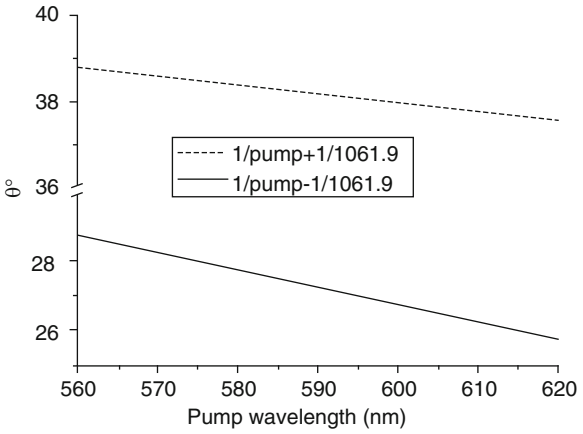

Fig. 55 Phase matching required in NGAB crystal by self-sum and difference-frequency mixing

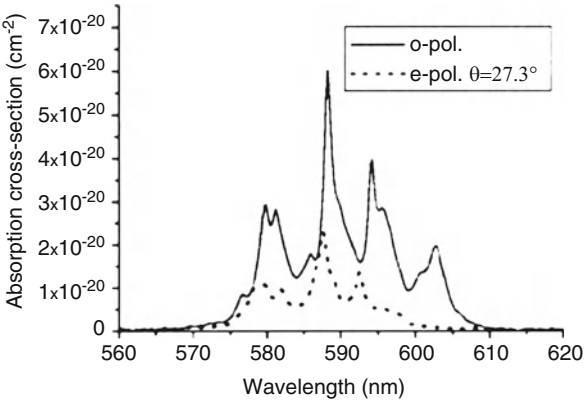

Fig. 56 Absorption cross section of NGAB corresponding to the $^4I_{9/2} \rightarrow {}^4G_{5/2}$, $^2G_{7/2}$ Nd^{3+} transition for σ-polarization and e-polarization

Since Nd^{3+}:$GdAl_3(BO_3)_4$ crystal is a negative uniaxial crystal, the phase-matching condition requires that the pump and the laser waves be ordinary (o) and the UV wave be extraordinary (e). In this case, the phase-matching polar angle is close to 38.2^0.

The crystal oriented at 35^0 with 4.3 mm in length was located inside a 8.5 cm length laser cavity consists of a flat input mirror 16MLB183, which was highly reflective at 1061.9 nm and transparent at the pump wavelength of 588 nm, and of an output Optical Model HR1064 concave mirror (18-cm radius of curvature), which was 100% reflective at 1061.9 nm and transparent in the UV range. This crystal was longitudinally pumped with a tunable pulse dye laser (bandwidth:0.04 cm^{-1}; dye,LDS750, waist 410 μm) equipped with a computer-driven motor from Laser Analytical Systems, pumped with a frequency doubled Nd:YAG laser from BM Industries. The duration of the pulse was 8 ns. A UV generation of 105 μJ/pulse with a 1.8% yield was obtained. The laser spectrum presented in Fig. 57 shows the tuning range of UV generation extends from 378 to 382 nm. Figure 58 shows the UV generation power versus the pump power incident on the crystal. Figure 59 shows the time evolutions of the pump, laser and UV radiation pulses. It can be seen that the UV

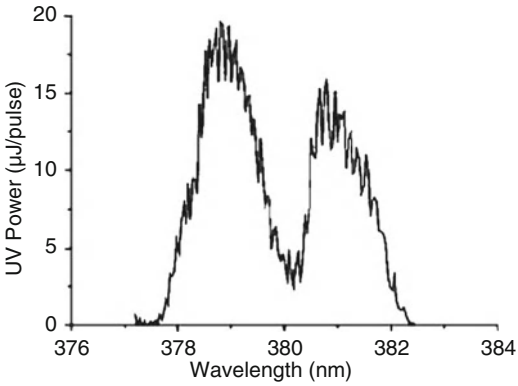

Fig. 57 The laser spectrum

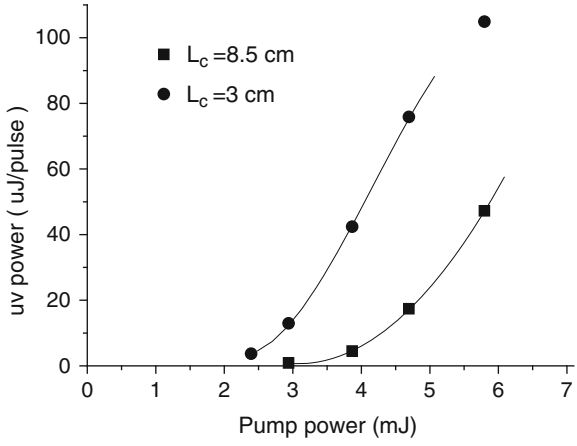

Fig. 58 The UV generation power versus the pump power incident on the crystal

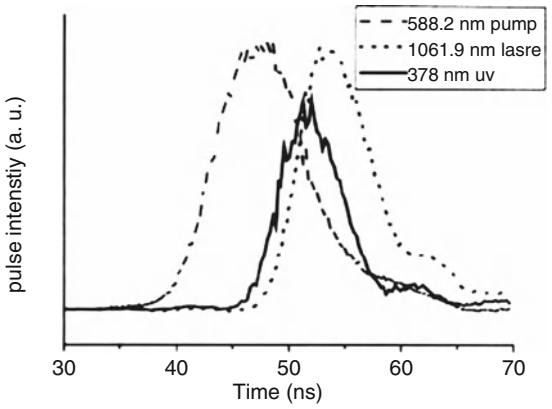

Fig. 59 The time evolutions of the pump, laser and UV radiation pulses

pulse is the temporal overlap of the pump and the laser pulses, as expected from self-frequency mixing process that occurs inside the nonlinear optical crystal.

Self-Sum-Frequency Mixing for Yellow Generation

A new self-frequency conversions from the bifunctional laser and optical nonlinear $GdAl_3(BO_3)_4$:Nd^{3+} crystal was demonstrated [120]. First, the laser worked in a dual-wavelength operation in the two ${}^4F_{3/2} \rightarrow {}^4I_{11/2}$ (at 1,062 nm) and ${}^4F_{3/2} \rightarrow {}^4I_{13/2}$ (at 1,338 nm) channels, under a fixed wavelength pumping (at 744.7 nm) and with a fixed crystal orientation (28.5°). Then the self-sum-frequency mixing 1/1,062 + 1/1,338 → 1/592 process occurred, leading to a weak yellow beam at 592 nm.

The NGAB crystal used in this work had 4.6 mm length and was cut at a $\theta = 29°$ polar angle and $\varphi = 0°$ azimuthal angle (XZ plane). Its Nd^{3+} concentration was 3%. This crystal orientation is close the 28.5° one required for birefringent phase-matching of the sum-frequency mixing: 1/1,062 + 1/1,338 → 1/592 (the 28.5° value is calculated from new Sellmeier formulas for NGAB, see next section). In this section, the NGAB lasing occurs in the two Nd^{3+} laser channels:

$$^4\mathrm{F}_{3/2} \rightarrow {}^4\mathrm{I}_{11/2}(\text{at } 1{,}062\,\text{nm}) \quad (1)$$

$$^4\mathrm{F}_{3/2} \rightarrow {}^4\mathrm{I}_{13/2}(\text{at } 1{,}338\,\text{nm}) \quad (2)$$

in order to obtain their self-frequency conversion in 592 nm yellow light.

The pumping beam near 750 nm was provided by a dye laser (LDS 751 dye) from Laser Analytical Systems, pumped by a BM Industries frequency doubled pulsed YAG:Nd laser.

In order to get a dual-wavelength lasing, the reflectivity R of the output coupler at 1,062 nm (channel 1) should be adapt because the laser emission cross sections of channels (1) and (2) are very different in NGAB: $\sigma_e = 3 \times 10^{-19}$ cm^2 and

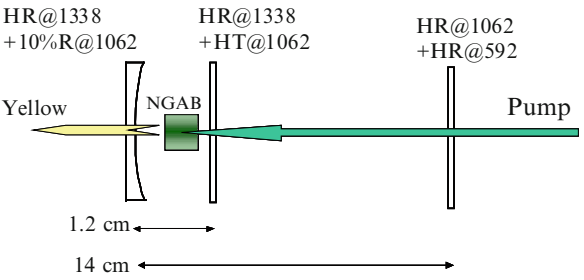

Fig. 60 Experimental set-up for self-sum-frequency mixing *1/1,062 + 1/1,338 → 1/592* from a dual-wavelength laser operation

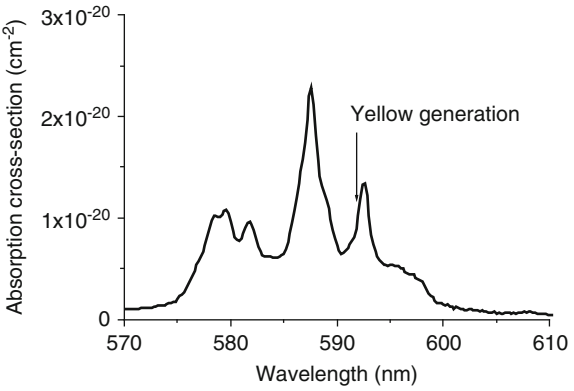

Fig. 61 Absorption spectrum of NGAB in extraordinary polarization in the wavelength range of interest near 592 nm

$\sigma_e = 5.5 \times 10^{-20}$ cm^2, respectively [90, 94]. On the other hand, only if the 1,338 nm laser cavity was much shorter than the 1,062 nm one, a temporal overlap will exist between the two 1,060 and 1,338 nm laser pulses following the pump pulse (10 nm duration), which promises the sum-frequency mixing 1/1,062 + 1/1,338 → 1/592 occurs. Hence, a typical experimental set-up, including dichroic mirrors determining two cavities and leading to yellow coherent generation at 592 nm, clearly visible to the naked eye, is represented in Fig. 60.

A yellow output of 1 μJ/pulse under 3 mJ/pulse pump was obtained. This weak output value is partly explained by some re-absorption at 592 nm (Fig. 61) from the crystal itself due to the $^4I_{9/2} \rightarrow {}^4G_{5/2}$-$^2G_{7/2}$ Nd^{3+} transition.

Figure 62 shows the time evolution of the output pulses: pump, 1,062 nm laser, second harmonic at 669 nm of 1,338 nm laser and 592 nm yellow generation. The 669 nm second harmonic was detected in place of the 1,338 nm pulse because the fast R1767 photomultiplier used is no more sensitive in the infrared range.

Self-Difference-Frequency Mixing for Infrared Tunable Generation

In this case, two new self-frequency-conversions for infrared generations are explored. First, the Nd^{3+}:$GdAl_3(BO_3)_4$ crystal was pumped at 588 nm and

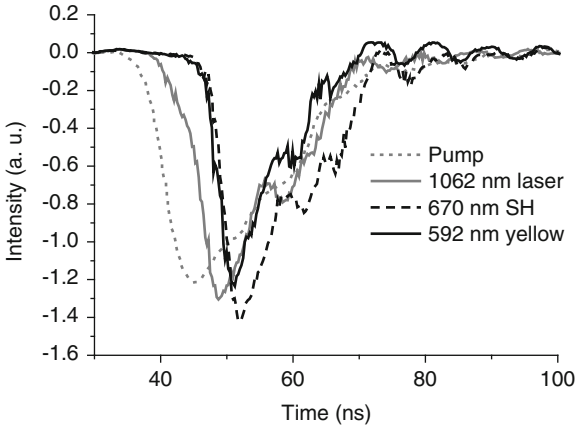

Fig. 62 Time evolution of the different output pulses

750 nm, respectively, into Nd^{3+} $^4G_{5/2} \rightarrow {}^2G_{7/2}$ levels and a laser emission at 1061.9 nm corresponding to the $^4F_{3/2} \rightarrow {}^4I_{11/2}$ was obtained [120]. Then the SDFM process leads to infrared generations near 1,340 and 2,530 nm, respectively:

$$\frac{1}{\text{pump}} - \frac{1}{1061.9} = \frac{1}{\text{Infrared}}.$$

The SDFM process should satisfy the phase-matching condition:

$$\varpi_1 n_1(\theta, \varphi) + \varpi_2 n_2(\theta, \varphi) = \varpi_3 n_3(\theta, \varphi).$$

For the IR generation at 1,340 nm, the phase-matching condition calculated from the Sellmeier [50] is shown in Fig. 52. A Nd^{3+}:$GdAl_3(BO_3)_4$ crystal oriented at 30° 5′ used for self-frequency-doubling was 4.6 mm long and rotated to optimize the IR power. It was located inside a 3-cm length laser cavity with two identical Melles-Griot MLB183 plane mirrors, which is highly reflective at 1,062 nm, transparent at the pump wavelength and also transparent for the wavelengths longer than 1,300 nm but ensured no lasing occurs at 1,338 nm in the Nd^{3+} $^4F_{3/2} \rightarrow {}^4I_{13/2}$. Replacing the plane output mirror with an Optilas HR1064 concave mirror with an 18-cmradius of curvature, an IR generation of 31 μJ/pulse with a 0.5% yield for a 5.8 mJ/pulse was obtained. Figure 63 shows the ratio of IR power to the pump power incident on the crystal. From the measured laser spectrum shown in Fig. 64, it can be seen that the tuning range extends from 1,305 nm to 1,365 nm. Two curves in Fig. 64 correspond to two slightly different crystal orientations, corresponding to the absorption peaks at 588 nm and 594 nm.

For the IR generation at 2,530 nm, the NGAB crystal used for yellow generation was located inside a laser cavity constituted of a flat input mirror 16MLB183 from Melles Griot, which is highly reflective at 1,062 nm, transparent at the pump wavelength, and of an output concave mirror HR1064 from Optilas (18 cm radius of curvature), which is 100% reflection at 1,062 nm and 65% transmission at 2,530 nm. The crystal was longitudinally pumped at a tunable wavelength near 750 nm resulting in a single wavelength laser operation at 1,062 nm.

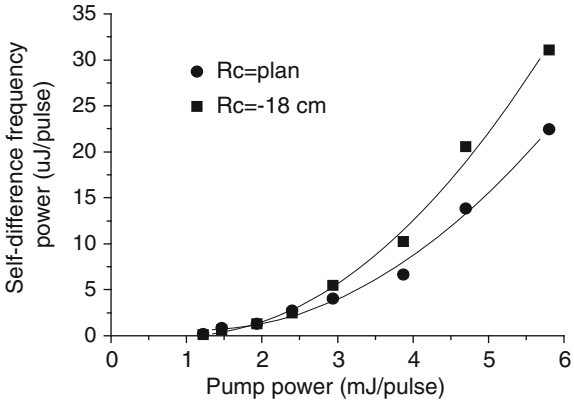

Fig. 63 Ratio of IR power obtained from SDFM of NGAB crystal pumped at 588 nm

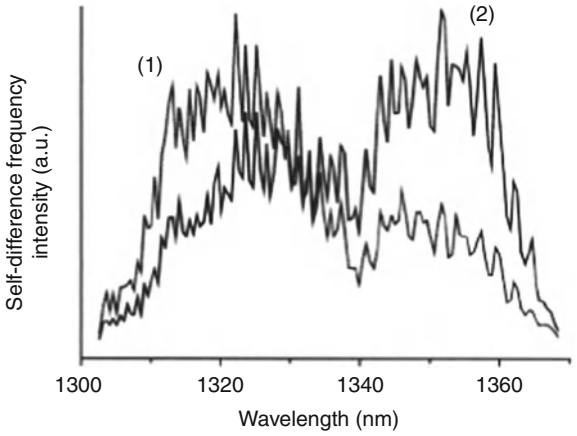

Fig. 64 IR tuning range obtained from SDFM of NGAB crystal

After a 1.5° rotation of the crystal, an infrared generation with a 0.12% efficiency was achieved. Figure 65 shows the Idler power at 2,536 nm versus pump power incident on the crystal. Figure 66 presents the laser spectrum, extending from 2,450 up to 2,600 nm and peaking at 2,530 nm. The laser wave-number $1/\lambda_I$ was measured and found to depend on the pump one $1/\lambda_P$, as it is represented in Fig. 67. It can be well fitted with the formula:

$$1/\lambda_P - 1/1062 = 1/\lambda_I.$$

From the experimental data, the Sellmeier formulas for NGAB crystal were extended to 2,450 up to 2,600 nm. Then lead to the polar phase-matching angle versus the pump wavelength for the self-difference-frequency mixing process represented above in Fig. 68.

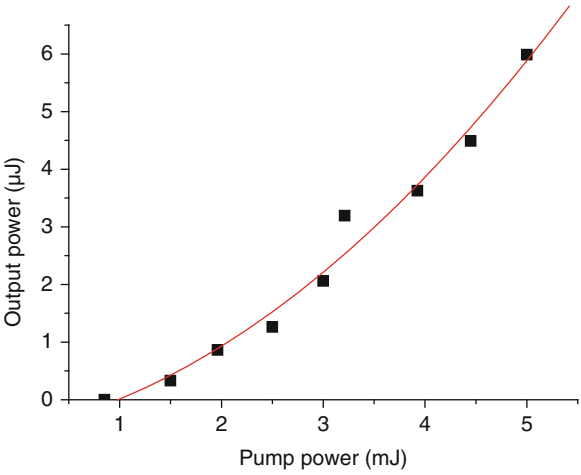

Fig. 65 Idler power at 2,536 nm versus pump power incident on the crystal (*black squares*). The *solid line* is a quadratic fitting

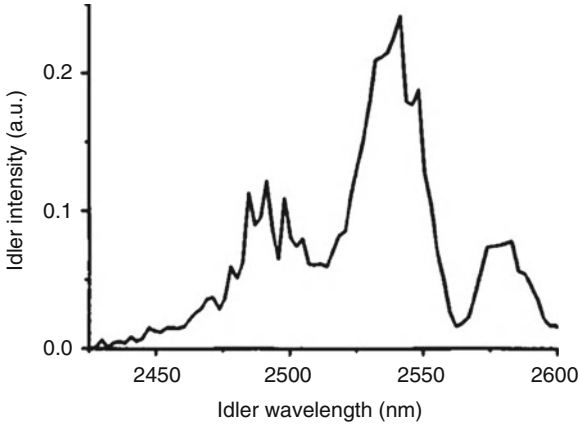

Fig. 66 Idler intensity vs wavelength

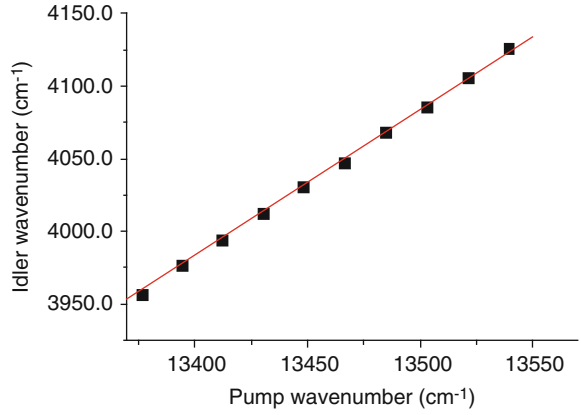

Fig. 67 Experimental values of the infrared wave-number versus the pump wave-number (*black squares*)

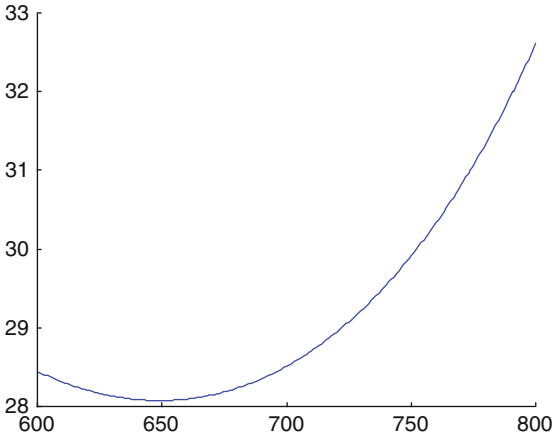

Fig. 68 Polar phase-matching angle versus the pump wavelength for the self-difference-frequency mixing process $1/\lambda_P - 1/1{,}062 = 1/\lambda_i$.

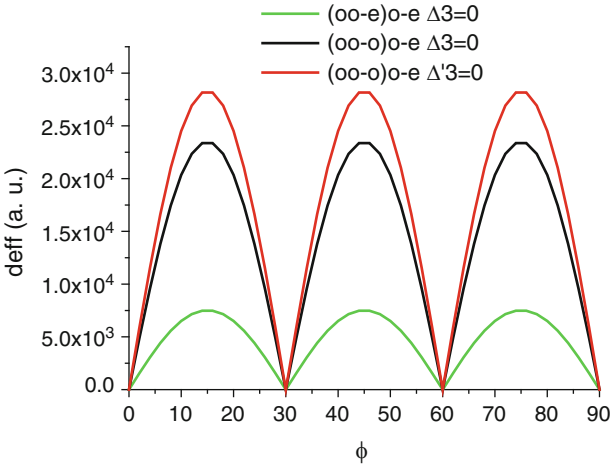

Fig. 69 Efficiency of the two cascaded second-order nonlinearities leading to self-frequency tripling in NGAB

Self-Frequency-Tripling Laser Characteristics

It was demonstrated for the first time in the case of NGAB that two cascaded second-order nonlinearities can work simultaneously with a stimulated emission inside the same crystal. The TH of the Nd^{3+} laser emission corresponding to the $^4F_{3/2} \rightarrow {}^4I_{11/2}$ channel was obtained [121].

Figure 65 shows the calculated efficiency of the two cascaded second-order nonlinearities leading to self-frequency-tripling in NGAB. Inspection of Fig. 69 leads

to the conclusion that the different processes (5–6–8) have their maximum efficiency at the azimuthal angle $\varphi = 15°$ and an NGAB crystal was accordingly cut. The polar angle of NGAB crystal was chosen $\theta = 53°$. NGAB crystal was pumped with a Laser Analytical Systems dye laser, pumped by a pulsed frequency doubled BM Industries Nd:YAG laser. The duration of the pulses was 10 ns. It was pumped near 750 nm in the $^4F_{7/2}$-$^4S_{3/2}$ Nd^{3+} levels or near 588 nm in the $^4G_{5/2}$-$^2G_{7/2}$ levels. Two different laser cavities were used. The first one is linear ((a) in Fig. 70) and is constituted of an input mirror (HR-1064) highly reflective at 1,063 and at 354 nm and with a high transmission in the visible range, and of an output mirror (HM-1037) highly reflective at 1,063 and 531.5 nm and with 50% transmission at 354 nm. The HR-1064 mirror is concave with 18 cm radius curvature and the HM-1037 mirror is plane. The second laser cavity is not linear ((b) in Fig. 70) due to a beam splitter having 85% transmission at 354 nm and high reflectivity at 1,063 nm.

A TH generation from self-frequency tripling of the 1062.8 nm NGAB laser emission was obtained. The wavelength of the laser NGAB emission was measured to be 1062.8 nm and a UV generation was detected at one third of this value. Its origin from lasing was proved by its excitation spectrum in Fig. 71: it is the image of the $^4F_{7/2}$-$^4S_{3/2}$ Nd^{3+} absorption. So this UV generation is interpreted as the TH of the laser emission corresponding to the $^4F_{3/2} \rightarrow {}^4I_{11/2}$ channel.

Figure 72 shows the angular acceptance of the TH from self-frequency tripling. It can be found that the TH signal increased drastically for two values of the polar angle: $\theta = 41.2°$ and 50.9°. The angular acceptance exhibited is about one tenth of degree but the TH signal did not vanish completely outside the range of acceptance. Figure 73 represents the time evolutions of the laser, SH and TH waves. It can be seen that the duration of the different pulses are not the same: the SH is shorter than the laser and the TH is shorter than the SH, as expected from the intensity dependence of nonlinear processes.

The efficiency of this process could be improved by using crystals exactly oriented in the phase-matching direction of the cascade.

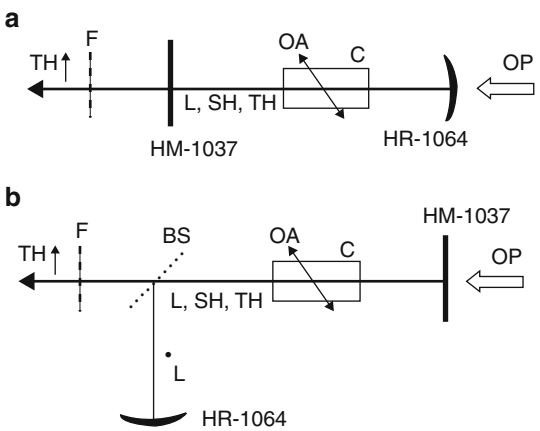

Fig. 70 Experimental set-up for self-frequency tripling demonstration. *C* NGAB crystal, *OA* optical axis, *OP* optical pumping, *F* filter, *BS* beam splitter

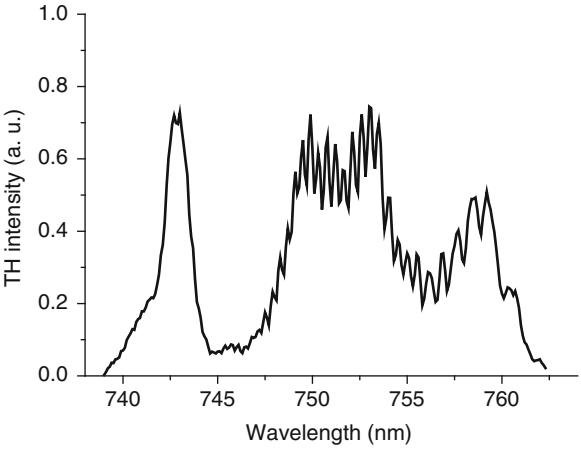

Fig. 71 Excitation spectrum of the TH from self-frequency tripling

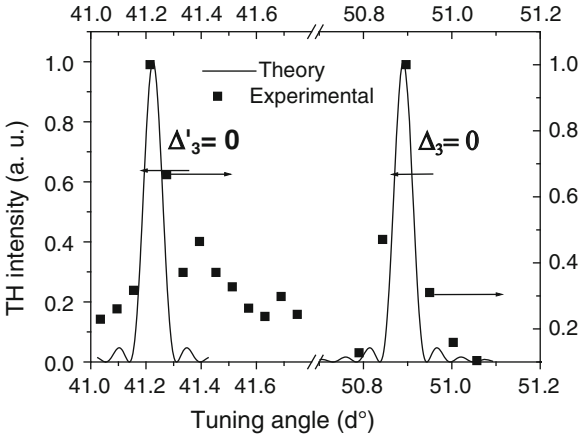

Fig. 72 Angular acceptance of the TH from self-frequency tripling

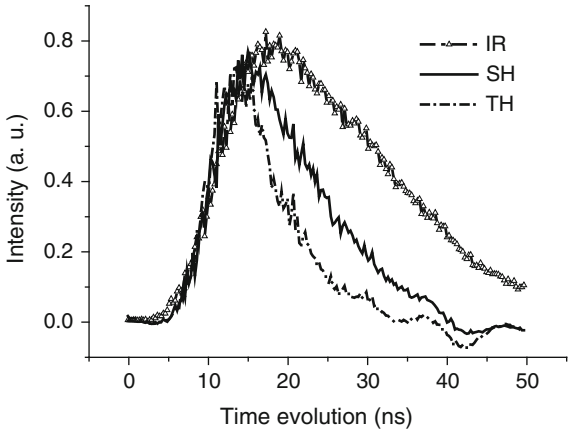

Fig. 73 Time evolutions of the fundamental (infrared laser), SH and TH waves

Self-Frequency-Conversion for Red–Green–Blue Generation

The simultaneous generation of the three red–green–blue color with a lone $GdAl_3(BO_3)_4:Nd^{3+}$ (NGAB) bifunctional crystal under a pumping wavelength at 744 nm and a fixed orientation of the crystal was demonstrated [121].

Figure 74 shows the calculated phase-matching angles (Type I) for second-harmonic generation (SHG) in (curve (1)) and for the two sum-frequency mixing (SFM) processes 1/1,063 + 1/pump (curve (2)) and 1/1,338 + 1/pump (curve (3)). The different processes for producing red, green, and blue colors are summarized in Table 22 and are visualized by the squares in Fig. 74.

The processes labeled 1/, 2/, and 5/ in Table 22 and in Fig. 74 were simultaneously exploited. This requires the simultaneous lasing of both channels (1) and (2).

$$^4F_{3/2} \rightarrow {}^4I_{11/2}\ (\text{near } 1{,}063\ \text{nm}) \quad (1)$$

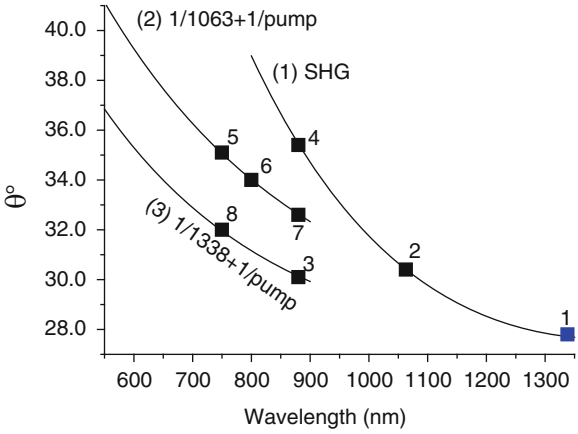

Fig. 74 $GdAl_3(BO_3)_4:Nd^{3+}$ phase-matching properties for frequency doubling (*1*) and sum-frequency mixing of the pump and the laser waves: (*2*) $^4F_{3/2} \rightarrow {}^4I_{11/2}$ laser transition, (*3*) $^4F_{3/2} \rightarrow {}^4I_{13/2}$ laser transition

Table 22 Processes for red–green–blue generation in NGAB crystal (the values of the wavelengths are approximate)

Color	Process	Pump wavelength (nm)
Red (669 nm)	**1**/SH ($^4F_{3/2} \rightarrow {}^4I_{13/2}$ laser)	750, 800, 880
Green (530 nm)	**2**/SH ($^4F_{3/2} \rightarrow {}^4I_{11/2}$ laser)	750, 800, 880
	3/SSFM ($^4F_{3/2} \rightarrow {}^4I_{13/2}$ laser and $^4I_{9/2} \rightarrow {}^4F_{3/2}$ pumping)	880
Blue (440 nm)	**4**/SH ($^4I_{9/2} \rightarrow {}^4F_{3/2}$ pumping)	880
(440 nm) (456 nm)	**5**/SSFM ($^4F_{3/2} \rightarrow {}^4I_{11/2}$ laser and $^4I_{9/2} \rightarrow {}^4F_{7/2} + {}^4S_{3/2}$ pumping)	750
(480 nm) (480 nm)	**6**/SSFM ($^4F_{3/2} \rightarrow {}^4I_{11/2}$ laser and $^4I_{9/2} \rightarrow {}^4F_{5/2} + {}^2H_{9/2}$ pumping)	800
	7/SSFM ($^4F_{3/2} \rightarrow {}^4I_{11/2}$ laser and $^4I_{9/2} \rightarrow {}^4F_{3/2}$ pumping)	880
	8/SSFM ($^4F_{3/2} \rightarrow {}^4I_{13/2}$ laser and $^4I_{9/2} \rightarrow {}^4F_{7/2} + {}^4S_{3/2}$ pumping)	750

$$^4F_{3/2} \rightarrow {}^4I_{13/2} \text{ (near 1,338 nm)} \quad (2)$$

In order to get a dual-wavelength lasing, the reflectivity R of the output coupler at 1,062 nm (channel 1) should be adapt because the laser emission cross sections of channels (1) and (2) are very different in NGAB: $\sigma_e = 3 \times 10^{-19}$ cm^2 and $\sigma_e = 5.5 \times 10^{-20}$ cm^2, respectively [88, 90].

The pumping beam was provided by a dye laser (LDS 751 dye) from Laser Analytical Systems. This laser was pumped by a BM Industries frequency-doubled pulsed YAG:Nd laser. The NGAB crystal had 4.6 mm length and was cut at a 29° polar angle in the $\varphi = 0°$ azimuthal angle. Its Nd^{3+} concentration was 3%. The cavity length was 4 cm. Under 744.7 nm pumping in ordinary polarization, red–green–blue generation at any fixed orientation of the crystal was obtained, but with a relative intensity depending of the orientation. Typical light spots on a white screen are photographed in Fig. 75, after dispersion with a Pellin–Brocca prism. Their wavelengths are 669, 531.5, and 480 nm and their polarizations are extraordinary.

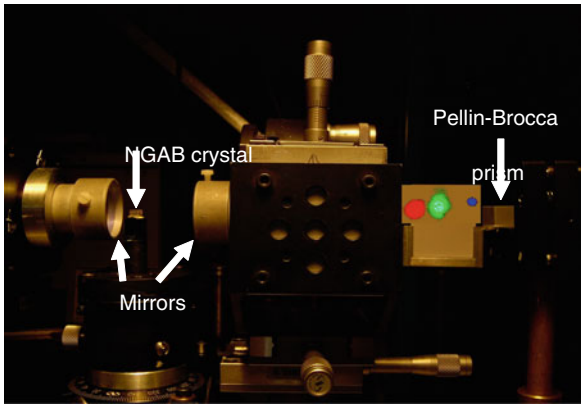

Fig. 75 Photograph of the experimental laser set-up and typical *red–green–blue* simultaneous generation

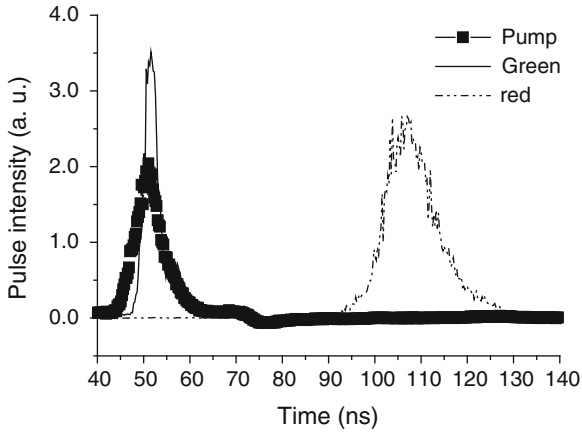

Fig. 76 Temporal evolution of the output pulses in the visible range from the dual-wavelength $GdAl_3(BO_3)_4$: Nd^{3+} laser

Figure 76 recorded the time evolutions of the pump and the 1,063 and 1,338 nm lasers, behind the output mirror. It can be seen that the pump and the 1,063 nm laser pulses have a good temporal overlap, allowing sum-frequency mixing. To the contrary, the 1,338 nm laser pulse is delayed, preventing any frequency mixing with the pump wave.

3 Summary

In the past decades, self-frequency conversion laser technology and $RX_3(BO_3)_4$ family crystals doped with Nd^{3+}, Yb^{3+}, Tm^{3+}, Cr^{3+}, and other rare earth ions have attracted much attention and received a number of publications. Especially, $GdAl_3(BO_3)_4$ crystal doped with Nd^{3+}, Yb^{3+}, Tm^{3+}, and Cr^{3+} have been widely studied and Nd^{3+}:$GdAl_3(BO_3)_4$ crystal has become a self-frequency conversion laser crystal, in which the laser outputs with high efficiency at various wavelengths ranged from UV to IR have been achieved. The great improvement in the growth technology for these crystals resulted from the invention of $K_2Mo_3O_{10}/B_2O_3$ flux system has promised these crystals with high quality and large dimensions, which will promote greatly the application process of these crystals. Although the advantage in the growth technology is seized by the rare earth ion doped $RCa_4O(BO_3)_3$ crystals, a much higher efficiency of self-frequency conversion was achieved in the rare earth ion doped $RX_3(BO_3)_4$ family crystals [9]. Compared to $YAl_3(BO_3)_4$ crystal, $GdAl_3(BO_3)_4$ crystal is easier to accept Nd^{3+} ion because the radius of Gd^{3+} is closer to that of Nd^{3+} ion than that of Y^{3+}, which will promise the higher quality crystal.

Acknowledgements Some works of this chapter were supported by National Nature Science Foundation of China (No.50902129, 61078076, 91122033), Major Projects from FJIRSM (SZD09001), the Knowledge Innovation Program of the Chinese Academy of Sciences (Grant No. KJCX2-EW-H03), Science and Technology Plan Major Project of Fujian Province of China (Grant No. 2010I0015).

References

1. Ishibashi S, Itoh H, Kaino T et al (1996) Opt Commun 125:177
2. Yamamoto JK, Sugimoto A, Yamagishi K (1994) Opt Lett 19(17):1311
3. Fan TY, Cordove Plaza A, Digonnet MJ et al (1986) J Opt Soc Am B3:140–148
4. Hemmati H (1992) IEEE J Quantum Electron 28(4):1169
5. Qui W, Fan YX et al (1993) Mol Cryst Liq Cryst Sci Technol Sec B; Nonlinear Opt 4:31
6. Amano S, Mochizuki T (1991) Nonlinear Opt 1:297
7. Schutz I, Freitag I, Wallenstein R (1990) Opt Commun 77(2, 3):221
8. Wang SC, Stone RE (1990) Advance solid state lasers, Topical Meeting of OSA, Salt Lake City, UT, March 1990
9. Bartschke J, Knappe R, Boller KJ et al (1997) IEEE Quant Electron 33(12):2295

10. Zhang S et al (1999) J Cryst Growth 206:197
11. Auge F, Mougel F, Balembois F et al. Advanced solid state lasers, Topical Meeting of OSA, MF7-1/185
12. Elchenholz M, Hammons DA, Shah L et al (1999) Appl Phys Lett 74(14):1954
13. Capmany J, Jaque D, Garcia Sole J, Kaminskii A (1998) Appl Phys Lett 72(5):531
14. Kaminskii AA, Jaque D, Nbagaev S et al (1999) J Capmany, Quant Electron 29(2):95
15. Capmany J, Jaque D, Sanz Garcia JA, Garcia Sole J (1999) Opt Commun 161:253
16. Li R, Xie C, Wang J, Liang X, Peng K, Xu G (1993) IEEE Quant Electron 29(9):2419
17. Dekker P, Huo Y, Dawes JM, Piper JA, Wang P, Lu BS (1998) Opt Commun 151:406
18. Ballman AA (1962) Am Mineral 47:1380–1383
19. Mills D (1962) Inorg Chem 1:960
20. Hong HH-p, Dwight K (1974) Mater Res Bull 9:1661
21. Lutz F, Huber G (1981) J Cryst Growth 52:646
22. Belokoneva EL, Timchenko TI (1983) Spv Phys Crystallorgr 28(1983):658
23. Wang GF, He MY, Chen WZ et al (1999) Mater Res Innovations 23:41
24. He MY, Wang GF, Chen WZ et al (1999) Mater Res Innovations 2:345
25. Wang GF, He MY, Luo ZD (1991) Mater Res Bull 26:1085
26. Jia G, Tu C, Li J et al (2006) Inorg Chem 45:9326
27. Hong HY-P (1975) Res Bull 10:1105
28. Zumsteg FC et al (1976) J Appl Phys 47:4980
29. Kuroda R et al (1981) J Chem Soc Faraday Trans 2 77:2125
30. Leonyuk NI (1976) Izv Aka Nauk SSSR, Neorg Matter 12:554
31. Akhmetov SF, Akhmetova GL, Leonyuk NI et al (1978) Kristtolografiya 23:230
32. Azizov V, Leonyuk NI, Timchenko STI et al (1979) Sov Phys Dokpl 24:313
33. Leonyuk NI, Pashkova AV, Timchenko TI et al (1979) Sov Phys Dokpl 24:233
34. Azizov AV, Leonyuk NI, Rezvyi VR et al (1982) Sov Phys Dokpel 27:95
35. Kolov VN, Peshev P (1994) J Cryst Growth 144:187
36. Leonyuk NI, Azizov AV, Belov ANV (1978) Sov Phys Dokpl 27:374
37. Azizov AV, Leonyuk NI, Rezvyi VR et al (1982) Sov Phys Dokpl 27:95
38. Kellendonk F, Blasse G (1981) J Chem Phys 75:561
39. Dianov EM, Dmitruk MV, Karasik AY et al (1980) Sov Quantum Electron 10:1222
40. Chani VI, Shimamura K, Inoue K et al (1993) J Cryst Growth 132:174
41. Jung ST, Choi DY, Kaug JK et al (1995) J Cryst Growth 148:207
42. Jung ST, Kaug JK, Chung SJ et al (1995) J Cryst Growth 149:345
43. Chin SR, Hong HY-P (1975) Opt Commun 15:345
44. Chen C (1988) J Cryst Growth 89:295
45. Timchenko TI, Leonyuk NI, Butzuova GS (1980) Sov Phys Crystallogr 25:515
46. Lutz F, Ieiss M, Muller J (1979) J Cryst Growth 47:130
47. Lutz F, Ruppel D, Ieiss M (1980) J Cryst Growth 48:4
48. Leonyuk NI, Pashkova AV, Semenova TDL et al (1975) Izv Aka Nauk SSSR, Neorg Matter 11:181
49. Elwell D, Scheel HJ (1974) Crystal growth from high temperature solutions. Academic, New York, pp 86–107
50. Wang GF, Gallagher HG, Han TPJ et al (1995) J Cryst Growth 153:169
51. Tu C, Zhu Z, Li J et al (2004) Opt Mater 27(2):167–171
52. Ye N, Zhang Y, Chen W et al (2006) J Cryst Growth 292(2):464–467
53. Wang GF, Gallagher HG, Han TPJ et al (1996) J Cryst Growth 163:272
54. Li W, Huang L, Zhang G, Ye N (2007) J Cryst Growth 307(2):405–409
55. Liu H (2011) Doctoral dissertation. Crystal growth and research on $YAl_3(BO_3)_4$ crystals. Graduated School of Chinese Academy of Sciences
56. Meyn J-P, Jensen T, Huber G (1994) IEEE J Quant Electron 30:913
57. Long XF, Wang GF, Han TPJ (2003) J Cryst Growth 249:191
58. Wang GF, Han TPJ, Han HPJ et al (1997) J Cryst Growth 181:48

59. Luo ZD, Jiang AD, Huang YC et al (1989) Chin Phys Lett 6:440
60. Zhu Z, Li J, Brenier A, Jia G et al (2007) J Appl Phys B 86:71
61. Jia GH, Tu CY, Li JF et al (2005) Cryst Growth Des 5:949
62. Jia GH, Tu CY, Li JF et al (2006) J Appl Phys 99:083502
63. Tu C, Qiu M, Li J et al (2000) J Cryst Growth 208:487
64. Zhu Z, Li J, Wu B et al (2008) J Synth Cryst 37(3):507–513 (in Chinese)
65. Tu CY, Zhu Z, Li J et al (2003) Spectrosc Spectral Anal (Chinese) 23(4):669–671
66. Tu C, Huang Y, Qiu M (1999) J Cryst Growth 206(3):249–251
67. Wang GF, Lin ZB, Hu ZS et al (2001) J Cryst Growth 233:755
68. Liao JS, Lin YF, Chen YJ et al (2004) J Cryst Growth 267:134
69. Jiang HD, Li J, Wang JY et al (2001) J Cryst Growth 233:248
70. Liao JS, Lin YF, Chen YJ et al (2004) J Cryst Growth 269:484
71. Oishi S, Teshima K, Kondo H (2004) J Am Chem Soc 126:4768
72. Choosuwan H, Guo R, Bhalla AS, Balachandran U (2002) J Appl Phys 91:5051
73. Carvajal JJ, Sole R, Gavalsa J et al (2003) Chem Mater 15:2730
74. Mu GG, Zhan YL (1978) Optics (in Chinese). People's Education press, Beijing
75. Born M, Wolf E (1975) Principles of optics. Pergamon, Oxford
76. Zhu Z, Li J, Wu B et al (2008) Chin J Cryst Growth 37(3):507–513
77. Zhu Z, Li J, Alain B et al (2007) Appl Phys B 86(1):71–75
78. Liao J, Lin Y, Chen Y, Luo Z, Huan Y (2004) J Cryst Growth 269:484
79. Wang P, Dawes JM, Dekker P et al (1999) J Opt Soc Am B 16:63
80. Deloach LD, Payne SA, Chase LL et al (1993) IEEE J Quantum Electron QE-29:1179
81. Payne SA, DeLoach LD, Smith LK et al (1994) J Appl Phys 76:497
82. Jiang H, Wang J, Zhang H et al (2002) Chem Phys Lett 361:499
83. Mougel F, Dardenne K, Aka G et al (1999) J Opt Soc Am B 16:164
84. Tu C, Huang Y, Qiu M et al (1999) J Cryst Growth 206:249–251
85. Carnall WT (1968) J Chem Phys 49:4424
86. Brenier A (2001) Opt Commun 200:355
87. Tian L (1998) Chin Sci Bull 43:1973
88. Long X et al (2002) J Alloys Compd 347:52
89. Imbush GF, Kogelman R (1981) Laser spectroscopy of solids. In: Yen WA, Selzer PM (eds) Topics applied physics. Springer, Berlin
90. Andrzej B et al (1987) J Lumin 37:29–44
91. Wang G et al (1995) Appl Phys Lett 67:3906
92. Andrews LJ et al (1989) J Lumin 42:365
93. Caird JA et al (1988) IEEE J Quant Electron QE-24:1077
94. Huber G et al (1988) J Lumin 39(5):259
95. Jia G (2005) Master dissertation. The study on the growth, structure, spectral, and laser properties of $Tm_xGd_{1-x}Al(BO_3)_4$ and rare-earth doped $SrWO_4$ crystals. Graduated School of Chinese Academy of Sciences
96. Jia G, Tu C, You Z et al (2006) J Appl Phys 99:083502
97. Jia G, Tu C, Li J et al (2004) J Cryst Growth 264(1–3):346–350
98. Ohta K, Saito H, Obara M (1993) J Appl Phys 73:3149
99. Fan TY, Huber G, Byer RL et al (1988) IEEE J Quantum Electron 24:924
100. Jia G, Tu C, You Z et al (2004) J Appl Phys 96:6262
101. Ryba-Romanowski W, Golab S et al (1999) Appl Phys B: Laser Opt 68:199
102. Payne SA, Chase LL, Smith LK et al (1992) IEEE J Quantum Electron 28:2619
103. Guell F, Gavalda J, Sole R et al (2004) J Appl Phys 95:919
104. Bagaev SN, Vatnik SM, Maiorvo AP et al (2004) Quantum Electron 30:310
105. Braud A, Tigreat PY, Doualan JL et al (2001) Appl Phys B: Laser Opt 72:909
106. Rustacd G, Stenerse K (1996) IEEE J Quantum Electron 32:1645
107. Sokolska I, Ryba-Romanowski W, Golab G et al (1998) J Appl Phys 84:5348
108. Yamanouchi T, Tanaka M (1985) J Quant Spectrosc Radiat Transfer 34:463

109. Krupke WF, Chase LL (1990) Opt Quantum Electron 22:51
110. Guohua Jia (2005) Master dissertation. The study on the growth, structure, spectral, and laser properties of $Tm_xGd_{1-x}Al(BO_3)_4$ and rare-earth doped $SrWO_4$ crystals. Graduated School of Chinese Academy of Sciences
111. Jia G, Tu C, Li J et al (2005) J Cryst Growth Des 5:949–952
112. Zhu Z, Li J, Wu B et al (2008) J Synth Cryst (Chinese) 37(3):507–513
113. Zhu Z (2006) Master dissertation. The study of pure and active ions doped $GdAl_3(BO_3)_4$ laser crystal. Graduated School of Chinese Academy of Sciences
114. Brenier A, Chaoyang Tu, Minwang Qiu et al (2001) J Opt Soc Am B 18(8):1104
115. Brenier A, Chaoyang Tu, Zhaojie Zhu et al (2001) Opt Commun 200:355–358
116. Mougel F, Aka G, Kahn A et al (1999) Opt Mater 13:293–297
117. Brenier A, Boulon G, Jaque D et al (1999) Opt Mater 13:311–317
118. Brenier A, Boulon G (2000) J Lumin 86:125–128
119. Brenier A, Tu C, Zhu Z et al (2002) Opt Lett 27:240–242
120. Brenier A, Tu C, Zhu Z et al (2005) J Appl Phys 97:013503
121. Brenier A, Tu C, Zhu Z et al (2004) Appl Phys Lett 84:16

Struct Bond (2012) 144: 181–222
DOI: 10.1007/430_2011_69
© Springer-Verlag Berlin Heidelberg 2012
Published online: 29 February 2012

Structure Design and Crystal Growth of UV Nonlinear Borate Materials

Ning Ye

Abstract Crystal design and growth of huntite-type and alkaline beryllium borates used for UV and deep-UV frequency conversion are summarized. A series borates crystallizing in the trigonal-huntite structure, $ReM_3(BO_3)_4$ (Re = La, Ga, Y, Lu; M = Y, Lu, Sc, Ga, Al), has been discovered through structural design with respect to the size tuning on trigonal prism or/and octahedral site in the structure. The structural, optical, and chemical–physical properties are detailed. They all have large NLO coefficients, moderate birefringence for UV phase matching, and robust chemical and physical properties. The NLO coefficients of those containing Bi are larger due to the contribution from the lone-pair electron of Bi, while the UV cutoff of these crystals is redshift for about 100 nm. The systematical synthesis of a series of new alkaline beryllium borates with the stoichiometry $NaBeB_3O_6$, $ABe_2B_3O_7$ (A = K, Rb), and $Na_2CsBe_6B_5O_{15}$ in order to obtain deep-UV NLO crystals containing new beryllium borate anionic groups or framework was presented. A new beryllium borate anionic group $[Be_2B_3O_{11}]^{9-}$ was found in the structure of $NaBeB_3O_6$ and α-$KBe_2B_3O_7$. β-$KBe_2B_3O_7$, γ-$KBe_2B_3O_7$, $RbBe_2B_3O_7$, and $Na_2CsBe_6B_5O_{15}$ consist of 2D alveolate beryllium borate network $[Be_2BO_5]_\infty$. Furthermore, the adjacent $[Be_2BO_5]_\infty$ layers in these compounds were connected by covalent bonds.

Keywords Borate · Nonlinear optical crystal · Structure design

N. Ye (✉)
Fujian Institute of Research on the Structure of Matter, Chinese Academy of Sciences, Fuzhou, People's Republic of China
e-mail: nye@fjirsm.ac.cn

Contents

1 Borate Crystals with Huntite Structure 182
1.1 $Y_xLa_ySc_z(BO_3)_4$, $(x + y + z = 4)$ [11, 12] 183
1.2 $Lu_xLa_ySc_z(BO_3)_4$, $(x + y + z = 4)$ [17] 189
1.3 $Gd_xLa_ySc_3(BO_3)_4$, $(x + y = 1)$ [20] 193
1.4 $Bi_xLa_ySc_z(BO_3)_4$ $(x + y + z = 4)$ [23] 198
1.5 *BiAlGa2(BO3)4* [24] 202
1.6 Summary 205
2 Alkaline Beryllium Borates for Deep-UV Applications [28, 29] 205
2.1 Synthesis 207
2.2 Borates Containing $[Be_2B_3O_{11}]^{9-}$ Group 208
2.3 Borates Containing Alveolate $[Be_2BO_3]_\infty$ Layers 210
2.4 Assembly of the Beryllium Borate Units 213
2.5 Structure and NLO Property Relations 216
References 219

By means of frequency conversion, nonlinear optical (NLO) crystals function to generate tunable laser beams covering various optical spectra regions. Currently, commercially available crystals are capable of harmonic generation in a region from UV to near IR. Significant efforts have been made to grow high-quality crystals to improve their laser performance in practical applications, on the one hand, and, on the other hand, to discover new crystals to extend spectra coverage into the UV and deep-UV regions. In this contribution, research work accomplished by our group on crystal design and growth of huntite-type and alkaline beryllium borates used for UV and deep-UV frequency conversion is summarized.

1 Borate Crystals with Huntite Structure

The structural, physical properties and the crystal growth of the trigonal-huntite derivative $YAl_3(BO_3)_4$ (YAB) have been extensively studied during the past four decades [1–3]. The crystal structure of YAB is illustrated in Fig. 1. It is a classical huntite type with nearly planar layers of BO_3 groups extending in the *a*–*b* plane. The larger trivalence ion Y and the smaller trivalence ion Al atoms occupy 6-coordinate sites between these layers with the Y atoms centering a distorted trigonal prism and Al atoms residing in a distorted octahedron. The trigonal prisms are completely isolated one from the other, while the AlO_6 octahedra share edges.

Interest in this material arises from its high frequency-conversion efficiency and ability to substitutionally accept lanthanide laser-active ions on the Y site. The major impediment, however, in developing the compound for practical applications has been the difficulty in growing large, high-quality crystals. At present, the best known flux for the growth of YAB is a complex polymolybdate [4], which suffers from a relatively high volatility and incorporation of Mo into the crystals. The latter problem leads to a near UV absorption band that limits numerous potential applications at shorter wavelengths.

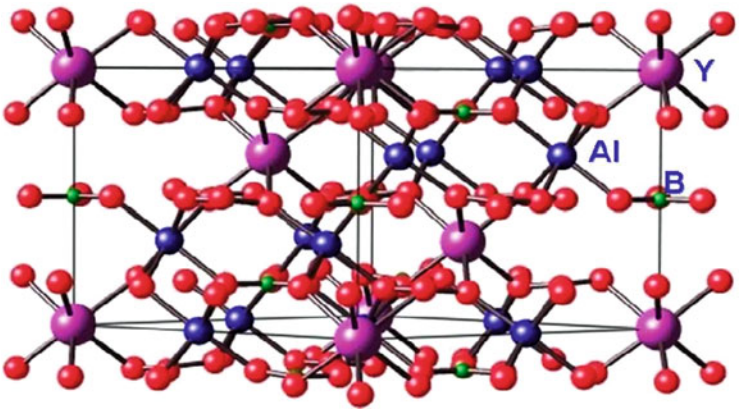

Fig. 1 Structure of YAB

To overcome these crystal growth problems, efforts have been directed to the development of other related huntite derivatives containing Sc, i.e., $LnSc_3(BO_3)_4$ (Ln = lanthanide) [5]. These materials crystallize in the noncentrosymmetric trigonal-huntite structure for a few lighter lanthanides, e.g., $CeSc_3(BO_3)_4$ [6], while the La derivative, $LaSc_3(BO_3)_4$ (LSB) [7], crystallizes in centrosymmetric monoclinic form. Although a trigonal phase of LSB has been reported [8], this result has not been reproduced by us and others [9]. Nevertheless, the monoclinic structure of LSB can be converted to the trigonal form by doping with a smaller lanthanide, e.g., $La_{1-x}Nd_xSc_3(BO_3)_4$ [9], undergoing alterations in structure over selected doping levels similar to those in the $Y_{1-x}Nd_xAl_3(BO_3)_4$ (NYAB) system [10]. To form a trigonal phase from huntite derivatives containing Sc, an appropriate size ratio of r(Ln)/r(Sc) must be satisfied, i.e., this ratio must be smaller than that observed in LSB. To maintain transparency at short wavelengths and form the trigonal phase, we have substituted Y, Lu, and Gd for La and/or Y, Lu, Ga, and Al for Sc in LSB to achieve this size tuning. The resulting trigonal phases are ready to crystal growth, yielding transparent, high-quality crystals. In the following sections, we describe the crystal structure, phase relations, and optical properties of the new, promising NLO crystals with trigonal-huntite-type structure, $ReM_3(BO_3)_4$ (Re = La, Gd, Y, Lu; M = Y, Lu, Sc, Ga, Al).

1.1 $Y_xLa_ySc_z(BO_3)_4$, $(x + y + z = 4)$ *[11, 12]*

1.1.1 Experimental

Powder samples of $Y_xLa_ySc_z(BO_3)_4$ (YLSB) were prepared by reacting stoichiometric ratios of La_2O_3 (Stanford Materials, 99.999%), Y_2O_3 (Stanford Materials, 99.999%), Sc_2O_3 (Stanford Materials, 99.99%), and B_2O_3 (Cerac, 99.95%).

Five weight percent $LiBO_2$ (Cerac, 99.9%) was added to promote the reaction and was later removed by washing the product in H_2O. The samples were ground and heated in Pt crucibles at 850°C for 2 h and 1,100°C for 12 h; the samples were additionally ground after the heat treatment at 850°C.

Crystals of approximate composition $Y_{0.57}La_{0.72}Sc_{2.71}(BO_3)_4$ were grown by using the flux $3Li_2O{\cdot}2B_2O_3$ (Li_2CO_3, Cerac, 99.9%; B_2O_3, Cerac, 99.9%); the composition of the mixture for crystal growth was 0.6 Y_2O_3 – 0.35 La_2O_3 – 1.5 Sc_2O_3 – 7 B_2O_3 – 7.5 Li_2O. The mixture was heated in a Pt crucible to 1,050°C and held at this temperature for 2 days. A seed with orientation $[11\bar{2}0]$ was then suspended in the melt to determine the crystallization temperature and initiate growth. Crystals were grown by cooling at a rate of 2°C/day, continuing until the desired boule size was obtained. The flux attached to the crystal was readily dissolved in nitric acid.

1.1.2 Crystal Structure and Phase Relations

The structure of YLSB is a classical huntite type according to single-crystal structure determination. The La atoms occupy the centers of distorted trigonal prism at the threefold axis, and Sc atoms reside in the centers of distorted octahedron. Y atoms replace not only the La atoms in the trigonal prisms but also the Sc atoms in the octahedra.

A differential thermal analysis for the composition $La_{0.7}Y_{0.3}Sc_3(BO_3)_4$ exhibits a broad melting event beginning at 1,220°C and ending near 1,475°C. In principle, a solid solution such as $La_xY_{1-x}Sc_3(BO_3)_4$ will not exhibit congruent melting. Therefore a flux must be used to grow crystals. Colorless and transparent YLSB crystals of composition $Y_{0.57}La_{0.72}Sc_{2.71}(BO_3)_4$ and dimensions near 30 × 30 × 25 mm (Fig. 2) have been grown by a high-temperature top-seeded solution method. The crystals have the typical morphology of the huntite series [4], clearly exhibiting $\{11\bar{2}0\}$ and $\{10\bar{1}1\}$ facets. They are chemically stable with respect to water and strong acid, and they are mechanically robust and sufficiently hard to be readily polished.

To better define the stability region for the trigonal phase, samples were prepared on the basis of the formula $Y_xLa_ySc_z(BO_3)_4$ ($x + y + z = 4$). All results are displayed in a quasi-ternary phase diagram (Fig. 3) with the three end members YBO_3, $LaBO_3$, and $ScBO_3$. LSB was found to be monoclinic at 1,100°C, and it is the only phase on the quasi-binary line between the end members $LaBO_3$ and $ScBO_3$. Two single phases were found inside the triangle – a calcite phase (C) near the composition $Y_2LaSc(BO_3)_4$ and a trigonal phase (R) covering the composition range of $0.29 < x < 0.67$, $0.67 < y < 0.82$, and $2.64 < z < 3.00$. The latter phase was proven to be a trigonal-huntite derivative on the basis of the single-crystal structure determination. Phase boundaries, as determined from interpretation of the diffraction patterns, are indicated in the diagram, cf., Fig. 3.

Fig. 2 As-grown YLSB crystal

For the general formula $Y_xLa_ySc_z(BO_3)_4$, Y atoms replace not only the La atoms in the trigonal prisms but also the Sc atoms in the octahedra. The formula for demonstrating Y-atom substitution in YLSB can be written as $(Y_{x'}La_{1-x'})_{tri}(Y_{y'}Sc_{3-y'})_{octa}(BO_3)_4$. The sizes of the trigonal prisms and the octahedra required to form the huntite structure are achieved by maintaining the suitable Y-atom doping level in each site. In general, the unit-cell volume varies with the sizes of both the trigonal prism and the octahedron. This can be expressed in the following equations by using atomic radii (R) [13] and appropriately weighted occupancies for the Y, La, and Sc atoms:

$$\begin{aligned} V &\propto R_Y^3 \cdot x' + R_{La}^3 \cdot (1 - x') + R_Y^3 \cdot y' + R_{Sc}^3 \cdot (3 - y'), \\ V &\propto R_{La}^3 + 3R_{Sc}^3 + (R_Y^3 - R_{La}^3)x' + (R_Y^3 - R_{Sc}^3)y'. \end{aligned} \tag{1}$$

If the Y atoms are distributed over both the La and Sc sites, the points in a three-dimensional (3D) plot of V, x', and y' should occupy a plane. By defining the effective concentration, C_{eff}, the results can be projected onto a two-dimensional (2D) plot of V versus C_{eff}:

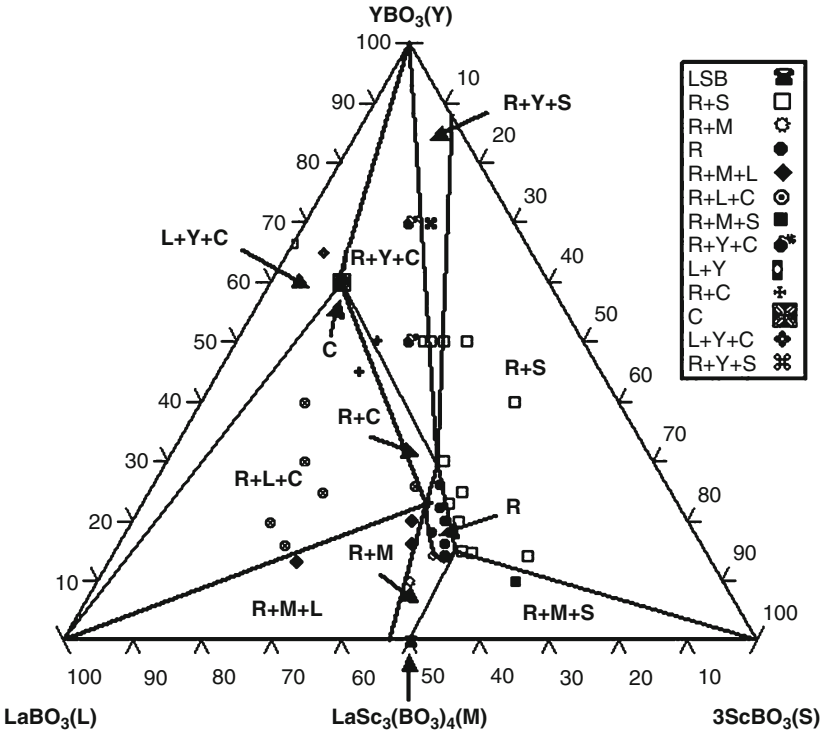

Fig. 3 Quasi-ternary phase diagram of $LaBO_3$ – YBO_3 – $ScBO_3$ system. *R* represents trigonal YLSB phase

$$C_{\text{eff}} = -\frac{(R_{\text{Y}}^3 - R_{\text{La}}^3)x' + (R_{\text{Y}}^3 - R_{\text{Sc}}^3)y'}{\sqrt{(R_{\text{Y}}^3 - R_{\text{La}}^3)^2 + (R_{\text{Y}}^3 - R_{\text{Sc}}^3)^2}},$$
$$V \propto R_{\text{La}}^3 + 3R_{\text{Sc}}^3 + \sqrt{(R_{\text{Y}}^3 - R_{\text{La}}^3)^2 + (R_{\text{Y}}^3 - R_{\text{Sc}}^3)^2} \cdot C_{\text{eff}}. \tag{2}$$

As seen from the linear relationship between C_{eff} and V in Fig. 4, the Y atoms do indeed appear to be distributed across both sites.

1.1.3 Optical Properties

As shown in Fig. 5, the crystals exhibit high transparency in the UV portion of the spectrum. The short-wavelength transmission cutoff extends to approximately 193 nm, opening a wide window for UV applications.

The refractive indices at wavelengths covering visible and near-infrared wavelengths were determined with the minimum-deviation method. The indices were fit to the Sellmeier equations:

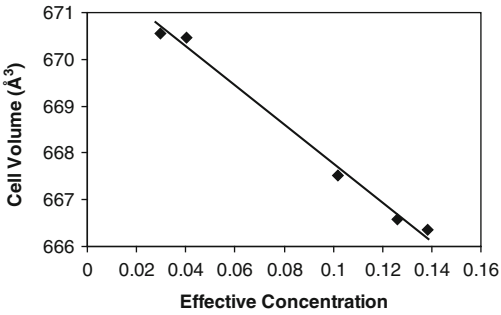

Fig. 4 Relationship between effective concentration, C_{eff}, and cell volume, V

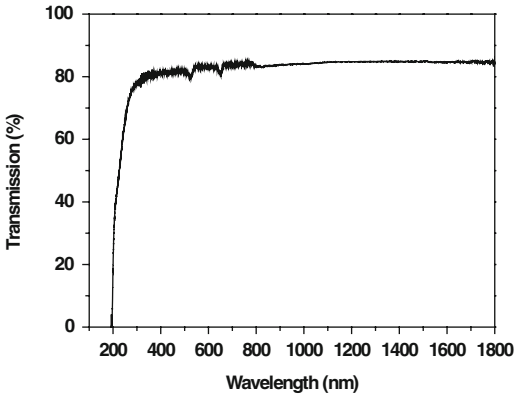

Fig. 5 Transmittance curve of YLSB crystal

$$\begin{aligned} n_{\text{o}}^2 &= 3.30760 + \frac{0.03027}{\lambda^2 - 0.02139} - 0.01309\lambda^2, \\ n_{\text{e}}^2 &= 3.01746 + \frac{0.02530}{\lambda^2 - 0.01755} + 0.00125\lambda^2, \end{aligned} \tag{3}$$

where n_{o} and n_{e} are the refractive indices for ordinary and extraordinary polarizations, respectively, and λ is the wavelength expressed in micrometers. YLSB is a negative uniaxial optical crystal, and the birefringence value ($\Delta n = n_{\text{o}} - n_{\text{e}}$) is approximately 0.085 over the measured wavelength region. This birefringence is consistent with the anisotropic nature of the crystal structure and the presence of layers of planar BO_3 groups.

On the basis of the Sellmeier equations, the phase-matching curves for second-harmonic generation (SHG) can be calculated for type I and type II phase matching, respectively (Fig. 6). The shortest wavelength for type I SHG is predicted to be 290 nm from the calculated phase-matching curves (Fig. 6), and the phase-matching angle for type I SHG at 532 nm is 33.5°. Some phase-matching angles (θ_{pm}) at selected wavelengths were verified by measurements with a dye laser; the results were found to consistent with calculated values (Fig. 6).

The effective SHG coefficient d_{eff} is given by

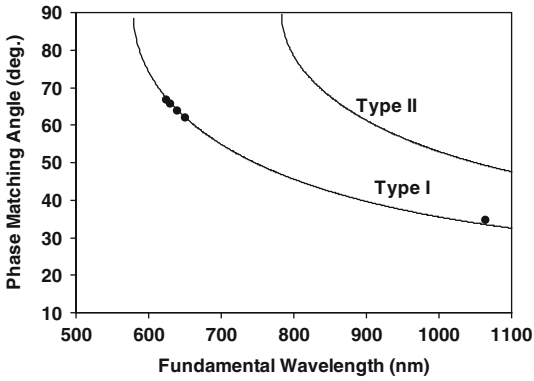

Fig. 6 Phase-matching curve for second-harmonic generation

$$d_{\text{eff}}^{\text{type-I}} = d_{11}\cos\theta\cos 3\phi,$$
$$d_{\text{eff}}^{\text{type-II}} = d_{11}\cos^2\theta\sin 3\phi. \tag{4}$$

YLSB has point-group symmetry D_3, so it has only one nonzero-independent SHG coefficient, i.e., d_{11}, assuming Kleinman symmetry relations. The magnitude of the coefficient d_{11} can be calculated on the basis of Anionic Group Theory by using the equation [14]

$$d_{11} = \frac{L^3}{V}\sum_{p=1}^{N}\sum_{ijk} R_{1i}R_{1j}R_{1k}\beta_{lmn}, \tag{5}$$

where L is the local-field factor [15], V is the unit-cell volume, R_{1x} is the orientation direction cosine for each BO_3 group, and β_{lmn} is the component of the hyperpolarizability tensor for each BO_3 group with the only nonzero component being β_{111}. As shown in Fig. 7, there are twelve BO_3 groups in a unit cell; three are centered by atom B(1) (light), and nine are centered by atom B(2) (dark). The two types of groups are related by an approximate center of symmetry, so the sum of β_{lmn} according to the orientation (R) of individual groups $d_{11} \propto (9-3)/12 \times \beta_{111}$, which is 50% of optimum. The same BO_3 group arrangement is found in YAB, and its d_{11} coefficient has been reported to be 1.79 pm/V [16]. The d_{11} value for YLSB may then be deduced by comparing the number densities of BO_3 groups in YAB and YLSB:

$$d_{11}(\text{YLSB}) = \frac{\text{BO}_3\text{ number group density(YLSB)}}{\text{BO}_3\text{ number group density(YAB)}} \times 1.79\ \text{pm/V}. \tag{6}$$

From the number densities of 1.8×10^{22} and 2.2×10^{22} for YLSB and YAB, respectively, the predicted value of d_{11} for YLSB is 1.43 pm/V, assuming the same local-field corrections for the two materials.

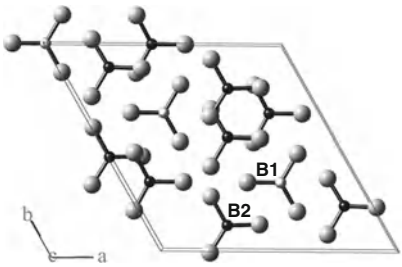

Fig. 7 YLSB structure: view down the *c*-axis. *Lightly shaded circles* represent B(1) atoms, and *heavily shaded circles* represent B(2) atoms

The second-harmonic signal produced by YLSB powders with a 1,064-nm fundamental corresponds to 0.67 × β-BaB_2O_4. These signals are proportional to the squares of the nonlinear *d* coefficients, assuming the phase-matching lengths for the two materials are the same. As a result, the ratio d_{obs} (YLSB)/d_{obs}(YAB) = 0.8. Since the reported d coefficient for β-BaB_2O_4 is 1.8 pm/V, the derived result for YLSB is 1.4 pm/V, a value in general agreement with the calculated value of 1.43 pm/V. The high nonlinear coefficients, small walk-off angles, and relatively wide acceptance angles make YLSB a promising crystal for frequency conversion in the UV region. These features coupled with higher chemical stability and mechanical durability relative to BBO and LBO make YLSB a promising NLO material for practical applications.

1.2 $Lu_xLa_ySc_z(BO_3)_4$, *(x + y + z = 4) [17]*

1.2.1 Experimental

Polycrystalline samples of $Lu_xLa_ySc_z(BO_3)_4$ (LLSB) were prepared by reacting stoichiometric ratios of Lu_2O_3 (high pure), La_2O_3 (high pure), Sc_2O_3 (high pure), and B_2O_3 (analytical grade). $LiBO_2$ (Li_2CO_3, analytical grade; B_2O_3, analytical grade) has been added to promote the reaction. Lanthanum oxide was calcinated in a muffle furnace at 1,000°C for 12 h prior to weighing in order to remove absorbed water and carbon dioxide. The samples were ground thoroughly in an agate mortar and then charged into alumina crucible. After preheating at 850°C for 2 h, the products were cooled to room temperature and ground up again, then sintered at 1,100°C for 12 h.

Large single crystals have been grown by a high-temperature top-seeded solution growth method with a $Li_6B_4O_9$ flux. The mixture was heated in a platinum crucible to 1,100°C and held for 48 h to ensure the complete melting and homogeneous mixture. A well-orientated $[11\bar{2}0]$ seed with the dimensions 3 × 3 × 10 mm^3 was bond at the end of a Pt rod with Pt wires and touched the surface of the melt at a temperature 5°C higher than the melting point. The temperature was then decreased at a rate of 0.5°C/day until the end of the growth. When the growth was completed, the crystal was drawn out of the melt and cooled down together with the furnace to room temperature at a rate of 15°C/h.

1.2.2 Crystal Structure and Phase Relations

The structure of LLSB is a classical huntite type as presented in the results from single-crystal structure determination. The La atoms occupy the centers of distorted trigonal prism (p) at the threefold axis and Sc atoms reside in the centers of distorted octahedron (o). Lu atoms replace not only the La atoms in the trigonal prisms but also the Sc atoms in the octahedra. The formula for demonstrating Lu-atom substitution in LLSB can be written as $(Lu_{0.05}La_{0.95})_p(Lu_{0.61}Sc_{2.39})_o(BO_3)_4$. The sizes of the trigonal prisms and the octahedra required to form the huntite structure are achieved by maintaining the suitable Lu-atom doping level in each site.

Colorless and transparent LLSB crystals of dimensions up to $30 \times 28 \times 6\ mm^3$ have been grown by a high-temperature top-seeded solution method (Fig. 8). The crystals have the typical morphology of the huntite series [4], clearly exhibiting $\{11\bar{2}0\}$ and $\{10\bar{1}1\}$ facets. They are chemically stable with respect to water and strong acid, and they are mechanically robust and sufficiently hard to be readily polished.

The concentrations of the metal elements of an LLSB crystal from the ICP elemental analysis were 18.84, 21.43, and 17.51 wt% for Lu, La, and Sc, respectively. According to the composition of members of the huntite family, the stoichiometry was calculated on the basis of 12 O atoms and 4 B atoms in each formula unit, giving a resulting formula $Lu_{0.66}La_{0.95}Sc_{2.39}(BO_3)_4$.

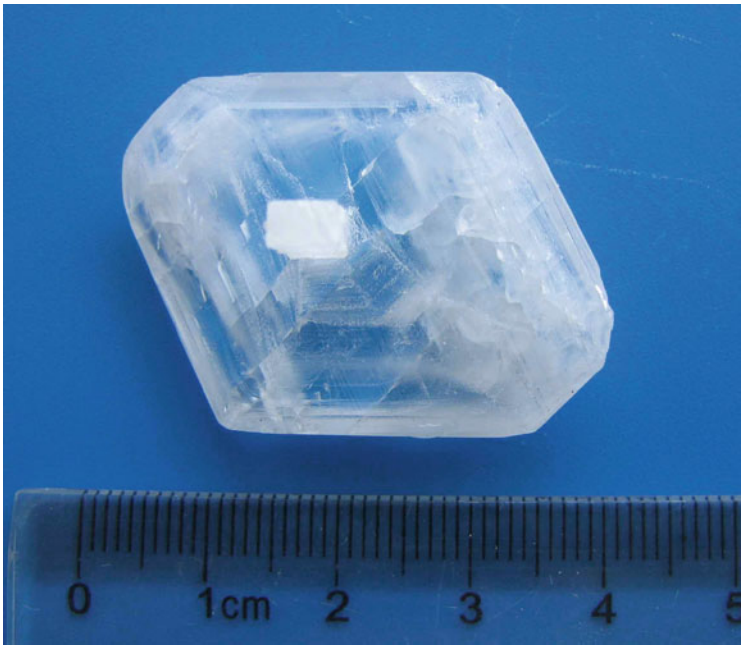

Fig. 8 As-grown LLSB crystal

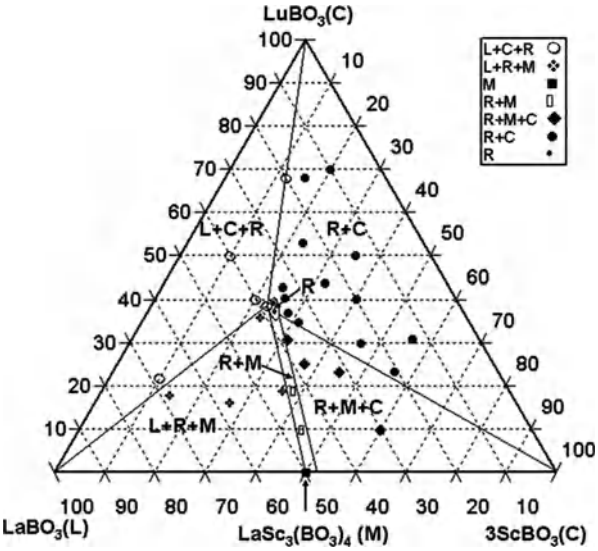

Fig. 9 Quasi-ternary phase diagram of $LuBO_3$–$LaBO_3$–$ScBO_3$ system; *R*, trigonal phase; *C*, solid solution of $Lu_xSc_{1-x}BO_3$; *L*, $LaBO_3$; *M*, monoclinic phase of $LaSc_3(BO_3)_4$

The stability region for the LLSB trigonal phase was defined by the analysis of a quasi-ternary phase diagram (Fig. 9) with the three end members $LuBO_3$ (C), $LaBO_3$ (L), and $ScBO_3$ (C). Ninety samples were prepared with a synthesis temperature of 1,100°C on the basis of the formula $Lu_xLa_ySc_z(BO_3)_4$ ($x + y + z = 4$); product phases were identified by using X-ray powder diffraction which are displayed in Fig. 2. LSB (M) was found to be monoclinic at 1,100°C, and it is the only phase on the quasi-binary line between the end members $LaBO_3$ and $ScBO_3$. $Lu_xSc_{1-x}BO_3$ (C) forms a solid solution of calcite type covering the quasi-binary line between the end members $LuBO_3$ and $ScBO_3$. A trigonal phase (R) was found to be the only quasi-ternary phase in the diagram which was proven to be a trigonal-huntite derivative on the basis of the single-crystal structure determination. Phase boundaries, as determined from interpretation of the diffraction patterns, are indicated in the diagram, cf., Fig. 9.

1.2.3 Optical Properties

As shown in Fig. 10, the crystals exhibit high transparency in the UV portion of the spectrum. In our measurement, the short-wavelength transmission cutoff extends to approximately 190 nm, opening a wide window for UV applications. The IR absorption edge is at about 5.8 μm, which could be also found out from the IR portion of the transmittance curve in Fig. 10.

The refractive indices for wavelengths of 0.473, 0.532, 0.6328, 1.064, and 1.338 μm at room temperature were measured by an auto-collimation method. The Sellmeier equations were obtained as follows using the method described in [18]:

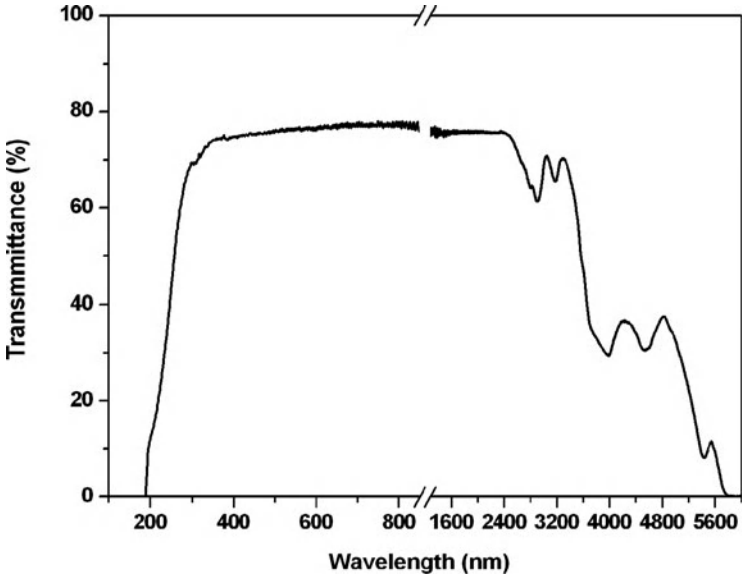

Fig. 10 Transmittance curves of LLSB crystal

$$n_o^2 = 3.29176 + \frac{0.02943}{\lambda^2 - 0.02352} - 0.01967\lambda^2,$$
$$n_e^2 = 3.01874 + \frac{0.01932}{\lambda^2 - 0.04291} - 0.01306\lambda^2, \quad (7)$$

where n_o and n_e are the refractive indices for ordinary and extraordinary polarizations, respectively. LLSB is a negative uniaxial optical crystal, and the birefringence value ($\Delta n = n_o - n_e$) is 0.077 at the wavelength of 1.064 μm. This birefringence is consistent with the anisotropic nature of the crystal structure and the presence of layers of flat BO_3 groups.

On the basis of the Sellmeier equations, the phase-matching angles for SHG can be calculated for type I and type II phase matching, respectively. The shortest wavelength for type I SHG is predicted to be 315 nm from the calculated phase-matching curves, and the phase-matching angle for type I SHG at 532 nm is 34.4°.

The effective SHG coefficient d_{eff} is given by (4).

LLSB has point-group symmetry D_3, so it has only one nonzero-independent SHG coefficient, i.e., d_{11}, assuming Kleinman symmetry relations. The magnitude of the coefficient d_{11} can be calculated on the basis of Anionic Group Theory by using (5). Given the value of the microscopic susceptibility $\beta_{111} = 0.641 \times 10^{-31}$ esu [14], the d_{11} coefficient can be calculated to be 1.3 pm/V.

Figure 11 gives the curves of SHG signal as a function of particle size from the measurements made on ground LLSB crystals, which are consistent with phase-matching behavior according to the rule proposed by Kurtz and Perry [19]. The second-harmonic signal produced by LLSB powders with a 1,064-nm fundamental

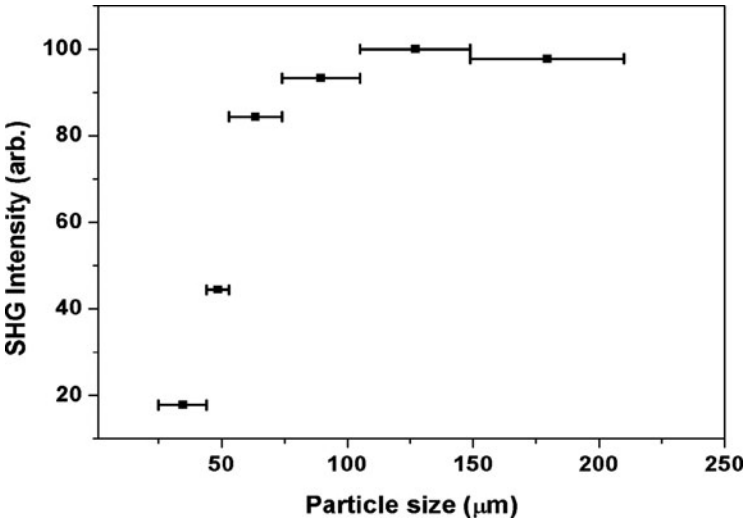

Fig. 11 Second-harmonic intensity for LLSB powders as a function of particle size

corresponds to 0.94 × YAB. These signals are proportional to the squares of the nonlinear *d* coefficients, assuming the coherent lengths for the two materials are the same. As a result, the ratio d_{obs}(LLSB)/d_{obs}(YAB) = 0.97. Since the reported *d* coefficient for YAB is 1.79 pm/V [16], the derived result for LLSB is 1.74 pm/V, a value in general agreement with the calculated value of 1.3 pm/V.

As a result, a new NLO crystal $Lu_xLa_ySc_z(BO_3)_4$ ($x + y + z = 4$) crystallized in trigonal-huntite structure has been discovered. Phase boundaries have been defined in the quasi-ternary phase diagram with the three end members $LuBO_3$, $LaBO_3$, and $ScBO_3$. Large single crystals have been grown by the high-temperature top-seeded solution method using $Li_6B_4O_9$ as the flux. Linear and nonlinear optical properties were measured, indicating a wide optical transparent region (190 nm to 5.8 μm), a moderate birefringence ($\Delta n = 0.077$) and high second-order susceptibility coefficient ($d_{11} = 1.3$ pm/V). There features coupled with higher chemical stability and mechanical durability make LLSB a promising NLO material for practical applications.

1.3 $Gd_xLa_ySc_3(BO_3)_4$, *(x + y = 1) [20]*

1.3.1 Experimental

Powder samples of $Gd_xLa_ySc_3(BO_3)_4$ (GLSB) were prepared by reacting stoichiometric ratios of oxides Gd_2O_3(4N), La_2O_3(4N), Sc_2O_3(4N), and B_2O_3(AR) with $LiBO_2$ (3.0 wt %, synthesized from Li_2CO_3(AR) and B_2O_3(AR)) added to promote the reaction. $LiBO_2$ acts as a flux in the system to decrease the temperature of

solid-state reaction. Lanthanum oxides were sintered in a muffle furnace at 1,100°C for 12 h prior to weighing in order to remove absorbed water and carbon dioxide. The initial mixture of the raw materials was ground thoroughly in an agate mortar and then heated in Pt crucibles at 800°C for 2 h and 1,100°C for 12 h. The samples were additionally ground after the heat treatment at 800°C. In order to determine the stability region in the trigonal phase, a series of polycrystalline samples were prepared with a formula $Gd_xLa_ySc_z(BO_3)_4$ ($x + y + z = 4$) through conventional solid-state reactions at a synthesis temperature of 1,100°C. Product phases were identified by X-ray powder diffraction.

GLSB crystals were grown by a high-temperature top-seeded solution method. Since $Li_6B_4O_9$ has been used as a flux for the growth of LLSB [17] and YLSB [11] and was found to be a good flux with low crystal growth temperature and low volatility, it was chosen as a flux to grow GLSB in our initial attempts. To further improve the crystal quality, LiF was introduced as an additive to the flux system in order to decrease the viscosity of the melt. Bulk crystals of GLSB were grown by using $Li_6B_4O_9$-LiF as a flux, where the composition of the mixture for crystal growth was GLSB : 2.5 $Li_6B_4O_9$: 5 LiF (mol). A seed with orientation [100] was used to determine the crystallization temperature and initiate growth. The crystal was subsequently pulled out of the melt and allowed to cool down together with the furnace to room temperature at a rate of 20°C/h. The remaining flux attached to the crystal was readily dissolved in diluted nitric acid.

1.3.2 Crystal Structure and Phase Relations

The structure of GLSB is a classical huntite type. The La atoms occupy the centers of distorted trigonal prism (p) at the threefold axis, and Sc atoms reside in the centers of distorted octahedron (o). Gd atoms replace the La atoms in the trigonal prisms. The sizes of the trigonal prisms required to form the huntite structure are achieved by maintaining the suitable Gd-atom doping level.

A series of polycrystalline samples were prepared by conventional solid-state reaction for the phase analysis, and the results reveal that the stoichiometry of the single trigonal phase followed the relationship of Sc /(Gd + La) = 3, and the composition region of this solid solution is $0.2 \leq Gd/(Gd + La) \leq 0.8$. The deviations from these values afford additional peaks of impurities in the X-ray powder diffraction patterns. Therefore, Gd occupies the La site rather than Sc site, and the general formula of the single trigonal phase for demonstrating Gd-atom substitution can be expressed as $Gd_xLa_{1-x}Sc_3(BO_3)_4$ ($0.2 \leq x \leq 0.8$). The unit-cell volume and cell parameters lessen with the increase of Gd concentration. From calculation, an approximately linear relationship between the unit-cell volume V and Gd concentration x can be established as shown in Fig. 12, which indicates that $Gd_xLa_{1-x}Sc_3(BO_3)_4$ is a real exited solid solution compound.

Bulk crystals were obtained with dimensions of near $28 \times 20 \times 10$ mm^3 (Fig. 13) using $Li_6B_4O_9$–LiF as a flux. No obvious volatilization from the melt was observed during the growth of GLSB with the $Li_6B_4O_9$–LiF flux.

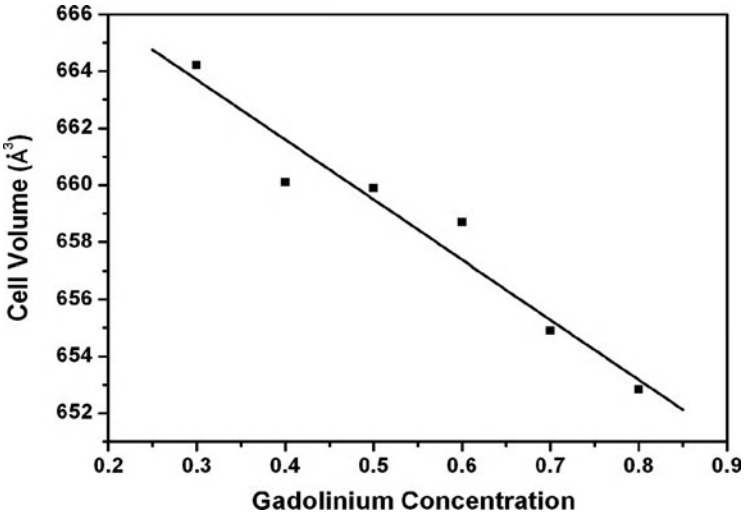

Fig. 12 Relationship between Gd concentration, x, and cell volume, V

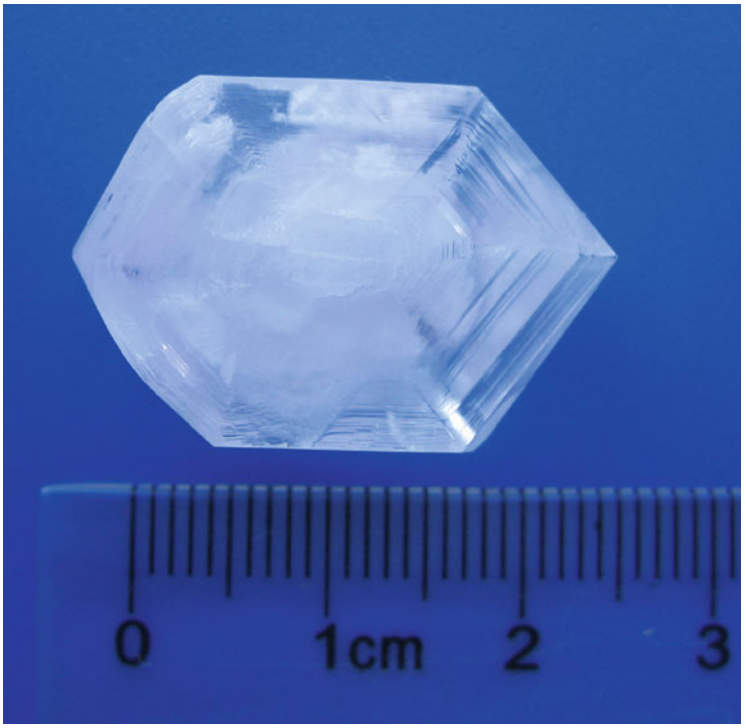

Fig. 13 As-grown GLSB crystal

These indicate that the $Li_6B_4O_9$–LiF flux is very stable and the volatility is very low. Chemically stable to both water and acids, these crystals were mechanically robust and sufficiently hard enough to be readily polished. The chemical compositions of the grown crystals were calculated by ICP elemental analysis, which is consistent with the composition of other members of the huntite family. The calculated molar ratios of Sc/(Gd + La) are all close to three, implying that Gd is indeed only distributed in the La site. The distribution coefficients for Gd were much less than one.

1.3.3 Optical Properties

Figure 14 presents the transmittance spectrum of GLSB crystal. In our measurement, the short-wavelength transmission cutoff extends to approximately 190 nm, and the IR absorption edge is at about 3.8 μm, implying that there is a wide window for nonlinear optical applications. In the ultraviolet region, seven absorption peaks exhibit at 312, 306, 274, 253, and 246 nm, respectively. These absorption peaks are presumably attributed to the electron 4f–4f transition of Gd ions [21, 22].

The optical homogeneity characterized by the root-mean-square of the gradient of refractive index was measured to be about 3×10^{-5} over a $15 \times 8 \times 1$ mm^3 polished sample. The result indicated that the optical homogeneity of the GLSB crystal was good enough for the further usage in optical device.

The refractive indices at wavelengths of 0.355, 0.473, 0.532, 0.6328, 1.064, and 1.338 μm at room temperature were measured by an auto-collimation method. The indices were fit to the Sellmeier equations:

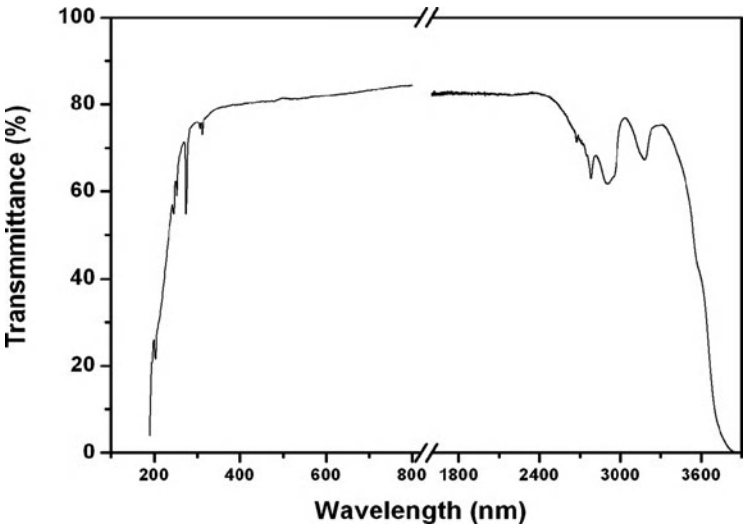

Fig. 14 Transmittance curve of the GLSB crystal

$$n_o^2 = 3.31737 + \frac{0.03209}{\lambda^2 - 0.01602} - 0.01753\lambda^2,$$
$$n_e^2 = 3.03056 + \frac{0.02604}{\lambda^2 - 0.01451} - 0.00603\lambda^2, \quad (8)$$

where n_o and n_e are the refractive indices for ordinary and extraordinary polarizations, respectively, and λ is the wavelength expressed in micrometers. GLSB is a negative uniaxial optical crystal, and the birefringence value ($\Delta n = n_o - n_e$) is 0.078 at the wavelength of 1.064 μm.

Figure 15 provides the calculated phase-matching curves for type I and type II SHG calculated on the basis of the Sellmeier equations. As revealed in the curves, the shortest wavelength for the type I SHG is predicted to be 287 nm, and the phase-matching angle for the type I SHG at 532 nm is 34.8°.

Figure 16 presents the curves of the SHG signal intensity as a function of the particle size of ground GLSB crystals. According to the rule proposed by Kurtz and Perry [19], the features of the curve agree well with the phase-matching behavior, and the GLSB crystal is determined to belong to the phase-matching class.

GLSB has point-group symmetry D_3; thus, it has only one nonzero-independent SHG coefficient, i.e., d_{11}, assuming the Kleinman symmetry relations. Since the powder SHG signal strongly depends on coherence length and the coherence lengths for crystals of huntite series are approximately equal, a YAB sample was selected as a reference to ensure the accuracy of measurement. The second-harmonic signal produced by GLSB with a 1,064-nm fundamental frequency light corresponds to 1.35 × YAB. These signals are proportional to the squares of the nonlinear coefficients d, assuming the coherence lengths for the two materials are the same. As a result, the ratio d_{obs} (GLSB)/d_{obs} (YAB) = 1.16. Since the reported d_{11} coefficient for YAB is 1.79 pm/V [16], the derived result for GLSB is 2.08 pm/V, a value about 5.3 times as large as of d_{36} (KDP) or of 2.4 times of d_{32} (LBO).

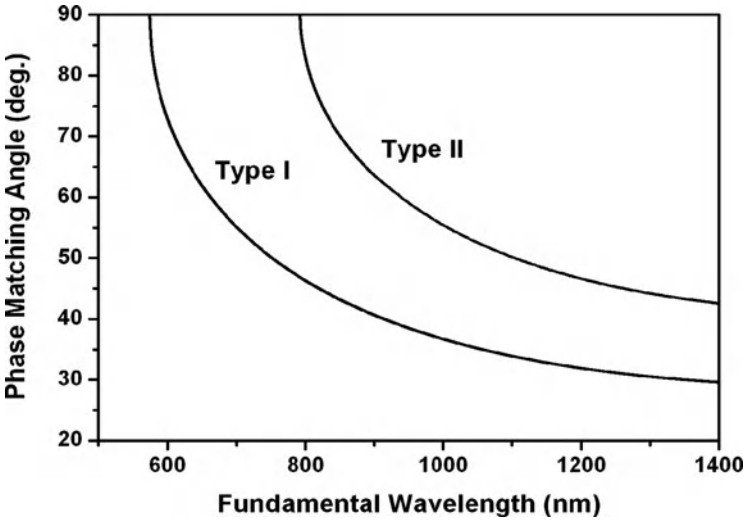

Fig. 15 Calculated phase-matching curves for second-harmonic generation

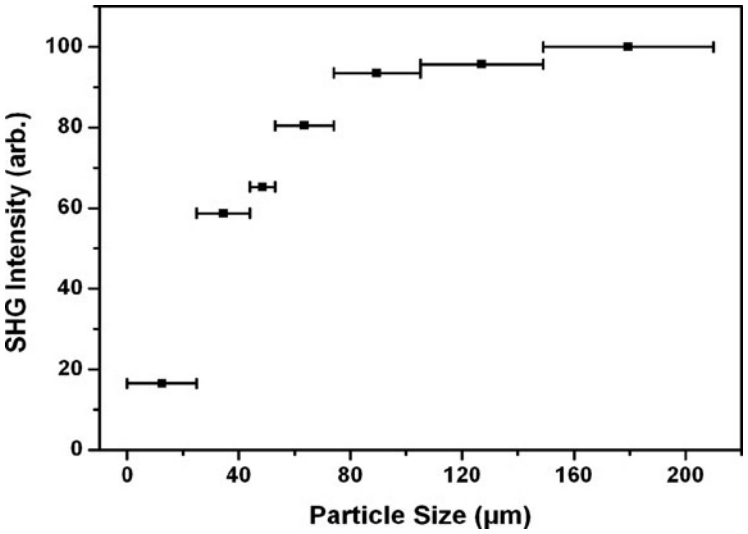

Fig. 16 SHG measurements of ground GLSB crystals

1.4 $Bi_xLa_ySc_z(BO_3)_4$ *(x + y + z = 4) [23]*

1.4.1 Experimental

Polycrystalline samples of $Bi_xLa_ySc_z(BO_3)_4$ (BLSB) were prepared by reacting stoichiometric ratios of oxides Bi_2O_3, La_2O_3, Sc_2O_3, and B_2O_3. La_2O_3 and Sc_2O_3 were sintered in a muffle furnace at 1,100°C for 12 h prior to weighing in order to remove absorbed water and carbon dioxide. The initial mixtures of the raw materials were ground thoroughly in an agate mortar and then heated at 750°C for 2 h and 950°C for 12 h. They were additionally ground after the heat treatment at 750°C.

Single crystals of BLSB were grown by a spontaneous crystallization method with Bi_2O_3–B_2O_3 as the flux. The molar ratio of the raw materials for crystal growth was $La_2O_3/Sc_2O_3/Bi_2O_3/B_2O_3$ = 1:1.5:*13*:13. The mixture was put in a platinum crucible and heated at 1,100°C for several hours, then was cooled down to 800°C at a rate of 5°C/h. The flux attached to the crystals was readily dissolved in diluted nitric acid.

1.4.2 Crystal Structure and Phase Relations

The flux method was used to grow BLSB single crystals because it melts incongruently. Since Li_2O–B_2O_3 has been reported to be a good flux system for the growth of NLSB [9], YLSB [11], and LLSB [17] crystals, $Li_6B_4O_9$ was chosen as a flux to

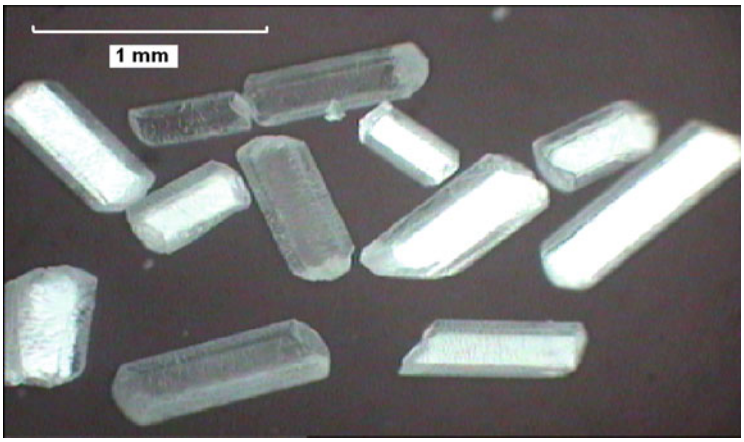

Fig. 17 As-grown $Bi_{0.27}La_{0.82}Sc_{2.91}(BO_3)_4$ crystals

grow BLSB in the initial attempts. However, only the monoclinic LSB crystals were obtained in most experiments. The use of excessive Bi_2O_3 significantly increased the yield of the trigonal BLSB. Consequently, the trigonal BLSB crystals without additive impurity phases were obtained with Bi_2O_3–B_2O_3 as the flux. Typical trigonal BLSB crystals as-grown are shown in Fig. 17. They are chemically stable with respect to water and acid.

The values of concentrations of metal elements in as-grown BLSB crystals from the ICP elemental analysis were 10.00, 20.19, and 23.35 wt% for Bi, La, and Sc, respectively. The stoichiometry was determined as $Bi_{0.27}La_{0.82}Sc_{2.91}(BO_3)_4$ on the basis of 12 O atoms and 4 B atoms in each formula unit, consistent with the composition of members of the huntite family. The distribution coefficient for Bi is very small in this system, presumably due to the difference in coordination environment between Bi^{3+} and rare earth ions.

In order to define the stability region for the trigonal phase, a series of polycrystalline samples were prepared by the conventional solid-state reaction on the basis of the formula $Bi_xLa_ySc_z(BO_3)_4$ ($x + y + z = 4$). The phase relations are displayed in a quasi-ternary phase diagram (Fig. 18) with the three end members $BiBO_3$, $LaBO_3$, and $ScBO_3$. The single trigonal phase covers the composition range of $0.27 < x < 0.52$, $0.67 < y < 0.82$, and $2.74 < z < 2.95$.

The structure of BLSB belongs to a classical huntite type with nearly planar layers of BO_3 groups extending in the *a*–*b* plane. Bi atoms replace not only the La atoms in the trigonal prisms but also the Sc atoms in the octahedra. The formula for demonstrating Bi-atom substitution in BLSB can be written as $(Bi_{x'}La_{1-x'})_{tri}(Bi_{y'}Sc_{3-y'})_{octa}(BO_3)_4$. The sizes of the trigonal prisms and the octahedra required to form the huntite structure are achieved by maintaining the suitable Bi-atom doping level in each site. We can also adopt (1) and (2) to interpret the relations between the composition and the cell volume. From the calculation, an approximately linear relationship between C_{eff} and V was established as shown in Fig. 19, which indicates that Bi atoms do indeed appear to be distributed across both sites.

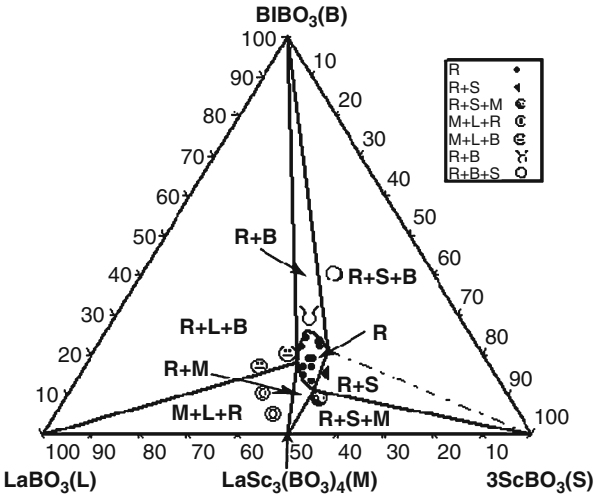

Fig. 18 Quasi-ternary phase diagram of $LaBO_3$–$BiBO_3$–$ScBO_3$ system; *R*, trigonal phase; *S*, $ScBO_3$; *L*, $LaBO_3$; *B*, $BiBO_3$; *M*, monoclinic phase of $LaSc_3(BO_3)_4$

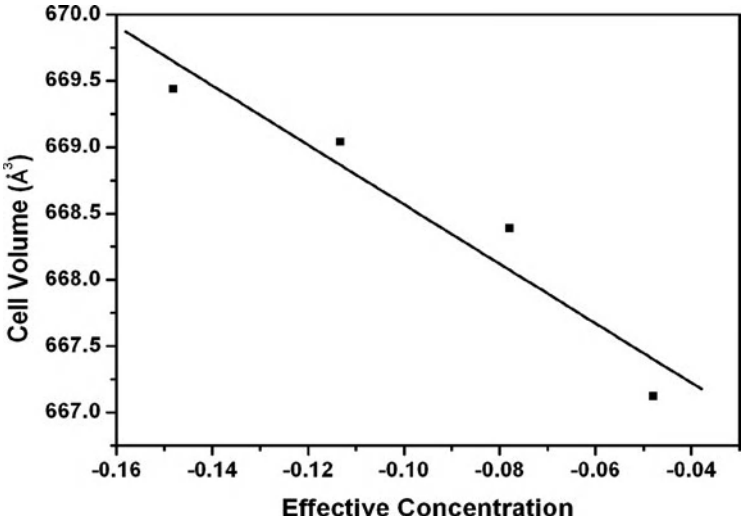

Fig. 19 Relationship between effective concentration, C_{eff}, and cell volume, *V*

1.4.3 Optical Properties

Figure 20 shows the diffuse reflection absorption spectrum of BLSB powder in the range of 200–800 nm. In our measurement, the short-wavelength absorption edge of BLSB extends to approximately 289 nm.

Figure 21 shows the curves of the SHG signal intensity as a function of particle size of ground BLSB crystals. The features of the curve are consistent well with

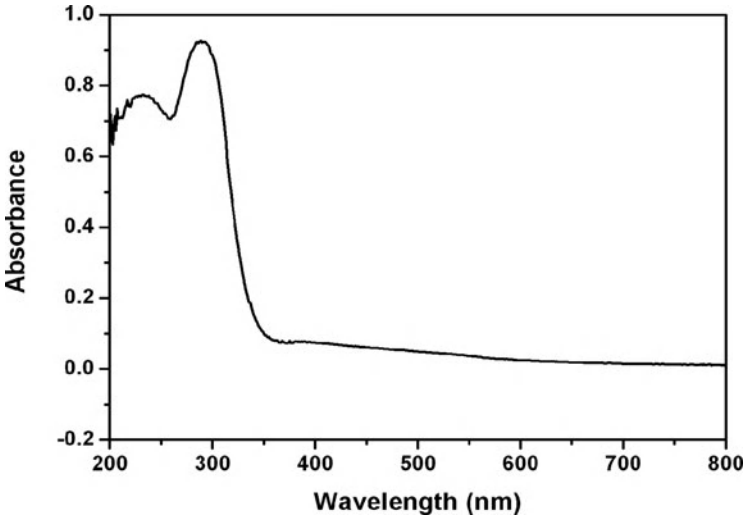

Fig. 20 Diffuse reflectance absorption curve of BLSB powder sample

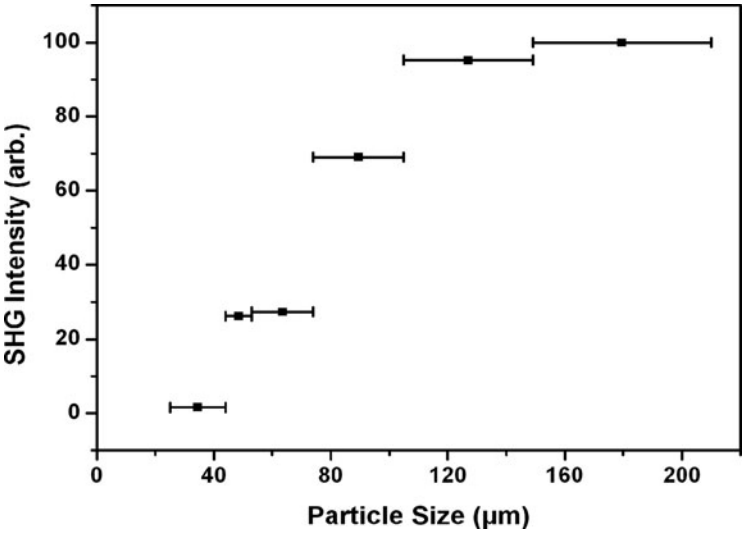

Fig. 21 SHG measurements of ground BLSB crystals

phase-matching behavior according to the rule proposed by Kurtz and Perry [19], and BLSB crystal is estimated to belong to the phase-matching class.

BLSB has point-group symmetry D_3, so it has only one nonzero-independent SHG coefficient, i.e., d_{11}, assuming Kleinman symmetry relations. The second-harmonic signal produced by BLSB with a 1,064-nm fundamental frequency light corresponds to 1.42 × YAB. These signals are proportional to the squares of the

nonlinear coefficients d, assuming the coherent lengths for the two materials are equal. As a result, the ratio d_{obs} (BLSB)/d_{obs} (YAB) = 1.19. Since the reported d_{11} coefficient for YAB is 1.79 pm/V [16], the derived result for BLSB is 2.13 pm/V, equal to about four times as large as d_{36} of KDP. The observed second-harmonic signal produced by BLSB is larger than that of YLSB in our measurements, indicating an additional contribution from the Bi–O groups to the nonlinear coefficients.

1.5 $BiAlGa_2(BO_3)_4$ *[24]*

1.5.1 Experimental

Powder samples of $BiAlGa_2(BO_3)_4$ (BAGB) were prepared by reacting stoichiometric ratios of Bi_2O_3, $Al(OH)_3$, Ga_2O_3, and B_2O_3. The mixture of the raw materials was ground and heated in an Al_2O_3 crucible at 600°C for 2 h and 750°C for 12 h; the samples were additionally ground after the heat treatment at 600°C.

Single crystals of BAGB, which melts incongruently, were grown by using Bi_2O_3–$4B_2O_3$ as a flux in a platinum crucible with Al_2O_3 lid from reagent-grade mixtures of Bi_2O_3, Al_2O_3, Ga_2O_3, and B_2O_3 at molar ratios Bi/Al/Ga/B = 4.5:1:2:18. These mixtures were heated in an electric furnace to 1,000°C, held for 1 day, and then cooled rapidly to the initial temperature of crystallization 750°C. The melt was then cooled to final crystallization temperature 650°C at the rate of 3°C/h and to room temperature by turning the power off. The flux attached to the crystal was readily dissolved in nitric acid and hot water.

1.5.2 Crystal Structure and Phase Relations

BAGB adopts the classical trigonal-huntite structure type with Bi-centered distorted trigonal prisms and Al- and Ga-centered distorted octahedra dispersed between planes consisting of BO_3 triangles.

The existence of the trigonal phase $BiFe_{1.35}Al_{1.65}(BO_3)_4$ [25] indicates that the optimal effective radii for a candidate ion in O site is between those of Al^{3+} and Fe^{3+}, e.g., from 0.535 to 0.645 Å [13]. Therefore, Ga^{3+} (ion radii 0.62 [13]) is the best closed shell ion to replace Fe^{3+} for the size tuning and to maintain the UV transparency. To better define the stability region for the trigonal phase, series samples were prepared on the basis of the formula $BiAl_xGa_{3-x}(BO_3)_4$; product phases were identified by using X-ray powder diffraction. The composition range of the above solid solution is very narrow centered at $x = 1$, indicating a common formula for BAGB, i.e., $BiAlGa_2(BO_3)_4$.

The results of ICP elemental analysis of a BAGB crystals, assuming stoichiometric amounts of B, were consistent with the composition of members of the

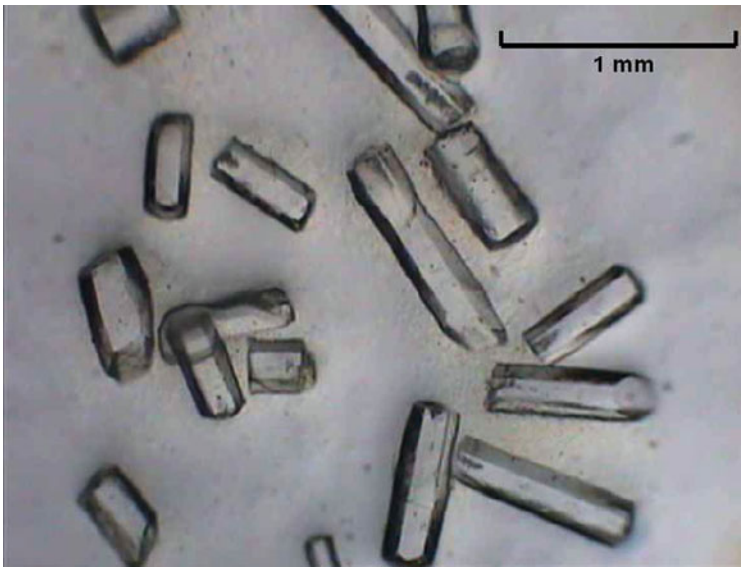

Fig. 22 As-grown BAGB crystals

huntite family. The mole ratio of (Al and Ga)/Bi is 3, indicating Al and Ga atoms occupy the same site. The compound adopts the classical trigonal-huntite structure type with Bi-centered distorted trigonal prisms and Al- and Ga-centered distorted octahedra.

A differential thermal analysis trace for the composition $BiAlGa_2(BO_3)_4$ exhibits a broad melting event beginning at 848°C and ending near 938°C which indicated that BAGB was an incongruently melting compound and a flux must be used to grow crystals. Hence, transparent and colorless BAGB crystals have been grown by spontaneous crystallization in a molten flux based on the self-fluxed system Bi_2O_3–$4B_2O_3$, which has low melting temperature and good solubility for the huntite borates [4]. The crystals have the typical morphology of the huntite series showing forms of hexagonal prisms elongated along the *c*-axis and combined with basal pinacoids (Fig. 22). They are chemically stable with respect to water and strong acid.

1.5.3 Optical Properties

Figure 23 shows the diffuse reluctant absorption curve of BAGB powder in the UV portion of the spectrum. In our measurement, the short-wavelength absorption edge of BABO extends to approximately 271 nm, opening a UV-Vis window for NLO applications.

Figure 24 gives the curves of SHG signal as a function of particle size from the measurements made on ground crystals for BAGB, which are consistent with

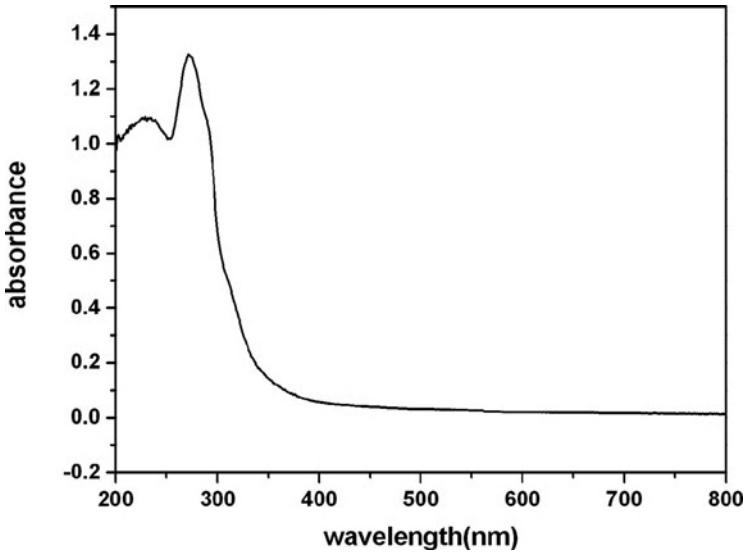

Fig. 23 Diffuse reflectance absorption curve of BAGB powder sample

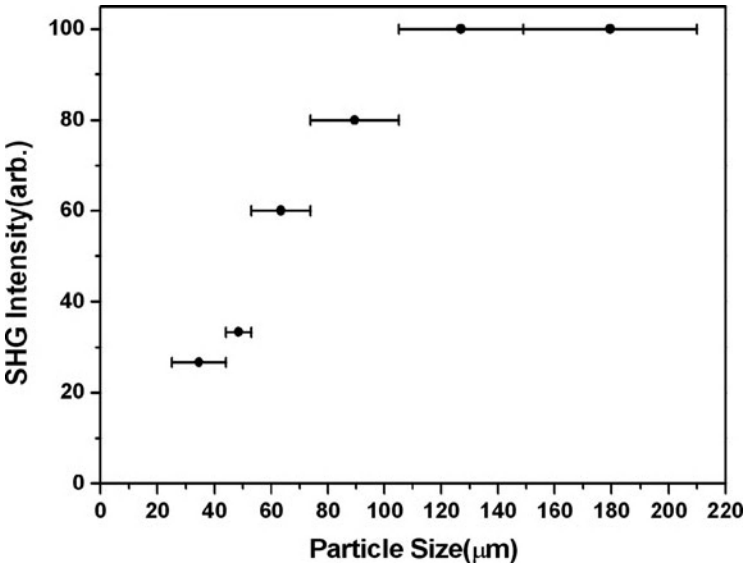

Fig. 24 SHG measurements of ground BAGB crystals

phase-matching behavior according to the rule proposed by Kurtz and Perry [19]. The second-harmonic signal produced by BAGB powders with a 1,064-nm fundamental corresponds to 1.25 × YAB. These signals are proportional to the squares of the nonlinear d_{11} coefficients, assuming the coherent lengths for the two

Table 1 Borates belongs to trigonal-huntite structure

Compounds	NLO coefficient (pm/V)	Birefringence	UV cutoff (nm)
$YAl_3(BO_3)_4$ [26, 27]	1.79	0.076	173
$Y_{0.57}La_{0.72}Sc_{2.71}(BO_3)_4$	1.43	0.085	190
$Lu_{0.66}La_{0.95}Sc_{2.39}(BO_3)_4$	1.3	0.077	190
$Gd_{0.22}La_{0.78}Sc_3(BO_3)_4$	2.08	0.078	190
$Bi_{0.27}La_{0.82}Sc_{2.91}(BO_3)_4$	2.13	–	289
$BiAlGa_2(BO_3)_4$	2.00	–	271

materials are the same. As a result, the ratio d_{obs} (BAGB)/d_{obs}(YAB) = 1.12. Since the reported d_{11} coefficient for YAB is 1.79 pm/V [16], the derived result for BAGB is 2.00 pm/V, equal to about four times as large as that of d_{36} (KDP). Since we observe larger second-harmonic signals for BAGB than that of YAB, there should be an additional electronic contribution from the Bi–O groups to the NLO coefficients, as observed in the case of BLSB.

1.6 Summary

A series borates crystallizing in the trigonal-huntite structure has been discovered through structural design with respect to the size tuning on trigonal prism or/and octahedral site in the structure. The structural, optical, and chemical-physical properties are summarized in Table 1. They all have large NLO coefficients, moderate birefringence for UV phase matching, and robust chemical and physical properties. The NLO coefficients of those containing Bi are larger due to the contribution from the lone-pair electron of Bi, while the UV cutoff of these crystals is redshift for about 100 nm.

2 Alkaline Beryllium Borates for Deep-UV Applications [28, 29]

Deep-ultraviolet (deep-UV) coherent light wavelengths below 200 nm have become increasingly important and are attracting more attention because of their promising applications, such as in semiconductor photolithography, laser micromachining, photochemical synthesis, material processing, as well as super-high-resolution and angle-resolved photoemission spectroscopy. The best way to produce deep-UV coherent light with solid-state lasers is through frequency conversion using deep-UV NLO crystals. However, it is a particularly difficult challenge to have suitable materials that possess high NLO coefficients and wide UV transparency.

Over the past three decades, many efforts have been made to understand the relationship between the composition, structure, and NLO properties of crystals. According to the Anionic Group Theory proposed by Chen [30–32], the overall

nonlinearity of crystal is the geometrical accumulation of the microscopic second-order susceptibility of the NLO-active anionic structural units. Favorable structural units in inorganic compounds with large nonlinear susceptibilities are, e.g., planar $[BO_3]^{3-}$ with π-conjugated system [33–35], polar ionic groups including asymmetric metal-oxide polyhedron, and coordination units with lone-pair cation [36–40]. Besides the microscopic nonlinear susceptibilities of the NLO-active structural units, the orientation of these structural units and their number density influence the bulk NLO properties as well. The ongoing intensive studies on borate anionic groups have resulted in the discovery of many new UV transparent NLO borates that include β-BaB_2O_4 (BBO) [41] with the anionic groups $[B_3O_6]^{3-}$, LiB_3O_5 (LBO) [42], CsB_3O_5 (CBO) [43], and $CsLiB_6O_{10}$ (CLBO) [44, 45] with $[B_3O_7]^{5-}$.

Borate frameworks and building blocks are usually constructed using planar $[BO_3]$ triangles and tetrahedral $[BO_4]$ polyhedra. The substitution of $[BeO_4]$ tetrahedron, a deep-UV transparent structural unit, for $[BO_4]$ may potentially lead to new NLO-active beryllium borate anionic groups and various types of framework connections, which may promote further development of novel UV NLO materials. Based on a theoretical study, Li has proposed that beryllium borates possess the largest energy gap among all alkaline and alkaline earth borates [46], hence the shortest transmission cutoff wavelength in the UV region. Due in part to the high toxicity of the beryllium oxide powders when inhaled during preparation, relatively few synthetic beryllium borate compounds are known, which include $MBe_2B_2O_6$ (M = Sr and Ba) [47, 48], $CaBeB_2O_5$ [49], $Li_{14}Be_5B(BO_3)_9$ [50], and $RbBe_4B_3O_9$ [51]. All of which have been found to crystallize in centrosymmetric space groups.

Typical examples of beryllium borate frameworks are the 2D $[Be_2BO_3O_2]_\infty$ or $[Be_2BO_3F_2]_\infty$ layers that can be found in hydrated beryllium borate $Be_2BO_3OH{\cdot}H_2O$ [52, 53], fluoroberyllium borate Be_2BO_3F, and $ABe_2BO_3F_2$ (A = Na, K, Rb, Cs and Tl) [54–57], among which KBBF ($KBe_2BO_3F_2$) has been shown to be the best material for deep-UV applications and is the only material that can generate coherent light at 170 nm by direct SHG [58]. The NLO properties, birefringence, and band gap in KBBF crystals are mainly determined by the identical direction of $[BO_3]^{3-}$ groups in the $[Be_2BO_3F_2]_\infty$ layers extending infinitely in the *a*–*b* plane. However, this crystal has very strong layer habit with respect to crystal growth due to the relatively weak F^-–K^+ ionic interactions between the adjacent $[Be_2BO_3F_2]_\infty$ layers along the *c*-axis. As a result, it may be feasible to grow deep-UV NLO crystals through covalent bonding of the adjacent $[Be_2BO_3O_2]_\infty$ or $[Be_2BO_3F_2]_\infty$ layers. Although alkaline earth beryllium borates $M_2Be_2B_2O_7$ (M = Sr and Ba) [30, 59, 60] consist of $[Be_3B_3O_6]_\infty$ 2D layers bridged by oxygen atoms bound to Be atoms, their structures were not fully determined; moreover, the optical uniformities of their crystals were found to be very poor [61].

Although many new beryllium borate frameworks were obtained using the methods described above, examples of beryllium borate anionic group derived from borate anionic groups through $[BeO_4]$ substitution are scant. In our previous study, we reported the synthesis of the first alkaline beryllium borate $Na_2BeB_2O_5$ that contains $[BeB_2O_7]^{6-}$ groups derived from $[B_3O_7]^{5-}$ by $[BeO_4]$ substitution [62]. While it crystallized in a centrosymmetric structure, this approach to beryllium

borate anionic group construction was successful and will allow further advances in NLO materials development.

In this section, we detail the systematical synthesis based on the A_2O–BeO–B_2O_3 (A = Na, K, Rb) systems in order to obtain deep-UV NLO crystals containing new beryllium borate anionic groups or framework. This has resulted in a series of new alkaline beryllium borates with the stoichiometry $NaBeB_3O_6$, $ABe_2B_3O_7$ (A = K, Rb), and $Na_2CsBe_6B_5O_{15}$. For the first time, a new beryllium borate anionic group $[Be_2B_3O_{11}]^{9-}$ was found in the structure of $NaBeB_3O_6$ and α-$KBe_2B_3O_7$. β-$KBe_2B_3O_7$, γ-$KBe_2B_3O_7$, $RbBe_2B_3O_7$, and $Na_2CsBe_6B_5O_{15}$ consist of 2D alveolate beryllium borate network $[Be_2BO_5]_\infty$ which were found in anhydrous beryllium borate compound for the first time. Furthermore, the adjacent $[Be_2BO_5]_\infty$ layers in these compounds were connected by covalent bonds. The synthesis, structures, thermal behaviors, spectra, and NLO properties of these borates were described as well.

2.1 Synthesis

Due to the toxicity of BeO, all of the experiments were performed in a ventilated system. Single crystals of $NaBeB_3O_6$ were grown from a high temperature solution by using Na_2O–$3B_2O_3$ as a flux. This solution was prepared in a platinum crucible by melting a mixture of Na_2CO_3, BeO, and B_2O_3 at molar ratio of Na_2O/BeO/B_2O_3 = 1:0.5:3. The mixture (10 g) was heated in a programmable temperature electric furnace at 1,050°C until the melt became transparent and clear. The homogenized melt solution was then cooled rapidly (50°C/h) to the initial crystallization temperature (800°C). It was further cooled slowly (3°C/h) to the final crystallization temperature (650°C), then allowed to cool to room temperature by powering off the furnace. The flux attached to the crystal was readily dissolved in water.

Similarly, single crystals of $ABe_2B_3O_7$ (A = K, Rb) were grown by spontaneous crystallization with alkaline borates as the flux. Moreover, by varying the crystallization temperature, three phases of polymorphous $KBe_2B_3O_7$ crystals were obtained. The three phases of polymorphous $KBe_2B_3O_7$ crystals were referred to as α-, β-, and γ-$KBe_2B_3O_7$. The molar ratios of the melt mixtures for growing α-, β-, and γ-$KBe_2B_3O_7$ were K_2O/BeO/B_2O_3 = 1:0.8:3, 1:0.7:3, and 1:0.6:3, respectively. The three phases were obtained by crystallizing the melts at 770°C, 750°C, and 730°C, for α-, β-, and γ-$KBe_2B_3O_7$, respectively, for 24 h and then quenched in the air by taking the crucibles out of the furnace.

Single crystals of $Na_2CsBe_6B_5O_{15}$ were grown from a high-temperature solution using Na_2O–Cs_2O–B_2O_3 as a flux. This solution was prepared in a platinum crucible after melting a mixture of Na_2CO_3, Cs_2CO_3, BeO, and B_2O_3 at a molar ratio of Na_2O/Cs_2O/BeO/B_2O_3 = 2:3:4:9. The growth procedure was similar to those described above. Transparent and colorless $Na_2CsBe_6B_5O_{15}$ crystals are found to be moisture stable.

Table 2 Borates belongs to trigonal-huntite structure

Compounds	Space group	Cell parameters a, b, c (Å); β (°)
$NaBeB_3O_6$	$Pna2_1$	9.153(6), 11.934(8), 4.372(3)
α-$KBe_2B_3O_7$	$C2/c$	10.405(10), 9.001(7), 6.559(14); 114.543(11)
β-$KBe_2B_3O_7$	$Pmn2_1$	7.639(6), 17.464(13), 4.376(3)
γ-$KBe_2B_3O_7$	$P2_1$	7.4766(13), 13.2701(18), 9.3263(17); 111.272(10)
$RbBe_2B_3O_7$	$Pmn2_1$	7.687(4), 17.724(9), 4.393(2)
$Na_2CsBe_6B_5O_{15}$	$C2$	13.885(4), 4.4332(9), 10.874(2); 103.141(12)

Relevant crystallographic data and details of the experimental conditions for $NaBeB_3O_6$, α-$KBe_2B_3O_7$, β-$KBe_2B_3O_7$, γ-$KBe_2B_3O_7$, $RbBe_2B_3O_7$, and $Na_2CsBe_6B_5O_{15}$ are summarized in Table 2.

2.2 *Borates Containing* $[Be_2B_3O_{11}]^{9-}$ *Group*

$NaBeB_3O_6$ crystallizes in orthorhombic crystal system with an acentric space group of $Pna2_1$. The structure is illustrated along the *c*-axis in Fig. 23. The B atoms are coordinated to three O atoms to form planar $[BO_3]$ triangles with B–O bond lengths ranging from 1.319(3) to 1.399(3) Å and O–B–O bond angles ranging from 110.9 (2)° to 126.6(2)°. The Be atoms are bound to four O atoms to form distorted $[BeO_4]$ tetrahedra with Be–O bond lengths ranging from 1.597(4) to 1.669(3) Å and O–Be–O bond angles from 108.39(18)° to 113.1(2)°. All O atoms are twofold coordinated except O_3, which is threefold coordinated. In the $NaBeB_3O_6$ structure, three $[BO_3]$ triangles and two $[BeO_4]$ tetrahedra share their vertexes to form a nearly coplanar double six-membered-ring $[Be_2B_3O_{11}]^{9-}$, which is similar to a naphthalene molecule and not observed before from other borate compounds (Fig. 25). The adjacent $[Be_2B_3O_{11}]^{9-}$ building blocks are connected vertically by sharing their $[BeO_4]$ tetrahedra to form endless cruciate chains along the *c*-axis. The adjacent cruciate chains are connected to each other by sharing the O6 atoms from $[BO_3]$ triangles to build tunnels along the *c*-axis, resulting in the final 3D open framework. Na^+ cations are located in the tunnels and a 5 + 1 coordination environment with one considerably longer Na–O bond of 2.980(3) Å. Being an NLO-active anionic group, the double six-membered-ring $[Be_2B_3O_{11}]^{9-}$ possesses larger π-conjugated electron system than that of $[B_3O_7]^{5-}$ in LBO; consequently, it may have larger microscopy second-order susceptibility. Furthermore, the vertical alignment of $[Be_2B_3O_{11}]^{9-}$ groups to the *a*–*c* plane in the unit cell tends to have larger anisotropic linear polarization, i.e., larger birefringence. Therefore, $NaBeB_3O_6$ is a promising deep-UV NLO crystal.

α-$KBe_2B_3O_7$ crystallizes in monoclinic crystal system with a centrosymmetric space group of C2/c. The structure is illustrated along the *c*-axis in Fig. 26. In the structure, B atoms are coordinated to three O atoms to form planar $[BO_3]$ triangles with B–O bond lengths ranging from 1.331(2) to 1.410(2) Å and O–B–O bond

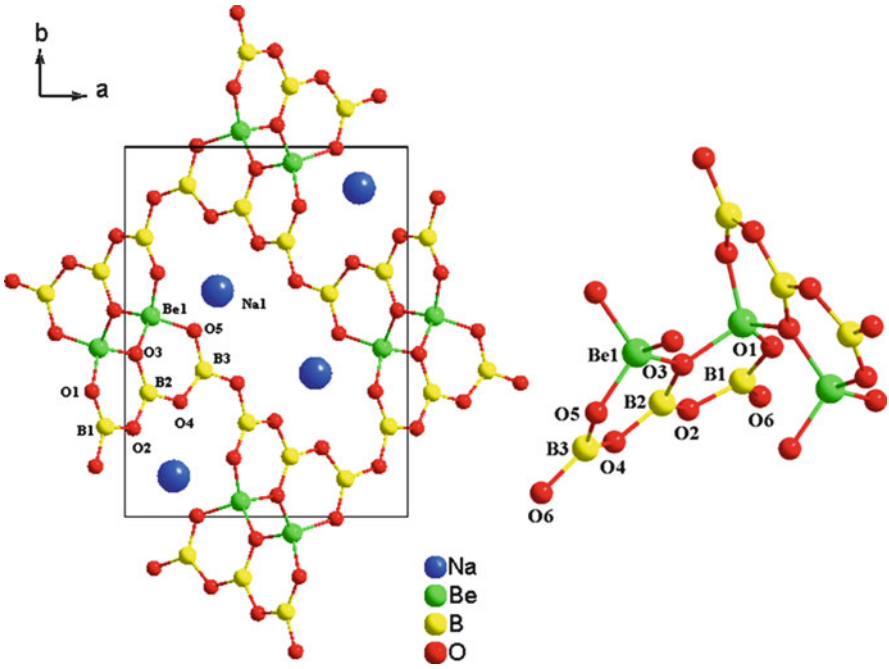

Fig. 25 Crystal structure of $NaBeB_3O_6$ and the anionic groups $[Be_2B_3O_{11}]^{9-}$ in the structure

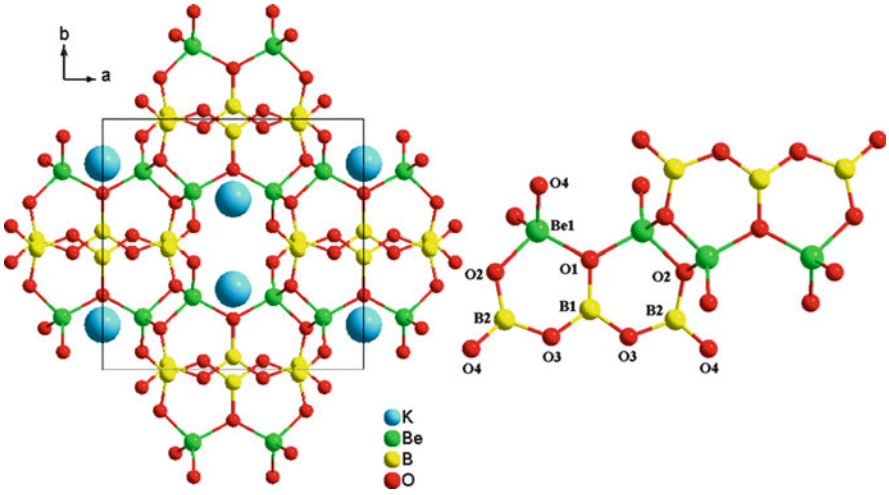

Fig. 26 Crystal structure of α-$KBe_2B_3O_7$ and the anionic groups $[Be_2B_3O_{11}]^{9-}$ in the structure

angles ranging from 113.28(19)° to 123.36(10)°. The Be atoms are bound to four O atoms to form distorted $[BeO_4]$ tetrahedra with Be–O bond lengths ranging from 1.564(2) to 1.684(4) Å and O–Be–O angles from 92.45(10)° to 117.65(14)°. O_1 and

O_2 atoms are threefold coordinated, while O_3 and O_4 are twofold coordinated. The basic building block of α-$KBe_2B_3O_7$ is $[Be_2B_3O_{11}]^{9-}$, which was found in the structure of $NaBeB_3O_6$ as described above. The adjacent $[Be_2B_3O_{11}]^{9-}$ anionic groups are connected parallely from opposite direction by sharing the edges of one of each $[BeO_4]$ tetrahedra to form a 3D open framework. K^+ cations reside in the cages of the framework and are located in a octa coordination environment with K–O bond lengths ranging from 2.781(3) to 2.858(5) Å. Although α-$KBe_2B_3O_7$ contains NLO-active $[Be_2B_3O_{11}]^{9-}$ groups, their centrosymmetric alignment results in the cancellation of NLO susceptibilities.

It is interesting that $NaBeB_3O_6$ adopts an acentric structure while α-$KBe_2B_3O_7$ adopts a centric structure, although they all have the common $[Be_2B_3O_{11}]^{9-}$ anionic group. The different connection modes of building blocks should originate from the difference in size of countering cations. Compared with larger K^+, Na^+ takes lower coordination number. The requirement of Na^+ for sixfold coordination environment leads to the relatively compact connection of $[Be_2B_3O_{11}]^{9-}$ groups in $NaBeB_3O_6$ by sharing their $[BeO_4]$ tetrahedra. Owing to this acentric connection between $[Be_2B_3O_{11}]^{9-}$ groups (right part of Fig. 25), the local acentric feature is constructively added to create overall acentric extended structure. In contrast, the eightfold coordination environment of K^+ results in the loose connection of $[Be_2B_3O_{11}]^{9-}$ groups in α-$KBe_2B_3O_7$ by sharing the edges of their $[BeO_4]$ tetrahedra. In α-$KBe_2B_3O_7$, such a connection (right part of Fig. 26) leads to a centric relation between adjacent $[Be_2B_3O_{11}]^{9-}$ groups, resulting in the cancellation of local NLO susceptibilities. Thus, it is interactions between the alkali metal and anionic group associated with the cation size that determines the macroscopic nonlinearity of materials.

2.3 *Borates Containing Alveolate* $[Be_2BO_3]_\infty$ *Layers*

β-$KBe_2B_3O_7$ and **$RbBe_2B_3O_7$** are isostructural and crystallize in orthorhombic crystal system with an acentric space group of $Pmn2_1$. The structure is illustrated along the *c*-axis in Fig. 27. In the structure, both B atoms are coordinated to three O atoms to form planar $[BO_3]$ triangles with B–O bond lengths ranging from 1.307(3) to 1.394(3) Å and O–B–O bond angles ranging from 119.21(13)° to 121.4(3)°. The Be atoms are bound to four O atoms to form distorted $[BeO_4]$ tetrahedra with Be–O bond lengths ranging from 1.572(3) to 1.672(3) Å and O–Be–O angles from 106.11(15)° to 115.48(16)°. An extended 2D alveolate beryllium borate network $[Be_2BO_5]_\infty$ lying in *a*–*c* plane was found in this structure, which was only found in a hydrated beryllium borate $Be_2BO_3OH{\cdot}H_2O$ previously [52, 53]. The adjacent $[Be_2BO_5]_\infty$ layers glide toward opposite direction along the *c*-axis. The layers are bridged by a parallely aligned one-dimensional (1D) metaborate chain $[BO_2]_\infty$ running along the *a*-axis that exists in lithium metaborate ($LiBO_2$), by sharing O atoms (twofold coordinated) to form a framework with two types of tunnels running through the *c*-axis. The K^+ cations reside in these tunnels, where $K1^+$ cations are

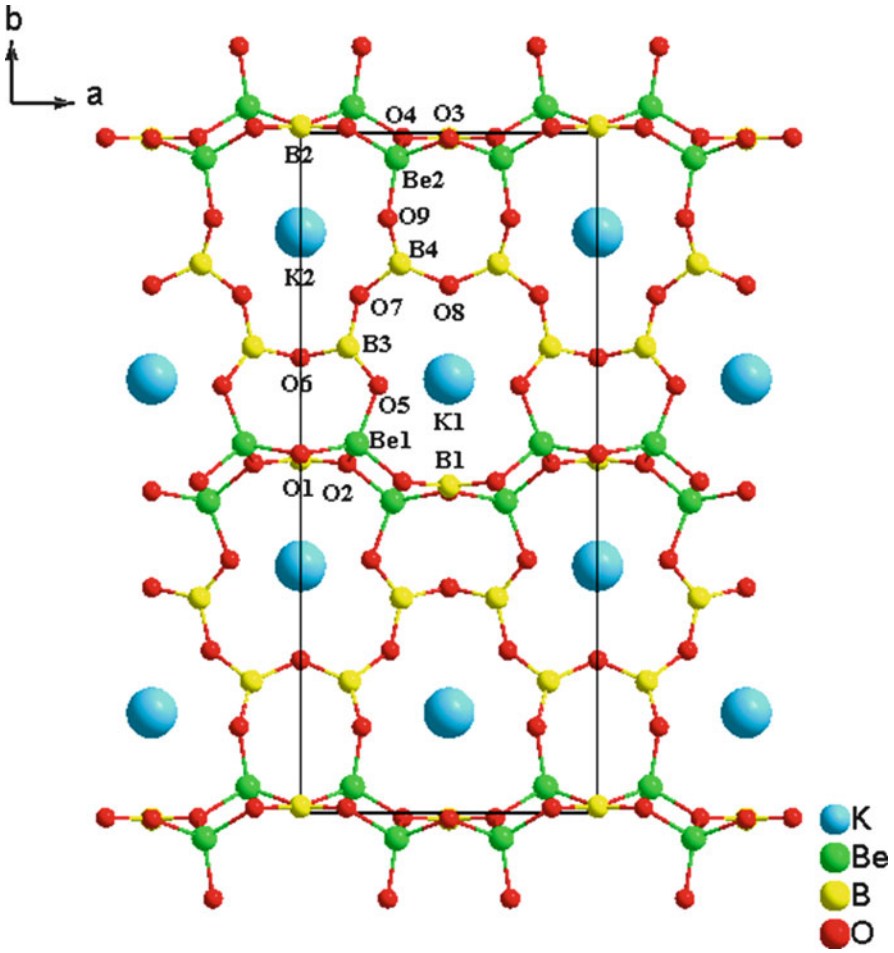

Fig. 27 Crystal structure of β-$KBe_2B_3O_7$

located in a nine-coordination environment with K–O bond lengths ranging from 2.746(2) to 3.325(3) Å and $K2^+$ cations are located in a 7 + 1 coordination environment with one considerably longer K–O bond of 3.363(3) Å.

γ-$KBe_2B_3O_7$ crystallizes in monoclinic crystal system with a chiral space group of $P2_1$. The structure along the *a*-axis is shown in Fig. 28. In the structure, B atoms are coordinated to three O atoms to form planar [BO_3] triangles with B–O bond lengths ranging from 1.293(4) to 1.421(6) Å and O–B–O bond angles ranging from 115.4(4)° to 123.7(4)°. The Be atoms are bound to four O atoms to form distorted [BeO_4] tetrahedra with Be–O bond lengths ranging from 1.593(4) to 1.665(6) Å and O–Be–O angles from 104.4(3)° to 115.7(4)°. A similar 2D layer $[Be_2BO_5]_\infty$ to that of β-$KBe_2B_3O_7$ was found in γ-$KBe_2B_3O_7$, except the connection between the adjacent $[Be_2BO_5]_\infty$ layers are different. The adjacent layers lying in *a*–*b* plane are

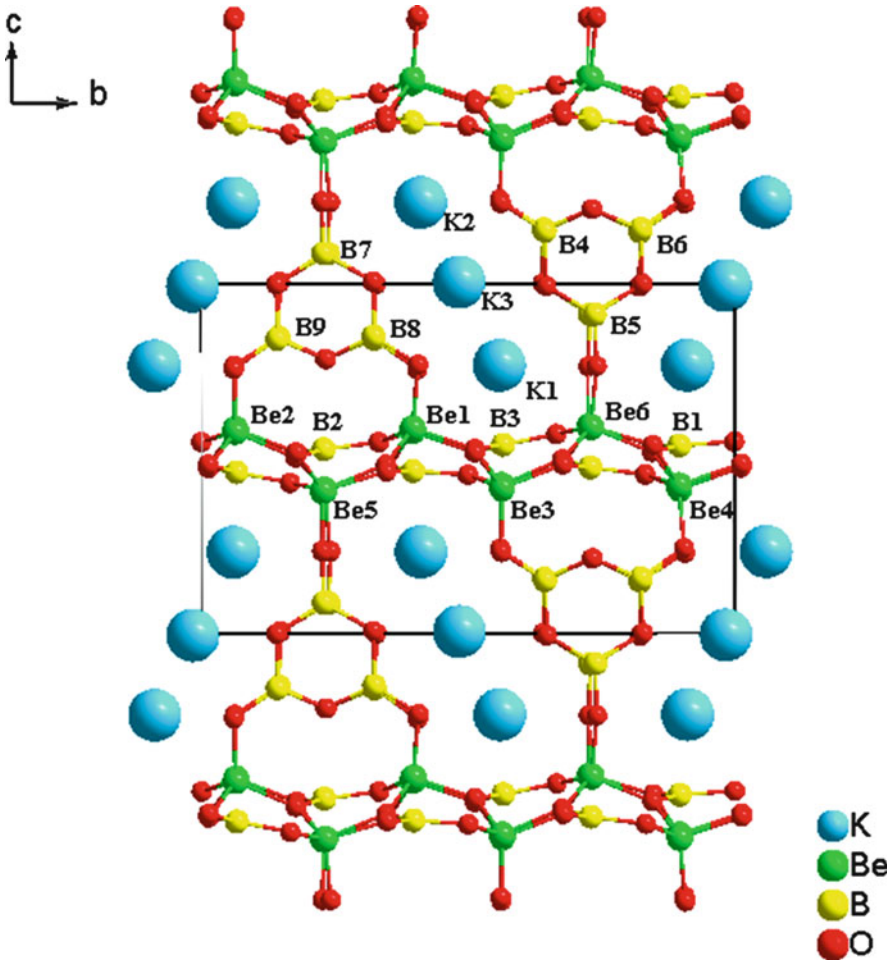

Fig. 28 Crystal structure of γ-$KBe_2B_3O_7$

bridged through $[B_3O_6]$ planar groups, which lay in the *b*–*c* plane and point to the opposite direction from each other, by sharing O atoms (twofold coordinated) to build a framework with three types of tunnels running through the *a*-axis. K^+ cations are found to reside in these tunnels, where $K1^+$ cations are located in a nine-coordination environment with K–O bond lengths ranging from 2.816(4) to 3.155(3) Å, $K2^+$ cations are located in a 9 + 1 coordination environment with one considerably longer K–O bond of 3.282(3) Å, and $K3^+$ cations are located in a 7 + 1 coordinated environment with one considerably longer K–O bond of 3.120(4) Å.

$Na_2CsBe_6B_5O_{15}$ crystallizes in monoclinic crystal system with a chiral space group of *C*2. The structure is illustrated along the *b*-axis in Fig. 29, where both B atoms are coordinated to three O atoms to form planar $[BO_3]$ triangles with B–O

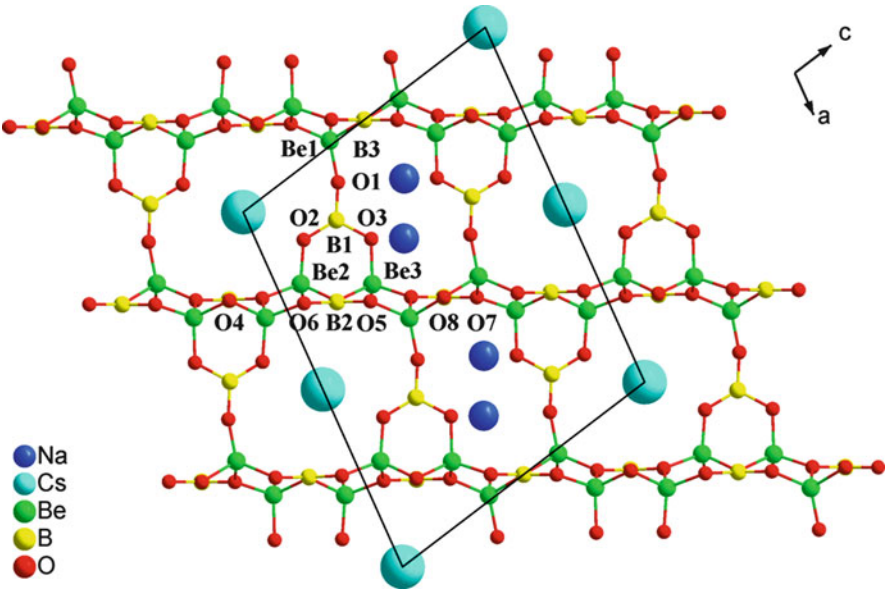

Fig. 29 Crystal structure of $Na_2CsBe_6B_5O_{15}$

bond lengths ranging from 1.339(10) to 1.419(3) Å and O–B–O bond angles from 115.6(2)° to 123.6(2)°. Each Be atom is bound to four O atoms to form distorted [BeO_4] tetrahedra with Be–O bond lengths between 1.519(4) and 1.682(6) Å and O–Be–O angles between 103.3(3)° and 122.5(3)°. Similar 2D alveolate beryllium borate layers $[Be_2BO_5]_\infty$ to those of β-$KBe_2B_3O_7$, $RbBe_2B_3O_7$, and γ-$KBe_2B_3O_7$ are found in this structure, except that the connections between the adjacent $[Be_2BO_5]_\infty$ layers are bridged via [BO_3] planar groups, which lay in the *a*–*c* plane and point to opposite directions from each other. Two types of tunnels exist in the 3D framework running along the *b*-axis. The Na^+ and Cs^+ cations reside, respectively, in these smaller and larger tunnels, where Na^+ cations are located in a seven-coordination environment with Na–O bond lengths ranging from 2.373(2) to 2.693(2) Å and Cs^+ cations are located in an eight-coordination environment with Cs–O bond lengths ranging from 3.230(6) to 3.453(2) Å.

2.4 Assembly of the Beryllium Borate Units

The effect of cation size on the overall structure has also been observed in $KBe_2B_3O_7$ and $RbBe_2B_3O_7$. The former has two structural isomer, i.e., β- and γ-phases, while, for the latter, only a single phase exists, which is isostructural to β-$KBe_2B_3O_7$. As mentioned above, in β-$KBe_2B_3O_7$ and $RbBe_2B_3O_7$, the $[Be_2BO_5]_\infty$ layers are bridged by flexible metaborate chains $[BO_2]_\infty$. Although the

coordination sphere surrounding Rb^+ is different in size from that of K^+, this different requirement can be met through increasing or decreasing the bond angles of B–O–B and Be–O–B in the flexible $[BO_2]_\infty$ chains (Fig. 27). One can find that the angles of Be_2–O_9–B_4 (146.33(19)°), B_4–O_7–B_3 (137.93(19)°), and B_3–O_5–Be_1 (118.78(15)°) in β-$KBe_2B_3O_7$ are smaller than those of $RbBe_2B_3O_7$ (152.0(4)°, 141.5(4)°, 121.2(4)°), respectively, leading to the changes of the distances between layers (β-$KBe_2B_3O_7$ (8.73 Å) and $RbBe_2B_3O_7$ (8.86 Å)). In γ-$KBe_2B_3O_7$, the adjacent layers (8.70 Å) are bridged by rigid $[B_3O_6]$ planar groups (Fig. 28). However, the phase $RbBe_2B_3O_7$ that is isostructural to γ-$KBe_2B_3O_7$ does not exist because the rigid framework consisting of $[B_3O_6]$ is not able to be adjusted to accommodate a larger Rb^+ ion.

It is worth noting the transformation from a monoclinic β-phase to an orthorhombic γ-phase occurs as follows. Because there is only one unique orientation of $[BO_3]^{3-}$ groups in the $[Be_2BO_5]_\infty$ layers of β- and γ-phase, the evolution of structure between them can be clearly explained by showing the structures with $[BO_3]^{3-}$ groups oriented to the same direction (Fig. 30). When the γ-phase transforms into the β-phase, old B–O bonds of the $[B_3O_6]$ groups break, and new

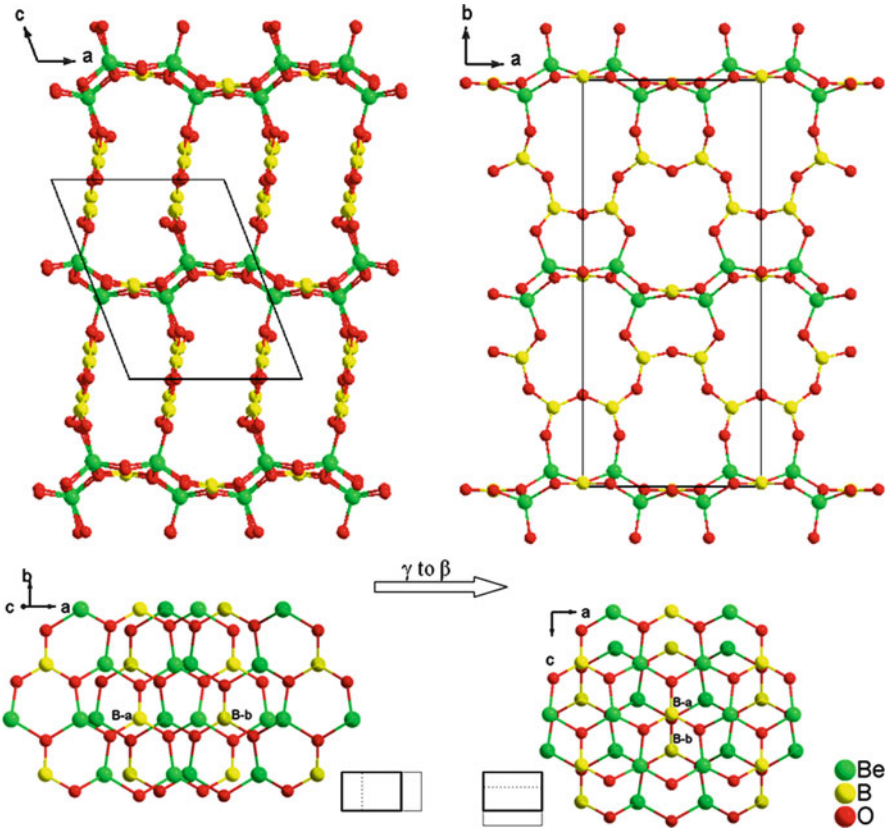

Fig. 30 Structural evolution from γ-$KBe_2B_3O_7$ to β-$KBe_2B_3O_7$

B–O bonds form between the adjacent parallel $[Be_2BO_5]_\infty$ layers to build new $[BO_2]_\infty$ chains that extend vertically to the former $[B_3O_6]$ plane. Meanwhile, the adjacent $[Be_2BO_5]_\infty$ layers glide from each other along the *a*–*b* plane. The driving force for the phase transformation may be attributed to the release of strain in γ-phase. Compared with β-phase in which layers are connected by flexible metaborate chains $[BO_2]_\infty$, γ-phase in which layers are bridged by rigid $[B_3O_6]$ groups has higher strain and therefore is less stable. As a result, increasing temperature causes phase transformation of γ-phase into more stable β-phase.

The structural evolution can be illustrated through the comparison of the layer structures of KBBF, β-$KBe_2B_3O_7$, γ-$KBe_2B_3O_7$, $RbBe_2B_3O_7$, and $Na_2CsBe_6B_5O_{15}$. Although they all have similar alveolate beryllium borate layers $[Be_2BO_3F_2]_\infty$ or $[Be_2BO_3O_2]_\infty$, the orientation periodicity of the O (or F) atoms that bond to the Be atoms and protrude out of the layers is different. Since there is only one unique orientation of $[BO_3]^{3-}$ groups in the $[Be_2BO_3]_\infty$ layers of the aforementioned compounds, the structural differences among them are clearly illustrated when $[BO_3]^{3-}$ groups are oriented in the same direction (Fig. 31).

To realize the structural design to increase the SHG effects of these layered compounds containing alveolate network, an ideal strategy is to construct a more compact structure through bridging the 2D layer via smaller $[BO_3]$ groups. As such, a hypothesized formula is readily derived as $A_3Be_6B_5O_{15}$ (A = alkali metal), by substituting $[BO_3]$ for $[B_3O_6]$ in γ-$KBe_2B_3O_7$, when the formula is viewed as a sum of three parts, i.e., cations, NLO-active 2D layers and connectors:

$$\gamma - KBe_2B_3O_7 \times 3 : \ 3K + 3[Be_2BO_3] + 2[B_3O_6],$$
$$A_3Be_6B_5O_{15} : \ 3A + 3[Be_2BO_3] + 2[BO_3].$$

Based on this, a target compound may be constructed by carefully arranging the framework connection and alkali metal allocation as following. The layer $[Be_2BO_3F_2]_\infty$ in KBBF is composed of repeating unit "A" (Fig. 31a). The distance between the adjacent Be atoms that have the same Be–O bond direction is too long (4.427 Å) to bond the two O atoms from a $[BO_3]$ group. In the case of β-$KBe_2B_3O_7$, meanwhile, the layer $[Be_2BO_3O_2]_\infty$ is composed of repeating unit "AB" (Fig. 31b). Although the aforementioned distance is acceptable (2.689 Å) to form a bidentation to bridge $[BO_3]$ groups, it is rather undesired to leave a dangling Be–O bond in the adjacent layer it connected to. Therefore, a more feasible dentation configuration is the alternate alignment of the mono- and bidentation to connect $[BO_3]$ groups, with a monodentation on one side of the two adjacent layers and a bidentation on the other. Such configuration is herein realized in the title compound $Na_2CsBe_6B_5O_{15}$, whose $[Be_2BO_3O_2]_\infty$ layer is composed of repeating unit "ABA" (Fig. 31c). The combination of the mono- and bidentate Be–O bond configuration, coupled with an acceptable distance (2.559 Å) between Be–Be atoms, enables the $[Be_2BO_3O_2]_\infty$ layers to be bridged via $[BO_3]$ groups. Consequently, such unequally aligned Be–O dentation inevitably results in the existence of two types of tunnels, bigger and smaller, between the adjacent $[Be_2BO_3O_2]_\infty$ layers. Two types of cations with different radius, i.e., Na^+ and Cs^+, are thus required to reside in these two tunnels,

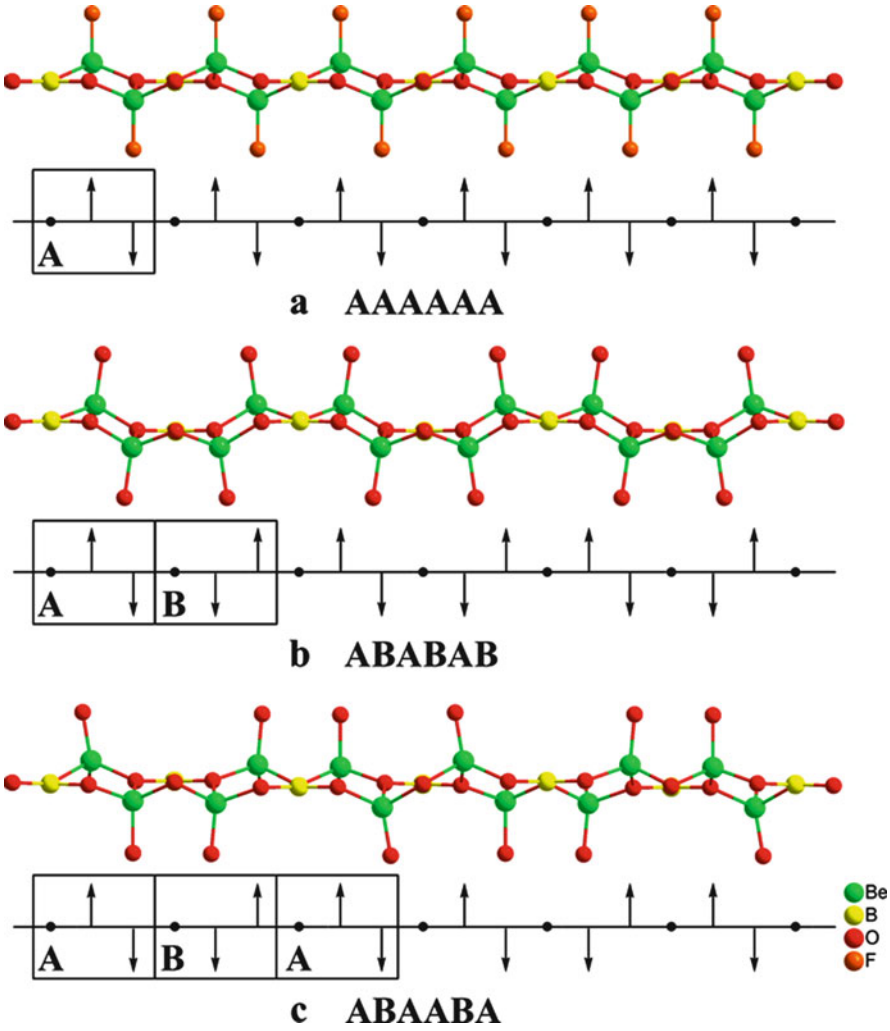

Fig. 31 Comparison of $[Be_2BO_3F_2]_\infty$ or $[Be_2BO_3O_2]_\infty$ layers in KBBF (**a**), β-$KBe_2B_3O_7$ (**b**), and $Na_2CsBe_6B_5O_{15}$ (**c**)

respectively (Fig. 29). This is likely the reason that we are unable to find alveolate beryllium borate $[Be_2BO_5]_\infty$ layers bridged via smaller planar $[BO_3]$ groups in unitary alkaline beryllium borates but rather in binary alkaline beryllium borates.

2.5 Structure and NLO Property Relations

The curves of SHG signal as a function of particle size from the measurements made on ground crystals for $NaBeB_3O_6$, β-$KBe_2B_3O_7$, γ-$KBe_2B_3O_7$, $RbBe_2B_3O_7$, and $Na_2CsBe_6B_5O_{15}$ are shown in Fig. 32. The results are consistent with

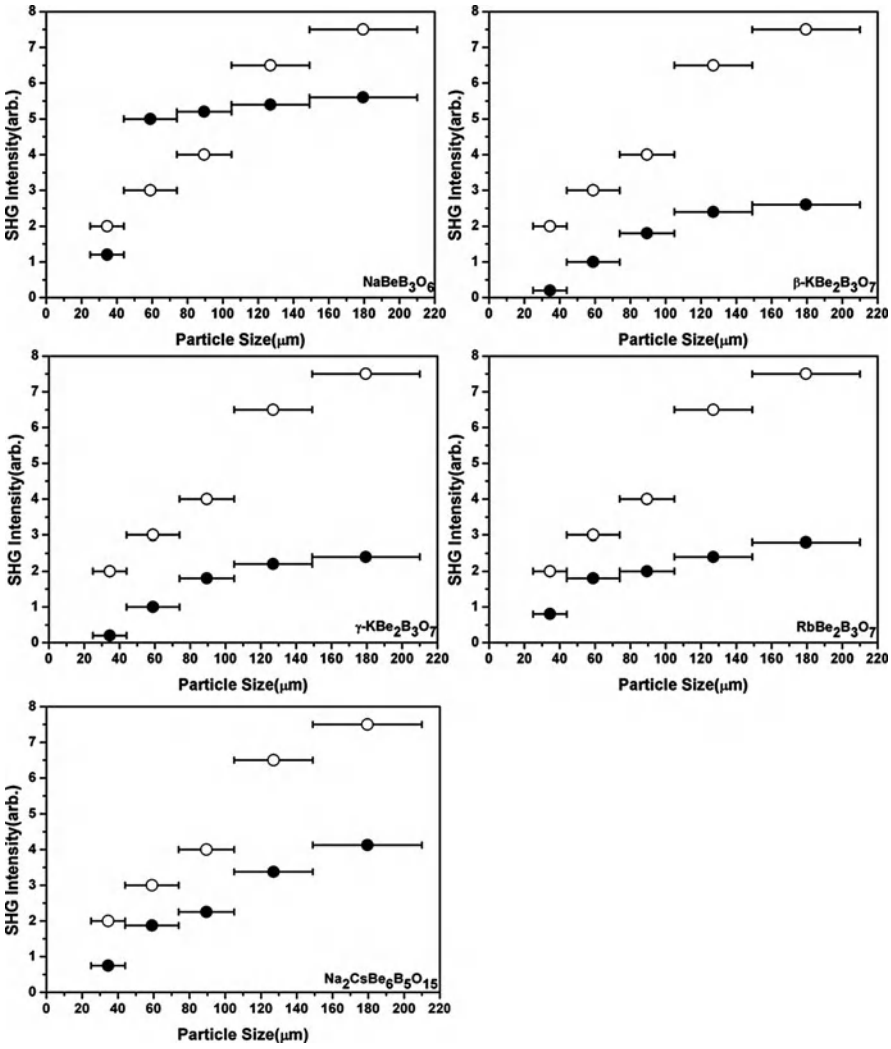

Fig. 32 SHG measurements of $NaBeB_3O_6$, β-$KBe_2B_3O_7$, γ-$KBe_2B_3O_7$, $RbBe_2B_3O_7$, and $Na_2CsBe_6B_5O_{15}$ ground crystals (*solid circle*) with LBO (*open circle*) as a reference

phase-matching behavior according to the rule proposed by Kurtz and Perry [19]. A LBO sample was selected as a reference to insure the accuracy of measurements because it is an optical biaxial crystal, same as the crystals to be measured. The second-harmonic signal was found to be 0.75, 0.35, 0.32, 0.37, and 0.55 × LBO for $NaBeB_3O_6$, β-$KBe_2B_3O_7$, γ-$KBe_2B_3O_7$, $RbBe_2B_3O_7$, and $Na_2CsBe_6B_5O_{15}$, respectively. These values are proportional to the squares of the nonlinear d_{eff} coefficients. Since the reported d_{eff} coefficient for LBO is 0.832 pm/V (2.133 × d_{36} (KDP)), the derived d_{eff} coefficients for $NaBeB_3O_6$, β-$KBe_2B_3O_7$, γ-$KBe_2B_3O_7$, $RbBe_2B_3O_7$,

Table 3 Borates belongs to trigonal-huntite structure

Crystals	Space group	Inter-layer bridging	Inter-layer distances (Å)	SHG coefficient (× KDP)
KBBF	$R32$	K^+–F^-	6.25	1.12
γ-$KBe_2B_3O_7$	$P2_1$	$[B_3O_6]$	8.70	0.68
β-$KBe_2B_3O_7$	$Pmn2_1$	$[BO_2]_\infty$	8.73	0.75
$RbBe_2B_3O_7$	$Pmn2_1$	$[BO_2]_\infty$	8.86	0.79
$Na_2CsBe_6B_5O_{15}$	$C2$	$[BO_3]$	6.23	1.17

and $Na_2CsBe_6B_5O_{15}$ are 0.62, 0.29, 0.27, 0.31, and 0.46 pm/V, which corresponded to about 1.60, 0.75, 0.68, 0.79, and 1.17 times as large as that of d_{36} (KDP), respectively.

Compared the layered compound described above, the distances between adjacent layers in β-$KBe_2B_3O_7$ (8.73 Å), $RbBe_2B_3O_7$ (8.86 Å), and γ-$KBe_2B_3O_7$ (8.70 Å) are longer than that in the KBBF (6.25 Å), resulting in a lower $[BO_3]$ density in the formers. Therefore, the SHG coefficients of β-$KBe_2B_3O_7$, $RbBe_2B_3O_7$, and γ-$KBe_2B_3O_7$ are found smaller than that of KBBF. $Na_2CsBe_6B_5O_{15}$ gives a successful example of structural design on constructing a "tight" structure through introducing smaller $[BO_3]^{3-}$ groups serving as bridges to increase their $[BO_3]^{3-}$ density. Consequently, a larger SHG effect is obtained through properly allocating binary alkaline cations to fit the cavities between adjacent layers.

The above argumentation on structure–property correlations is in good agreement with the SHG measurements. According to the anionic group theory, the nonlinearity of $Na_2CsBe_6B_5O_{15}$ relative to that of KBBF ($1.115 \times d_{36}$ (KDP)) is determined by the density of $[BO_3]^{3-}$ groups in the $[Be_2BO_3O_2]_\infty$ layers within a unit cell, based on the same arrangement of the NLO-active $[BO_3]^{3-}$ groups. The density of the $[BO_3]^{3-}$ groups is 0.00921 per unit volume in $Na_2CsBe_6B_5O_{15}$, which is comparable to that of KBBF (0.00946). Therefore, the nonlinearity of $Na_2CsBe_6B_5O_{15}$ is calculated to be 97.4% of KBBF. These results agree approximately with the experimental values, which are 1.05 times relative to KBBF for $Na_2CsBe_6B_5O_{15}$. The correlations between the NLO effects and structural characters are summarized in Table 3. As seen from this table, the nonlinearity of this type of borate containing 2D alveolate beryllium borate layers is approximately inversely proportional to the inter-layer distance. Among these compounds, $Na_2CsBe_6B_5O_{15}$ possesses the largest NLO coefficient owning to its shortest inter-layer distance, i.e., the compact layer structure bridged via small $[BO_3]$ groups.

Acknowledgments This work was supported by the National Natural Science Foundation of China (Grants Nos. 60608018, 90922035 and 50872132) and the National High Technology Research and Development Program of China (Grant No. 2006AA030107).

References

1. Mills AD (1962) Crystallographic data for new rare earth borate compounds, RX3(BO3)4. Inorg Chem 1:960–961
2. Ballman AA (1962) New series of synthetic borates isostructural with carbonate mineral huntite. Am Miner 47:1380–1383
3. Aka G, Viegas N, Teisseire B et al (1995) Flux growth and characterization of rare-earth-doped nonlinear huntite-type borate crystals – Y1-XNDX(Al0.7Ga0.3)(3)(BO3)(4) and Y1-XYBXAL3(BO3)(4). J Mater Chem 5:583–587
4. Leonyuk NI, Leonyuk LI (1995) Growth and characterization of RM(3)(BO3)(4) crystals. Prog Cryst Growth Charact Mater 31:179–278
5. Kutovoi SA, Laptev VV, Mastsnev SY (1991) Sov J Quantum Electron 21:131
6. Peterson GA, Keszler DA, Reynolds TA (2000) Stoichiometric, trigonal huntite borate CeSc3 (BO3)(4). Int J Inorg Mater 2:101–106
7. Meyn JP, Jensen T, Huber G (1994) Spectroscopic properties and efficient diode-pumped laser operation of neodymium-doped lanthanum scandium borate. IEEE J Quantum Electron 30:913–917
8. He MY, Wang G, Lin ZB et al (1999) Structure of medium temperature phase beta-LaSc3 (BO3)(4) crystal. Mater Res Innov 2:345–348
9. Li YK, Aka G, Kahn-Harari A et al (2001) Phase transition, growth, and optical properties of NdxLa1-xSc3(BO3)(4) crystals. J Mater Res 16:38–44
10. Jung ST, Yoon JT, Chung SJ (1996) Phase transition of neodymium yttrium aluminum borate with composition. Mater Res Bull 31:1021–1027
11. Ye N, Stone-Sundberg JL, Hruschka MA et al (2005) Nonlinear optical crystal YxLayScz (BO3)4 (x plus y plus z = 4). Chem Mater 17:2687–2692
12. Ye N, Zhang Y, Chen W et al (2006) Growth of nonlinear optical crystal Y0.57La0.72Sc2.71 (BO3)(4). J Cryst Growth 292:464–467
13. Shannon RD (1976) Revised effective ionic-radii and systematic studies of interatomic distances in halides and chalcogenides. Acta Crystallogr Sect A 32:751–767
14. Chen CT (1993) In: Letokhov VS, Shank CV, Shen YR (eds) Development of new nonlinear optical crystals in the borate series. Harwood Academic Publishers, New York
15. Armstrong JA, Bloembergen N, Ducuing J et al (1962) Interactions between light waves in a nonlinear dielectric. Phys Rev 127:1918–1939
16. Amano S, Mochizuki T (1991) Nolinear Opt 1:297
17. Li W, Huang LX, Zhang G et al (2007) Growth and characterization of nonlinear optical crystal Lu0.66La0.95SC2.39(BO3)(4). J Cryst Growth 307:405–409
18. Zeng ZD, Shen HY, Huang ML et al (1990) Measurement of the refractive-index and thermal refractive-index coefficients of Nd-YAP crystal. Appl Opt 29:1281–1286
19. Kurtz SK, Perry TT (1968) A powder technique for evaluation of nonlinear optical materials. J Appl Phys 39:3798–3813
20. Xu X, Ye N (2011) Gd(x)La(1-x)Sc(3)(BO(3))(4): a new nonlinear optical crystal. J Cryst Growth 324:304–308
21. Liu LQ, Ma E, Li RF et al (2007) Effects of phonon confinement on the luminescence dynamics of Eu(3+) in Gd(2)O(3) nanotubes. Nanotechnology 18: 015403
22. Chen XY, Ma E, Liu GK (2007) Energy levels and optical spectroscopy of Er(3+) in Gd(2)O (3) nanocrystals. J Phys Chem C 111:10404–10411
23. Xu X, Wang SC, Ye N (2009) A new nonlinear optical crystal Bi(x)La(y)Sc(z)(BO(3))(4) (x plus y plus z = 4). J Alloy Compd 481:664–667
24. Wang S, Ye N (2007) Nonlinear optical crystal BiAlGa2(BO3)(4). Solid State Sci 9:713–717
25. Brixner LH, Licis MS (1971) Synthesis and structure of BiFe1.35Al1.65(BO3)4. J Solid State Chem 3:172–173
26. Liu H, Li J, Fang SH et al (2011) Growth of YAl(3)(BO(3))(4) crystals with tungstate based flux. Mater Res Innov 15:102–106

27. Liu H, Chen X, Huang LX et al (2011) Growth and optical properties of UV transparent YAB crystals. Mater Res Innov 15:140–144
28. Wang SC, Ye N, Li W et al (2010) Alkaline beryllium borate NaBeB(3)O(6) and ABe(2)B(3)O(7) (A = K, Rb) as UV nonlinear optical crystals. J Am Chem Soc 132:8779–8786
29. Wang SC, Ye N (2011) Na2CsBe6B5O15: an alkaline beryllium borate as a deep-UV nonlinear optical crystal. J Am Chem Soc 133:11458–11461
30. Chen CT, Wang YB, Wu BC et al (1995) Design and synthesis of an ultraviolet-transparent nonlinear-optical crystal Sr2Be2B2O7. Nature 373:322–324
31. Chen CT, Liu GZ (1986) Recent advances in nonlinear optical and electrooptical materials. Annu Rev Mater Sci 16:203–243
32. Chen CT, Wu YC, Li RK (1989) The anionic group theory of the non-linear optical effect and its applications in the development of new high-quality NLO crystals in the borate series. Int Rev Phys Chem 8:65–91
33. Keszler DA (1996) Borates for optical frequency conversion. Curr Opin Solid State Mater Sci 1:204–211
34. Pan S, Smit JP, Watkins B et al (2006) Synthesis, crystal structure, and nonlinear optical properties of Li6CuB4O10: a congruently melting compound with isolated CuB4O10 (6-) units. J Am Chem Soc 128:11631–11634
35. Wu HP, Pan SL, Poeppelmeier KR et al (2011) K(3)B(6)O(10)Cl: a new structure analogous to perovskite with a large second harmonic generation response and deep UV absorption edge. J Am Chem Soc 133:7786–7790
36. Halasyamani PS, Poeppelmeier KR (1998) Noncentrosymmetric oxides. Chem Mater 10:2753–2769
37. Chang HY, Kim SH, Ok KM et al (2009) New polar oxides: synthesis, characterization, calculations, and structure-property relationships in RbSe(2)V(3)O(12) and TlSe(2)V(3)O(12). Chem Mater 21:1654–1662
38. Chang HY, Kim SH, Ok KM et al (2009) Polar or nonpolar? A(+) cation polarity control in A(2)Ti(IO(3))(6) (A = Li, Na, K, Rb, Cs, Tl). J Am Chem Soc 131:6865–6873
39. Chang HY, Kim SH, Halasyamani PS et al (2009) Alignment of lone pairs in a new polar material: synthesis, characterization, and functional properties of Li(2)Ti(IO(3))(6). J Am Chem Soc 131:2426–2427
40. Sun CF, Hu CL, Xu X et al (2009) BaNbO(IO(3))(5): a new polar material with a very large SHG response. J Am Chem Soc 131:9486–9487
41. Chen CT, Wu BC, Jiang AD et al (1985) A new-type ultraviolet SHG crystal – beta-BAB2O4. Sci Sin Ser B Chem Biol Agric Med Earth Sci 28:235–243
42. Chen CT, Wu YC, Jiang AD et al (1989) New nonlinear-optical crystal: LIB3O5. J Opt Soc Am B Opt Phys 6:616–621
43. Wu YC, Sasaki T, Nakai S et al (1993) CsB3O5: a new nonlinear-optical crystal. Appl Phys Lett 62:2614–2615
44. Tu JM, Keszler DA (1995) CsLiB6O10 – a noncentrosymmetric polyborate. Mater Res Bull 30:209–215
45. Mori Y, Kuroda I, Nakajima S et al (1995) New nonlinear-optical crystal – cesium lithium borate. Appl Phys Lett 67:1818–1820
46. Li RK (1989) The interpretation of UV absorption of borate glasses and crystals. J Non-Cryst Solids 111:199–204
47. Schaffers KI, Keszler DA (1994) Tetrahedral triangular 3-D framework and europium luminescence in the borate BaBe2(BO3)2. Inorg Chem 33:1201–1204
48. Schaffers KI, Keszler DA (1990) The layered borate SrBe2(BO3)2. J Solid State Chem 85:270–274
49. Schaffers KI, Keszler DA (1993) Alkaline-earth beryllium borate CaBeB2O5. Acta Crystallogr Sect C-Cryst Struct Commun 49:647–650
50. Luce JL, Schaffers KI, Keszler DA (1994) Structure of the borate Li14Be5B(BO3)9. Inorg Chem 33:2453–2455

51. Wen XH, Li RK, Chen CT (2006) Acta Crystallogr Sect C-Cryst Struct Commun 62:121
52. Zachariasen WH (1931) The crystalline structure of hambergite, Be2BO3(OH). Z Kristall 76:289–302
53. Zachariasen WH, Plettinger HA, Marezio M (1963) Structure and birefringence of hambergite, Be2BO3.OH. Acta Crystallogr 16:1144–1146
54. McMillen CD, Hu J, VanDerveer D et al (2009) Trigonal structures of ABe(2)BO(3)F(2) (A = Rb, Cs, Tl) crystals. Acta Crystallogr Sect B-Struct Sci 65:445–449
55. McMillen CD, Kolis JW (2008) Hydrothermal crystal growth of ABe(2)BO(3)F(2) (A = K, Rb, Cs, Tl) NLO crystals. J Cryst Growth 310:2033–2038
56. Mei L, Huang X, Wang Y et al (1995) Crystal-structure of KBe2BO3F2. Z Kristall 210:93–95
57. Mei LF, Wang YB, Chen CT (1994) Crystal-structure of sodium beryllium borate fluoride. Mater Res Bull 29:81–87
58. Chen CT, Wang GL, Wang XY et al (2009) Deep-UV nonlinear optical crystal KBe(2)BO(3)F (2)-discovery, growth, optical properties and applications. Appl Phys B-Lasers Opt 97:9–25
59. Qi H, Chen CT (2001) Growth of a new nonlinear optical crystal Ba2Be2B2O7 by TSSG method. Chem Lett 352–353
60. Qi H, Chen CT (2001) Synthesis and characterization of Ba2Be2B2O7. Inorg Chem Commun 4:565–567
61. Chen CT, Bai L, Wang ZZ et al (2006) Development of new NLO crystals for UV and IR applications. J Cryst Growth 292:169–178
62. Li W, Ye N (2007) Acta Crystallogr Sect E Struct Rep 63:1160

Struct Bond (2012) 144: 223–234
DOI: 10.1007/430_2011_68
© Springer-Verlag Berlin Heidelberg 2012
Published online: 3 March 2012

Cation Effect in Doped BBO and Halogen Anion Effect in $Pb_2B_5O_9X$ ($X^- = I^-$, Br^-, Cl^-)

Yi-Zhi Huang, Li-Ming Wu, and Mao-Chun Hong

Abstract This chapter is intended to be a small research progress report on borate nonlinear optical (NLO) materials focusing on the cation and anion effects in two selected systems. The cation-doped BBO, $Ba_{1-x}B_{2-y-z}O_4$-$Si_xAl_yGa_z$ ($x = 0$–0.15, $y = 0$–0.1, $z = 0$–0.04), has improved NLO-related performance relative to the undoped one, and the origins of the second harmonic generation (SHG) improvement on the basis of the whole electron structures are discussed. And halide borates, $Pb_2B_5O_9X$ ($X^- = I^-$, Br^-, Cl^-), are presented to emphasize the discrepancy in optical properties, crystallographic and electronic structures, and origin of SHG response. Importantly, the cation and anion effects are both crucial to improve the SHG performance and to design NLO materials.

Keywords BBO · Borates · Electronic effects · NLO materials · SHG

Contents

1 Introduction 224
2 $Ba_{1-x}B_{2-y-z}O_4$-$Si_xAl_yGa_z$ 225
2.1 NLO-Related Properties 226
2.2 A Speculation on the Cation Effect 227
3 $Pb_2B_5O_9X$ Including Anionic $X^- = I^-$, Br^-, Cl^- 227
3.1 Optical Properties 227
3.2 Crystallographic Structures 228
3.3 Electronic Structures 229
3.4 Cutoff-Energy-Dependent SHG Coefficients 230
4 Concluding Remarks 232
References 233

Y.-Z. Huang, L.-M. Wu (✉), and M.-C. Hong
Key Laboratory of Optoelectronic Materials Chemistry and Physics, Fujian Institute of Research on the Structure of Matter, Chinese Academy of Sciences, Fuzhou 350002, People's Republic of China
e-mail: huangyizhi@fjirsm.ac.cn; liming_wu@fjirsm.ac.cn

Abbreviations

BBO	β-BaB_2O_4
BBOSAG	$Ba_{1-x}B_{2-y-z}O_4$-$Si_xAl_yGa_z$
CB	Conduction bands
DFT	Density function theory
DOS	Densities of states
E_F	Fermi level
NCS	Noncentrosymmetric
NLO	Nonlinear optical
SHG	Second harmonic generation
SOJT	Second-order John–Teller
VB	Valence bands

1 Introduction

To improve the application performance of some materials, cation doping was a commonly used strategy. But it was not true for the well-known NLO materials, β-BaB_2O_4 (BBO), of which the excellent SHG effect had long been considered to originate merely from the distorted planar anionic groups of $[B_3O_6]^{3-}$ and had nothing to do with the barium cations [1, 2]. Based on such an opinion from the anionic group theory, a great deal of efforts in more than 20 years had been focused on the techniques on the BBO single crystal growth, and process yield and crystal qualities including size, perfection, transparency, and inclusions had been significantly improved [3–7]. However, the major disadvantage of highly deliquescence of BBO single crystal still had not been overcome. Even after a coated process, the SHG intensity would still be attenuated in the humid air with increased timing. Besides, the hardness was not strong enough so that breaking was often suffered during the processing. Moreover, its SHG efficiency and optical damage threshold were also expected to be improved to keep up with the progress in frequency converters. Until 2008, some cation-doped BBO, i.e., $Ba_{1-x}B_{2-y-z}O_4$-$Si_xAl_yGa_z$ ($x = 0-0.15$, $y = 0-0.1$, $z = 0-0.04$) [8–11], exhibited improved properties relative to the undoped BBO in many respects, such as almost no deliquescence, significantly increased hardness, higher optical damage threshold, and stronger SHG intensity, which might be attributed to the cation effect. Details were presented in the second section.

On the other hand, cations such as d^0 transition metals (Ti^{4+}, Nb^{5+}, W^{6+}, etc.) and lone-pair cations (Pb^{2+}, Bi^{3+}, Se^{4+}, Te^{4+}, I^{5+}, etc.) are susceptible to the second-order John–Teller (SOJT) distortion and so as to serve as asymmetric building units to construct noncentrosymmetric (NCS) compounds [12–23]. Among them, I^{5+} with lone pairs was very attractive and served as one of the active components in

a variety of compounds with excellent SHG response [18–23], whereas the I^- anion without lone pairs attracted less attention. In spite of some halogen borates were known, the SHG contributions of halide anions, F^-, Cl^-, Br^-, and I^-, had been neglected to some degree because of the widely accepted importance of the borate anionic groups [24–27].

In 2005, a systematic investigation on halide borates $M_2B_5O_9X$ ($M^{2+} = Ca^{2+}$, Sr^{2+}, Ba^{2+}, Pb^{2+}, Eu^{2+}; $X^- = Cl^-$, Br^-), including experimental powder SHG measurements and theoretical calculations of SHG coefficients [28], was reported. The contributions from lone pairs and halogen anions were observed experimentally, i.e., the powdery SHG intensity drastically increased along with the trends of not only $Ca^{2+} < Sr^{2+} < Ba^{2+} < Pb^{2+}$ but also $Cl^- < Br^-$. Unfortunately, this had not been explained because their bond theory calculations indicated the planar BO_3 triangle as the sole SHG functional group. Till 2010, the isostructural iodide, $Pb_2B_5O_9I$ [29], was synthesized and exhibited strong powdery SHG activity with a significant improvement along with $Cl^- < Br^- < I^-$. The density function theory (DFT) electronic structure and SHG coefficient calculations [30, 31] revealed the strong anionic effect of I^-. Details were presented in the third section.

2 $Ba_{1-x}B_{2-y-z}O_4$-$Si_xAl_yGa_z$

$Ba_{1-x}B_{2-y-z}O_4$-$Si_xAl_yGa_z$ (BBOSAG), doped by Si^{4+}, Al^{3+}, and Ga^{3+} in very small proportions ($x = 0-0.15$, $y = 0-0.1$, $z = 0-0.04$), crystallizes in space group $R3$ [10]. The parent structure, BBO, is constructed by alternative layers of $B_3O_6^{3-}$ rings and Ba^{2+} cations (Fig. 1). Every planar borate six-membered ring is perpendicular to c axis and is formed by three corner-shared BO_3 triangles. Such rings are well isolated to each other but are surrounded by Ba^{2+}.

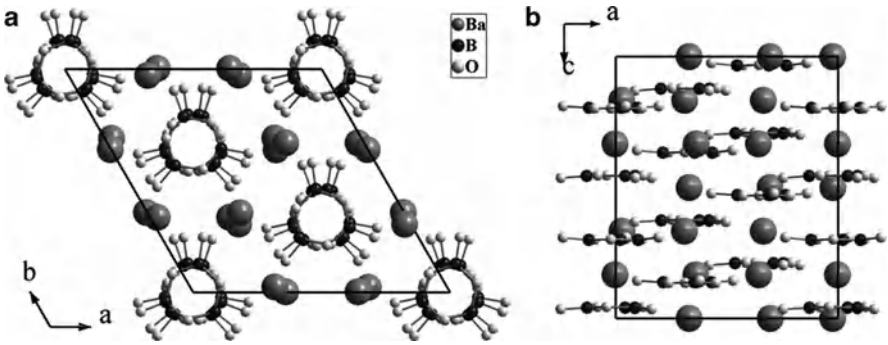

Fig. 1 Crystal structure of BBO viewed down c and b axes with Ba–O bonds omitted for clarity

2.1 NLO-Related Properties

BBOSAG crystals show overall improvement on the NLO-related properties, including SHG efficiency, moisture resistance, optical damage threshold, and hardness (Tables 1–4).

On the one hand, the disadvantages, to be hygroscopic and frangible shown by BBO, have been well resolved in the case of BBOSAG, which suggest that a coating process is not necessary for the application of BBOSAG, and the cutting and polishing processes will be much more facile. On the other hand, the advantages of BBO, strong SHG intensity and high optical damage threshold, have also been improved. Furthermore, considering the mature BBO crystal growth

Table 1 Experimental maximum output light intensity of frequency-doubled signal of BBOSAG and BBO crystals

	Output light intensity (arbitrary unit)			
	1st read	2nd read	3rd read	Mean value
BBOSAG	4.7×10^3	5.2×10^3	5.1×10^3	5×10^3
BBO	3.4×10^3	4.6×10^3	4.1×10^3	4×10^3

The crystal lengths are 3.15 and 3.17 mm for BBOSAG and BBO, respectively. Adapted with permission from [10]

Table 2 SHG intensities of BBOSAG and BBO crystals before and after the moisture exposure

	SHG intensity (arbitrary unit)			Decrement		
	Day 1	Day 18	Day 34	Days 1–18	Days 18–34	Days 1–34
BBOSAG	3.8×10^3	3.8×10^3	3.8×10^3	0	0	0
BBO	3.8×10^3	1.8×10^3	1.1×10^3	53%	39%	71%

The moist condition was provided by a constant humidity chamber with 83–84% relative humidity (RH) and 12–15°C. Adapted with permission from [10]

Table 3 Optical damage tests on BBOSAG and BBO crystals

	Incident laser spot[a]				
Diameter (mm)	5	3	2.5	2.2	2
Energy density (J/cm^2)	4.56	12.67	18.24	23.65	28.50
Power density (MW/cm^2)	651.4	1809.7	2605.7	3365.2	4071.4
	Will be damaged				
BBOSAG	No	No	No	No	Yes
BBO	No	No	Yes		

[a]Produced by an electro-optic Q-switch YAG laser, with wavelength of 1,064 nm, single pulse width of 7 nsA, and single pulse energy of 895 mJ. Adapted with permission from [10]

Table 4 Hardness of BBOSAG and BBO crystals

	Mohs hardness	Shore hardness
BBOSAG	6	101.2
BBO	4	71

and processing technologies, further improvement is still possible. The present BBOSAG crystal still has inclusions; thus, the transmittance in the UV–vis region is no higher than 80%, which means 20% energy degradation. If such energy could be effectively recovered, an SHG improvement of more than 50% would be expected (vs the present 25%). Note that the polish machining on crystal surface in the present research was not good enough so that the optical damage threshold for both BBOSAG and BBO were undervalued.

2.2 A Speculation on the Cation Effect

The classical anionic group theory precludes cations from a given system, only considers the remained anionic groups, and geometrically superposes the local NLO susceptibilities from the isolated anionic groups as the microscopic NLO susceptibility [2]. However, the whole electronic structures of BBO confirmed that the interaction between Ba^{2+} cations and $B_3O_6^{3-}$ rings in BBO could not be simply neglected. Nonbonding O 2p states are discovered just above the filled B–O states, occupying the top of valence bands (VB), while empty Ba 6s are below the unfilled B–O ones, occupying the bottom of conduction bands (CB) [32–34]. That is, the fundamental band gap should be attributed to the transitions from O 2p to Ba 6s rather than those within the anionic groups according to the anionic group theory. We therefore speculate that Ba^{2+} cations may strongly attract the conjugated π electrons on the $B_3O_6^{3-}$ rings to generate a dynamic dipole moment, which together with the borate anionic groups may response for the overall SHG response.

In BBOSAG, the cationic dopants, Si^{4+}, Al^{3+}, and Ga^{3+}, have higher formal charge relative to Ba^{2+} and smaller electronegativity relative to B^{3+}, so as to attract the electrons on the $B_3O_6^{3-}$ rings more strongly than Ba^{2+} does, and lead to stronger dynamic dipole moment. On the other hand, if the dopant substitutes the boron position, the electrons on the $B_3O_6^{3-}$ rings would concentrate more on the oxygen sites and thus generate stronger static dipole moment within the rings. In a word, cation doping will enhance both the dynamic and the static dipole moments, and results in SHG efficiency improvement.

3 $Pb_2B_5O_9X$ Including Anionic $X^- = I^-, Br^-, Cl^-$

3.1 Optical Properties

Experimentally, $Pb_2B_5O_9X$ shows a remarkable improvement in the powder SHG intensity on going from Cl^- to I^- but has a slight decrease of the band gap and exhibits similar infrared absorption edges (Table 5), which are in accordance with the primary calculation results (Table 5). Apparently, one may conclude that the

Table 5 Optical properties for $Pb_2B_5O_9X$ ($X^- = I^-$, Br^-, Cl^-)

X^-	Experimental		Calculated	
	SHG intensity[a]	Transparent region (μm)	Band-gap energy (eV)[b]	SHG coefficients (pm/V)[c]
I^-	13.5, PM	0.40–6.96	3.33/3.36	16.6/9.4/1.8
Br^-	4.7, PM	0.38–6.86	3.54/3.54	7.4/2.6/−1.2
Cl^-	0.7, PM	0.31–6.80	3.72/3.69	4.5/1.0/−1.8

Adapted with permission from [29]. Copyright 2010 American Chemical Society
[a]Relative to KDP (150–210 μm) with $\lambda_{incident} = 1{,}064$ nm. PM = phase matchable
[b]Direct/indirect gaps
[c]Static $d_{15}/d_{24}/d_{33}$ ($d_{15} = d_{31}$, $d_{24} = d_{32}$) according to the length-gauge formalism

reduction of band-gap energy will likely to improve the SHG activity, which is, however, excluded by the additional calculations on band-gap corrections. For example, if $Pb_2B_5O_9I$ had a band gap of 3.7 eV (same as the calculated value for $Pb_2B_5O_9Cl$), d_{15} would decrease to 11.1 pm/V but was still significantly greater than 4.5 pm/V for $Pb_2B_5O_9Cl$.

3.2 Crystallographic Structures

$Pb_2B_5O_9X$ ($X^- = I^-$, Br^-, Cl^-) crystallizes in space group *Pnn*2 (No. 34) and constructed by three types of NCS units in a ratio of 2/3/2, BO_3 triangle, BO_4 tetrahedron, and PbO_7X_2 monocapped hexagonal bipyramid. The chains of BO_4 are connected via BO_3 to form the three-dimensional network of $[B_5O_9^{3-}]_n$, the chains of PbO_7X_2 are knitted into $[Pb_2O_9X^{15-}]_n$ (Fig. 2).

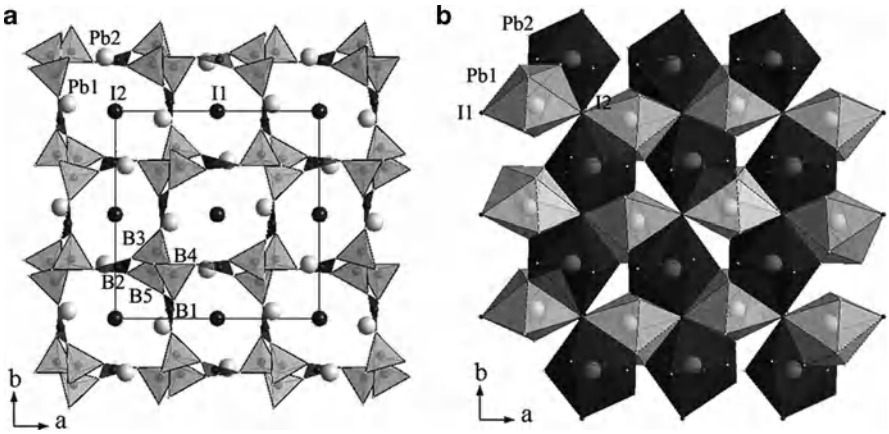

Fig. 2 (**a**) Crystal structure of $Pb_2B_5O_9I$ viewed down *c* axis with Pb–O and Pb–I bonds omitted for clarity. *Gray*: BO_4 tetrahedra, *black*: BO_3 triangles. (**b**) $[Pb_2O_9I^{15-}]_n$ substructure along *c* axis. *Gray* and *black*: PbO_7I_2 monocapped hexagonal bipyramids. Reprinted with permission from [29]. Copyright 2010 American Chemical Society

Table 6 Structural parameter comparison among $Pb_2B_5O_9X^-$ ($X^- = I^-$, Br^-, Cl^-)

X^-	I^-	Br^-	Cl^-	Δ(I^- vs Br^-)	Δ(I^- vs Cl^-)
a (Å)	11.561	11.434	11.381	1.1%	1.6%
b (Å)	11.700	11.491	11.384	1.8%	2.8%
c (Å)	6.524	6.538	6.563	−0.2%	−0.6%
B–O[a] (Å)	1.33–1.39	1.33–1.42	1.34–1.39	−3.0–2.3%	−2.4–2.9%
O–B–O[a] (°)	117–127	111–129	117–124	−2.4–3.0%	−1.7–3.0%
B–O[b] (Å)	1.44–1.53	1.44–1.51	1.45–1.50	−3.6–3.0%	−2.0–4.4%
O–B–O[b] (°)	103–114	104–115	103–115	−2.8–3.3%	−4.2–3.6%
X–Pb–X[c] (°)	137, 152	150, 160	157, 163	−8.4%, −4.7%	−12.8%, −6.3%
Pb–O[c] (Å)	2.50–3.28	2.48–3.02	2.50–2.92	−3.8–8.6%	−4.7–12.2%
Pb–X[c] (Å)	3.13–3.29	3.01–3.14	2.96–3.08	3.0–4.9%	3.8–7.0%
Ref.	[29]	ICSD #245774	ICSD #246036		

[a]The bonds and angles in BO_3 triangles
[b]The bonds and angles in BO_4 tetrahedra
[c]The bonds and angles in PbO_7I_2 monocapped hexagonal bipyramids

The crystallographic data comparison (Table 6) indicates small changes in the borate building units but somewhat obvious changes in the PbO_7I_2 units, especially the angle reduction for X–Pb–X on going from I^- to Br^- and Cl^- (up to −8.4% and −12.8%) and the elongation of Pb–O distances (up to 8.6% and 12.2%). These data suggest an enhancement of the SOJT distortion of the PbO_7I_2 polyhedron caused by the larger electronegativity difference between I^- and O^{2-} anions, which has also been revealed by the electronic structure studies.

3.3 *Electronic Structures*

The densities of states (DOS) of $Pb_2B_5O_9X$ (Fig. 3) were carefully examined to discern the bonding characters for VB and CB around E_F (Table 7). The B–O states, filled or unfilled, are hardly disturbed by the variation of X^-.

On the contrary, an unusual formation mechanism for the lone pairs on Pb^{2+} is uncovered. As commonly accepted, the sterically active lone pairs have been expected to be the result of the hybridization of Pb 6s and 6p orbitals. Recently, such a classical metal-based sp hybrid model has been revised based on the convincing theoretical and experimental evidences [35, 36]. That is, the indirect mixing of Pb 6s and 6p mediated by O 2p (in Pb/O polyhedra) accounts for the distorted lone pairs. In the present PbO_7X_2 polyhedra, the mechanism is more complicated due to the coordination of X^- anions. The symmetric and asymmetric electron distributions around Pb^{2+} originate from the Pb 6s–O 2p bonding interactions at VB-4 and the (Pb 6s–O 2p)–X np antibonding–antibonding interactions at VB-1, respectively (Fig. 4). And only the latter is responsible for the lone-pair effects. From Cl^- to I^-, VB-1 is dominated by O 2p, the mixture of O 2p and Br 4p, and I 5p, respectively. Such steadily variations indicate that

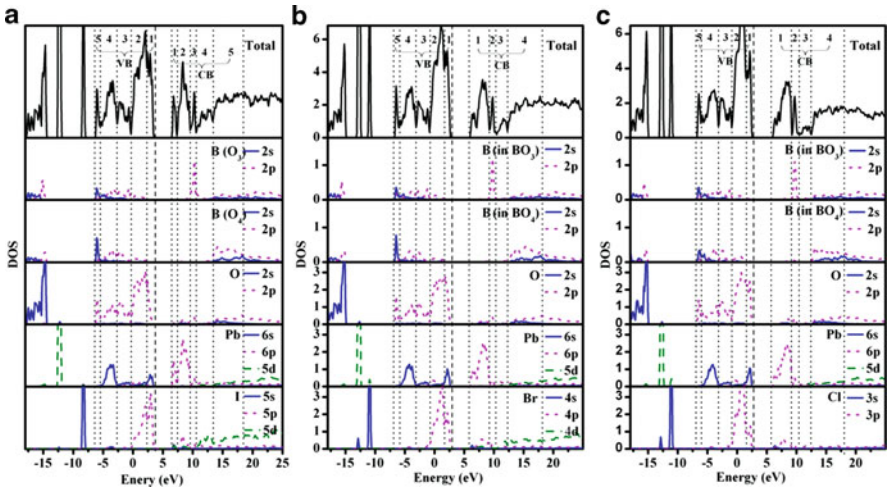

Fig. 3 Densities of states for $Pb_2B_5O_9X$ ($X^- = I^-$, Br^-, Cl^-). Adapted with permission from [29]. Copyright 2010 American Chemical Society

Table 7 Main orbital interactions around E_F for $Pb_2B_5O_9X$ ($X^- = I^-$, Br^-, Cl^-)

Band regions	NCS units		
	BO_3	BO_4	PbO_7X_2
CB-4	B 2p–O 2p	B 2p–O 2p	X nd
CB-3			X nd
CB-2		B 2p–O 2p	
CB-1			Pb 5p, X np
VB-1			(Pb 6s–O 2p)–X np
VB-2	O 2p	O 2p	O 2p, X np
VB-3	B 2p–O 2p	B 2p–O 2p	(Pb 6s–O 2p)–X np
VB-4	B 2p–O 2p	B 2p–O 2p	Pb 6s–O 2p
VB-5	B 2s–O 2p	B 2s–O 2p	

I^- anions with smaller electronegativity leads to a rapid enhancement of the lone-pair effects.

The other notable changes are the nonbonding X nd states. I 5d states with strong penetration effect disperse around the empty B–O states, at CB-3 and CB-4, where much less Br 4d are found (none Cl 3d).

3.4 Cutoff-Energy-Dependent SHG Coefficients

Cutoff-energy-dependent static SHG coefficients were studied to evaluate the local contributions from individual VB or CB regions. All the bands with energies higher than the negative cutoff or lower than the positive cutoff were included (Fig. 5).

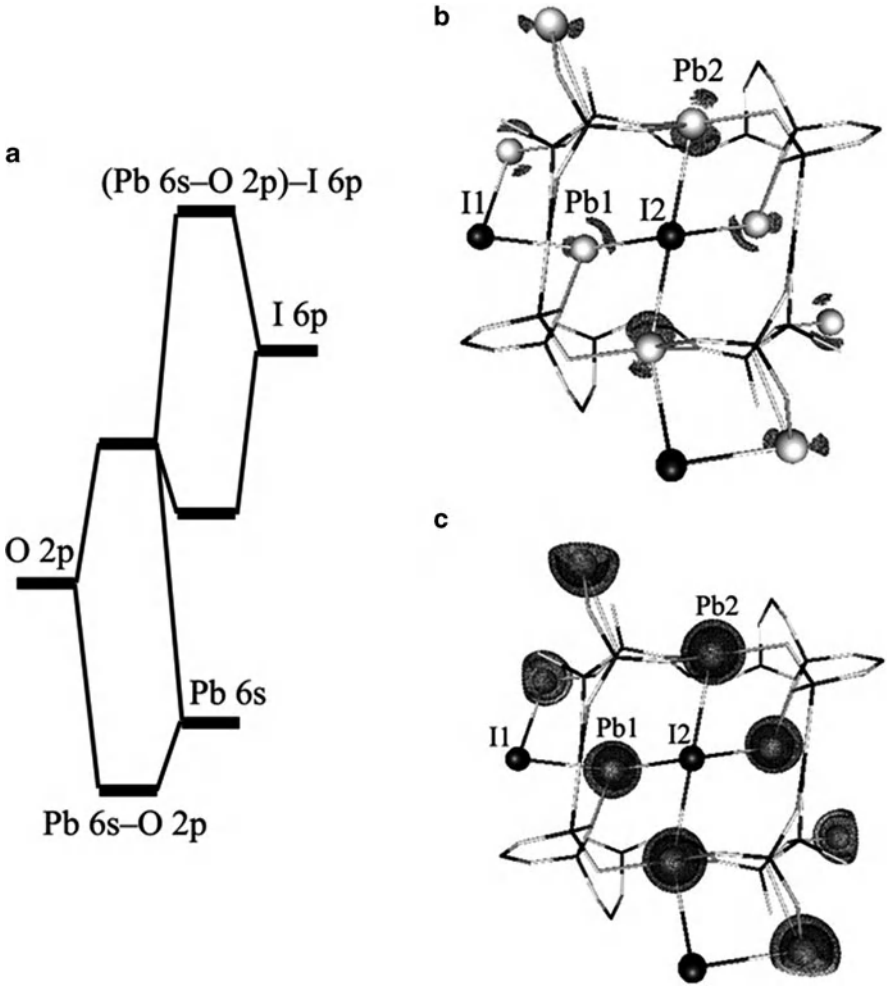

Fig. 4 (**a**) Schematic orbital interactions on the formation of Pb^{2+} lone pairs in $Pb_2B_5O_9I$. (**b**) Asymmetric electron distribution (>0.06 eV/Å^3) around Pb^{2+} at VB-1 region. (**c**) Symmetric electron distribution (>0.13 eV/Å^3) around Pb^{2+} at VB-4 region. Adapted with permission from [29]. Copyright 2010 American Chemical Society

The most significant contributions to the overall SHG coefficients in $Pb_2B_5O_9I$ come from the states at VB-1, CB-3, and CB-4. For $Pb_2B_5O_9Cl$ and $Pb_2B_5O_9Br$, three regions are similarly important but contribute much less in absolute values. These states are responsible for the significant improvement of the SHG activity in $Pb_2B_5O_9I$ compound. And a cooperation of Pb^{2+} (VB-1), I^- (VB-1, CB-3, CB-4), and B–O groups (CB-4) is concluded. Note that this mechanism could not be simply explained by the electronic transitions from Pb 6s or I 5p to I 5d and B–O states. Such a speculation has been excluded by a hypothetical "$Ba_2B_5O_9I$" model

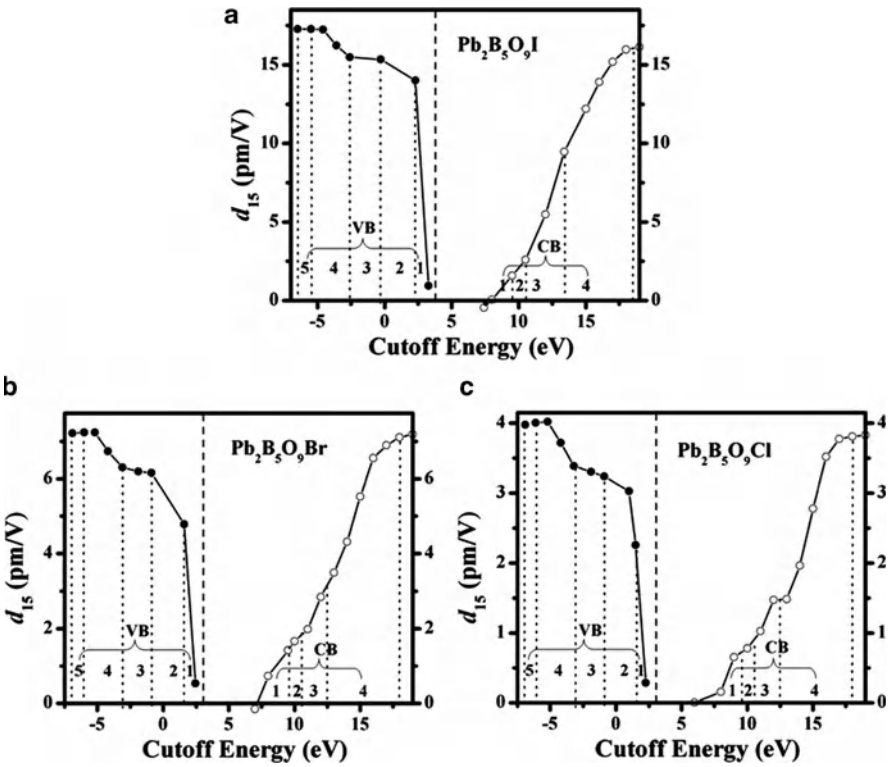

Fig. 5 Cutoff-energy-dependent static SHG coefficients for $Pb_2B_5O_9X$ ($X^- = I^-$, Br^-, Cl^-). Adapted with permission from [29]. Copyright 2010 American Chemical Society

constructed by the same crystallographic structure as that of $Pb_2B_5O_9I$ except the lone pairs. Such a model exhibits a very small coefficient of 3.2 pm/V, even smaller than 4.5 pm/V of $Pb_2B_5O_9Cl$. Consequently, I^- anions do not contribute independently to the SHG activity; instead, it cooperates with the lone-pair effects of Pb^{2+} and B–O groups.

4 Concluding Remarks

BBOSAG crystals exhibit a significant improvement on SHG response in comparison to BBO owing to the multiple cation doping. Whereas, the $Pb_2B_5O_9X$ series show sharp increase of SHG activity on going from $Cl^- < Br^- < I^-$, in which I^- anions participate in the lone-pair effect of Pb^{2+} cation. Cation and anion effects as well as their cooperation are important to SHG performance, which may serve as useful strategies to modify the properties of NLO materials and to design new NLO compounds.

Acknowledgments We are grateful for financial support from the National Natural Science Foundation of China under Projects (90922021, 21171168, 20733003, 20973175, 21103190), the "Knowledge Innovation Program of the Chinese Academy of Sciences" (KJCX2-YW-H20).

References

1. Becker P (1998) Adv Mater 10:979–992
2. Chen CT, Wu BC, Jiang AD et al (1985) Sci Sin B 28:235–243
3. Jiang AD (1985) Patent: CN851016170
4. Jiang AD (1992) Patent: CN927729211
5. Zhong WZ, Lu ZP, Zhao TD et al (1990) Patent: CN901028940
6. Zhong WZ, Lu ZP, Zhao TD et al (1999) Patent: ZL941122948
7. Tang DY, Wang YK, Yao ZJ et al (2002) Patent: ZL981047459
8. Chen CZ, Hong MC, Li D et al (2008) Patent: PCT/CN2008001379
9. Chen CZ, Hong MC, Li D et al (2008) Patent: PCT/CN2008072619
10. Chen CZ, Hong MC, Li D et al (2008) Patent: EP088766035
11. Chen CZ, Hong MC, Li D et al (2008) Patent: CN2008801299070
12. Halasyamani PS (2004) Chem Mater 16:3586–3592
13. Ok KM, Halasyamani PS, Casanova D et al (2006) Chem Mater 18:3176–3183
14. Kim SH, Yeon J, Halasyamani PS (2009) Chem Mater 21:5335–5342
15. Kong F, Huang S-P, Sun Z-M et al (2006) J Am Chem Soc 128:7750–7751
16. Ra HS, Ok KM, Halasyamani PS (2003) J Am Chem Soc 125:7764–7765
17. Zhang W-L, Cheng W-D, Zhang H et al (2010) J Am Chem Soc 132:1508–1509
18. Chang HY, Kim SH, Halasyamani PS et al (2009) J Am Chem Soc 131:2426–2427
19. Nguyen SD, Yeon J, Kim S-H et al (2011) J Am Chem Soc 133:12422–12425
20. Phanon D, Gautier-Luneau I (2007) Angew Chem Int Ed 46:8488–8491
21. Mao JG, Yang BP, Hu CL et al (2010) Chem Mater 22:1545–1550
22. Sun CF, Hu CL, Xu X et al (2009) J Am Chem Soc 131:9486–9487
23. Sykora RE, Ok KM, Halasyamani PS et al (2002) J Am Chem Soc 124:1951–1957
24. Chen CT, Wang GL, Wang XY et al (2009) Appl Phys B 97:9–25
25. Wang X, Zhang GC, Zhao Y et al (2007) Opt Mater 29:1658–1661
26. Zhang M, Pan S-L, Fan X-Y et al (2011) Cryst Eng Comm 13:2899–2903
27. Wu H, Pan S, Poeppelmeier KR et al (2011) J Am Chem Soc 133:7786–7790
28. Plachinda PA, Dolgikh VA, Stefanovich SY et al (2005) Solid State Sci 7:1194–1200
29. Huang YZ, Wu LM, Wu XT et al (2010) J Am Chem Soc 132:12788–12789
30. Rashkeev SN, Lambrecht WRL, Segall B (1998) Phys Rev B 57:3905–3919
31. Aversa C, Sipe JE (1995) Phys Rev B 52:14636–14645
32. Hsu WY, Kasowski RV (1993) J Appl Phys 73:4101–4103
33. French RH, Ling JW, Ohuchi FS et al (1991) Phys Rev B 44:8496–8502
34. Li J, Duan CG, Gu ZQ et al (1998) Phys Rev B 57:6925–6932
35. Watson GW, Parker SC (1999) J Phys Chem B 103:1258–1262
36. Payne DJ, Egdell RG, Walsh A et al (2006) Phys Rev Lett 96:157403

Index

A
$AgGaS_2$, 44
$AgGaSe_2$, 44
$AMoO_3(IO_3)$ (A = Rb^+, Cs^+), 49

B
$Ba_{1-x}B_{2-y-z}O_4$-$Si_xAl_yGa_z$ (BBOSAG), 183, 225
$Ba_3Bi\ (PO_4)_3$, 14
$BaMo_2TeO_9$, 70
$Ba_2NaNb_5O_{15}$ (BNN), 123
$BaNbO(IO_3)_5$, 59
$BaPd(IO_3)_4$, 64
Barium borate (BBO), 44, 223
β-Barium borate (β-BBO), 2, 206, 224
BBOSAG. *See* $Ba_{1-x}B_{2-y-z}O_4$-$Si_xAl_yGa_z$ (BBOSAG)
Beryllium borates, 181
$BiAlGa_2(BO_3)_4$ (BAGB), 202
$Bi_xLa_ySc_z(BO_3)_4$ (BLSB), 198
Borate crystals, 105, 121, 181, 223

C
$Ca_4GdO(BO_3)_3$ (GCOB), 123
$CaMg_3(CO_3)_4$ (huntite), 106, 124, 131, 182, 203
2-Carboxylic acid-4-nitropyridine-1-oxide (POA), 3
$Ca_4YO(BO_3)_3$ (YCOB), 123
$Cd_4BiO(BO_3)_3$, 28
$CeSc_3(BO_3)_4$, 183
Chromophores, π-charge asymmetrical distributions, 3
Cr^{3+}:$GdAl_3(BO_3)_4$ crystal, 130, 146
Cr^{3+}:$LaSc_3(BO_3)_4$, 110
Cross-superimposed laser crystal multiplier, 159
Crystal growth, 121, 181
$CsLiB_6O_{10}$ (CLBO), 206

D
Deep-UV, alkaline beryllium borates, 205
Densities of states (DOS), 229
Density functional theory calculations, 1
d^0-TM–I(V)–O systems, 57

E
Electronic effects, 223
Eulytite-type compounds, 14

F
Figure of merit (FOM), 2
Frequency-doubling coefficients, 2

G
$Ga_2(TeO_3)_3$, 98
$GdAl_3(BO_3)_4$ crystal, 121, 123, 129, 157
$Gd_xLa_ySc_z(BO_3)_4$ (GLSB), 193

H
Huntite $CaMg_3(CO_3)_4$, 106, 124, 131, 182, 203

I
Infrared tunable generation, 168
Iodates, 43, 44

K
$KBe_2B_3O_6$, 208
$KBe_2BO_3F_2$ (KBBF), 45, 92, 206
KH_2PO_4 (KDP), 44
$K_2Ti(IO_3)_6$, 58
$KTiOPO_4$ (KTP), 44
$K(VO)_2O_2(IO_3)_3$, 55
$KVO_2(IO_3)_2(H_2O)$, 53
$K(VO_2)_3(SeO_3)_2$, 71
$K_2Zn(IO_3)_4(H_2O)_2$, 65
KZn_4SbO_7, 20
$KZn_4Sb_3O_{12}$, 20

L
$LaBGeO_5$ (LBG), 123
$LaSc_3(BO_3)_4$, 106, 123, 183
$LaVO_2(IO_3)_4{\cdot}H_2O$, 57
LiB_3O_5 (LBO), 44, 206
$LiIO_3$, 44
$LiMoO_3(IO_3)$, 49
$LiNbO_3$, 44, 123
Lithium niobate (LN), 2
Lithium triborate (LBO), 2
Ln-d^0 TM–Se(IV)/Te(IV)–O system, 75
$LnMoO_2(OH)(IO_3)_4$, 51
$Ln_2MoTe_3O_{12}$, 76
$Ln_3Pb_3(IO_3)_{13}(\mu^3\text{-}O)$, 61
Lone pairs, 43
  cations, iodate groups, 60
$Lu_xLa_ySc_z(BO_3)_4$ (LLSB), 189

M
$M_2B_5O_9X$, 20
Metal chalcogenides, 44
Metal iodates, d^0 transition metal ions, 47
2-Methyl-4-nitroaniline (MNA), 12
$Mn(MoO_3)(SeO_3)(H_2O)$, 85
Mo(VI)–I(V)–O system, 48

N
$NaBeB_3O_6$, 207, 208
$Na_2CsBe_6B_5O_{15}$, 212
$Na_2Mo_3Te_3O_{16}$, 69
$Na_2Ti(IO_3)_6$, 58
$NaVO_2(IO_3)_2(H_2O)$, 52
$Na_2W_2TeO_9$, 69
$NaY(IO_3)_4$, 65
$NdAl_3(BO_3)_4$, 124
Nd^{3+}:$GdAl_3(BO_3)_4$ crystal, 130, 138
Niobates, 44
N-(4-Nitrophenyl)-(L)-prollnol (NPP), 12
4-Nitropyridine-1-oxide, 12
Noncentrosymmetricity (NCS), 1, 2, 43, 224
Nonlinear optical (NLO) crystals, 2, 44, 105, 181, 223

O
Optical parameter oscillator (OPO), 44

P
$Pb_2B_5O_9X$, 227, 231
$Pb_3Bi(PO_4)_3$, 14
Photophysical characterization, 1
Potassium titanyl phosphate (KTP), 2
Pyridine-2-carboxylic acid, 3

R
$RAl_3(BO_3)_4$, 105
$RbBe_2B_3O_7$, 210
$RbMoO_3(IO_3)$, 50
$RX_3(BO_3)_4$, 105, 124

S
Second-harmonic generation (SHG), 1, 43, 223
  cutoff-energy-dependent, 230
Second-order John–Teller (SOJT) effect/distortion, 2, 224
Selenites, 43
Self-difference-frequency mixing (SDFM) laser, 122
Self-frequency conversion, 121, 161, 175
Self-frequency doubling (SFD), 106, 161
Self-frequency tripling laser, 172
Self-sum-frequency mixing (SSFM), 122, 162
Stereochemically active lone pair (SCALP), 1, 2
Structural design, 1, 181
Sum-frequency mixing (SFM), 175

T
Tellurites, 43
Ti^{3+}:$YAl_3(BO_3)_4$, 109
$TmAl_3(BO_3)_4$ crystal, 121, 131
Tm^{3+}:$GdAl_3(BO_3)_4$ crystal, 132, 151

V
V(V)–I(V)–O system, 51

Y
$YAl_3(BO_3)_4$, 110, 123, 182
Yd^{3+}:$GdAl_3(BO_3)_4$ crystal, 141
$Y_xLa_ySc_z(BO_3)_4$ (YLSB), 183

Z
ZnO crystal, 20